STUDY ON THE ROLE OF IRON SPECIES IN PHOTO-RESPONSIVE MONTMORILLONITE COMPOSITES

張, 俐

九州大学
KYUSHU UNIVERSITY

STUDY ON THE ROLE OF IRON SPECIES IN PHOTO-RESPONSIVE MONTMORILLONITE COMPOSITES

By

Li Zhang

A thesis submitted to Kyushu University

for the degree of Doctor of Engineering

Department of Earth Resources Engineering

Graduate School of Engineering

Kyushu University

Fukuoka, Japan

September 2022

Abstract

Montmorillonite (Mt) is one of the most representative clay minerals, belonging to 2:1-type clay (smectite group) in which one octahedral Al–O(H) sheet is sandwiched by two tetrahedral Si–O sheets, and well known with its very high cation exchange capacity. Based on the structure and the properties, Mt sometimes plays an important role in environmental remediation of pollutants through adsorption and intercalation in nature. Montmorillonite has been also regarded as an ideal support for photocatalysts because of its great chemical and physical stabilities. In this case it can be possibly developed to the environmental remediation materials by combination with a natural photocatalyst like TiO_2 under solar energy, even though Mt is categorized to an insulator in itself which cannot act as a photocatalyst. Band gap engineering such as heteroatom doping was focused to improve optical properties of insulators and semiconductors by creating middle gap states, resulting in decrease in bandgap energy (*Eg*). However, heteroatom doping affects sometimes different ways in photocatalysts, that is, sometimes decrease in the crystallinity of the photocatalysts resulting in the decrease in the photocatalytic activity and sometimes generate the new electron trap states leading to increase in photocatalytic activity. Among of transition metal dopants, iron (Fe) is an ideal choice as a doping element because it is a common heavy metal in environments and known to control a number of geochemical cycles in nature. In the present work, the effects of location and localization of Fe^{III} on the photocatalytic mechanism for the composite of Mt with TiO_2 are studied using structural, optical, and electronical characterization techniques to propose the role of Fe species in photo-responsive montmorillonite composites.

In **Chapter 1**, the research background is introduced from both aspects of geochemistry and material sciences. The structures and properties for each component in the composites of titanium oxide (TiO_2) on Mt were described in detail in relation with the photocatalytic reactions. Anatase phase of TiO_2 is well known as a UV-responsive photocatalyst and Mt is one

type of clay minerals as well as one of natural 2D materials. Then, the target contaminant models used here were briefly introduced. Hereafter, the objectives of this study were explained. In **Chapter 2**, the methodologies used in the present work were described for synthesis and characterizations of the TiO_2-Mt composites and the Fe-doping procedures as well as solution analysis.

The potential photocatalytic activity of Mt after Fe^{III} doping was detected via the photocatalytic reduction of chromate ($Cr^{VI}O_4^{2-}$) in **Chapter 3**. Ferric ions (Fe^{III}) -doped Mt prepared by ion-exchange at pH 2 was verified by X-ray diffraction patterns (XRD), Fourier transformed infrared spectroscopy (FTIR), X-ray photoelectron spectroscopy (XPS), and X-ray absorption near edge structure (XANES). The Fe^{III} doping on Mt at a ratio less than 0.274 mmol-Fe^{III}/g-Mt gained the photocatalytic activity in photocatalytic reduction of Cr^{VI} into Cr^{III} on Fe-Mt, turning into a semiconductor from an insulator. On the other hand, the excess amounts of Fe^{III} doping caused the negative effects probably due to light shielding effect and reduction of active sites for the reaction. The *Eg* of Mt was lowered by generation of a new electron trap state between valence band and conduction band of Mt. This can explain the role of Fe in Fe/Mt as a photocatalyst.

Furthermore, in the composite of Mt with TiO_2, the location of Fe^{III} was investigated from an aspect of photocatalytic activity in **Chapter 4**, that is, whether Fe is located in Mt (Fe-Mt/TiO_2) or in TiO_2 (Mt/Fe-TiO_2). Diffused reflectance spectra (DRS), photo-luminescence spectra (PL), photocurrent (PC), and electrochemical impedance spectroscopy (EIS) measurements revealed that Fe-Mt/TiO_2 composite has greater optical properties, resulting in higher photocatalytic activity in phenol degradation than Mt/Fe-TiO_2 composite. This can be explained by migration of excited electrons from a newly generated electron trap state in Fe-Mt to TiO_2 via Z-scheme heterojunction. Also, the formation of heterojunction could avoid the recombination of photogenerated charge carriers, resulting in enhancement of phenol photocatalytic degradation.

Meanwhile, in Mt/Fe-TiO_2, there are no transportation of excited electrons from Mt side via the heterojunction in the composite, resulting in high recombination rate of electron-hole pairs in Fe-TiO_2 side, confirmed by PL.

A replenished study was added to further distinguish the structural Fe^{III} and surface adsorbed Fe^{III} on Mt/TiO_2 composites (*x*Fe-Mt/(1-*x*)Fe-TiO_2 and Fe/Mt/TiO_2) under the same dosage of Fe^{III}. **Chapter 5** compared these two Mt/TiO_2 composites. The photocatalytic activity was greater in the later than the former in phenol degradation, which was also supported by DRS, PL, PC and EIS results. In particular, energy-resolved distribution of electron traps (ERDT) patterns revealed that the amorphous rutile on crystal anatase was the dominant in the later composite (Fe/Mt/TiO_2) which is the most key component to control the photocatalytic activity, while it was lesser in the former one (*x*Fe-Mt/(1-*x*)Fe-TiO_2). Moreover, existence of Fe^{III} in TiO_2 structure disturbed crystallization of TiO_2 caused the formation of isolated TiO_2 which has less photocatalytic activity.

In **Chapter 6**, environmental implication of the present work was discussed, the conclusions of all chapters were summarized, and the accompanying new challenges were finally proposed.

Contents

STUDY ON THE ROLE OF IRON SPECIES IN PHOTO-RESPONSIVE MONTMORILLONITE COMPOSITES

List of tables

List of figures

Chapter 1

Introduction

1.1 Background

1.1.1 Photocatalytic remediation of wastewater

Recently, water shortages are becoming an increasing problem due to rapid industrial growth, environmental pollution, depleted water resources, global warming causing abnormal climate changes, and uncontrolled groundwater development [1], [2]. Organic compounds, toxic pesticides, and manure emissions from industry are polluting drinking and becoming a worldwide problem. The wide area of water pollution, diversification and non-biodegradable substance was tough be solved by the natural cleansing cycle [3]–[5]. In the case of water treatment technology, coagulation/precipitation [6]–[8], ion exchange [9]–[11], Fenton technology [12]–[14], electrochemical treatment [15]–[17], biological treatment [18]–[20] or other technique have been applied. However, these methods having the problem of intensive consumption of chemicals, production of secondary contaminations, pathological threatening, or other shortages. Photocatalysis can avoid these and effectively remove the pollutants.

1.1.2 Concepts and principles of photocatalysis

Photocatalysis was unanimously considered as the acceleration of a photoreaction in the presence of a catalyst [21]–[23]. It should be distinguished from photolysis and catalysis which are defined as a chemical reaction in which molecules are broken down by photons and a chemical reaction in which the reaction rate is accelerated without equilibrium changing.

The photolysis can be divided into homogeneous and heterogeneous photocatalysis. In the homogeneous photocatalysis process, all the reacting species exist in similar physical states either liquid, solid, or gas. The typical homogeneous photocatalysis are ozone (eq. 1.1-1.4) [24],

$$O_3 + h\nu \rightarrow O_2 + O(1D) \quad (1.1)$$

$$O(1D) + H_2O \rightarrow 2^{\bullet}OH \quad (1.2)$$

$$O(1D) + H_2O \rightarrow H_2O_2 \quad (1.3)$$

$$H_2O_2 + h\nu \rightarrow 2^{\bullet}OH \quad (1.4)$$

and photo-Fenton systems (Fe^{+} and Fe^{+}/H_2O_2) (eq. 1.5-1.9) [24], [25].

$$Fe^{2+} + H_2O_2 \rightarrow {}^{\bullet}OH + Fe^{3+} + OH^{-} \quad (1.5)$$

$$Fe^{3+} + H_2O_2 \rightarrow Fe^{2+} + 2^{\bullet}OH + H^{+} \quad (1.6)$$

$$Fe^{2+} + {}^{\bullet}OH \rightarrow Fe^{3+} + OH^{-} \quad (1.7)$$

$$H_2O_2 + h\nu \rightarrow 2^{\bullet}OH \quad (1.8)$$

$$Fe^{3+} + H_2O_2 + h\nu \rightarrow Fe^{2+} + {}^{\bullet}OH + H^{+} \quad (1.9)$$

Heterogeneous photocatalysis usually refers to a technology based on the irradiation of a semiconductor photocatalyst (**Fig. 1.1**). Several electronic and photochemical processes occur following the bandgap (*Eg*) excitation of a semiconductor. Absorption of light energy greater than or equal to the *Eg* of the semiconductor results in a shift of electrons (e^{-}) from the valence

band (VB) to the conduction band (CB) and the creation of holes (h^+) in the VB. The charge carriers rapidly diffuse to the surface or recombine where the resulting non-equilibrium distribution of electrons and holes gives rise to reduction or oxidation processes of adsorbed species, surface groups, and the semiconductor components. When illuminated with light of sufficient energy, the semiconductor particle becomes part of a particulate system capable of mimicking a micro-photoelectrochemical cell at which efficient reductive and oxidative processes may take place [26]. The efficiency of these processes is largely determined by five factors [27]: (1) efficient absorption of irradiation with minimal entropy production; (2) fast charge separation after light absorption; (3) separation of products in order to prevent reverse reactions; (4) adjustment of the redox potentials of the excited states to the redox reactions which store the energy; and (5) long-term stability or continuous reproduction. The dominant competitive process to charge separation is recombination, which for semiconductor clusters primarily occur via nonradiative processes. Two principal pathways have been established in mineralization of organic substrates and oxidation of inorganic materials. One considers surface OH^- groups or H_2O as the primary target(s) for the reaction of photogenerated holes, a reaction which yields hydroxyl radicals ($^{\bullet}OH$). The prevailing view favors these radicals as primary oxidizing species. The alternative route implicates direct hole oxidation of the organic substance [28]. Another pathway is e^- are scavenged by pre- and photo-adsorbed molecular oxygen to give superoxide radical anions ($^{\bullet}O_2^-$) [22].

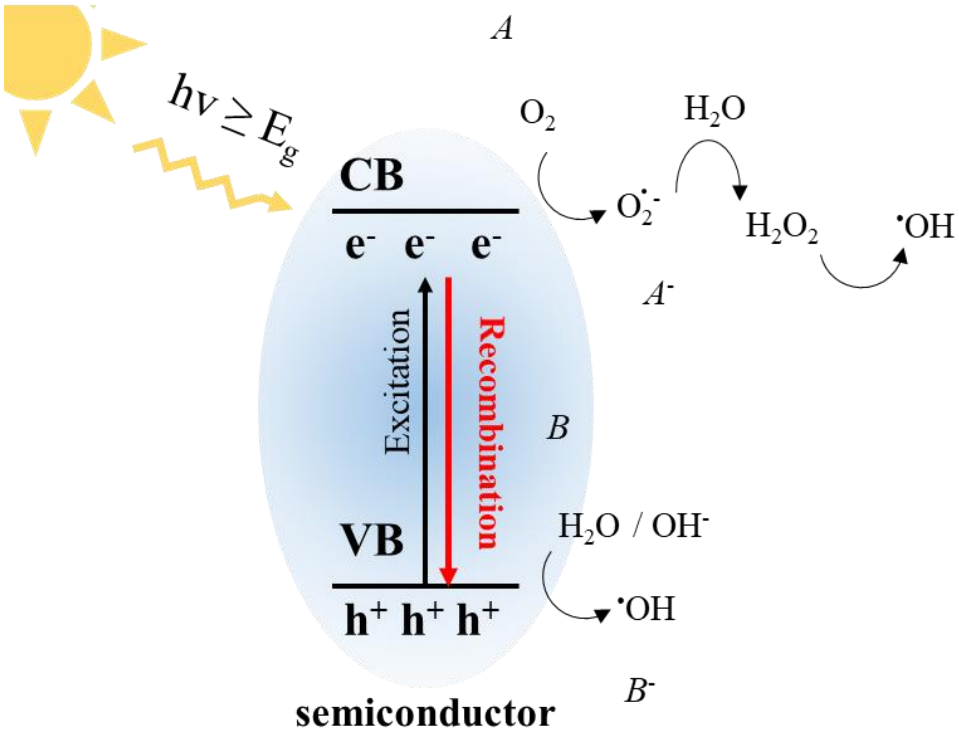

Fig. 1.1 General mechanism of photocatalysis on a semiconductor [29].

Fig. 1.2 illustrates bandgaps and band edge positions for several typical semiconductors and the regions of redox potential for the oxidation of organic groups to illustrate the thermodynamic limitations of the type of photoreactions that can be carried out with the photogenerated e^- and h^+. Thus, reduction of *A* substance (**Fig. 1.1**) occurs if the redox level of A lies below the CB level of the semiconductor. Similarly, if oxidation of *B* is to be carried out, its redox level must be positioned above the valence band of the semiconductor. When the redox level of *A* (or *B*) is located between the valence and conduction bands of the semiconductor, both reduction, and oxidation processes can occur.

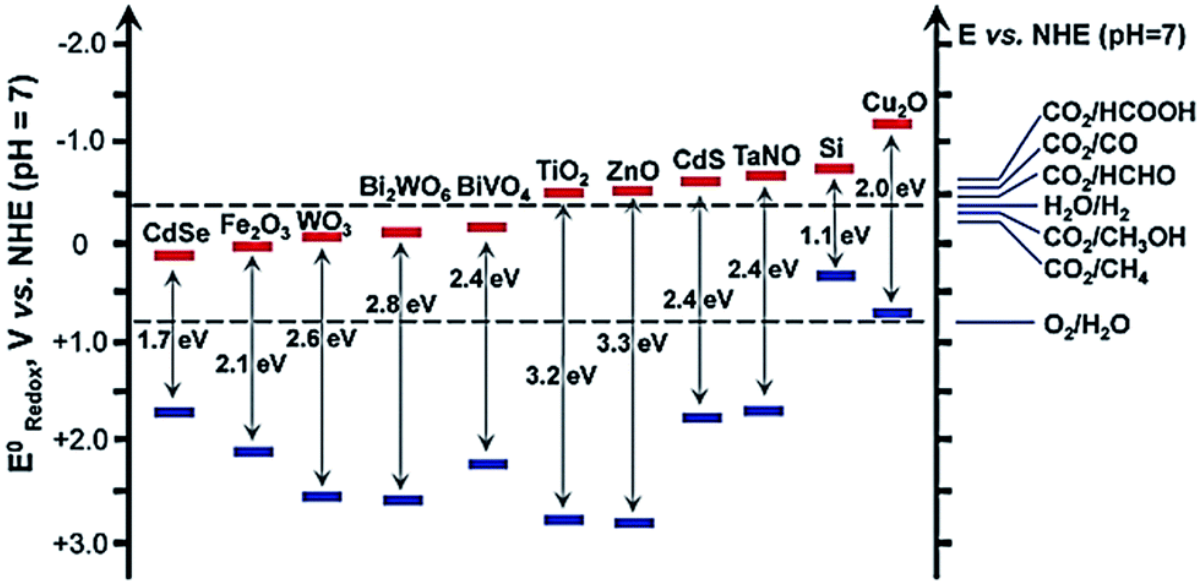

Fig. 1.2 Band-edge positions of some typical semiconductor photocatalysts relative to the energy levels of the redox couples involved in the reduction of CO_2 [30].

1.2 TiO_2 and TiO_2 based composites as photocatalyst

1.2.1. Abundance and occurrence of TiO_2 in nature

Titanium is the 9th most common element and the 7th most abundant metal in Earth's crust (0.63% by mass) [31]. Most igneous rocks, sediments generated from them, living creatures, and natural bodies of water all contain it in the form of oxides. It makes up 0.5 to 1.5% of soils [31]. In the ocean, titanium concentrations are about 4 picomolar, and little evidence of a biological function exists, however unusual species have been reported to acquire high titanium concentrations [32]. Common titanium-containing minerals are ilmenite, leucoxene, rutile, anatase, brookite, perovskite, etc. (**Table 1.1**) [33], [34].

Table 1.1 Titanium minerals, chemical compositions, and TiO_2 concentration [33].

Minerals	Composition	TiO_2 content (%)
Rutile	TiO_2 (tetragonal)	94-99
Anatase	TiO_2 (tetragonal, near octahedral)	90-95
Brookite	TiO_2 (orthorhombic)	90-100
Brookite	TiO_2 (orthorhombic)	90-100
Ilmenite	$FeTiO_3$	40-65
Leucoxene	$Fe_2O_3TiO_2$	60-90
Perovskite	$CaTiO_3$	40-60
Loparite	$(CeNaCa)(TiNb)O_3$	38
Titanite	$CaTiSiO_3$	30-42
Titaniferous magnetite	$(Fe{\cdot}Ti)_2O_3$	2-20

In 2021, about 8.4 million tons of titanium dioxide (TiO_2) pigments were mined. The main countries for TiO_2 mine production were China, the United States, the United Kingdom, Japan, Mexico, Australia, and others (ordered by TiO_2 pigment production). Ilmenite, leucoxene, and rutile were the most common TiO_2 ores, with annual output reported by the United States Geological Survey and given in **Table 1.2**. Anatase, ilmenite, and rutile deposits are estimated to be more than 2 billion tons [35].

Table 1.2 World production of titanium minerals concentrates, by country or locality (metric tons, by gross) [35].

Minerals	Australia	Brazil	China	India	South Africa	United States	World
Ilmenite and leucoxene	1,213	80[1]	3,830	510	N.A.	100	9,090
rutile	300	2[1]	N.A.	10	100[1]	N.A.[2]	803
Titanium slag	N.A.	N.A.	N.A.	N.A.	643	N.A.	1670

[1]Estimated.

[2]Included with ilmenite and leucoxene to avoid disclosing company proprietary data.

1.2.2. TiO_2 photocatalysis for remediation of wastewater

The most common compound of Ti is TiO_2 [36] which mainly occurs in nature as rutile, anatase, and brookite as shown in **Fig. 1.3**. All three types are, in general, composed of the TiO_6 octahedra with different distortions [37]–[40]. The characteristics of Ti-O bonds play very important roles in the properties of different TiO_2 phases (such as structural and electronic properties) [38].

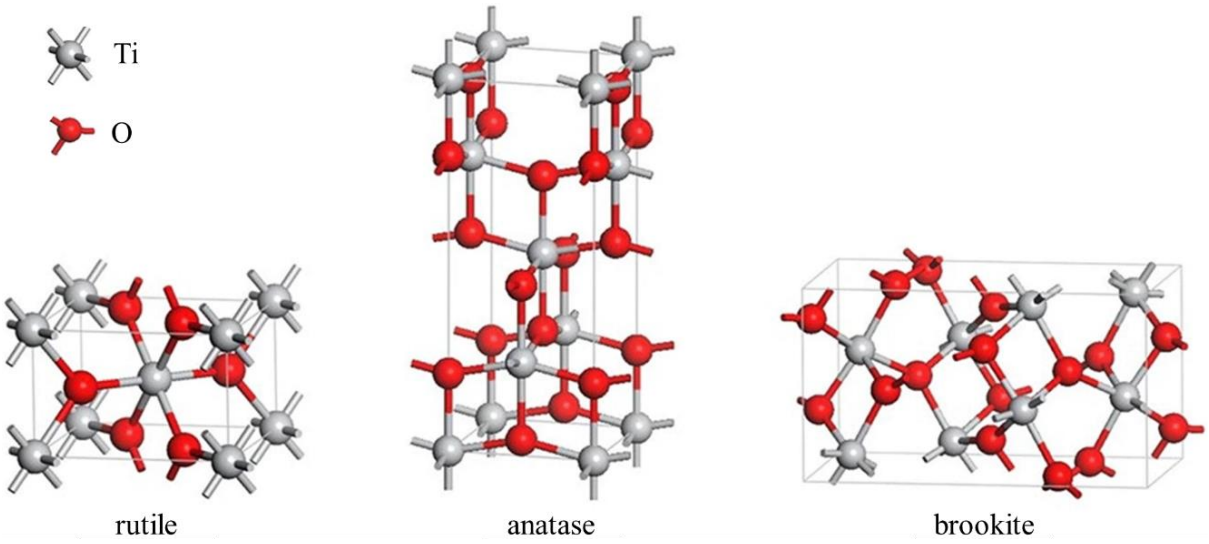

Fig. 1.3 Tetragonal structures of crystalline forms of rutile, anatase and brookite [40].

Compared with rutile, anatase has a higher surface area, resulting in more active sites. The concentration of oxygen vacancies on anatase nanoparticles is higher than on rutile nanoparticles, leading to an enhanced charge separation efficiency [41]. Furthermore, the larger *Eg* of anatase causes it to have a slightly higher redox capability than rutile. Because of these advantages, anatase is usually more active than rutile [41].

Charge separation in TiO_2 photocatalyst occurs rapidly after their generation upon light absorption as shown in **Fig. 1.4**. Unfortunately, ≈90% of photogenerated electron–hole pairs recombine rapidly after electron–hole pair separation, only less than 10% of separated electrons or holes could be used for semiconductor photocatalysts (including TiO_2) [42]. Generally, charge recombination occurs in the following two ways: irradiative and nonirradiative recombination. In the case of radiative recombination, the energy is emitted in the form of photons. A nonradiative pathway occurs via the emission of multiple phonons. For a TiO_2 photocatalyst, the nonradiative pathway is generally believed to be the major route of charge recombination, and adsorbates and additives can strongly affect the process [43].

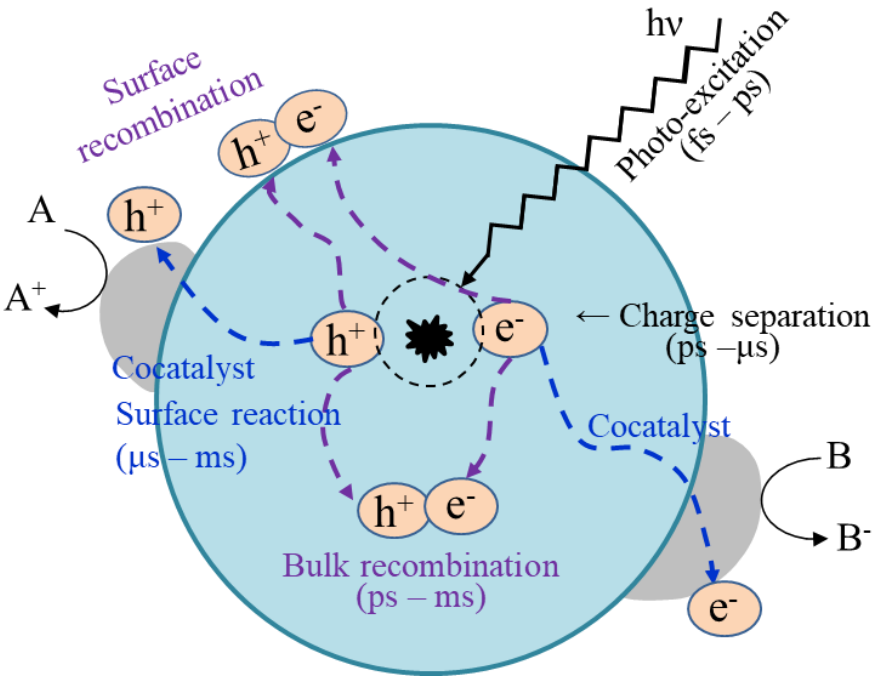

Fig. 1.4 Important processes in TiO_2 photocatalysis: electron–hole pair generation, charge transfer, electron–hole pair recombination in the bulk or at the surface, and electron and hole induced chemistry at the surface [44], [45].

Because nonradiative recombination usually occurs via the emission of multiple phonons, the direct detection of this process is generally considered to be impossible. However, using time-resolved photoacoustic spectroscopy (TRPAS) (an indirect method), Leytnar and Hupp [46] found that ≈60% of the charge recombination occurs in the nonradiative pathway in the colloidal anatase samples within 25 ns. Conversely, radiative recombination mainly contributes to light emission.

Charge recombination usually takes place following charge thermalization and trapping. Therefore, the energy of light emitted in radiative recombination is generally slightly smaller than the TiO_2 *Eg*. In principle, by analyzing the optical spectroscopies emitted from TiO_2 surfaces using the photoluminescence (PL) spectroscopy method, information about the dynamics and structural properties of TiO_2 related to charge carrier thermalization and trapping could be obtained. The combination of time-resolved PL, Time-resolved spectroscopy, and photoconductivity (PC) measurements of the dynamics of charge carrier decay in both the R-TiO_2(100) and A-TiO_2(100) surfaces have been studied by Yamada and Kanemits [47]. In rutile, the lifetimes of electrons and holes are a few tens of ns (24 ns for electron, 48 ns for hole). In contrast, in anatase, the holes decay rapidly within a few ns, and electrons exist in the TiO_2 CB for more than a few microseconds. These authors suggested that the long-living electrons may be beneficial for the high photoactivity of anatase. A similar result was also observed by Dozzi et al.[48].

Besides charge recombination as the main limitation of the TiO_2 photocatalyst, the large *Eg* and low adsorption ability of TiO_2 nanoparticles also reduced the photocatalytic activity of TiO_2. Therefore, much effort has been focused to solve these problems such as surface sensitization [49]–[51], metal nanoparticle deposition [52], [53], morphology modification [54], element doping [55]–[58], building heterojunction [41], composition with other materials, etc.

1.2.3. Heteroatom-doping on TiO_2

To modify TiO_2, doping or bandgap engineering principles are employed as shown in **Fig. 1.5**. The *Eg* of TiO_2 is formed by Ti 3d and 4s states and O 2p levels [59], [60], with the lower edge of the CB being formed by Ti d_{xy} and the upper edge of the CB being formed by O 2p.

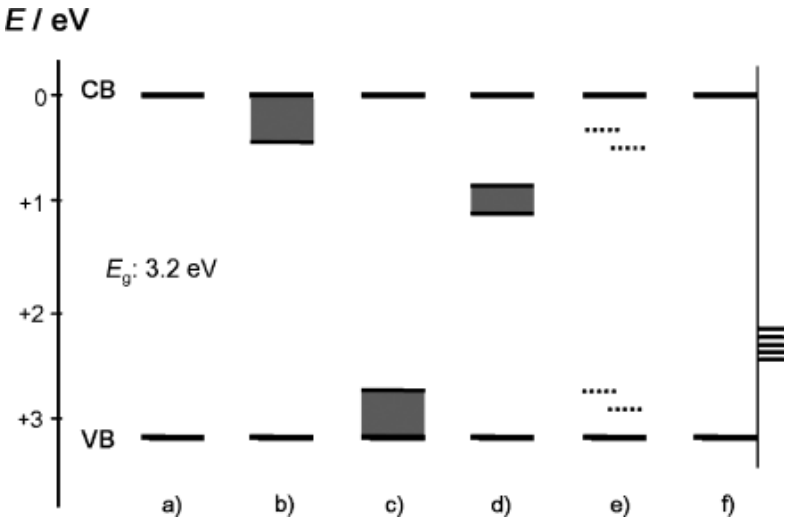

Fig. 1.5. Schematic illustration of the possibilities to alter the TiO_2 band structure: (a) pristine TiO_2, (b) conduction band (CB) lowering by state mixing, (c) valence band (VB) increase by state mixing, (d) creation of discrete band in the band gap, (e) discrete doping level, and (f) surface doping (sensitization).

Approaches for TiO_2 modification by doping cover a wide range of elements, such as transition-metal ions implantation and nonmetals doping. Metallic nanoparticles including Gd [61], La [62], Nd [58], Sm [63], Ce [64], [65], Er [66]–[69], Fe [56], [70], [71], Pt [72], [73], and Cu [74] have been used (**Table 1.3**) to enhance the photocatalytic activity on the TiO_2 surfaces by suppressing the e^-/h^+ recombination. The e^- migrates to the metal due to the relatively low Fermi level of metals, which makes the h^+ stable on the TiO_2 surfaces by increasing the lifetime of the charge carrier [75], [76]. Therefore, more $^{\bullet}OH$ and $^{\bullet}O_2^-$ are generated.

In addition to the characteristics discussed above, Fe^{III}-doped TiO_2 show greatly improved photocatalytic activity compared to crude TiO_2. Fe^{III} can be suitably inserted into the TiO_2 lattice structures because the ionic radius of Fe^{III} and Ti^{IV} is similar [77], [78]. The Fe^{III} doping on TiO_2 will influence the photocatalytic activity of TiO_2 mainly because that the photo-induced electrons and holes are separated by the doped Fe^{III} anchored on the TiO_2 surface, which suppresses recombination and promotes the generation of the hydroxyl radical. Despite numerous studies proposed a facilitate photocatalytic performance of iron doping on TiO_2 crystal [79]–[82], Zhijie Li et al. reported a rather reduced photocatalytic performance of amorphous Fe-TiO_2 than amorphous TiO_2. They believed that the Fe^{III} in matrix rather on surface, as suggested by the XPS, was mainly the reason for the phenomenon [83].

Moreover, the O in the TiO_2 lattice can be substituted with a range of heteroatoms, including B [57], [84], N [85]–[87], F [88], P [121], [122], S [89], [90], and co-doping of S-I [91] and W–N [92], etc. (**Table 1.4**), to take advantage of visible light in the TiO_2 photocatalysis. Furthermore, both metals and anions are introduced simultaneously to decompose organic contaminants by enhancing the photocatalytic activity of modified TiO_2 [129], [130].

Table 1.3 Comparison of the photocatalytic degradation rate of different organic pollutants on the cations doped/undoped TiO_2.

Material	Morphology	Light source	Target	Reaction time (min)	Degradation (%)		Year	Authors
					with doping	without doping		
Gd^{3+} doped TiO_2	Nanoparticles	00-W high-pressure mercury lamp	nitrate	60	99	80		An-Wu Xu et al. [61]
La^{3+} TiO_2	spherical	Sunlight	MB	240	80	30	2008	K.M. Parida [62]
Nd^{3+}-TiO_2	spherical	Fluorescent lamp (Germicid (254 nm))	Orange II	35	95	90	2009	Václav Štengl et al. [58]
Sm^{3+} doped TiO_2	spherical	UV light	MO	120	96	40	2016	G.V. Khade et al. [63]
Ce-doped TiO_2	Nano sheets	UV light	RB	120	95	85	2016	Zhenghun Fan et al. [64]
Er doped TiO_2/Poly(vinylidene difluoride)-co-trifluoroethylene	polyhedral shape	UV light	MB	110	97	81	2014	P. M. Martins et al. [66]

Er doped TiO_2		visible	phenol	180	75	45	2015	Joanna Reszczyńska et al. [68]
Er^{3+}:$YAlO_3$/Fe-doped TiO_2–ZnO	nubbly form	Solar light	Acid Red B	50	90.15	70.92	2011	Jingqun Gao et al. [67]
Er^{3+}:$YFeO_3$-doped TiO_2	Irregular	Visible light	MO	80	92	36	2012	Dianxun Hou et al. [69]
Fe^{3+} ion doping to TiO_2	spherical	Visible light	Malachite green	60	78	63	2009	Meltem Asiltürk et al. [56]
Fe–TiO_2	spherical	Visible light	Yellow XRG dye	480	37	18	2004	Jiefang Zhu et al. [70]
Fe^{3+}-doped TiO_2	porous microspheres	Visible light	Methyl orange	360	70	50	2008	Tianzhong Tong et al. [93]
ion doped TiO_2	spherical	UV light	Dichloro methane	120	88	82	2007	Wen-Chi Hung et al. [71]
Pt–TiO_2/zeolites	spherical	UV light	Methyl orange	90	98	90	2008	Miaoliang Huang et al. [73]
Pt–TiO_2	spherical		Acid green 16	60	100	98	2004	S Sakthivel et al. [72]
cerium doped TiO_2	mesoporous	Visible light	4-chloro-phenol	240	78	20	2006	Jiangrong Xiao et al. [65]
Cu,S-codoped TiO_2	spherical	Visible light	Methylene orange	45	100	70	2010	M. Hamadanian et al. [74]

Table 1.4 Comparison of the photocatalytic degradation rate of different organic pollutants on the heteroatoms doped/undoped TiO_2.

Material	Morphology	Light source	Target	Irradiation time (min)	Degradation (%)		Year	Author
					with doping	without doping		
B-doped TiO_2	spherical	Visible light	4-chlorophenol	240	78	20	2007	M. Bettinelli et al. [57]
boron-doped titania	spherical	UV light	Methylene blue	240	98	78	2009	Jingjing Xu et al. [84]
N-doped TiO_2	nanoparticles	Visible light	Methylene orange	60	14	1	2010	Shaozheng Hu et al.[87]
N-doped TiO_2	spherical	Visible light	4 chlorophenol	360	88	5	2010	J. Senthilnathan and Ligy Philip [86]
N-TiO_2	nanoparticles	UV light	Methylene orange	100	98	70	2008	Feng Peng et al. [85]
fluorinated TiO_2	spherical	UV light	Methylene blue	60	92	30	2009	Changlin Yu et al. [88]
S-doped TiO_2	nanoparticles	Visible light	Methylene blue	240	90	20	2009	Hua Tian et al. [90]
S-doped TiO_2	spherical	UV light	Phenol	240	93	83	2006	Wingkei Ho et al. [89]
S(2%)–I(2%)/TiO_2	spherical	Visible light	Salicylic acid	300	65	3	2010	Changlin Yu et al. [91]
W,N-TiO_2	spherical	Visible light	Acid orange 7	300	90	8	2008	Jingxia Li et al. [92]

1.2.4. TiO_2 composites for wastewater treatment

To enhance its adsorption capability and reduce its aggregation tendency a wide variety of materials have been used as supports for TiO_2 such as silica [94], activated carbon [95], carbon nanotube (CNT) [96], [97], C_xN_y [98], [99], zeolites [100] and clays. These support materials can provide high surface area, porosity, and reactive sites to TiO_2. They also hinder the aggregation of TiO_2 to enhances the recovery. Clays are easily available in the earth's crust, non-toxic, chemically stable, mechanically strengthen, and have porosity [101], [102].

Clays have gained a lot of popularity as supports for TiO_2. Pristine TiO_2 NPs, such as commercial Degussa P25, are less photoactive than clay supported TiO_2. The enhancement of photocatalytic activity can be due to the high surface area, adsorption capability, porosity, and presence of surface-active sites in TiO_2/clay nanocomposites [103]. The increase in photocatalytic activity is also due to lower charge recombination rate in TiO_2/clay nanocomposites. The decrease in charge recombination in TiO_2/clay nanocomposites by clay particles can be due to the presence of interlayer cations in clay which tend to trap electrons and let the holes free for oxidation [104]. Clay also enhances the reusable efficiency of TiO_2 by making it separable from the reaction mixture. Clay minerals such as montmorillonite (Mt), bentonite, montmorillonite, kaolinite, smectite, rectorite, hectorite, laponite, palygorskite, halloysite, attapulgite, diatomite and layered double hydroxides (LDH) have been utilized as TiO_2 supports.

Table 1.5 Comparative overview of different TiO_2/Mt nanocomposites for photodegradation of different pollutants [105].

Nanocomposite	Model organic pollutant	Reaction conditions	Degradation efficiency (%)	Reaction time (min)	Year	Author
Fe-TiO_2/Mt	β Naphthol	8 lamps each of 15 W emitting UV-A light ($\lambda = 365$ nm)	97	300	2016	Hazrat Ali and Ezzat Khan [106]
TiO_2/Aluminum Pillard Mt	Methylene Blue dye	lamps of 10 W each emitting UV-B light	N.A.	180	2017	Aakash C. Rai et. al [107]
TiO_2/Mt	Solophenyl red 3BL dye	250 W high pressure Hg lamp ($\lambda \geq 310$ nm)	95	220	2011	M. A. Meetani et. al [108]
Ag-TiO_2/Mt	Methylene blue	500 W high pressure Hg Lamp	>99	20	2015	Sammy W. Verbruggen [109]
TiO_2/Mt	Methylene blue	250 W High pressure Hg Lamp as UV light source	83	90	2015	Jaya Pala and Tarasankar Pal [110]
TiO_2/Mt	Methyl Orange	30 W UV lamp (254 nm)	>99	50	2013	N.R.Khalid et al. [111]

1.3 Clay minerals

1.3.1 Concepts, categories, structure, and mineralogy of clay minerals

The word “clay mineral” is difficult to define. As a first approximation, the phase implies a class of hydrated phyllosilicates (**Table 1.6**) making up the fine-grained portion of rocks, sediments, and soils. The definition offered is “…phyllosilicate minerals and minerals which lend flexibility to clay, and which harden upon drying or firing” [112].

Clays are layered phyllosilicate minerals that occur naturally in the earth’s crust and are important constituents of soils [113], [114]. Most of the clay minerals show plasticity depending upon the water content and harden up when dried [115]. It consists of a tetrahedral (T) silica sheet and an octahedral sheet of either gibbsite ($Al(OH)_3$) or brucite ($Mg(OH)_2$) stacked upon each other. Depending upon the number of silica sheets stacked to either octahedral gibbsite or brucite the clay minerals are classified into two types 1:1 and 2:1 [116]. The 1:1 clay layer consists of one tetrahedral silica sheet stacked to octahedral gibbsite or brucite sheet. The unit cell in the 1:1 layer structure has six octahedral sites (four cis-oriented octahedral sites and two trans-oriented octahedral sites) and four tetrahedral sites. Kaolinite is 1:1 clay consisting of tetrahedral silica and octahedral gibbsite sheet. On the other hand, 2:1 clay having two tetrahedral silica sheets and one octahedral gibbsite sheet. The 2:1 layer unit cell is characterized by the presence of six octahedral sites and eight tetrahedral sites. The trioctahedral structures are those in which all six octahedral sites are occupied at the same time

(**Fig. 1.6a**). The dioctahedral structure is referred to those in which only four of the six octahedra in a structure are used (**Fig. 1.6b**). When reporting the structural formula, it is often done so based on half-unit-cell content, which means that it is based on three octahedral sites. Isomorphic substitution of Al^{III} for Si^{IV} in tetrahedral silica sheet and Mg^{II} for Al^{III} in octahedral sheet gives rise to a negative charge on the clay surface and is balanced by the exchangeable cations in the interlayer space. Based upon the charge possessed by their surface clays can be classified as cationic or anionic groups. Cationic clay minerals consist of negatively charged aluminosilicate layers and contain positively charged cations in their interlayer space to balance the surface charge, and some of the clay minerals have interstitial water molecules [116], [117]. Smectites, as 2:1 phyllosilicate, have a total (negative) layer charge between 0.2 and 0.6 per half unit cell. A wide range of cations can occupy tetrahedral, octahedral, and interlayer positions. Commonly Si^{4+}, Al^{3+}, and Fe^{3+} are found in tetrahedral sites. Substitution of R^{3+} for Si^{4+} in tetrahedral sites creates an excess of negative charge on the three basal oxygens and the apical oxygen. This affects the total charge of the 2:1 layer as well as the local negative charge at the layer surface. Al^{3+}, Fe^{3+}, Fe^{2+}, Mg^{2+}, Ni^{2+}, Zn^{2+}, and Li^{+} generally occupy octahedral sites. These events have implications for many physical properties of smectites such as swelling and rheological behavior. On the other hand, anionic clays, such as layered double hydroxides (LDH), possessing positively charged surface are mostly synthetic and do not occur as crude clay mineral forms in nature [116].

Table 1.6. Classification of planar hydrous phyllosilicates [118].

Interlayer material	Group	Octahedral character	Species
1:1 Clay minerals			
None or H_2O only, ξ~0	Serpentine-kaolin	Tri	Amesite, berthierine, brindleyite, cronstedtite, fraipontite, kellyite, lizardite, nepouite
		Di	Dickite, halloysite (planar), kaolinite, nacrite
		Di-Tri	Odinite
2:1 Clay minerals			
None, ξ~0	Talc-pyrophyllite	Tri	Kerolite, pimelite, talc, willemsite
		Di	Ferripyrophyllite, pyrophyllite
Hydrated exchangeable cations, ξ~0.2-0.6	Smectite	Tri	Hectorite, saponite, sauconite, stevensite, swinefordite
		Di	Beidellite, montmorillonite, nontronite, volkonskoite
Hydrated exchangeable cations, ξ~0.6-0.9	Vermiculite	Tri	Trioctahedral vermiculite
		Di	Dioctahedral vermiculite
Non-hydrated monovalent cations, ξ~0.6-1.0	True(flexible) mica	Tri	Biotite, lepidolite, phlogopite, etc.
		Di	Celadonite, illite, glauconite, muscovite, paragonite, etc.
Non-hydrated divalent cations, ξ~1.8-2.0	Brittle mica	Tri	Anandite, bityite, clintonite, kinoshitalite
		Di	Margarite
Hydroxide sheet, ξ variable	Chlorite	Tri	Baileychlore, chamosite, clinochlore, nimite, pennantite
		Di	Donbassite
		Di-Tri	Cookeite, sudoite
Regularly interstratified 2:1 clay mineral			
ξ variable		Tri	Aliettite, corrensite, hydrobiotite, kulkeite
		Di	Rectorite, tosudite

[1]ξ, net layer charge per formula unit.

[2]tri, trioctahedral; di, dioctahedral.

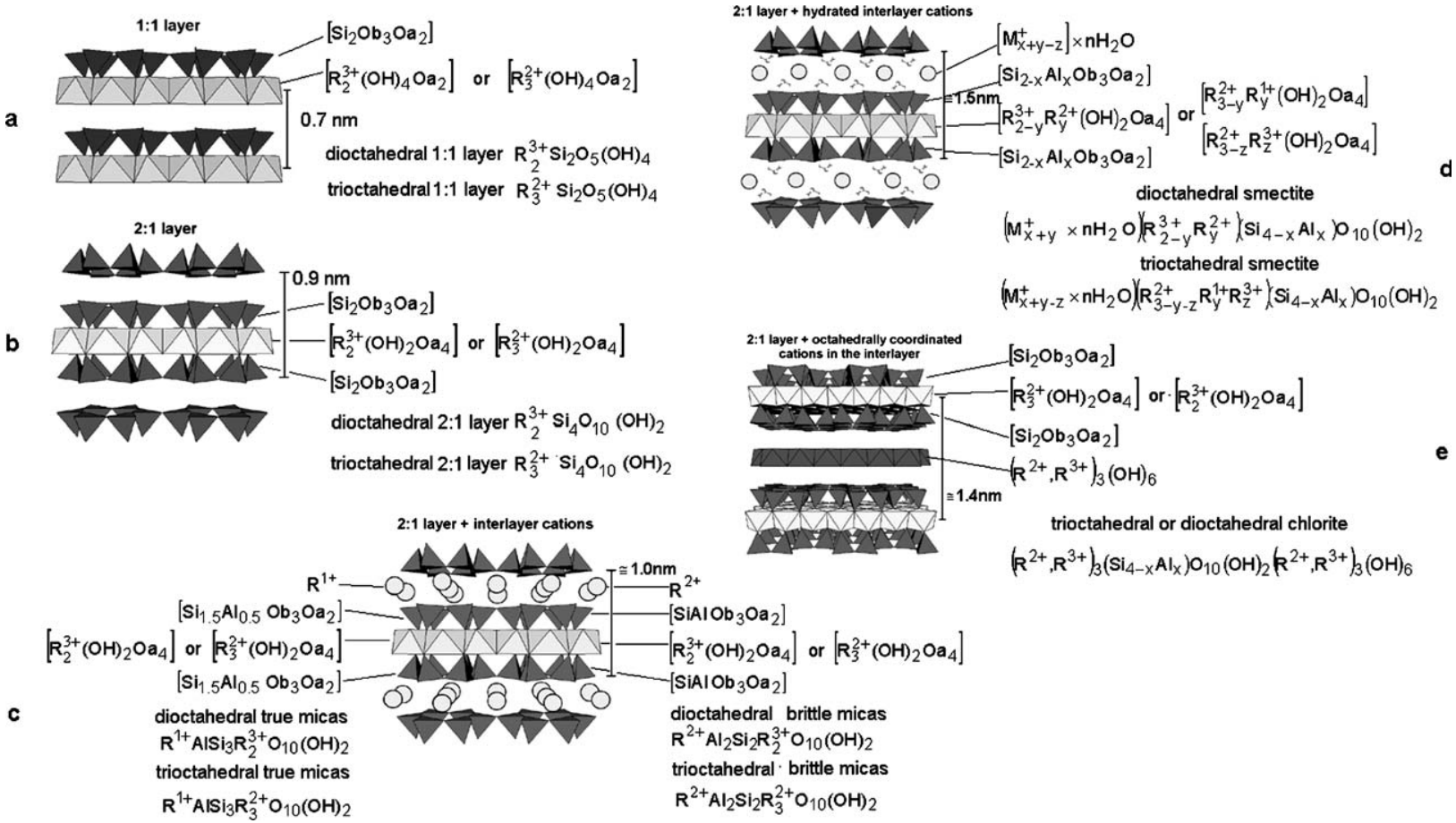

Fig. 1.6. Different layer structures: (a) 1:1 layer (i.e., kaolinite- and serpentine-like layer); (b) 2:1 layer (i.e., pyrophillite- and talc-like layer); (c) 2:1 layer with anhydrous interlayer cations (i.e., the mica-like layer); (d) 2:1 layer with hydrated interlayer cations (i.e., smectite- and vermiculite-like layer); (e) 2:1 layer with octahedrally coordinated interlayer cations (i.e., chlorite-like layer) [118].

1.3.2 Acidic activation of clay

Acidity in untreated smectites comes from two places: (i) compensating cations, which have polarizing effects on water molecules, most of which are in interlayer spaces and not easily accessible; (ii) specific sites at the layer edges, where unsaturated "broken" bonds occur; these may be compensated by OH group formation, leading to Brønsted acid sites such as Si–OH and also coordinately polarizing sites such as Si–OH.

Before attacking the layers, protons must first replace the exchangeable cations [119]. The exchange process occurs fast if the acid and smectite are in good contact and there are enough protons available. Proton-saturated smectites are more prone to rupture than metal-cation smectites. The layers of dried activated smectite are still attacked by surface and interlayer hydrated protons, just as in solution. 'Auto-transformation' occurs when H^{+}-smectites mature and spontaneously convert into their (Al^{III}, Fe^{III}, Mg^{II}) -forms [120]. The method requires 4 days using aqueous dispersion at 90°C [121].

1.3.3 Clay minerals and the origin of life

Aqueous modification of silicate minerals produces most clay minerals. Once liquid water is present on the earth's surface, clay minerals aggregate and distribute in the water reservoir, several prebiotic scenarios and experiments have utilized clays. Anyone who has seen mineral crystallization triggered by seeds in a supersaturated solution is inclined to connect life with mineral crystals. Complicated dislocation networks in crystals might sometimes resemble living units and rise to crystalline physiology [122].

There is no convincing reason to link the last common ancestor of organic molecules with first life, according to Cairns-Smith (1982) [123]. Despite the ease of availability to many biological building elements of life, the overwhelming utilization of these molecules in living creatures may be considered as a byproduct of evolution rather than a requirement. Cairns-Smith (1982)

argued that the earliest biological systems and chemical evolution may have used a different chemistry than we know today. Modern life's structural and functional complexity comes secondarily from a less efficient basic system with a larger chance of spontaneous assembly. This author recommended crystalline inorganic materials that may store and duplicate information in the form of defaults, dislocations, and replacements as genetic possibilities. These clay minerals crystallize from aqueous solutions of silicate rock weathering products at ambient temperatures. Cairns-Smith (1982) hypothesized the following scenario for mineral beginnings of life. Clays with favorable synthesis characteristics multiply, while replication faults proliferate.

Some non-clay species, such polyphosphates and tiny organic molecules, benefit from the development of rudimentary photochemical machinery. The organic chemicals produced by these clays may catalyze clay formation. Following particular adsorption, polymers of defined sequence form, initially serving merely structural functions. Based polynucleotides reproduce, generating supplementary genetic material. This secondary substance helps align amino acids during polymerization. Producing sequence-specific polypeptides and proteins also allows for the production of specialized enzymes. Eventually, the clay machinery is replaced by a polynucleotide-based replication–translation system. Although the potential sequence of events is detailed, it is not validated by experimental data.

A similar era saw the publication of a work by Armin Weiss (1981) of the Institute of Inorganic Chemistry in Munich [124]. A montmorillonite ($(Si,Al)_4O_{10}$) matrix with a 0.28 e/formula unit was selected. The breeding solution is concentrated to produce montmorillonites with isomorphous substitution of 0.42 e/formula unit. Charge density of D1-daughter first generation montmorillonite is 0.28 e/formula unit. In turn, the D1-generation serves as a template for the D2-generation synthesis. A charge density of 0.28 e/formula unit is the principal product up to the 10th generation. From the 16th to the 18th generation, mistakes

quickly grow. There is practically no material left with the initial value of 0.28e /formula unit. Although the quality of replication declines rapidly after the 20th generation, the trials show that clay minerals may replicate. Sadly, this publication is not replicated. Several requests for experimental information are made to the author. For this reason, the clay-mediated replication cannot be regarded established.

1.3.4 Property and behavior of Iron in clay

The structural Fe^{III} and Fe^{II} in smectite have both been shown to have a substantial effect on the smectite–water interaction. It was discovered that the cationic composition of the mineral layer has an impact on the swelling of smectite and that the presence of octahedral Fe^{III} has a minor but generally negative effect on the water retention capacity [125]. When the structural iron content is decreased, a more dramatic impact was discovered that the blue-grey form of Wyoming montmorillonite swelled to about half the water volume of the olive-green form, and that the Fe^{II}/Fe^{III} ratio of the blue-grey form was twice that of the olive-green form. When the blue-grey sample was reoxidized, the Fe^{II} concentration and swelling volume of the sample returned to their olive-green values [126]. Structural Fe^{II} had a lowering impact on the swelling of smectites [127]. Variations in the swelling of numerous reference clay minerals when they were reduced with pH-buffered sodium dithionite in the laboratory [128]. Similar findings have been reported for dithionite-reduced smectites [129]–[131], and for bacteria-reduced smectites [132]–[134].

Although our understanding of the exact mechanism by which structural Fe^{II} alters the hydration of clay mineral surfaces is still incomplete, the observations of Viani et al. [135], [136], Yan et al. [137], [138], Yan and Stucki [139], [140], Fialips et al. [141], [142], Wu et al. [143], and Cervini-Silva et al. [144], [145] provided convincing and self-contained evidence that interlayer H_2O molecules interact directly with the oxygen ions that comprise the basal

surfaces of clay mineral layers, and that this interaction is coupled with the vibrational energies of Si–O groups in a smectite hexahedral sheet. Through this interaction at the clay mineral–water interface, forces altering the structure of either the adsorbed H_2O or the Si–O tetrahedra would change the swelling of the clay mineral [135], [136], [139]–[142], [146], [147]. In addition, reduction of octahedral Fe^{III} to Fe^{II} affects both H_2O and the Si–O tetrahedra by disrupting the crystallographic structure of the tetrahedra. The electron density and proton attraction at the surface oxygen atoms (as revealed by increased Brønsted basicity) are increased as a result of the reduction of octahedral Fe^{III} to Fe^{II} [141], [142], [148], [149].

1.4 Geochemical significance of photocatalytic properties in Fe-doped montmorillonite

Most of the research recognized that clay only acts as a supporting material to improve the adsorption capacity of the pollutant, the surface to volume ratio during photocatalytic reaction, and the sedimentation properties but don't participate any photocatalytic reaction [150], [151]. However, some researchers also attempted to detect the possible mechanisms between the Mt and the semiconductors on the optical and photocatalytic aspect. As is proposed in 2016, in the Mt/g-C_3N_4 composite, the electron excited to the conduction band has electrostatic repulsion with the negative charge of Mt layers, enabling a more freely migrated electron-hole pairs to improve the efficiency of photocatalytic reaction [152]. Based on theoretical calculation, the intimate interface contacts between g-C_3N_4 and the clay mineral promises more charge carriers production, a faster carrier migration and more efficient separation [99]. In the composite ZnTi – LDH / clay with the existence of Fe^{III}/ Fe^{II}, a non-negligible promoting effect on the Cr^{VI} removal was achieved [153]–[155]. But these studies didn't independently discuss how the Mt performed the photocatalytic function in the photocatalytic reaction system. As a matter of fact, clay minerals including Mt have very large band gap and theoretically should only play as an insulating and supporting material in the composites [156]–[160]. The band gap of Mt is 5.3

eV [161].

For semiconductors, the large band gap can be reduced by element-doping [162]–[165]. By the DFT calculation, a new mid-gap electron trap state was generated by the doped ferric ions in sepiolite, and consequently, the photocatalytic efficiency of the ZnTi – LDH / clay samples were improved [166]. In this study, the ferric doped Mt was synthesized at pH 2 for only 1 hour. The main purpose to use this acidic condition is to avoid the precipitation of added Fe^{III} source. Based on previous reports, acid activation endued Mt the photocatalytic activate, but this treatment requires very strong acidic condition (usually the concentration of $H^+ > 1$ M) and long time (usually more than 12h) [167], [168]. Even though that the short time mild acid treatment did endue the photocatalytic property to the Fe-Mt, the acid solution should have little influence on the structure of Mt.

The iron element is widely distributed in the nature environment, such as in water and soil. The role of iron in the photocatalytic reaction arouses the researchers' interest. Within the knowledge of the author, there is no other research reported the photocatalytic activity Fe^{III} cations endowed the smectites, but other clay minerals itself with iron doping can act as a photocatalyst independently. A Zn/Fe LDH, where Zn^{II} and Fe^{III} have replaced Mg^{II} and Al^{III} in the hydrotalcite surface, has been observed to photodegrade various azo dyes more efficiently than bare Fe_2O_3 or ZnO under visible light. The authors proposed that this may be due to the important role that the Fe^{III} ions in the FeO_6 octahedrons of the Zn/Fe LDH structure have in the absorbance of visible light. Also, the hydroxide groups in the LDH capture the photo-induced holes (h^+) thus preventing the recombination of the hole and electron leading to enhanced photoactivity. Further, the authors also surmise that the LDH acts as a doped semiconductor with the dopant Fe(III) shifting the light absorbance towards the visible range [62]. Other researchers have attributed the prevention of recombination to the oxo-bridges between the two different metals in the brucite layer [169]. Similar structure can be formed in

Mt. However, these assumptions explaining the mechanisms of Cr^{VI} photoreduction are still controversial in the literatures. Therefore, it is essential for us to design and develop visible light active photocatalysts to efficiently reduce Cr^{VI} and clarify their mechanisms of Cr^{VI} photoreduction.

Moreover, the harmless Fe^{III}, Mt, and TiO_2 have the potential to be intensively utilized in practice and application field since no second contamination can be predict for the utilization of these materials. For example, the Fe^{III}, Mt, and TiO_2 constructed composite can be put into the remediation of photo-chemical smog since Fe^{III} doped TiO_2 has been intensively applied in the NOx remediation [170]–[172]. The three contents are also very abundant in nature. Thus, the highly possible combination could occur and trigger photocatalytic reaction to participate in the geochemical reaction in nature. The illustration for the occurrence and potential remediation function for the Fe^{III}, Mt, and TiO_2 combined composite in environment was shown in **Fig. 1.7**.

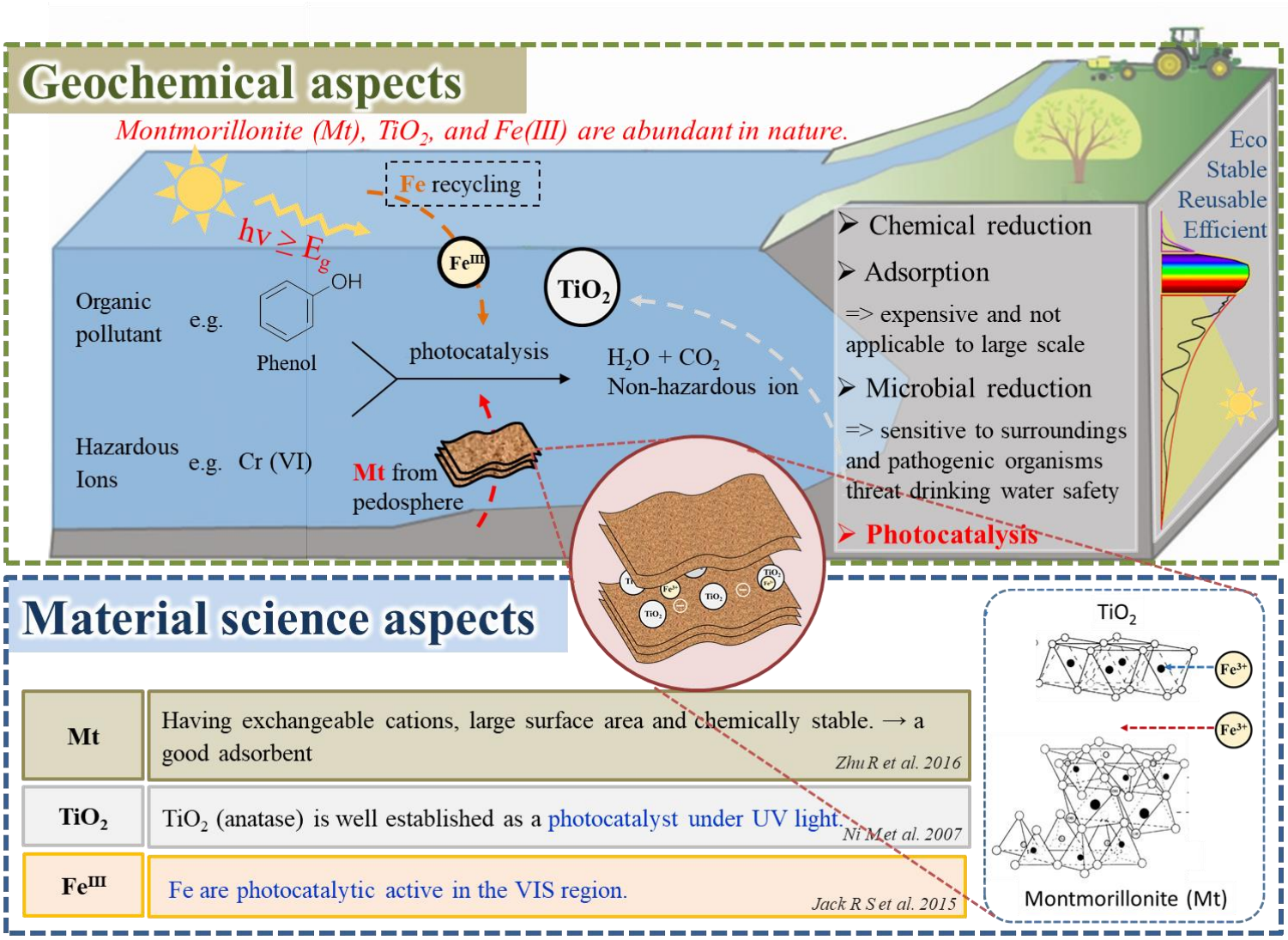

Fig. 1.7 Illustration of the geochemical significance of Fe^{III}, Mt, and TiO_2 composite.

1.5 Photocatalytic remediation for wastewater

1.5.1. Photocatalytic reduction for hexavalent chromium

It has long been recognized that the presence of heavy metals in aquatic bodies might result in pollution issues. The inappropriate discharge of diverse industrial wastewaters [173] is the most significant source of heavy metals [174]. Among the possible sources of chromium are the leather tanning industry, paints and dyes, photographic materials, steel alloy cement industries, mining, and other related sectors [175].

Chromium exists in a variety of valencies, the most prevalent of which are trivalent and hexavalent. The behavior of Cr-species is highly influenced by the condition of their oxidation. Chromite (VI) is a highly mobile and poisonous metal, while chromite (III) is a generally immobile and environmentally beneficial metal [175]. chromium is essential for life; nevertheless, a daily intake of 0.1–0.3 mg is needed for proper growth, and the quantity required may be obtained through a variety of foods and beverages. The trivalent form of chromium is required for plant and animal metabolism, but the hexavalent form of chromium is hazardous to humans, animals, and plants [176]. Moreover, since the chloride ion in Cr^{VI} salts does not easily precipitate or become attached to soil components, Cr^{VI} may flow freely throughout underground aquifers, contaminating ground water and other sources of drinking water, as well as posing a hazardous threat to animals and wildlife. Because the hexavalent form is more stable than the trivalent form, it may readily permeate through the cell membrane in animals, where it is retained within the cell by creating stable complexes with the other elements present. The chromium hexavalent form is 100 times more poisonous than the trivalent form [176]. The subsequent rise in chromium levels and concomitant rise in chromium intake express themselves in many metabolic illnesses such as dermatitis, nasal septal perforation and abortion, DNA damage, and ultimately cancer in a wide range of organs.

Chemical precipitation, reverse osmosis, ion exchange, foam flotation, electrolysis, photocatalytic reduction, adsorption, and other processes are used to remove hexavalent chromium from water. Other methods include adsorption. Although most of these ways involve a lot of energy or a lot of chemicals, it has been discovered that using the photocatalytic process is preferable than using any other approach out there.

The photocatalytic process in aqueous suspension of semiconductor has gained a great deal of interest in recent years, particularly in the context of solar energy conversion [177]. This photocatalytic technology was developed for the effective elimination of environmental contaminants in a short period of time. When the semiconductor–electrolyte interface is illuminated with light energy larger than the semiconductor band gap, electron–hole pairs (e^-–h^+) are generated in the semiconductor's conduction band and valence band, respectively [177], [178]. These charge carriers, which migrate to the semiconductor surface, are capable of reducing or oxidizing species in solution with an appropriate redox potential when they come into contact with the semiconductor surface. The transformation of Cr^{VI} into Cr^{III} results in a significant reduction in the bioavailability and toxicity of this element. In the literature, it has been reported that the photocatalytic reduction of Cr^{VI} with semiconductors such as CdS [179], ZnS, WO_3, ZnO [173], and TiO_2 [178] under UV light has occurred. Because of its inexpensive cost of manufacture and high activity, TiO_2 is proven to be an excellent photocatalyst among these materials.

1.5.2. Photocatalytic decomposition and mineralization for organic pollutants

Nanostructured semiconductors show great potential for environmental remediation because of photocatalytic oxidation, which is activated under the solar light or UV light [180]. Numerous organic pollutants are being released form manufacturers such as textile, paint, and leather into water bodies. The aquatic systems and human health may be seriously affected by

these organic effluents, which are extremely difficult to be degraded or eliminated by nature [181]. Several conventional methods such as biological methods, chemical precipitation, and membrane filtration are proposed for wastewater treatment. However, these methods may not always be very effective or feasible. A number of studies reported that microalgae can be cultivated to apply to wastewater treatment. However, when using microalgae, the wastewater effluent usually needs to be diluted several-fold before biological treatments. Microalgae are susceptible to concentrated toxicity, wastewater effluent may need to be diluted up to five-fold with synthetic media to reduce the toxicity before adding green algae. A study indicated that undiluted wastewater with a high NH_4–N concentration of 1197 mg/L could cause adverse effects on the photosynthesis of S. obliquus [182]. Biological process is also difficult to control, operators need to handle fluctuations in effluent composition and volumes because of variable wastewater composition and quantity [183], [184]. On the other hand, insufficient biodegradable potential is still existing for some of organic effluent [185], [186]. Chemical precipitation has been widely used in removal of contaminants from various wastewaters. Based on the composition of the wastewater, chemical precipitation can be used to remove ammonia (NH_4^+) and phosphate (PO_4^{3-}), etc. However, chemical precipitation poses several disadvantages: (1) high chemical consumption such as lime, oxidants, or H_2S; (2) physicochemical monitors such as pH are needed for the effluent; (3) high sludge generation [187]; (4) the excessive chemical usually causes a secondary pollution issue [188]. Membrane filtration is an alternative physical method for wastewater treatment [189]. Separation mechanisms depend on particle size, solubility, diffusivity, and charge. It has advantages of simple, effective, and rapid removal even at high concentrations of pollutants such as solids, microorganisms, inorganic matter, and phenols [190]. However, most of the commercial membranes are not considered semi-permeable, the membrane with the smallest pore size and reverse osmosis are not capable of restricting solute, especially for low molecular weight non-

charged organics [191]. In addition, in spite of high efficiency at lab scale, commercial scale investment costs including maintenance and operation costs are usually high for medium or small industries. Moreover, low throughput or low flow rates due to clogging or fouling problems, may limit some application for membrane separations at high concentrations of pollutants.

As a result, photocatalysis treatment has a lot of promise for organic pollution degradation [192]. In 1967, a claim was made for heterogeneous photocatalytic oxidation. A rutile TiO_2 electrode was chosen as a transition metal oxide with a sufficiently positive valence band to produce oxidation among a selection of transition metal oxides. Because it can be used under sun light, this notion has gotten a lot of press [193]. Then, to breakdown and mineralize certain harmful organic chemicals in wastewater, significant investigations were carried out. TiO_2 was found to be one of the most effective catalysts for removing organic molecules from aqueous solutions. Although numerous reviews have reviewed various photocatalysts for the application of eradicating microorganisms and hazardous chemical compounds in wastewater, few reviews have summarized organic pollutant degradation as a function of various process parameters under TiO_2-based photocatalysts. Through the degradation of organic pollutants under light irradiation, the process parameters of catalyst structure, supported type, pH value, particle size, dopant type, and dopant concentration will be comprehensively examined.

1.6 Objectives in the present work

The main purpose of the present work is to clarify the role of clay in the composite and detect the contribution of iron in the photocatalytic reaction. A heterojunction formed between main catalyst TiO_2 and the iron-doped clay was expected. To prove the effect of isomorphic substituted Fe^{III} and Fe^{II}, and adsorbed Fe^{III} and/or Fe^{II} in clay on photocatalytic reaction, the obtained iron-doped Mt will be combined with TiO_2 to make composites, and the composites

will be characterized by various methods including an emergent technique and applied in photocatalytic reaction. This work is the first time trying to illustrate the mechanism about how iron-doped Mt coordinate with the photocatalyst in the composite to improve the effectiveness not only by optimize the dispersion of the photocatalyst, but also construct a heterojunction with the main catalyst. Most previous studies just consider the Mt as the support material whose role is physically endowing a better dispersion of the main catalyst on it.

The basic investigation of the novelty and expected influence was described in **Chapter 1**. Firstly, the concept and principles about photocatalysis was introduced. Then, the TiO_2, Mt, and Fe^{III}, as the three dominant composite of the tentatively studied composites was mentioned. The hazardous of Cr^{VI} and phenol was finally illustrated.

Chapter 2 summarized all the solid and solution analysis methods.

In **Chapter 3**, Fe-Mt (Fe^{III}-doped montmorillonite) photocatalyzed Cr^{VI} redox process was explored. Unlike previous studies, the Fe-Mt synthesis was carried out in an acidic environment with a pH below 2 to avoid ferric oxides or ferric hydroxide. The synthesized Fe-Mt was used in theoretical calculations and characterization of the photocatalytic reaction to reveal the process mechanism. To the authors' knowledge, no research has been done on employing Fe^{III} -doped Mt for photocatalytic redox remediation of Cr^{VI}.

Chapter 4 describes how to make Fe-Mt/TiO_2, where Fe^{III} is first doped on Mt layers, and Mt/Fe-TiO_2, where Fe^{III} is first doped in TiO_2-$Ti(OH)_4$ sol-gel, then grown on Mt layers. The photocatalytic activity of two ferric-doped Mt/TiO_2 composites was investigated to establish the reaction mechanism.

In **Chapter 5**, he distribution of Fe^{III} on Mt/TiO_2 composites was controlled by varying the timing of Fe^{III} addition. Fe^{III} should always be cation. The Fe/Mt/TiO_2, where Fe^{III} was adsorbed in the surface of the composites, and *x*Fe-Mt/(1-*x*) Fe-TiO_2, where Fe^{III} was doped in the structure of the TiO_2, have been described by characterization, photocatalytic activity,

and photocatalytic reaction mechanisms.

The conclusion of the thesis and the outlook for the next step in the future was summarized in **Chapter 6**.

References

[1] M. Rodell, I. Velicogna, and J. S. Famiglietti, "Satellite-based estimates of groundwater depletion in India," *Nature 2009 460:7258*, vol. 460, no. 7258, pp. 999–1002, Aug. 2009, doi: 10.1038/nature08238.

[2] J. Tollefson, "How green is my future?," *Nature*, vol. 473, no. 7346, pp. 134–135, May 2011, doi: 10.1038/473134A.

[3] L. Tajeddine, M. Nemmaoui, H. Mountacer, A. Dahchour, and M. Sarakha, "Photodegradation of fenamiphos on the surface of clays and soils," *Environmental Chemistry Letters 2008 8:2*, vol. 8, no. 2, pp. 123–128, Jan. 2009, doi: 10.1007/S10311-008-0198-2.

[4] A. Biati, F. Moattar, A. R. Karbassi, and A. H. Hassani, "Role of saline water in removal of heavy elements from industrial wastewaters," *International Journal of Environmental Research*, vol. 4, no. 1, pp. 177–182, 2010.

[5] M. Heikkinen, H. Poutiainen, M. Liukkonen, T. Heikkinen, and Y. Hiltunen, "Subtraction analysis based on self-organizing maps for an industrial wastewater treatment process," *Mathematics and Computers in Simulation*, vol. 82, no. 3, pp. 450–459, Nov. 2011, doi: 10.1016/J.MATCOM.2010.10.021.

[6] Ö. Hanay and H. Hasar, "Effect of anions on removing Cu^{2+}, Mn^{2+} and Zn^{2+} in electrocoagulation process using aluminum electrodes," *Journal of Hazardous Materials*, vol. 189, no. 1–2, pp. 572–576, May 2011, doi: 10.1016/J.JHAZMAT.2011.02.073.

[7] L. ben Mansour and I. Kesentini, “Treatment of effluents from cardboard industry by coagulation-electroflotation,” *Journal of Hazardous Materials*, vol. 153, no. 3, pp. 1067–1070, May 2008, doi: 10.1016/J.JHAZMAT.2007.09.061.

[8] M. S. Tahir, M. Saleem, S. R. Malik, J. R. Khan, and M. Siebenhofer, “An innovative and advanced oxidation process for effluent treatment through wet tube-type electrostatic precipitation,” *Chemical Engineering and Processing: Process Intensification*, vol. 52, pp. 16–20, Feb. 2012, doi: 10.1016/J.CEP.2011.12.006.

[9] A. Antony, J. H. Low, S. Gray, A. E. Childress, P. Le-Clech, and G. Leslie, “Scale formation and control in high pressure membrane water treatment systems: A review,” *Journal of Membrane Science*, vol. 383, no. 1–2, pp. 1–16, Nov. 2011, doi: 10.1016/J.MEMSCI.2011.08.054.

[10] I. Ali, “Water Treatment by Adsorption Columns: Evaluation at Ground Level,” *http://dx.doi.org/10.1080/15422119.2012.748671*, vol. 43, no. 3, pp. 175–205, Jul. 2013, doi: 10.1080/15422119.2012.748671.

[11] “Adsorption Processes for Water Treatment - Samuel D. Faust, Osman M. Aly - Google book.” https://books.google.co.jp/books?hl=zh-CN&lr=&id=LwUcBQAAQBAJ&oi=fnd&pg=PP1&dq=adsorption+water+treatment&ots=8Qf4aT0VxW&sig=tB7rM7OTT9E-qSrhUDzavj_eKe8&redir_esc=y#v=onepage&q=adsorption%20water%20treatment&f=false (accessed May 02, 2022).

[12] O. B. Ayodele and B. H. Hameed, “Synthesis of copper pillared bentonite ferrioxalate catalyst for degradation of 4-nitrophenol in visible light assisted Fenton process,” *Journal of Industrial and Engineering Chemistry*, vol. 19, no. 3, pp. 966–974, May 2013, doi: 10.1016/J.JIEC.2012.11.018.

[13] P. Ghosh, A. N. Samanta, and S. Ray, “Reduction of COD and removal of Zn^{2+} from

rayon industry wastewater by combined electro-Fenton treatment and chemical precipitation," *Desalination*, vol. 266, no. 1–3, pp. 213–217, Jan. 2011, doi: 10.1016/J.DESAL.2010.08.029.

[14] G. Centi, S. Perathoner, T. Torre, and M. G. Verduna, "Catalytic wet oxidation with H_2O_2 of carboxylic acids on homogeneous and heterogeneous Fenton-type catalysts," *Catalysis Today*, vol. 55, no. 1–2, pp. 61–69, Jan. 2000, doi: 10.1016/S0920-5861(99)00226-6.

[15] Á. Anglada, A. Urtiaga, and I. Ortiz, "Contributions of electrochemical oxidation to waste-water treatment: fundamentals and review of applications," *Journal of Chemical Technology & Biotechnology*, vol. 84, no. 12, pp. 1747–1755, Dec. 2009, doi: 10.1002/JCTB.2214.

[16] B. P. Chaplin, "The Prospect of Electrochemical Technologies Advancing Worldwide Water Treatment," *Accounts of Chemical Research*, vol. 52, no. 3, pp. 596–604, Mar. 2019, doi: 10.1021/ACS.ACCOUNTS.8B00611/SUPPL_FILE/AR8B00611_SI_001.PDF.

[17] B. P. Chaplin, "Critical review of electrochemical advanced oxidation processes for water treatment applications," *Environmental Science: Processes & Impacts*, vol. 16, no. 6, pp. 1182–1203, May 2014, doi: 10.1039/C3EM00679D.

[18] E. J. Bouwer and P. B. Crowe, "Biological Processes in Drinking Water Treatment," *J Am Water Works Assoc*, vol. 80, no. 9, pp. 82–93, Sep. 1988, doi: 10.1002/J.1551-8833.1988.TB03103.X.

[19] B. E. Rittmann and P. M. Huck, "Biological treatment of public water supplies," *http://dx.doi.org/10.1080/10643388909388362*, vol. 19, no. 2, pp. 119–184, Jan. 2009, doi: 10.1080/10643388909388362.

[20] "Handbook Biological Waste Water Treatment - Design and Optimisation of ... - Google

book.” https://books.google.co.jp/books?hl=zh-CN&lr=&id=w-tsKUD23TsC&oi=fnd&pg=PR5&dq=biological+water+treatment&ots=OAClQ63GH5&sig=MCVYAyn9Kd01Mo3ktLYsxPj-Al0&redir_esc=y#v=onepage&q=biological%20water%20treatment&f=false (accessed May 02, 2022).

[21] J. Zhang, B. Tian, L. Wang, M. Xing, and J. Lei, “Photocatalysis,” vol. 100, 2018, doi: 10.1007/978-981-13-2113-9.

[22] N. Serpone, “Photocatalysis,” *Kirk-Othmer Encyclopedia of Chemical Technology*, Dec. 2000, doi: 10.1002/0471238961.1608152019051816.A01.

[23] I. Shafiq, S. Shafique, P. Akhter, G. Abbas, A. Qurashi, and M. Hussain, “Efficient catalyst development for deep aerobic photocatalytic oxidative desulfurization: recent advances, confines, and outlooks,” *https://doi.org/10.1080/01614940.2020.1864859*, 2021, doi: 10.1080/01614940.2020.1864859.

[24] Z. Moradi, S. Z. Jahromi, and M. Ghaedi, “Design of active photocatalysts and visible light photocatalysis,” *Interface Science and Technology*, vol. 32, pp. 557–623, Jan. 2021, doi: 10.1016/B978-0-12-818806-4.00012-7.

[25] M. B. Tahir, T. Iqbal, M. Rafique, M. S. Rafique, T. Nawaz, and M. Sagir, “Nanomaterials for photocatalysis,” *Nanotechnology and Photocatalysis for Environmental Applications*, pp. 65–76, Jan. 2020, doi: 10.1016/B978-0-12-821192-2.00005-X.

[26] N. Serpone, E. Borgarello, and E. Pelizzetti, “Utilization of the Semiconductor Particle as a Microphotoelectrochemical Cell: Electrochemical Evidence for Interparticle Electron Transfer and Application to Photocatalysis,” *Journal of The Electrochemical Society*, vol. 135, no. 11, p. 2760, Nov. 1988, doi: 10.1149/1.2095425.

[27] H. Gerischer, “Heterogeneous electrochemical systems for solar energy conversion,”

Pure and Applied Chemistry, vol. 52, no. 12, pp. 2649–2667, Jan. 1980, doi: 10.1351/PAC198052122649/MACHINEREADABLECITATION/RIS.

[28] R. B. Draper and M. A. Fox, "Titanium Dioxide Photooxidation of Thiocyanate. $(SCN)_2$~ Studied by Diffuse Reflectance Flash Photolysis," *J. Phys. Chem*, vol. 94, pp. 4628–4634, 1990, Accessed: May 02, 2022. [Online]. Available: https://pubs.acs.org/sharingguidelines

[29] K. H. Leong, L. C. Sim, S. Pichiah, and S. Ibrahim, "Light Driven Nanomaterials for Removal of Agricultural Toxins," pp. 225–242, 2016, doi: 10.1007/978-3-319-48009-1_9.

[30] Y. Yang, S. Ajmal, X. Zheng, and L. Zhang, "Efficient nanomaterials for harvesting clean fuels from electrochemical and photoelectrochemical CO_2 reduction," *Sustainable Energy & Fuels*, vol. 2, no. 3, pp. 510–537, Feb. 2018, doi: 10.1039/C7SE00371D.

[31] "The encyclopedia of the chemical elements : Hampel, Clifford A : Free Download, Borrow, and Streaming : Internet Archive." https://archive.org/details/encyclopediaofch00hamp/page/732/mode/2up (accessed Apr. 28, 2022).

[32] K. M. Buettner and A. M. Valentine, "Bioinorganic chemistry of titanium," *Chemical Reviews*, vol. 112, no. 3, pp. 1863–1881, Mar. 2012, doi: 10.1021/CR1002886/ASSET/IMAGES/MEDIUM/CR-2010-002886_0012.GIF.

[33] P. A. Demina, A. M. Zybinskii, G. M. Kuz'Micheva, L. N. Obolenskaya, E. v. Savinkina, and N. A. Prokudina, "Adsorption ability of samples with nanoscale anatase to extract Nb(V) and Ta(V) ions from aqueous media," *Crystallography Reports 2014 59:3*, vol. 59, no. 3, pp. 430–436, May 2014, doi: 10.1134/S1063774514030079.

[34] J. Emsley, "Naturés Building: An A-Z Guide to the Elements," p. 538, 2003, Accessed: Apr. 28, 2022. [Online]. Available: http://books.google.com/books?id=j-

Xu07p3cKwC&pgis=1

[35] “Titanium Statistics and Information | U.S. Geological Survey.” https://www.usgs.gov/centers/national-minerals-information-center/titanium-statistics-and-information (accessed Apr. 28, 2022).

[36] “The History and Use of Our Earth’s Chemical Elements: A Reference Guide - Robert E. Krebs - Google book.” https://books.google.co.jp/books?id=yb9xTj72vNAC&printsec=frontcover&hl=zh-CN&source=gbs_ge_summary_r&cad=0#v=onepage&q&f=false (accessed May 01, 2022).

[37] T. P. Feist and P. K. Davies, “The soft chemical synthesis of TiO_2 (B) from layered titanates,” *Journal of Solid State Chemistry*, vol. 101, no. 2, pp. 275–295, Dec. 1992, doi: 10.1016/0022-4596(92)90184-W.

[38] S. Nosheen, F. S. Galasso, and S. L. Suib, “Role of Ti-O bonds in phase transitions of TiO_2,” *Langmuir*, vol. 25, no. 13, pp. 7623–7630, Jul. 2009, doi: 10.1021/LA9002719/ASSET/IMAGES/MEDIUM/LA-2009-002719_0013.GIF.

[39] D. Dambournet, I. Belharouak, and K. Amine, “Tailored preparation methods of TiO_2 anatase, rutile, brookite: Mechanism of formation and electrochemical properties,” *Chemistry of Materials*, vol. 22, no. 3, pp. 1173–1179, Feb. 2010, doi: 10.1021/CM902613H/ASSET/IMAGES/MEDIUM/CM-2009-02613H_0012.GIF.

[40] E. Baranowska-Wójcik, D. Szwajgier, P. Oleszczuk, and A. Winiarska-Mieczan, “Effects of Titanium Dioxide Nanoparticles Exposure on Human Health—a Review,” *Biological Trace Element Research*, vol. 193, no. 1, pp. 118–129, Jan. 2020, doi: 10.1007/S12011-019-01706-6/TABLES/3.

[41] Y. Ma, X. Wang, Y. Jia, X. Chen, H. Han, and C. Li, “Titanium dioxide-based nanomaterials for photocatalytic fuel generations,” *Chemical Reviews*, vol. 114, no. 19,

pp. 9987–10043, Oct. 2014, doi: 10.1021/CR500008U/ASSET/IMAGES/MEDIUM/CR-2014-00008U_0040.GIF.

[42] M. R. Hoffmann, S. T. Martin, W. Choi, and D. W. Bahnemann, "Environmental Applications of Semiconductor Photocatalysis," *Chemical Reviews*, vol. 95, no. 1, pp. 69–96, 1995, doi: 10.1021/CR00033A004/ASSET/CR00033A004.FP.PNG_V03.

[43] A. Kudo and Y. Miseki, "Heterogeneous photocatalyst materials for water splitting," *Chemical Society Reviews*, vol. 38, no. 1, pp. 253–278, Dec. 2008, doi: 10.1039/B800489G.

[44] Q. Guo, C. Zhou, Z. Ma, and X. Yang, "Fundamentals of TiO_2 Photocatalysis: Concepts, Mechanisms, and Challenges," *Advanced Materials*, vol. 31, no. 50, p. 1901997, Dec. 2019, doi: 10.1002/ADMA.201901997.

[45] A. L. Linsebigler, G. Lu, and J. T. Yates, "Photocatalysis on TiO_2 Surfaces: Principles, Mechanisms, and Selected Results," *Chemical Reviews*, vol. 95, no. 3, pp. 735–758, 1995, doi: 10.1021/CR00035A013/ASSET/CR00035A013.FP.PNG_V03.

[46] S. Leytner and J. T. Hupp, "Evaluation of the energetics of electron trap states at the nanocrystalline titanium dioxide/aqueous solution interface via time-resolved photoacoustic spectroscopy," *Chemical Physics Letters*, vol. 330, no. 3–4, pp. 231–236, Nov. 2000, doi: 10.1016/S0009-2614(00)01112-X.

[47] Y. Yamada and Y. Kanemitsu, "Determination of electron and hole lifetimes of rutile and anatase TiO_2 single crystals," *Applied Physics Letters*, vol. 101, no. 13, p. 133907, Sep. 2012, doi: 10.1063/1.4754831.

[48] M. V. Dozzi, C. D'Andrea, B. Ohtani, G. Valentini, and E. Selli, "Fluorine-doped TiO_2 materials: Photocatalytic activity vs time-resolved photoluminescence," *Journal of Physical Chemistry C*, vol. 117, no. 48, pp. 25586–25595, Dec. 2013, doi: 10.1021/JP4095563/ASSET/IMAGES/LARGE/JP-2013-095563_0012.JPEG.

[49] J. van de Lagemaat and A. J. Frank, "Effect of the Surface-State Distribution on Electron Transport in Dye-Sensitized TiO_2 Solar Cells: Nonlinear Electron-Transport Kinetics," *Journal of Physical Chemistry B*, vol. 104, no. 18, pp. 4292–4294, May 2000, doi: 10.1021/JP000836O.

[50] J. Wang and Z. Lin, "Dye-sensitized TiO_2 nanotube solar cells with markedly enhanced performance via rational surface engineering," *Chemistry of Materials*, vol. 22, no. 2, pp. 579–584, Jan. 2010, doi: 10.1021/CM903164K/SUPPL_FILE/CM903164K_SI_001.PDF.

[51] J. Wang and Z. Lin, "Dye-Sensitized TiO_2 Nanotube Solar Cells: Rational Structural and Surface Engineering on TiO_2 Nanotubes," *Chemistry – An Asian Journal*, vol. 7, no. 12, pp. 2754–2762, Dec. 2012, doi: 10.1002/ASIA.201200349.

[52] V. Subramanian, E. Wolf, and P. v. Kamat, "Semiconductor−Metal Composite Nanostructures. To What Extent Do Metal Nanoparticles Improve the Photocatalytic Activity of TiO_2 Films?," *Journal of Physical Chemistry B*, vol. 105, no. 46, pp. 11439–11446, Nov. 2001, doi: 10.1021/JP011118K.

[53] M. Altomare and E. Selli, "Effects of metal nanoparticles deposition on the photocatalytic oxidation of ammonia in TiO_2 aqueous suspensions," *Catalysis Today*, vol. 209, pp. 127–133, Jun. 2013, doi: 10.1016/J.CATTOD.2012.12.001.

[54] K. Nakata and A. Fujishima, "TiO_2 photocatalysis: Design and applications," *Journal of Photochemistry and Photobiology C: Photochemistry Reviews*, vol. 13, no. 3, pp. 169–189, Sep. 2012, doi: 10.1016/J.JPHOTOCHEMREV.2012.06.001.

[55] W. Choi, A. Termin, and M. R. Hoffmann, "The role of metal ion dopants in quantum-sized TiO_2: correlation between photoreactivity and charge carrier recombination dynamics," *The Journal of Physical Chemistry*, vol. 98, no. 51, pp. 13669–13679, 2002.

[56] M. Asiltürk, F. Sayilkan, and E. Arpaç, "Effect of Fe^{3+} ion doping to TiO_2 on the

photocatalytic degradation of Malachite Green dye under UV and vis-irradiation," *Journal of Photochemistry and Photobiology A: Chemistry*, vol. 203, no. 1, pp. 64–71, Mar. 2009, doi: 10.1016/J.JPHOTOCHEM.2008.12.021.

[57] M. Bettinelli, V. Dallacasa, D. Falcomer, P. Fornasiero, V. Gombac, T. Montini, L. Romanò, and A. Speghini, "Photocatalytic activity of TiO_2 doped with boron and vanadium," *Journal of Hazardous Materials*, vol. 146, no. 3, pp. 529–534, Jul. 2007, doi: 10.1016/J.JHAZMAT.2007.04.053.

[58] V. Štengl, S. Bakardjieva, and N. Murafa, "Preparation and photocatalytic activity of rare earth doped TiO_2 nanoparticles," *Materials Chemistry and Physics*, vol. 114, no. 1, pp. 217–226, Mar. 2009, doi: 10.1016/J.MATCHEMPHYS.2008.09.025.

[59] S. di Mo and W. Y. Ching, "Electronic and optical properties of three phases of titanium dioxide: Rutile, anatase, and brookite," *Physical Review B*, vol. 51, no. 19, pp. 13023–13032, 1995, doi: 10.1103/PHYSREVB.51.13023.

[60] R. v. Kasowski and R. H. Tait, "Theoretical electronic properties of TiO_2 (rutile) (001) and (110) surfaces," *Physical Review B*, vol. 20, no. 12, pp. 5168–5177, 1979, doi: 10.1103/PHYSREVB.20.5168.

[61] A. W. Xu, Y. Gao, and H. Q. Liu, "The Preparation, Characterization, and their Photocatalytic Activities of Rare-Earth-Doped TiO_2 Nanoparticles," *Journal of Catalysis*, vol. 207, no. 2, pp. 151–157, Apr. 2002, doi: 10.1006/JCAT.2002.3539.

[62] K. M. Parida and N. Sahu, "Visible light induced photocatalytic activity of rare earth titania nanocomposites," *Journal of Molecular Catalysis A: Chemical*, vol. 287, no. 1–2, pp. 151–158, May 2008, doi: 10.1016/J.MOLCATA.2008.02.028.

[63] G. v. Khade, M. B. Suwarnkar, N. L. Gavade, and K. M. Garadkar, "Sol–gel microwave assisted synthesis of Sm-doped TiO_2 nanoparticles and their photocatalytic activity for the degradation of Methyl Orange under sunlight," *Journal of Materials Science:*

Materials in Electronics, vol. 27, no. 6, pp. 6425–6432, Jun. 2016, doi: 10.1007/S10854-016-4581-7/FIGURES/11.

[64] Z. Fan, F. Meng, J. Gong, H. Li, Z. Ding, and B. Ding, "One-step hydrothermal synthesis of mesoporous Ce-doped anatase TiO_2 nanoparticles with enhanced photocatalytic activity," *Journal of Materials Science: Materials in Electronics*, vol. 27, no. 11, pp. 11866–11872, Nov. 2016, doi: 10.1007/S10854-016-5329-0/FIGURES/9.

[65] J. Xiao, T. Peng, R. Li, Z. Peng, and C. Yan, "Preparation, phase transformation and photocatalytic activities of cerium-doped mesoporous titania nanoparticles," *Journal of Solid State Chemistry*, vol. 179, no. 4, pp. 1161–1170, Apr. 2006, doi: 10.1016/J.JSSC.2006.01.008.

[66] P. M. Martins, V. Gomez, A. C. Lopes, C. J. Tavares, G. Botelho, S. Irusta, and S. Lanceros-Mendez, "Improving photocatalytic performance and recyclability by development of Er-doped and Er/Pr-codoped TiO_2/Poly(vinylidene difluoride)-trifluoroethylene composite membranes," *Journal of Physical Chemistry C*, vol. 118, no. 48, pp. 27944–27953, Dec. 2014, doi: 10.1021/JP509294V/ASSET/IMAGES/LARGE/JP-2014-09294V_0011.JPEG.

[67] J. Gao, X. Luan, J. Wang, B. Wang, K. Li, Y. Li, P. Kang, and G. Han, "Preparation of Er^{3+}:$YAlO_3$/Fe-doped TiO_2–ZnO and its application in photocatalytic degradation of dyes under solar light irradiation," *Desalination*, vol. 268, no. 1–3, pp. 68–75, Mar. 2011, doi: 10.1016/J.DESAL.2010.09.052.

[68] J. Reszczyńska, T. Grzyb, J.W. Sobczak, W. Lisowski, M. Gazda, B. Ohtani, and A. Zaleska, "Visible light activity of rare earth metal doped (Er^{3+}, Yb^{3+} or Er^{3+}/Yb^{3+}) titania photocatalysts," *Applied Catalysis B: Environmental*, vol. 163, pp. 40–49, Feb. 2015, doi: 10.1016/J.APCATB.2014.07.010.

[69] D. Hou, L. Feng, J. Zhang, S. Dong, D. Zhou, and T. T. Lim, "Preparation,

characterization and performance of a novel visible light responsive spherical activated carbon-supported and Er^{3+}:$YFeO_3$-doped TiO_2 photocatalyst," *Journal of Hazardous Materials*, vol. 199–200, pp. 301–308, Jan. 2012, doi: 10.1016/J.JHAZMAT.2011.11.011.

[70] J. Zhu, W. Zheng, B. He, J. Zhang, and M. Anpo, "Characterization of Fe–TiO_2 photocatalysts synthesized by hydrothermal method and their photocatalytic reactivity for photodegradation of XRG dye diluted in water," *Journal of Molecular Catalysis A: Chemical*, vol. 216, no. 1, pp. 35–43, Jul. 2004, doi: 10.1016/J.MOLCATA.2004.01.008.

[71] W. C. Hung, S. H. Fu, J. J. Tseng, H. Chu, and T. H. Ko, "Study on photocatalytic degradation of gaseous dichloromethane using pure and iron ion-doped TiO_2 prepared by the sol–gel method," *Chemosphere*, vol. 66, no. 11, pp. 2142–2151, Feb. 2007, doi: 10.1016/J.CHEMOSPHERE.2006.09.037.

[72] S. Sakthivel, M. v. Shankar, M. Palanichamy, B. Arabindoo, D. W. Bahnemann, and V. Murugesan, "Enhancement of photocatalytic activity by metal deposition: characterisation and photonic efficiency of Pt, Au and Pd deposited on TiO_2 catalyst," *Water Research*, vol. 38, no. 13, pp. 3001–3008, Jul. 2004, doi: 10.1016/J.WATRES.2004.04.046.

[73] M. Huang, C. Xu, Z. Wu, Y. Huang, J. Lin, and J. Wu, "Photocatalytic discolorization of methyl orange solution by Pt modified TiO_2 loaded on natural zeolite," *Dyes and Pigments*, vol. 77, no. 2, pp. 327–334, Jan. 2008, doi: 10.1016/J.DYEPIG.2007.01.026.

[74] M. Hamadanian, A. Reisi-Vanani, and A. Majedi, "Synthesis, characterization and effect of calcination temperature on phase transformation and photocatalytic activity of Cu,S-codoped TiO_2 nanoparticles," *Applied Surface Science*, vol. 256, no. 6, pp. 1837–1844, Jan. 2010, doi: 10.1016/J.APSUSC.2009.10.016.

[75] V. Iliev, D. Tomova, and S. Rakovsky, "Nanosized N-doped TiO_2 and gold modied

semiconductors - photocatalysts for combined UV-visible light destruction of oxalic acid in aqueous solution," *Desalination*, vol. 260, no. 1–3, pp. 101–106, 2010, doi: 10.1016/J.DESAL.2010.04.058.

[76] M. Ni, M. K. H. Leung, D. Y. C. Leung, and K. Sumathy, "A review and recent developments in photocatalytic water-splitting using TiO_2 for hydrogen production," *Renewable and Sustainable Energy Reviews*, vol. 11, no. 3, pp. 401–425, Apr. 2007, doi: 10.1016/J.RSER.2005.01.009.

[77] X. Lu, Y. Ma, B. Tian, and J. Zhang, "Preparation and characterization of Fe-TiO_2 films with high visible photoactivity by autoclaved-sol method at low temperature," *Solid State Sciences*, vol. 13, no. 3, pp. 625–629, Mar. 2011, doi: 10.1016/J.SOLIDSTATESCIENCES.2010.12.036.

[78] N. Farhangi, R. R. Chowdhury, Y. Medina-Gonzalez, M. B. Ray, and P. A. Charpentier, "Visible light active Fe doped TiO_2 nanowires grown on graphene using supercritical CO_2," *Applied Catalysis B: Environmental*, vol. 110, pp. 25–32, Nov. 2011, doi: 10.1016/J.APCATB.2011.08.012.

[79] Y. Niu, M. Xing, J. Zhang, and B. Tian, "Visible light activated sulfur and iron co-doped TiO_2 photocatalyst for the photocatalytic degradation of phenol," *Catalysis Today*, vol. 201, no. 1, pp. 159–166, Mar. 2013, doi: 10.1016/J.CATTOD.2012.04.035.

[80] Q. Wu and R. van de Krol, "Selective photoreduction of nitric oxide to nitrogen by nanostructured TiO_2 photocatalysts: Role of oxygen vacancies and iron dopant," *J Am Chem Soc*, vol. 134, no. 22, pp. 9369–9375, Jun. 2012, doi: 10.1021/JA302246B/ASSET/IMAGES/LARGE/JA-2012-02246B_0007.JPEG.

[81] Y. Cong, J. Zhang, F. Chen, M. Anpo, and D. He, "Preparation, photocatalytic activity, and mechanism of nano-TiO_2 Co-doped with nitrogen and iron (III)," *Journal of Physical Chemistry C*, vol. 111, no. 28, pp. 10618–10623, Jul. 2007, doi:

10.1021/JP0727493/ASSET/IMAGES/LARGE/JP0727493F00009.JPEG.

[82] C. Y. Wang, D. W. Bahnemann, and J. K. Dohrmann, "A novel preparation of iron-doped TiO_2 nanoparticles with enhanced photocatalytic activity," *Chemical Communications*, no. 16, pp. 1539–1540, Jan. 2000, doi: 10.1039/B002988M.

[83] Z. Li, W. Shen, W. He, and X. Zu, "Effect of Fe-doped TiO_2 nanoparticle derived from modified hydrothermal process on the photocatalytic degradation performance on methylene blue," *Journal of Hazardous Materials*, vol. 155, no. 3, pp. 590–594, Jul. 2008, doi: 10.1016/J.JHAZMAT.2007.11.095.

[84] J. Xu, Y. Ao, M. Chen, and D. Fu, "Low-temperature preparation of Boron-doped titania by hydrothermal method and its photocatalytic activity," *Journal of Alloys and Compounds*, vol. 484, no. 1–2, pp. 73–79, Sep. 2009, doi: 10.1016/J.JALLCOM.2009.04.156.

[85] F. Peng, L. Cai, L. Huang, H. Yu, and H. Wang, "Preparation of nitrogen-doped titanium dioxide with visible-light photocatalytic activity using a facile hydrothermal method," *Journal of Physics and Chemistry of Solids*, vol. 69, no. 7, pp. 1657–1664, Jul. 2008, doi: 10.1016/J.JPCS.2007.12.003.

[86] J. Senthilnathan and L. Philip, "Photocatalytic degradation of lindane under UV and visible light using N-doped TiO_2," *Chemical Engineering Journal*, vol. 161, no. 1–2, pp. 83–92, Jul. 2010, doi: 10.1016/J.CEJ.2010.04.034.

[87] S. Hu, A. Wang, X. Li, and H. Löwe, "Hydrothermal synthesis of well-dispersed ultrafine N-doped TiO_2 nanoparticles with enhanced photocatalytic activity under visible light," *Journal of Physics and Chemistry of Solids*, vol. 71, no. 3, pp. 156–162, Mar. 2010, doi: 10.1016/J.JPCS.2009.10.012.

[88] C. Yu, J. C. Yu, and M. Chan, "Sonochemical fabrication of fluorinated mesoporous titanium dioxide microspheres," *Journal of Solid State Chemistry*, vol. 182, no. 5, pp.

1061–1069, May 2009, doi: 10.1016/J.JSSC.2009.01.033.

[89] W. Ho, J. C. Yu, and S. Lee, "Low-temperature hydrothermal synthesis of S-doped TiO_2 with visible light photocatalytic activity," *Journal of Solid State Chemistry*, vol. 179, no. 4, pp. 1171–1176, Apr. 2006, doi: 10.1016/J.JSSC.2006.01.009.

[90] H. Tian, J. Ma, K. Li, and J. Li, "Hydrothermal synthesis of S-doped TiO_2 nanoparticles and their photocatalytic ability for degradation of methyl orange," *Ceramics International*, vol. 35, no. 3, pp. 1289–1292, Apr. 2009, doi: 10.1016/J.CERAMINT.2008.05.003.

[91] C. Yu, D. Cai, K. Yang, J. C. Yu, Y. Zhou, and C. Fan, "Sol–gel derived S,I-codoped mesoporous TiO_2 photocatalyst with high visible-light photocatalytic activity," *Journal of Physics and Chemistry of Solids*, vol. 71, no. 9, pp. 1337–1343, Sep. 2010, doi: 10.1016/J.JPCS.2010.06.001.

[92] J. Li, J. Xu, W. L. Dai, H. Li, and K. Fan, "One-pot synthesis of twist-like helix tungsten–nitrogen-codoped titania photocatalysts with highly improved visible light activity in the abatement of phenol," *Applied Catalysis B: Environmental*, vol. 82, no. 3–4, pp. 233–243, Aug. 2008, doi: 10.1016/J.APCATB.2008.01.022.

[93] T. Tong, J. Zhang, B. Tian, F. Chen, and D. He, "Preparation of Fe^{3+}-doped TiO_2 catalysts by controlled hydrolysis of titanium alkoxide and study on their photocatalytic activity for methyl orange degradation," *Journal of Hazardous Materials*, vol. 155, no. 3, pp. 572–579, Jul. 2008, doi: 10.1016/J.JHAZMAT.2007.11.106.

[94] A. Mehta, A. Mishra, M. Sharma, S. Singh, and S. Basu, "Effect of silica/titania ratio on enhanced photooxidation of industrial hazardous materials by microwave treated mesoporous SBA-15/TiO_2 nanocomposites," *Journal of Nanoparticle Research 2016 18:7*, vol. 18, no. 7, pp. 1–9, Jul. 2016, doi: 10.1007/S11051-016-3523-X.

[95] M. Asiltürk and Ş. Şener, "TiO_2-activated carbon photocatalysts: Preparation,

characterization and photocatalytic activities," *Chemical Engineering Journal*, vol. 180, pp. 354–363, Jan. 2012, doi: 10.1016/J.CEJ.2011.11.045.

[96] W. Wang, P. Serp, P. Kalck, C. G. Silva, and J. L. Faria, "Preparation and characterization of nanostructured MWCNT-TiO_2 composite materials for photocatalytic water treatment applications," *Materials Research Bulletin*, vol. 43, no. 4, pp. 958–967, Apr. 2008, doi: 10.1016/J.MATERRESBULL.2007.04.032.

[97] K. Woan, G. Pyrgiotakis, and W. Sigmund, "Photocatalytic carbon-nanotube-TiO_2 composites," *Advanced Materials*, vol. 21, no. 21, pp. 2233–2239, Jun. 2009, doi: 10.1002/ADMA.200802738.

[98] N. Guo, Y. Zeng, H. Li, X. Xu, H. Yu, and X. Han, "Novel mesoporous TiO_2@g-C_3N_4 hollow core@shell heterojunction with enhanced photocatalytic activity for water treatment and H_2 production under simulated sunlight," *Journal of Hazardous Materials*, vol. 353, pp. 80–88, Jul. 2018, doi: 10.1016/J.JHAZMAT.2018.03.044.

[99] S. Luan, D. Qu, L. An, W. Jiang, X. Gao, S. Hua, X. Miao, S. Hua, X. Miao, Y. Wen, and Z. Sun, "Enhancing photocatalytic performance by constructing ultrafine TiO_2 nanorods/g-C_3N_4 nanosheets heterojunction for water treatment," *Science Bulletin*, vol. 63, no. 11, pp. 683–690, Jun. 2018, doi: 10.1016/J.SCIB.2018.04.002.

[100] M. N. Chong, Z. Y. Tneu, P. E. Poh, B. Jin, and R. Aryal, "Synthesis, characterisation and application of TiO_2–zeolite nanocomposites for the advanced treatment of industrial dye wastewater," *J Taiwan Inst Chem Eng*, vol. 50, pp. 288–296, May 2015, doi: 10.1016/J.JTICE.2014.12.013.

[101] A. Mishra, A. Mehta, M. Sharma, and S. Basu, "Enhanced heterogeneous photodegradation of VOC and dye using microwave synthesized TiO_2/Clay nanocomposites: A comparison study of different type of clays," *Journal of Alloys and Compounds*, vol. 694, pp. 574–580, Feb. 2017, doi: 10.1016/J.JALLCOM.2016.10.036.

[102] J. Pérez-Carvajal, P. Aranda, S. Obregón, G. Colón, and E. Ruiz-Hitzky, "TiO_2-clay based nanoarchitectures for enhanced photocatalytic hydrogen production," *Microporous and Mesoporous Materials*, vol. 222, pp. 120–127, Mar. 2016, doi: 10.1016/J.MICROMESO.2015.10.007.

[103] E. Manova, P. Aranda, M. Angeles Martín-Luengo, S. Letaïef, and E. Ruiz-Hitzky, "New titania-clay nanostructured porous materials," *Microporous and Mesoporous Materials*, vol. 131, no. 1–3, pp. 252–260, Jun. 2010, doi: 10.1016/J.MICROMESO.2009.12.031.

[104] M. Tahir and N. A. S. Amin, "Photocatalytic reduction of carbon dioxide with water vapors over montmorillonite modified TiO_2 nanocomposites," *Applied Catalysis B: Environmental*, vol. 142–143, pp. 512–522, Oct. 2013, doi: 10.1016/J.APCATB.2013.05.054.

[105] A. Mishra, A. Mehta, and S. Basu, "Clay supported TiO_2 nanoparticles for photocatalytic degradation of environmental pollutants: A review," *Journal of Environmental Chemical Engineering*, vol. 6, no. 5, pp. 6088–6107, Oct. 2018, doi: 10.1016/J.JECE.2018.09.029.

[106] H. Ali and E. Khan, "Environmental chemistry in the twenty-first century," *Environmental Chemistry Letters 2016 15:2*, vol. 15, no. 2, pp. 329–346, Dec. 2016, doi: 10.1007/S10311-016-0601-3.

[107] A. C. Rai, P. Kumar, F. Pilla, A.N. Skouloudis, S.D. Sabatino, C. Ratti, A. Yasar, and D. Rickerby, "End-user perspective of low-cost sensors for outdoor air pollution monitoring," *Science of The Total Environment*, vol. 607–608, pp. 691–705, Dec. 2017, doi: 10.1016/J.SCITOTENV.2017.06.266.

[108] M. A. Meetani, M. A. Rauf, S. Hisaindee, A. Khaleel, A. Alzamly, and A. Ahmad, "Mechanistic studies of photoinduced degradation of Orange G using LC/MS," *RSC Advances*, vol. 1, no. 3, pp. 490–497, Sep. 2011, doi: 10.1039/C1RA00177A.

[109] S. W. Verbruggen, "TiO_2 photocatalysis for the degradation of pollutants in gas phase: From morphological design to plasmonic enhancement," *Journal of Photochemistry and Photobiology C: Photochemistry Reviews*, vol. 24, pp. 64–82, Sep. 2015, doi: 10.1016/J.JPHOTOCHEMREV.2015.07.001.

[110] J. Pal and T. Pal, "Faceted metal and metal oxide nanoparticles: design, fabrication and catalysis," *Nanoscale*, vol. 7, no. 34, pp. 14159–14190, Aug. 2015, doi: 10.1039/C5NR03395K.

[111] N. R. Khalid, E. Ahmed, Z. Hong, M. Ahmad, Y. Zhang, and S. Khalid, "Cu-doped TiO_2 nanoparticles/graphene composites for efficient visible-light photocatalysis," *Ceramics International*, vol. 39, no. 6, pp. 7107–7113, Aug. 2013, doi: 10.1016/J.CERAMINT.2013.02.051.

[112] s. Guggenheim and R. T. Martin, "Definition of clay and clay mineral: joint report of the AIPEA and CMS Nomenclature Committees," *Clay Minerals*, vol. 30, no. 3, pp. 257–259, Sep. 1995, doi: 10.1180/CLAYMIN.1995.030.3.09.

[113] B. Mueller, "Experimental Interactions Between Clay Minerals and Bacteria: A Review," *Pedosphere*, vol. 25, no. 6, pp. 799–810, Dec. 2015, doi: 10.1016/S1002-0160(15)30061-8.

[114] C. de S. F. Gomes and J. B. P. Silva, "Minerals and clay minerals in medical geology," *Applied Clay Science*, vol. 36, no. 1–3, pp. 4–21, Apr. 2007, doi: 10.1016/J.CLAY.2006.08.006.

[115] M. K. Uddin, "A review on the adsorption of heavy metals by clay minerals, with special focus on the past decade," *Chemical Engineering Journal*, vol. 308, pp. 438–462, Jan. 2017, doi: 10.1016/J.CEJ.2016.09.029.

[116] M. Ghadiri, W. Chrzanowski, and R. Rohanizadeh, "Biomedical applications of cationic clay minerals," *RSC Advances*, vol. 5, no. 37, pp. 29467–29481, Mar. 2015, doi:

10.1039/C4RA16945J.

[117] W. T. Reichel, “Synthesis of anionic clay minerals,” *Solid State Ionics*, vol. 22, p. 135142, 1986.

[118] “Handbook of Clay Science - Google book.” https://books.google.co.jp/books?hl=zh-CN&lr=&id=UmNJ5FGxUxwC&oi=fnd&pg=PP1&dq=handbook+of+clay&ots=AdSD1b70_7&sig=bXcW118Klgj6El5N3RDHfwBZWrU&redir_esc=y#v=onepage&q=handbook%20of%20clay&f=false (accessed May 02, 2022).

[119] M. Janek, P. Komadel, and G. Lagaly, “Effect of autotransformation on the layer charge of smectites determined by the alkylammonium method,” *Clay Minerals*, vol. 32, no. 4, pp. 623–632, Dec. 1997, doi: 10.1180/CLAYMIN.1997.032.4.12.

[120] S. Goldberg, “Modeling selenate adsorption behavior on oxides, clay minerals, and soils using the triple layer model,” *Soil Science*, vol. 179, no. 12, pp. 568–576, Dec. 2014, doi: 10.1097/SS.0000000000000097.

[121] R. P. Janek, W. R. Fawcett, and A. Ulman, “Impedance Spectroscopy of Self-Assembled Monolayers on Au(111): Evidence for Complex Double-Layer Structure in Aqueous $NaClO_4$ at the Potential of Zero Charge,” *Journal of Physical Chemistry B*, vol. 101, no. 42, pp. 8550–8558, Oct. 1997, doi: 10.1021/JP971698E.

[122] E. K. Schneider, “Axially symmetric steady-state models of the basic state for instability and climate studies. Part II. Nonlinear calculations,” *Journal of Atmospheric Sciences*, vol. 34, no. 2, pp. 280–296, 1977.

[123] A. G. Cairns-Smith, *Genetic takeover: And the mineral origins of life/A. g. cairns-Smith*. 1982.

[124] A. Weiss, “Replication and Evolution in Inorganic Systems,” *Angewandte Chemie International Edition in English*, vol. 20, no. 10, pp. 850–860, Oct. 1981, doi: 10.1002/ANIE.198108501.

[125] J. W. Stucki, “Structural Iron in Smectites,” *Iron in Soils and Clay Minerals*, pp. 625–675, 1988, doi: 10.1007/978-94-009-4007-9_17.

[126] A. S. Foster, “Structure and Ontogeny of Terminal Sclereids in Boronia serrulata,” *American Journal of Botany*, vol. 42, no. 6, p. 551, Jun. 1955, doi: 10.2307/2438692.

[127] K. Egashira and M. Ohtsubo, “Swelling and mineralogy of smectites in paddy soils derived from marine alluvium, Japan,” *Geoderma*, vol. 29, no. 2, pp. 119–127, Feb. 1983, doi: 10.1016/0016-7061(83)90036-8.

[128] J. W. Stucki, D. C. Golden, and C. B. Roth, “Effects of Reduction and Reoxidation of Structural Iron on the Surface Charge and Dissolution of Dioctahedral Smectites,” *Clays and Clay Minerals 1984 32:5*, vol. 32, no. 5, pp. 350–356, Oct. 1984, doi: 10.1346/CCMN.1984.0320502.

[129] P. W. Lear and J. W. Stucki, “Role of Structural Hydrogen in the Reduction and Reoxidation of Iron in Nontronite,” *Clays and Clay Minerals 1985 33:6*, vol. 33, no. 6, pp. 539–545, Dec. 1985, doi: 10.1346/CCMN.1985.0330609.

[130] L. Yan and J. W. Stucki, “Effects of Structural Fe Oxidation State on the Coupling of Interlayer Water and Structural Si−O Stretching Vibrations in Montmorillonite,” *Langmuir*, vol. 15, no. 13, pp. 4648–4657, 1999, doi: 10.1021/LA9809022.

[131] L. Yan and J. W. Stucki, “Structural Perturbations in the Solid–Water Interface of Redox Transformed Nontronite,” *Journal of Colloid and Interface Science*, vol. 225, no. 2, pp. 429–439, May 2000, doi: 10.1006/JCIS.2000.6794.

[132] A. Manceau, B. Lanson, V.A. Drits, D. Chateigner, W.P. Gates, J. Wu, D. Huo, and J.W. Stucki, “Oxidation-reduction mechanism of iron in dioctahedral smectites: I. Crystal chemistry of oxidized reference nontronites,” *American Mineralogist*, vol. 85, no. 1, pp. 133–152, Jan. 2000, doi: 10.2138/AM-2000-0114.

[133] D. M. (David M. Gates, “Climate change and its biological consequences,” p. 280, 1993.

[134] J. E. Kostka, E. Haefele, R. Viehweger, and J. W. Stucki, “Respiration and Dissolution of Iron(III)-Containing Clay Minerals by Bacteria,” *Environmental Science and Technology*, vol. 33, no. 18, pp. 3127–3133, Sep. 1999, doi: 10.1021/ES990021X.

[135] B. E. Viani, C. B. Roth, and P. F. Low, “Direct Measurement of the Relation Between Swelling Pressure and Interlayer Distance in Li-Vermiculite,” *Clays and Clay Minerals 1985 33:3*, vol. 33, no. 3, pp. 244–250, Jun. 1985, doi: 10.1346/CCMN.1985.0330311.

[136] B. E. Viani, P. F. Low, and C. B. Roth, “Direct measurement of the relation between interlayer force and interlayer distance in the swelling of montmorillonite,” *Journal of Colloid and Interface Science*, vol. 96, no. 1, pp. 229–244, Nov. 1983, doi: 10.1016/0021-9797(83)90025-5.

[137] N. Yan and J. H. Masliyah, “Characterization and demulsification of solids-stabilized oil-in-water emulsions Part 1. Partitioning of clay particles and preparation of emulsions,” *Colloids and Surfaces A: Physicochemical and Engineering Aspects*, vol. 96, no. 3, pp. 229–242, Mar. 1995, doi: 10.1016/0927-7757(94)03058-8.

[138] N. Yan and J. H. Masliyah, “Effect of pH on Adsorption and Desorption of Clay Particles at Oil–Water Interface,” *Journal of Colloid and Interface Science*, vol. 181, no. 1, pp. 20–27, Jul. 1996, doi: 10.1006/JCIS.1996.0352.

[139] L. Yan and J. W. Stucki, “Effects of Structural Fe Oxidation State on the Coupling of Interlayer Water and Structural Si−O Stretching Vibrations in Montmorillonite,” *Langmuir*, vol. 15, no. 13, pp. 4648–4657, 1999, doi: 10.1021/LA9809022.

[140] L. Yan and J. W. Stucki, “Structural Perturbations in the Solid–Water Interface of Redox Transformed Nontronite,” *Journal of Colloid and Interface Science*, vol. 225, no. 2, pp. 429–439, May 2000, doi: 10.1006/JCIS.2000.6794.

[141] C. I. Fialips, D. Huo, L. Yan, J. Wu, and J. W. Stucki, “Infrared study of reduced and reduced-reoxidized ferruginous smectite,” *Clays and Clay Minerals 2002 50:4*, vol. 50,

no. 4, pp. 455–469, Aug. 2002, doi: 10.1346/000986002320514181.

[142] C. I. Fialips, D. Huo, L. Yan, J. Wu, and J. W. Stucki, "Effect of Fe oxidation state on the IR spectra of Garfield nontronite," *American Mineralogist*, vol. 87, no. 5–6, pp. 630–641, May 2002, doi: 10.2138/AM-2002-5-605.

[143] Y. Wu, Y. Si, D. Zhou, and J. Gao, "Adsorption of diethyl phthalate ester to clay minerals," *Chemosphere*, vol. 119, pp. 690–696, Jan. 2015, doi: 10.1016/J.CHEMOSPHERE.2014.07.063.

[144] J. Cervini-Silva, J. Wu, J. W. Stucki, and R. A. Larson, "Adsorption Kinetics of Pentachloroethane by Iron-Bearing Smectites," *Clays and Clay Minerals 2000 48:1*, vol. 48, no. 1, pp. 132–138, Feb. 2000, doi: 10.1346/CCMN.2000.0480116.

[145] J. Cervini-Silva, J. Wu, R. A. Larson, and J. W. Stucki, "Transformation of chloropicrin in the presence of iron-bearing clay minerals," *Environmental Science and Technology*, vol. 34, no. 5, pp. 915–917, 2000, doi: 10.1021/ES990900J/ASSET/IMAGES/MEDIUM/ES990900JE00004.GIF.

[146] F. Yan, S. Schubert, and K. Mengel, "Soil pH changes during legume growth and application of plant material," *Biology and Fertility of Soils 1996 23:3*, vol. 23, no. 3, pp. 236–242, 1996, doi: 10.1007/BF00335950.

[147] H. Yan, J. Downes, P. J. Boden, and S. J. Harris, "A Model for Nanolaminated Growth Patterns in Zn and Zn-Co Electrodeposits," *Journal of The Electrochemical Society*, vol. 143, no. 5, pp. 1577–1583, May 1996, doi: 10.1149/1.1836682/XML.

[148] J. W. Stucki, C. B. Roth, and W. E. Baitinger, "Analysis of Iron-Bearing Clay Minerals by Electron Spectroscopy for Chemical Analysis (ESCA)," *Clays and Clay Minerals 1976 24:6*, vol. 24, no. 6, pp. 289–292, Dec. 1976, doi: 10.1346/CCMN.1976.0240603.

[149] A. Manceau, M.L. Schlegel, M. Musso, V.A. Sole, C. Gauthier, P.E. Petit, and F. Trolard, "Crystal chemistry of trace elements in natural and synthetic goethite," *Geochimica et*

Cosmochimica Acta, vol. 64, no. 21, pp. 3643–3661, Nov. 2000, doi: 10.1016/S0016-7037(00)00427-0.

[150] N. Praneeth and S. Paria, "Clay-semiconductor nanocomposites for photocatalytic applications," *Clay minerals: properties, occurrence and uses*, 2017.

[151] J. Liu and G. Zhang, "Recent advances in synthesis and applications of clay-based photocatalysts: a review," *Physical Chemistry Chemical Physics*, vol. 16, no. 18, pp. 8178–8192, 2014.

[152] Y. Li, C. Zhang, D. Shuai, S. Naraginti, D. Wang, and W. Zhang, "Visible-light-driven photocatalytic inactivation of MS_2 by metal-free g-C3N4: Virucidal performance and mechanism," *Water Research*, vol. 106, pp. 249–258, Dec. 2016, doi: 10.1016/J.WATRES.2016.10.009.

[153] R. S. Jack, G. A. Ayoko, M. O. Adebajo, and R. L. Frost, "A review of iron species for visible-light photocatalytic water purification," *Environmental Science and Pollution Research*, vol. 22, no. 10, pp. 7439–7449, 2015, doi: 10.1007/s11356-015-4346-5.

[154] K. M. Parida and L. Mohapatra, "Carbonate intercalated Zn/Fe layered double hydroxide: A novel photocatalyst for the enhanced photo degradation of azo dyes," *Chemical Engineering Journal*, vol. 179, pp. 131–139, 2012, doi: 10.1016/j.cej.2011.10.070.

[155] S. J. Kim, Y. Lee, D. K. Lee, J. W. Lee, and J. K. Kang, "Efficient Co-Fe layered double hydroxide photocatalysts for water oxidation under visible light," *Journal of Materials Chemistry A*, vol. 2, no. 12, pp. 4136–4139, 2014, doi: 10.1039/c3ta14933a.

[156] W. P. Gates, J. S. Anderson, M. D. Raven, and G. J. Churchman, "Mineralogy of a bentonite from Miles, Queensland, Australia and characterisation of its acid activation products," *Applied Clay Science*, vol. 20, no. 4–5, pp. 189–197, Jan. 2002, doi: 10.1016/S0169-1317(01)00072-2.

[157] H. Yoneyama, S. Haga, and S. Yamanaka, “Photocatalytic activities of microcrystalline titania incorporated in sheet silicates of clay,” *The Journal of Physical Chemistry*, vol. 93, no. 12, pp. 4833–4837, 1989.

[158] B. Tansel, “Significance of thermodynamic and physical characteristics on permeation of ions during membrane separation: Hydrated radius, hydration free energy and viscous effects,” *Separation and Purification Technology*, vol. 86, pp. 119–126, 2012, doi: 10.1016/j.seppur.2011.10.033.

[159] S. J. Kim, Y. Lee, D. K. Lee, J. W. Lee, and J. K. Kang, “Efficient Co-Fe layered double hydroxide photocatalysts for water oxidation under visible light,” *Journal of Materials Chemistry A*, vol. 2, no. 12, pp. 4136–4139, Mar. 2014, doi: 10.1039/c3ta14933a.

[160] R. S. Jack, G. A. Ayoko, M. O. Adebajo, and R. L. Frost, “A review of iron species for visible-light photocatalytic water purification,” *Environmental Science and Pollution Research*, vol. 22, no. 10, pp. 7439–7449, May 2015, doi: 10.1007/s11356-015-4346-5.

[161] D. Chen, Q. Zhu, F. Zhou, X. Deng, and F. Li, “Synthesis and photocatalytic performances of the TiO_2 pillared montmorillonite,” *Journal of Hazardous Materials*, vol. 235–236, pp. 186–193, Oct. 2012, doi: 10.1016/j.jhazmat.2012.07.038.

[162] R. Asahi, T. Morikawa, T. Ohwaki, K. Aoki, and Y. Taga, “Visible-light photocatalysis in nitrogen-doped titanium oxides,” *Science (1979)*, vol. 293, no. 5528, pp. 269–271, 2001, doi: 10.1126/science.1061051.

[163] T. Ohno, Z. Miyamoto, K. Nishijima, H. Kanemitsu, and F. Xueyuan, “Sensitization of photocatalytic activity of S- or N-doped TiO_2 particles by adsorbing Fe^{3+} cations,” *Applied Catalysis A: General*, vol. 302, no. 1, pp. 62–68, 2006, doi: 10.1016/j.apcata.2005.12.010.

[164] S. U. M. Khan, M. Al-Shahry, and W. B. Ingler, “Efficient photochemical water splitting by a chemically modified n-TiO_2,” *Science (1979)*, vol. 297, no. 5590, pp. 2243–2245,

2002, doi: 10.1126/science.1075035.

[165] T. H. Xie, X. Sun, and J. Lin, “Enhanced photocatalytic degradation of RhB driven by visible light-induced MMCT of Ti(IV)-O-Fe(II) formed in Fe-doped $SrTiO_3$,” *Journal of Physical Chemistry C*, vol. 112, no. 26, pp. 9753–9759, 2008, doi: 10.1021/jp711797a.

[166] C. Chuaicham, Y. Xiong, K. Sekar,W. Chen, L. Zhang, B. Ohtani, I. Babo, and K. Sasaki, “A promising Zn-Ti layered double hydroxide/Fe-bearing montmorillonite composite as an efficient photocatalyst for Cr(VI) reduction: Insight into the role of Fe impurity in montmorillonite,” *Applied Surface Science*, vol. 546, no. December 2020, p. 148835, 2021, doi: 10.1016/j.apsusc.2020.148835.

[167] V.V. Krupskaya, S.V. Zakusin, E.A. Tyupina, O.V. Dorzhieva, A.P. Zhukhlistov, P.E. Belousov, and M.N. Timofeeva, “Experimental study of montmorillonite structure and transformation of its properties under treatment with inorganic acid solutions,” *Minerals*, vol. 7, no. 4, pp. 1–15, 2017, doi: 10.3390/min7040049.

[168] F. Bergaya and G. Lagaly, *Handbook of clay science*. Newnes, 2013.

[169] T. H. Kim, G. J. Lee, J. H. Kang, H. J. Kim, T. il Kim, and J. M. Oh, “Anticancer drug-incorporated layered double hydroxide nanohybrids and their enhanced anticancer therapeutic efficacy in combination cancer treatment,” *BioMed Research International*, vol. 2014, 2014, doi: 10.1155/2014/193401.

[170] J. Patzsch and J. Z. Bloh, “Improved photocatalytic ozone abatement over transition metal-grafted titanium dioxide,” *Catalysis Today*, vol. 300, pp. 2–11, Feb. 2018, doi: 10.1016/J.CATTOD.2017.07.010.

[171] Q. Wu and R. van de Krol, “Selective photoreduction of nitric oxide to nitrogen by nanostructured TiO_2 photocatalysts: Role of oxygen vacancies and iron dopant,” *J Am Chem Soc*, vol. 134, no. 22, pp. 9369–9375, Jun. 2012, doi: 10.1021/JA302246B/ASSET/IMAGES/LARGE/JA-2012-02246B_0007.JPEG.

[172] M. Pérez-Nicolás, I. Navarro-Blasco, J. M. Fernández, and J. I. Alvarez, "Atmospheric NOx removal: Study of cement mortars with iron- and vanadium-doped TiO_2 as visible light–sensitive photocatalysts," *Construction and Building Materials*, vol. 149, pp. 257–271, Sep. 2017, doi: 10.1016/J.CONBUILDMAT.2017.05.132.

[173] J. Doménech and J. Muñoz, "Photocatalytical reduction of Cr(VI) over ZnO powder," *Electrochimica Acta*, vol. 32, no. 9, pp. 1383–1386, Sep. 1987, doi: 10.1016/0013-4686(87)85071-5.

[174] J. Pradhan, S. N. Das, and R. S. Thakur, "Adsorption of Hexavalent Chromium from Aqueous Solution by Using Activated Red Mud," *Journal of Colloid and Interface Science*, vol. 217, no. 1, pp. 137–141, Sep. 1999, doi: 10.1006/JCIS.1999.6288.

[175] J. Kotaś and Z. Stasicka, "Chromium occurrence in the environment and methods of its speciation," *Environmental Pollution*, vol. 107, no. 3, pp. 263–283, Mar. 2000, doi: 10.1016/S0269-7491(99)00168-2.

[176] F. C. Richard and A. C. M. Bourg, "Aqueous geochemistry of chromium: A review," *Water Research*, vol. 25, no. 7, pp. 807–816, Jul. 1991, doi: 10.1016/0043-1354(91)90160-R.

[177] J. C. Crittenden, Y. Zhang, D. W. Hand, D. L. Perram, and E. G. Marchand, "Solar detoxification of fuel-contaminated groundwater using fixed-bed photocatalysts," *Water Environment Research*, vol. 68, no. 3, pp. 270–278, May 1996, doi: 10.2175/106143096X127703.

[178] G. Colón, M. C. Hidalgo, and J. A. Navío, "Photocatalytic deactivation of commercial TiO_2 samples during simultaneous photoreduction of Cr(VI) and photooxidation of salicylic acid," *Journal of Photochemistry and Photobiology A: Chemistry*, vol. 138, no. 1, pp. 79–85, Jan. 2001, doi: 10.1016/S1010-6030(00)00372-5.

[179] S. Wang, Z. Wang, and Q. Zhuang, "Photocatalytic reduction of the environmental

pollutant Cr^{VI} over a cadmium sulphide powder under visible light illumination," *Applied Catalysis B: Environmental*, vol. 1, no. 4, pp. 257–270, Dec. 1992, doi: 10.1016/0926-3373(92)80052-2.

[180] S. Feizpoor and A. Habibi-Yangjeh, "Ternary $TiO_2/Fe_3O_4/CoWO_4$ nanocomposites: Novel magnetic visible-light-driven photocatalysts with substantially enhanced activity through p-n heterojunction," *Journal of Colloid and Interface Science*, vol. 524, pp. 325–336, Aug. 2018, doi: 10.1016/J.JCIS.2018.03.069.

[181] C. Fernández, M. S. Larrechi, and M. P. Callao, "An analytical overview of processes for removing organic dyes from wastewater effluents," *TrAC Trends in Analytical Chemistry*, vol. 29, no. 10, pp. 1202–1211, Nov. 2010, doi: 10.1016/J.TRAC.2010.07.011.

[182] M. K. Ji, H. Kim, V.R. Sapireddy, H. Yun, R.A.I. Abou-Shanab, J. Choi, W. Lee, T.C. Timmes, Inamuddin, B. Jeon, "Simultaneous nutrient removal and lipid production from pretreated piggery wastewater by Chlorella vulgaris YSW-04," *Applied Microbiology and Biotechnology*, vol. 97, no. 6, pp. 2701–2710, Mar. 2013, doi: 10.1007/S00253-012-4097-X/FIGURES/5.

[183] K. P. M. Mosse, A. F. Patti, E. W. Christen, and T. R. Cavagnaro, "Review: Winery wastewater quality and treatment options in Australia," *Australian Journal of Grape and Wine Research*, vol. 17, no. 2, pp. 111–122, Jun. 2011, doi: 10.1111/J.1755-0238.2011.00132.X.

[184] L. Roy, "Eaux industrielles contaminées Réglementation, paramètres chimiques et biologiques & procédés d'épuration innovants Nadia Morin-Crini et Grégorio Crini préface de", Accessed: May 02, 2022. [Online]. Available: http://presses-ufc.univ-fcomte.fr

[185] A. K. Rathoure and V. K. Dhatwalia, "Toxicity and waste management using

bioremediation," *Toxicity and Waste Management Using Bioremediation*, pp. 1–421, Jan. 2015, doi: 10.4018/978-1-4666-9734-8.

[186] Y. Wang, X. Li, L. Zhen, H. Zhang, Y. Zhang, and C. Wang, "Electro-Fenton treatment of concentrates generated in nanofiltration of biologically pretreated landfill leachate," *Journal of Hazardous Materials*, vol. 229–230, pp. 115–121, Aug. 2012, doi: 10.1016/J.JHAZMAT.2012.05.108.

[187] G. Crini, E. Lichtfouse, L. D. Wilson, and N. Morin-Crini, "Conventional and non-conventional adsorbents for wastewater treatment," *Environmental Chemistry Letters 2018 17:1*, vol. 17, no. 1, pp. 195–213, Jul. 2018, doi: 10.1007/S10311-018-0786-8.

[188] "Advances in Water Treatment and Pollution Prevention - Google book." https://books.google.co.jp/books?hl=zh-CN&lr=&id=thEigV6yl64C&oi=fnd&pg=PR7&ots=PKOUEUWhER&sig=SVUlImHRPLsCVxsxR2YNbj8zzsg&redir_esc=y#v=onepage&q&f=false (accessed May 02, 2022).

[189] M. A. Barakat, "New trends in removing heavy metals from industrial wastewater," *Arabian Journal of Chemistry*, vol. 4, no. 4, pp. 361–377, Oct. 2011, doi: 10.1016/J.ARABJC.2010.07.019.

[190] P. J. Strong and J. E. Burgess, "Treatment Methods for Wine-Related and Distillery Wastewaters: A Review," *http://dx.doi.org/10.1080/10889860802060063*, vol. 12, no. 2, pp. 70–87, 2008, doi: 10.1080/10889860802060063.

[191] C. Bellona, J. E. Drewes, P. Xu, and G. Amy, "Factors affecting the rejection of organic solutes during NF/RO treatment—a literature review," *Water Research*, vol. 38, no. 12, pp. 2795–2809, Jul. 2004, doi: 10.1016/J.WATRES.2004.03.034.

[192] E. Rossetto, D. I. Petkowicz, J. H. Z. dos Santos, S. B. C. Pergher, and F. G. Penha, "Bentonites impregnated with TiO_2 for photodegradation of methylene blue," *Applied*

Clay Science, vol. 48, no. 4, pp. 602–606, May 2010, doi: 10.1016/J.CLAY.2010.03.010.

[193] S. Yurdakal, G. Palmisano, V. Loddo, V. Augugliaro, and L. Palmisano, "Nanostructured rutile TiO_2 for selective photocatalytic oxidation of aromatic alcohols to aldehydes in water," *J Am Chem Soc*, vol. 130, no. 5, pp. 1568–1569, Feb. 2008, doi: 10.1021/JA709989E/SUPPL_FILE/JA709989E-FILE002.PDF.

Chapter 2

Methodology

2.1 Solid characterizations

2.1.1 X-ray diffraction (XRD)

Powder X-ray diffraction (PXRD) on an Ultima IV diffractometer (Rigaku, Akishima, Japan) was used to describe the crystal phases of the original and composite materials, utilizing Cu Kα radiation with 40 kV acceleration voltage and 40 mA applied current at a 2°/min scanning speed and 0.02° step size. The powder diffraction analysis software PDXL was used to identify the obtained XRD patterns based on the International Centre for Diffraction Data (ICDD) (Rigaku).

2.1.2 Fourier-transform infrared spectroscopy (FTIR)

FTIR on a Jasco FTIR-670 Plus was used to characterize the functional groups of the original and composite materials (Tokyo, Japan). The KBr pellet method (sample 5% (w/w)) was used to acquire FT-IR spectra of precipitates in the range of 360–4000 cm^{-1} and resolution: 4 cm^{-1}.

2.1.3 X-ray fluorescence (XRF)

X-ray fluorescence (XRF) spectroscopy Rigaku ZSX Primus II in the wavelength dispersive mode was used to determine the elemental compositions of sepiolite (Akishima, Japan). The Rh-anode, 3kW or 4kW, 60kV, and wavelength dispersive type are the experimental conditions.

2.1.4 X-ray photoelectron spectroscopy (XPS)

The materials' X-ray photoelectron spectroscopy (XPS) data were acquired using a

monochromated Al Kα X-ray source at 200 W on an ESCA 5800 (ULVAC-PHI, Inc. Kanagawa, Japan). Casa XPS software was used to analyze the data (version 2.3.12.8). The contamination peak obtained from vacuum oil in the device, EB[C 1s] at 284.6 eV, was used to calibrate the binding energy. In the analysis, the Shirley background was used. The binding energy at the point of intersection of the tangent line and the horizontal axis is the valence band, which is drawn tangent to the point of inflection on the curve of the XPS spectra.

2.1.5 N_2 adsorption/desorption isotherms

The BET (Brunauer–Emmett–Teller) theory (BEL-Max, Microtrac BEL) based on adsorption isotherms utilizing N_2 gas at 196°C was used to determine the specific surface area of original and composite samples. Before measurement, adsorbent water and gases were removed under vacuum at 150°C for 10 hours.

2.1.6 Scanning electron microscope (SEM)

A VE-9800 scanning electron microscope was used for the scanning electron microscopy (SEM) examination (Keyence, Osaka, Japan). 20 kV is the accelerating voltage.
FlexSEM 1000II and AZteclive light FX scanning electron microscopes (SEM-EDX) were used (Hitachi, Tokyo, Japan). We used the Aztec application from AZteclive light FX to process the EDX results, which included baseline correction.

2.1.7 Transmission electron microscopy (TEM)

On a transmission electron microscope (JEOL JEM-2100HCKM), TEM pictures of the original and composite samples were examined (Akishima, Japan). The grid dispersion approach was

used to prepare the sample for TEM examination. Ethanol was used to scatter the solid sample. The suspension was put on the Cu grid and completely dried at room temperature in a desiccator for 2 hours after being sonicated for 20 minutes to reduce aggregation.

2.1.8 Diffuse reflectance spectroscopy (DRS)

UV–vis diffuse reflectance spectroscopy was used to determine the light absorption and optical characteristics of synthetic materials (DRS). The diffuse reflectance was measured from 350 nm to 800 nm on a UV-2450 spectrophotometer (Shimadzu, Tokyo, Japan) using barium sulfate as the standard, scan speed medium, 5 nm step width, and 1.0 nm sampling pitch with the sample pushed into a sample cup using a glass rod and the sample cup inserted in the ISR-2600Plus integrating sphere attachment.

2.1.9 Photoluminescence spectroscopy (PL)

The effectiveness of photogenerated charge carriers' separation and the photocatalyst's lifespan were investigated using photoluminescence spectroscopy. In general, a low PL intensity during light irradiation could suggest a poor rate of photogenerated electron and hole recombination. In the experiment, the solid sample was pressed into a sample holder and placed in the FP-6600 spectrofluorometer (JASCO, Tokyo, Japan). The photoluminescence spectrum was measured in emission spectrum mode from 300nm to 600nm, with an excitation wavelength of 330-400 nm.

2.1.10 Photocurrent responsiveness and electrochemical impedance spectroscopy

Two mg of the sample was dispersed in 6 mL Nafion (5 %, Wako Pure Chemical Industries, Osaka, Japan) 30 mL and ethanol (95.8%, Wako Pure Chemical Industries, Osaka, Japan) for

the electrochemical properties (photocurrent responsive and electrochemical impedance spectroscopy (EIS)) measurement of 0.274Fe-Mt and Fe-Mt. The resulting dispersion was then dropped and dried on a Pt sheet electrode that served as the working electrode. The 1280c AMETEK advanced measurement technology (Berkshire, United Kingdom) investigated a three-electrode system with Ag/ AgCl/ KCl as reference electrode, Pt wise as counter electrode, and the sample coted electrode as mentioned above as working electrode with 0.1 M NaCl as electrolyte in ambient.

2.1.11 Synchrotron

At the Synchrotron Light Application Center, the X-ray absorption near edge structure (XANES) spectra in Fe Kα-edge were measured at BL06 (Saga, Fukuoka, Japan).

2.1.12 Reversed double-beam photoacoustic spectroscopy (RDB-PAS)

RDB-PAS (reversed double-beam photoacoustic spectroscopy) is a strong technique for determining the crystallinity and amorphous phase of metal oxides. By observing the pattern of energy-resolved distribution of electron traps (ERDT) in combination with conduction band bottom position (CBB), this method has been utilized to identify metal-oxide in the solid phase. The electron from the valence-band (VB) was excited by continuous scanning light and accumulated in the electron trap, to summarize the principle of this technology (ETs). The photoacoustic signal (PA) was detected by modulated LED light (625 nm) during the irradiation of continuous scanning light, and the signal strength was converted to the absolute density of ETs. The surface structure and bulk structure, which may be a property of metal oxide, are included in the ERDT. Based on the degree of coincidence for a specific pair of samples, the combined result of ERDT and CBB was employed as a fingerprint of metal oxide.

The RDB-PAS approach was employed in this study to investigate ZnTi mixed metal oxide samples prepared under various conditions in order to better understand the phase components, including the amorphous phase that cannot be seen using the XRD technique. The energy resolved distribution of electron trap (ERDT) patterns of the composites were characterized using the innovative reversed double-beam photoacoustic spectroscopy (RDB-PAS) approach. A PAS cell with an electret condenser microphone and a quartz window was used to place 200 mg of powder sample. A light beam from a xenon lamp with a grating monochromator modulated at 80 Hz was also used on the upper side under N^2 flow, which was saturated with methanol vapor for at least 30 minutes. The PAS signal was detected utilizing a digital lock-in amplifier after a light chopper was irradiated from 650 nm to 350 nm through the cell window, and then photoacoustic (PA) spectra were collected about a graphite PA spectrum for calibration. The amount of photo-absorption change for accumulated electrons can be used to create an ERDT pattern. The RDB-PAS arrangement was as follows: (**Fig. 2.1**).

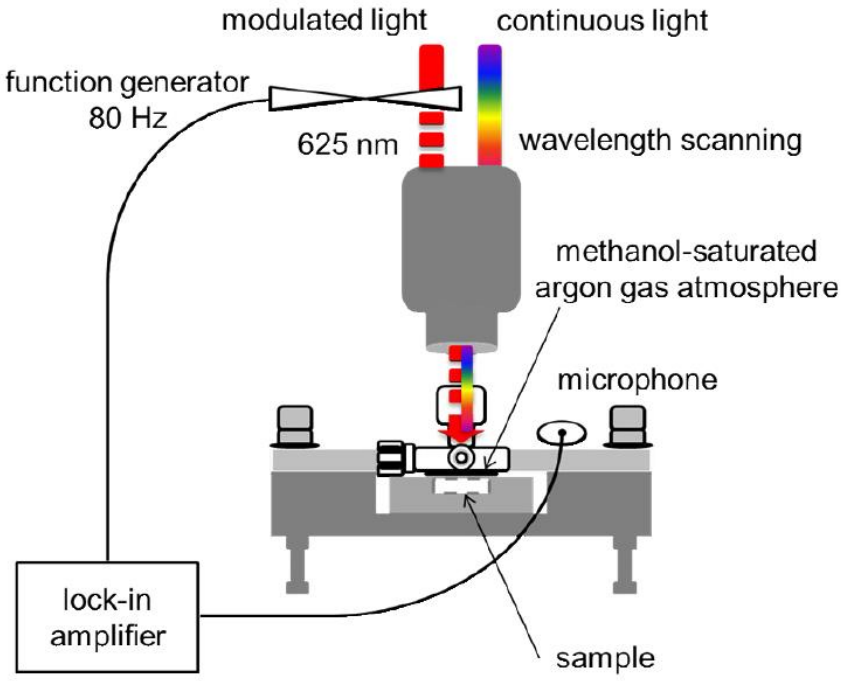

Fig. 2.1. Schematic representation of the setup for RDB-PAS.

2.2 Solution analysis

2.2.1 Inductively coupled plasma - optical emission spectrometry (ICP-OES)

Inductively coupled plasma optical emission spectrometry (ICP-OES, Optima 8300, Perkin Elmer, Boston Waltham, US) was adopted to quantify the concentrations of Fe(III), Ca(II), Mg(II), and Al(III).

2.2.2 Atomic Absorption Spectrometry (AAS)

Solar AAS Thermo Elemental (Thermo Fisher, Waltham, US) was used to measure the and released Na(I) after Fe(III) modification of Mt.

2.2.3 High Performance Liquid Chromatography (HPLC)

High performance liquid chromatography (HPLC) (Jasco: CO-2065 Plus, Jasco, Kyoto, Japan) measurement at a wavelength of 270 nm was applied for measuring phenol and the biproducts for phenol photocatalytic degradation.

Chapter 3

Effect of ionic Fe^{III} doping on montmorillonite for photocatalytic reduction of Cr^{VI} in wastewater

3.1 Introduction

Because of its toxicity to most organisms, hexavalent chromium (Cr^{VI}) is widely acknowledged as one of the most serious public health issues [1]–[4]. It has been found in large quantities in natural water and soil, posing a pathogenic threat to human health [5]–[8]. The World Health Organization has set a limit of 0.05 mg/L for chromium in drinking water [9], which is far lower than the typical Cr^{VI} amount found in most natural water systems [10], [11]. Finding an appropriate technique to provide water in where the Cr^{VI} controlled within the WHO limit is critical. Physical or chemical adsorption and photocatalytic reduction of Cr^{VI} to Cr^{III}, which is non-toxic and easily immobilized, are the two main types of therapy [12]–[14].

For decades, conventional chemical, electrochemical, and biological techniques have been investigated. Ion exchangers, such as ion exchange columns, membrane filtration, surface adsorption, and so on, have also been studied extensively in recent years. However, any of these processes or approaches may be expensive, unable to completely mineralize or remediate the pollutant, inapplicable on a large scale, or resulting in secondary contamination [10], [15]–[17]. These issues can be overcome via photocatalysis. This innovative approach has received a lot of attention in recent decades, especially in the disciplines of material science, modern energy generation, CO_2 collecting, and water treatment [18]–[22]. TiO_2 [2], [12], [14], [23], [24], ZnO_2 [25], Fe_2O_3 [26], [27], ZnS, Cu_2O [28], [29], bismuth oxyhalides [29], [30], and other photocatalysts have all been explored as photocatalysts for the photocatalytic remediation of Cr^{VI}. These, however, more crucially, when composites are created using supporting materials such as clay or other materials, the reduced efficiency in the absorption of radiation due to nanoparticle aggregation can be solved [15], [21], [22], [31]–[33].

When making photocatalytically active composites, Mt is widely used as one of the supporting elements for the major photocatalysts [21], [22], [34], [35]. Isomorphic substitutions are most

common in the octahedral sheet, allowing the center Al^{III} to be replaced by Fe^{III}, Mg^{II}, Fe^{II}, or other cations, and Si^{IV} to be replaced by Al^{III}, Mg^{II}, Fe^{II}, or other cations. Exchangeable cations, such as Na^{I} and Ca^{II}, as well as trace amounts of $Fe^{II/III}$, Mg^{II}, and Al^{III} in the octahedral layer and Ti^{IV} in the tetrahedral layer, can be used to balance the permanent negative charge induced by isomorphic substitution [36], [37]. Clay is mostly used as a supporting material to improve pollutant adsorption capacity, surface-to-volume ratio during photocatalytic reactions, and sedimentation qualities, but it does not engage in any photocatalytic processes [38], [39]. Some researchers, on the other hand, have looked for optical and photocatalytic pathways between Mt and semiconductors. Electrons driven to the conduction band in the Mt/g-C_3N_4 composite undergo electrostatic repulsion with the negative charge of the Mt layers, allowing more freely migrating electron-hole pairs to boost photocatalytic reaction efficiency as predicted in 2016 [40]. The intimate interface contacts between g-C_3N_4 and clay minerals promises increased charge carrier formation, faster carrier migration, and more efficient separation, according to theoretical estimates [41]. The removal of Cr^{VI} from ZnTi – layered double hydroxide (LDH)/clay composites was greatly aided in the presence of $Fe^{III/II}$ [42]–[44]. However, none of these investigations investigated how Mt accomplished the photocatalytic function in the photocatalytic reaction system independently. Clay minerals, especially Mt, have very significant band gaps and should only be used in composites as insulating supporting materials [21], [22], [35], [45], [46]. Mt has a band gap of 5.3 eV [47].

Element doping can help to close the huge band gap [48]–[51]. The mid-gap electron trap state was created on the ZnTi – LDH/clay composites by doping with ferric ions, according to DFT calculations. As a result, the samples' photocatalytic performance was improved [47]. Ferric-doped Mt was produced in this study for only 1 hour at pH 2. The major goal of employing this acidic state is to prevent the precipitation of additional Fe^{III} sources. According to earlier publications, acid-activated Mt was subjected to photocatalytic activation, which demands

extremely harsh acidic conditions (typically a concentration of $H^+ > 1$ M) and a long period of time (generally more than 12 h) [52], [53]. Even though Fe-Mt was imbued with photocatalytic properties after a short-term moderate acid treatment, the acid solution should have no effect on Mt's structure. Iron is found in abundance in the natural world, such as in water and soil. Iron's role in photocatalytic processes has piqued researchers' curiosity. Clay minerals treated with iron have been shown to have photocatalytic capabilities in a number of investigations. When compared to bare Fe_2O_3 or ZnO, a Fe^{III}-centered FeO_6 structure has been proposed for Zn/Fe LDH that can improve visible light absorption and consequently boost photocatalytic activity on the degradation of azo dyes [54]. However, these assumptions were not tested on clay groups, and theories on how this inhibition works are still debated. As a result, it is critical that we examine effective photocatalysts and their underlying mechanisms.

The photocatalytic redox reaction of Cr^{VI} catalyzed by Fe-Mt (Fe^{III}-doped montmorillonite) was investigated in this paper. Unlike prior investigations, the Fe-Mt synthesis was carried out in an acidic environment with a pH of less than 2 to keep the Fe element as Fe^{III} cation rather than ferric oxides or ferric hydroxide. The synthesized Fe-Mt was employed in theoretical calculations and characterization in conjunction with the photocatalytic reaction to disclose the process mechanism, with the parent Mt serving as a comparison. To the authors' knowledge, there has been no investigation into regulating F^{III}-doped Mt in the synthesis of cations and using the material for photocatalytic redox remediation of Cr^{VI}.

3.2 Materials and methods

3.2.1 Materials

The Mt material was Kunipia-F from Kunimine Industries (Tokyo, Japan), which has a cation exchange capacity (CEC) of 1.114 mmol/g [55]. By using the ME-ICP61 method (ALS Global,

North Vancouver, Canada), the chemical formula was estimated to be $(Na_{0.97}Ca_{0.08})^{+1.13}$ $(Si_{7.68}Al_{0.32})$ $(Al_{2.94}Fe^{III}_{0.25}Fe^{II}_{0.03}Mg_{0.78})$ O_{20} $(OH)_4^{-1.13}$ · n H_2O. Wako Pure Chemical Industries provided iron(III) nitrate ninehydrate ($Fe(NO_3)_3 \cdot 9H_2O$, 99.0%), sodium hydroxide (NaOH, 97.0+%), and nitric acid (HNO_3, sp. gr. 1.38) for this study (Osaka, Japan). 1,5-diphenyl carbazide was acquired from Merck for the carbazide technique (Darmstadt, Germany). Synergy UV created ultrapure water (Merck, Darmstadt, Germany).

3.2.2 Synthesis of iron-doped Mt

$Fe(NO_3)_3 \cdot 9H_2O$ roughly equivalent to 0.25, 0.5, 1, 2, and 4 times the CEC of Mt were added to 200 mL of ultrapure water to synthesize iron-doped Mt (Fe-Mt); the relevant dosage of Fe^{III} is listed in **Table 3.1**. The pH was then adjusted to 2 (±0.1) using 0.01 and 0.1 mol/L NaOH or HNO_3. Separately, 2 g Mt was disseminated in Fe^{III} solutions and rapidly agitated for 1 h at S/L = 10 g/L under ambient conditions. The adsorption of Fe^{III} takes only 1 minute, and the absorption isotherm follows the Langmuir isotherm model (**Fig. 3.1**). Mt's long-term stirring procedure ensured equal dispersion and controlled the synthesis time consistency. The mixture was centrifuged after modification, and the solid products were rinsed three times to eliminate any remaining Fe^{III}. The material was subsequently lyophilized, crushed into minute particles, sieved through a 149 m mesh, collected, and given the names 0.091Fe-Mt, 0.175Fe-Mt, 0.274Fe-Mt, 0.299Fe-Mt, and 0.312Fe-Mt, which are based on the adsorbed Fe^{III} on Mt. A 0.45 m membrane filter was used to filter the supernatant and eluent. Inductively coupled plasma-optical emission spectroscopy (ICP-OES, Perkin Elmer 8500, Waltham, MA, USA) was used to compute the Fe^{III} concentrations as well as the Ca^{II}, Mg^{II}, and Al^{III} liberated from the Fe-Mt, which are listed in **Table 3.1**.

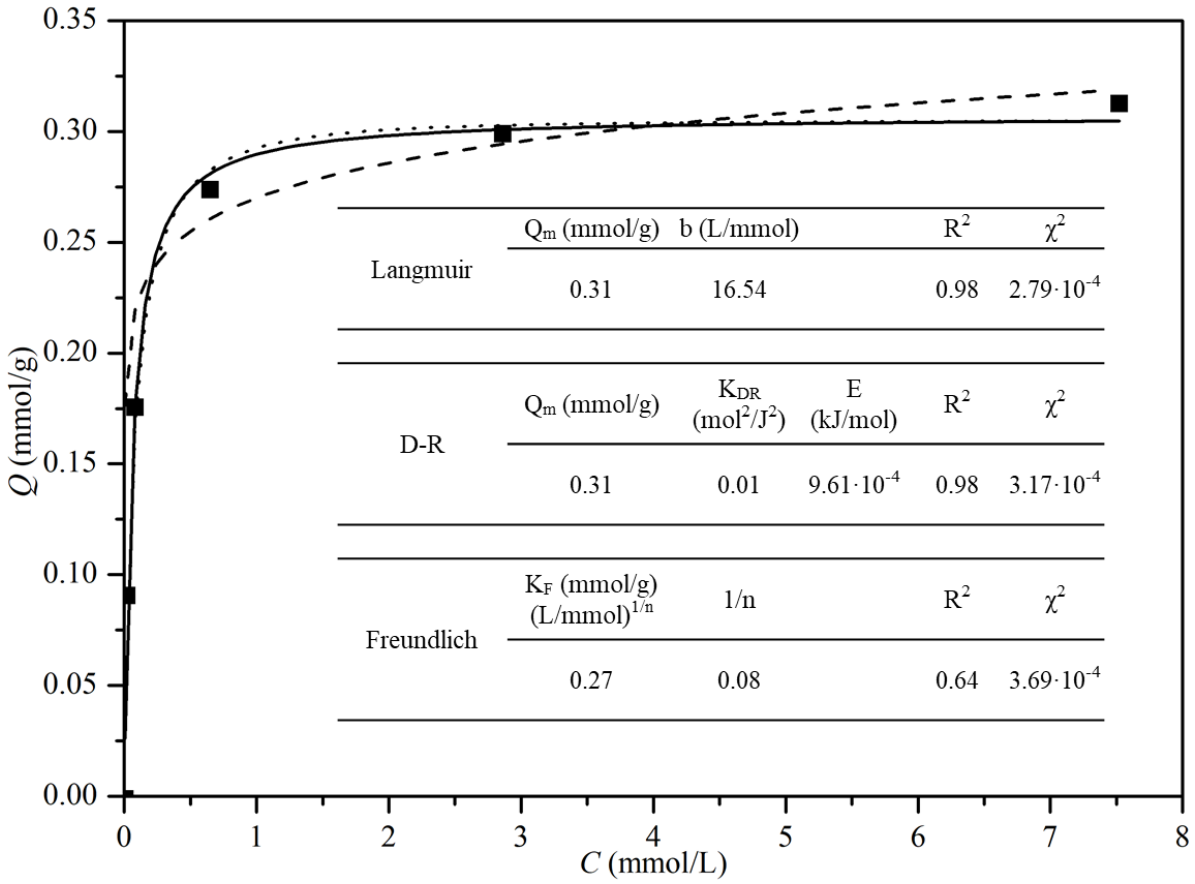

Fig. 3.1. Isotherms of Fe^{III} adsorption on Mt. Sample dosage, 0.5 g; volume, 500 mL; initial Fe^{III} concentration, 0.95-15.2 mmol/L.

3.2.3 Characterization

Cu Kα was used as the radiation in an X-ray diffraction (XRD) experiment using an Ultima IV X-ray diffractometer (Rigaku, Akishima, Japan) at 40 kV and 40 mA. A 670 Plus Fourier transform infrared spectrometer (JASCO, Tokyo, Japan) was used to record the Fourier transform infrared spectra (FTIR) of Fe-Mt samples. 95 wt.% KBr (spectroscopic grade) was mixed with 5 wt.% samples to make the tablet samples. The wavenumber ranged from 4000 to 400 cm^{-1} with a resolution of 4 cm^{-1}. An ESCA 5800 system (Ulvac-PHI, Kanagawa, Japan) with an Al Kα X-ray source at 200 W was used to conduct the survey and high-resolution X-ray photoelectron spectroscopy (XPS) scans. Peak separations were performed with Casa XPS

software (Version 2.3.16 PR 1.6) using a Shirley baseline for subtraction, and their binding energies (EBs) were calibrated with EB [C 1s = 284.6 eV]. On a BELSORP-max equipment, N_2 adsorption/desorption isotherms were measured (BEL Inc., Osaka, Japan). The samples were degassed for 10 hours at 150 °C. The temperature was then kept at 77 K during the measurement by filling the chamber with 99.99% N_2. The program calculated the Brunauer–Emmett–Teller surface area (S_{BET}), and the statistic distribution of pore size was calculated in BELMaster software using the Horvath–Kawazoe (HK) and Barrett–Joyner–Hanlenda (BJH) methods. On a UV-2450 spectrophotometer (Shimadzu, Tokyo, Japan), diffuse reflectance spectroscopy (DRS) was performed. The wavelength range was chosen at 200–800 nm. As a reference, $BaSO_4$ was employed. A VE-9800 scanning electron microscope was used for the scanning electron microscopy (SEM) examination (Keyence, Osaka, Japan). 20 kV is the accelerating voltage. FlexSEM 1000II and AZteclive light FX scanning electron microscopes (SEM-EDX) were used (Hitachi, Tokyo, Japan). We used the Aztec application from AZteclive light FX to process the EDX results, which included baseline correction. Two mg of the sample was dispersed in 6 mL Nafion (5 %, Wako Pure Chemical Industries, Osaka, Japan) 30 mL and ethanol (95.8%, Wako Pure Chemical Industries, Osaka, Japan) for the electrochemical properties (photocurrent responsive and electrochemical impedance spectroscopy (EIS)) measurement of 0.274Fe-Mt and Fe-Mt. The resulting dispersion was then dropped and dried on a Pt sheet electrode that served as the working electrode. The 1280c AMETEK advanced measurement technology (Berkshire, United Kingdom) investigated a three-electrode system with Ag/ AgCl/ KCl as reference electrode, Pt wise as counter electrode, and the sample coted electrode as mentioned above as working electrode with 0.1 M NaCl as electrolyte in ambient. At the Synchrotron Light Application Center, the X-ray absorption near edge structure (XANES) spectra in Fe k-edge were measured (Saga, Fukuoka, Japan).

3.2.4 Photocatalytic activity test

Under irradiation with a 300 W xenon lamp, photocatalytic reduction of Cr^{VI} with or without ethanol as the hole scavenger was performed. Fifty milligrams of photocatalyst were suspended in 50 mL of 10 mg/L Cr^{VI} ($K_2Cr_2O_7$) solution and agitated at 500 rpm for 5 minutes without irradiation to achieve Cr^{VI} adsorption equilibrium. Every 15 minutes, a sample of the responding solution was obtained, and the Cr^{VI} content in the filtered supernatant was detected using a UV–Vis spectrophotometer (UV-2450, Shimadzu, Tokyo, Japan) at a wavelength of 540 nm. The Cr^{VI} photocatalytic reduction with scavenger addition followed the same process as the Cr^{VI} photocatalytic reduction without scavenger addition, but 1 mL of ethanol and 49 mL of 10 mg/L Cr^{VI} ($K_2Cr_2O_7$) solution were added to the reactor first.

3.3 Results and discussion

3.3.1 Characterizations of the H-Mt and Fe-Mt samples

The phase structure of the pristine and manufactured Fe-Mt samples was shown in **Fig. 3.2**. The 001 peak of Mt at 7.25° (2θ) corresponds to 1.21 nm, which includes one of the 0.96 nm thick aluminosilicate layers. As a result, the interlayer gap was estimated to be 0.25 nm [56]. The resulting Fe-Mt had a d_{001} value of 1.39 nm after acidic activation at pH = 2 for 1 h, which was a modest increase over the initial Mt. This is due to the octahedral layers releasing $Fe^{II/III}$,

which is then adsorbed by Mt [57]. The extended interlayers predominated not only by the substitution of exchangeable cations with Fe^{III} from solution, but also by the transition of the structural $Fe^{II/III}$ from the aluminosilicate layers to the interlayer space for other Fe-Mt with initial Fe^{III} addition. There should be no metal hydroxides or metal oxides formed because the Fe^{III} alteration of Mt was carried out at pH 2. $Fe^{II/III}$ has hydrated ionic sizes of 0.39 nm [58] and 0.45 nm [59], while Cr^{III}, Mg^{II}, and Al^{III} have hydrated ionic sizes of 0.47 nm [60], 0.43 nm [61], [62], and 0.42 nm [63], respectively. These are greater than the 0.36 nm and 0.41 nm of Na^{I} and Ca^{II} [61], [62], [64]. The interlayer distance was determined to be 0.42 nm for Fe-Mt, 0.091Fe-Mt, 0.175Fe-Mt, 0.274Fe-Mt, and 0.299Fe-Mt, and 0.44 nm for 0.312Fe-Mt, respectively. For Fe-Mt, 0.091Fe-Mt, 0.175Fe-Mt, 0.274Fe-Mt, and 0.299Fe-Mt, some cations may have a lower hydrated ionic size than their ideal hydrated ionic size due to the van der Waals force in the interlayer space squeezing out the initial spherical water shell of $Fe^{II/III}$ and deforming it to an imperfect shape [65]. The higher content of Fe^{III} in the interlayer creates an acceptable cation density, resulting in a more complete hydration shell for the cations, resulting in a larger interlayer space of 0.312Fe-Mt.

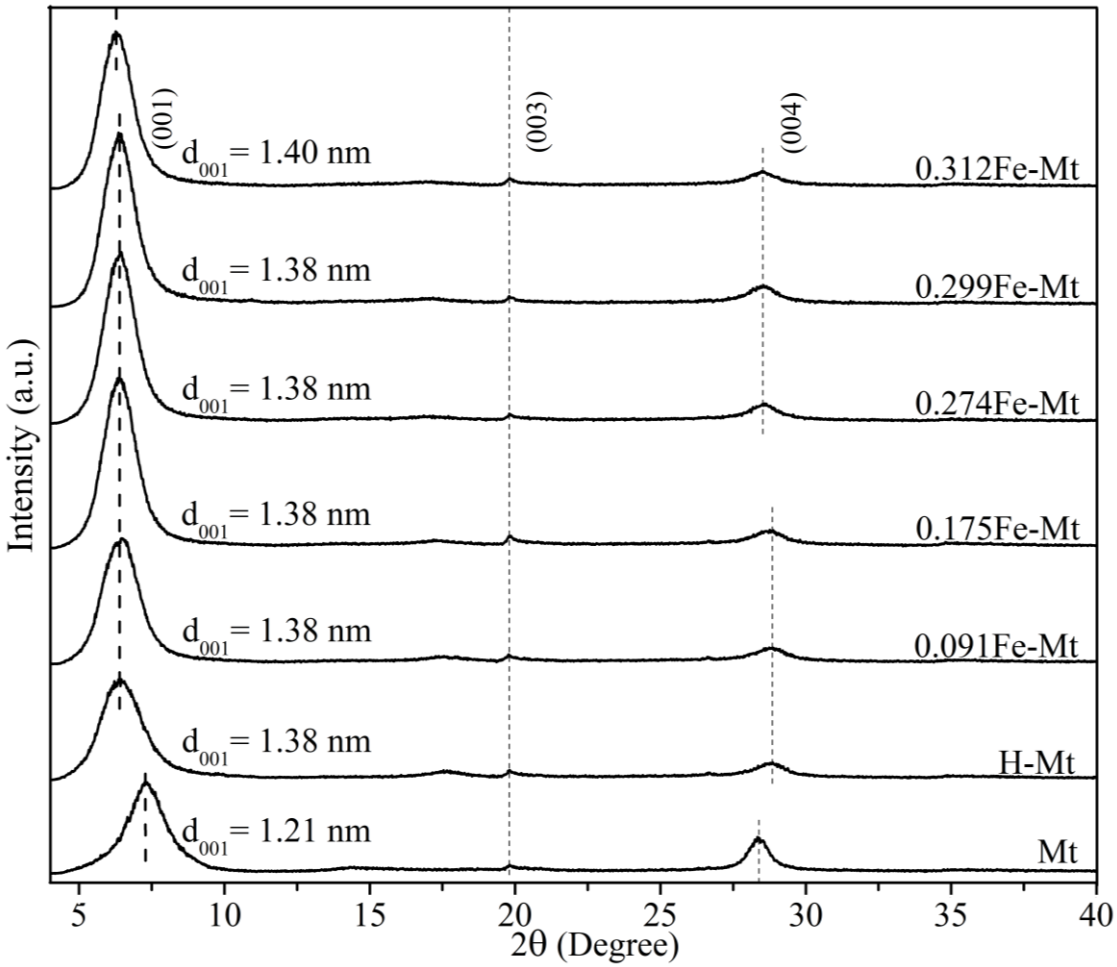

Fig. 3.2. XRD patterns of Mt, Fe-Mt, 0.091Fe-Mt, 0.175Fe-Mt, 0.274Fe-Mt, 0.299Fe-Mt, and 0.312Fe-Mt (42-40° in 2θ).

ICP-OES and AAS tests validated the release of ions after proton or Fe^{III} cation alteration of Mt. (**Table 3.1** and **Fig. 3.3**). Exchangeable cations in the interlayers and structural cations in the octahedrons and tetrahedrons are the two types of cations found in Mt [53]. The amount of exchangeable Na^{I} and Ca^{II} released in each sample was far more than the structural $Fe^{II/III}$, Mg^{II}, and Al^{III}. Acidification at a low proton concentration for a short time had no damaging effect on the tetrahedral and octahedral structures of Mt layer [52], [53], because the Mt structure is

highly resistant against acid erosion. Thus, in aqueous, the proton and added Fe^{III} primarily interchange with the interlayer Na^{I} and Ca^{II}, causing small defects on Mt layers.

Intercalated Fe^{III} rose linearly when the initial addition of Fe^{III} increased until 0.274Fe-Mt, after which only minor enhancements of Fe^{III} intercalation were seen in 0.299Fe-Mt and 0.312Fe-Mt (**Fig. 3.3**). In solution, the exchange of Na^{I} and Ca^{II} with proton and Fe^{III}, as well as the isomorphic substitution of structural $Fe^{II/III}$, Mg^{II}, and Al^{III} with Fe^{III}, was a dynamic equilibrium process; however, not all interlayer and structural cations could be replaced by Fe^{III}. In 0.274Fe-Mt, the doped Fe^{III} became subsaturated at 0.720 meq./gMt of Fe^{III}. Except for a very evident drop on 0.312Fe-Mt, the released exchangeable Na^{I} rose with the higher Fe^{III} adding amount. Ca^{II} release was roughly linearly proportional to the amount of Fe^{III} added in Fe-Mt, 0.091Fe-Mt, 0.175Fe-Mt, and 0.274Fe-Mt. There was also a modest increase in 0.299Fe-Mt and 0.312Fe-Mt. The proton easily replaced the exchangeable Na^{I} cations and added Fe^{III}, so the value of its releasing amount had already reached a significant figure in Fe-Mt. Further additions of Fe^{III} had just a minor effect on its release. The well-hydrated environment in the interlayer in 0.312Fe-Mt, as evidenced by XRD data (**Fig. 3.2**), may have adsorbed the Na^{I} back to the interlayer. Because Ca^{II} interacts more strongly with the Mt layer than Na^{I}, Fe^{III} will be preferred for exchange with Na^{I}, followed by Ca^{II}. The amount of Al^{III} released grew in lockstep with the rise in Fe^{III} initial addition, but Mg^{II} release was increased initially and then stabilized at 0.274Fe-Mt, 0.299Fe-Mt, and 0.312Fe-Mt. Both ion exchange

in the interlayer and isomorphic substitution in the Al-O octahedral layer, which happened preferentially between the trivalent cations, could govern the release of Al^{III}. Acid erosion, on the other hand, was the sole cause of Mg^{II} release. As a result, the isomorphic substitution of structural cations with Fe^{III} should greatly reduce acid erosion. Mg^{II} and Al^{III} release is ten times lower than Fe^{III} doping and Ca^{II} release.

Table. 3.1. Adsorbed Fe^{III} and released Na^{I}, Ca^{II}, Mg^{II}, and Al^{III} during the Mt modification. Positive values indicate adsorption, and negative values indicates release.

Sample	Fe(III) added (mmol/g)	Fe(III) adsorbed [1]		Na^{I} released [2] (mmol/g)	Ca^{II} released [1] (mmol/g)	Mg^{II} released [1] (mmol/g)	Al^{III} released [1] (mmol/g)
		Q (mmol/g)	meq./g				
H-Mt	0.000	-0.001	-0.003	-0.849	-0.029	-0.004	0.000
0.091Fe-Mt	0.094	0.091	0.238	-0.920	-0.041	-0.006	-0.001
0.175Fe-Mt	0.188	0.175	0.462	-0.943	-0.054	-0.008	-0.001
0.274Fe-Mt	0.377	0.274	0.720	-0.941	-0.107	-0.012	-0.007
0.299Fe-Mt	0.753	0.299	0.786	-0.957	-0.122	-0.012	-0.015
0.312Fe-Mt	1.507	0.312	0.822	-0.927	-0.124	-0.011	-0.019

[1] Measured by ICP-OES.

[2] Measured by AAS.

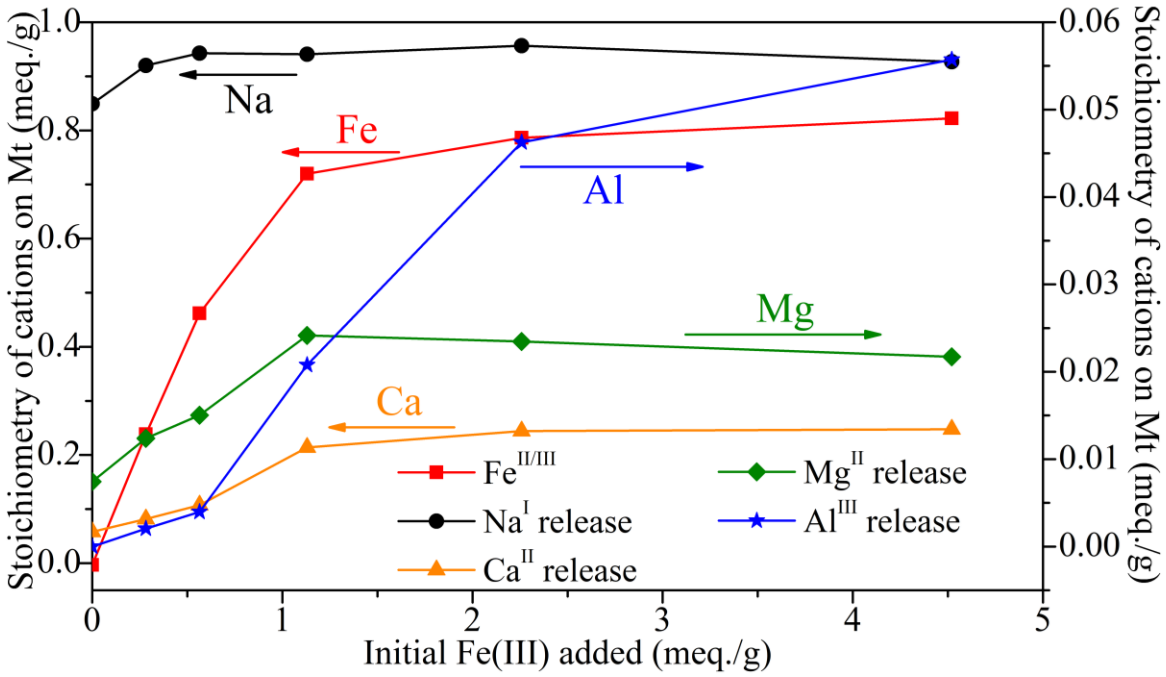

Fig. 3.3. Stoichiometry of adsorbed Fe(Ⅲ) and released Na(Ⅰ), Ca(Ⅱ), Mg(Ⅱ), and Al(Ⅲ) during modification of Mt by different amount of Fe(Ⅲ). Solid line refers to left y-axis and dash line refers to right y-axis.

Fig. 3.4 shows the FTIR spectra of synthetic Fe-Mt and hematite (γ-Fe_2O_3) standards. The Fe-O stretching mode should be assigned to the two vibration modes of Fe_2O_3 at 536 and 468 cm^{-1} [66]. Unlike Fe_2O_3, the stretching vibration mode of the Al-O bond at 531 cm^{-1} has a sharper form and occurs at various wavenumbers in all Fe-Mt samples. At 468 cm^{-1}, the bending vibration mode of the Si-OH bond has a sharper form. The stretching vibration mode of Si-O, Al-OH-Al bending vibration mode, and Al-OH-Mg bending vibration mode were attributed to the peaks at 1043, 914, and 846 cm^{-1} [67], [68]. The results clearly show that the Fe-Mt samples exhibited no impurity peaks in the FTIR spectrum.

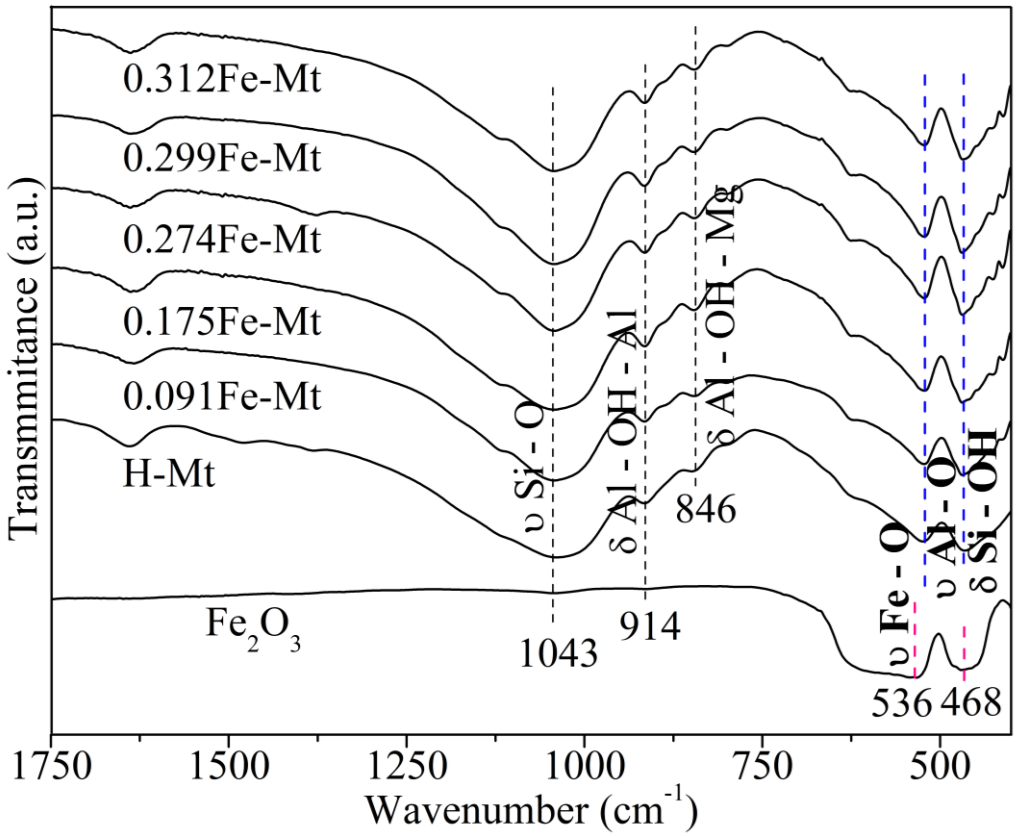

Fig. 3.4. FTIR spectra for Fe-Mt, 0.091Fe-Mt, 0.175Fe-Mt, 0.274Fe-Mt, 0.299Fe-Mt, 0.312Fe-Mt and hematite (γ-Fe_2O_3).

To establish the chemical composition and electronic level of Fe-Mt, XPS measurements were carried out. **Fig. 3.5a** depicts a survey spectrum for the 0.274Fe-Mt element. Two peaks at 102.3 and 100.2 eV are observed in the deconvoluted spectra of Si 2p, which are attributed to Si-O and silane, respectively (**Fig. 3.5b**) [69]. It has been suggested that the surface hydroxyl and lattice oxygen groups in the O 1s area (**Fig. 3.5c**) are responsible for the two peaks at 531.4 and 528.8 eV, respectively, in the O 1s spectrum [70]. The peak of the Al 2p spectrum is depicted in **Fig. 3.5d** at 74.3 eV and is represented by the arrow. It corresponds to the element Al-O [71]. In the Fe 2p area (**Fig. 3.5e**), two peaks at 725.3 and 712.8 eV were found to be due

to Fe^{III} $2p_{1/2}$ and $2p_{3/2}$. **Fig. 3.5f** illustrates the VB XPS for 0.274Fe-Mt. When the tangent and the horizontal base line connect, the semiconductor's valance band top (VBT) is exposed [72], [73].

XANES and FT-EXAFS were used to confirm the oxidation state and form of Fe in Fe-Mt samples, as shown in **Fig. 3.6**. Essentially, each compound's unique XANES spectra can be utilized as a fingerprint. The edge energy positions of 0.274Fe-Mt and 0.312Fe-Mt essentially overlapped in **Fig. 3.6a**, indicating that the bigger dosage and increased intercalation of Fe^{III} were not decisive factors in the Fe^{III} interacting with the surface of the Mt layers. In the spectra of 0.274Fe-Mt and 0.312Fe-Mt, the peak at 7133 eV roughly coincided with Fe_2O_3, however the shoulder peaks (7145 eV) were left shifted. The oscillation in the post-edge spectra of 0.274Fe-Mt and 0.312Fe-Mt was distinguished from that of all hematite (Fe_2O_3), goethite (FeOOH), and magnetite (Fe_3O_4) (e.g., 7183 and 7196 eV), implying that intercalated Fe^{III} was formed, which is a different interaction than the three reference minerals. The Fe_2O_3, FeOOH, and Fe_3O_4 revealed the first shell of oxygen and the second shell of iron in the FT-EXAFS in **Fig. 3.6b**. Only one oxygen shell developed for both 0.274Fe-Mt and 0.312Fe-Mt. This suggests that the Fe^{III} in 0.274Fe-Mt and 0.312Fe-Mt should be intercalated rather than replaced into the aluminosilicate layers.

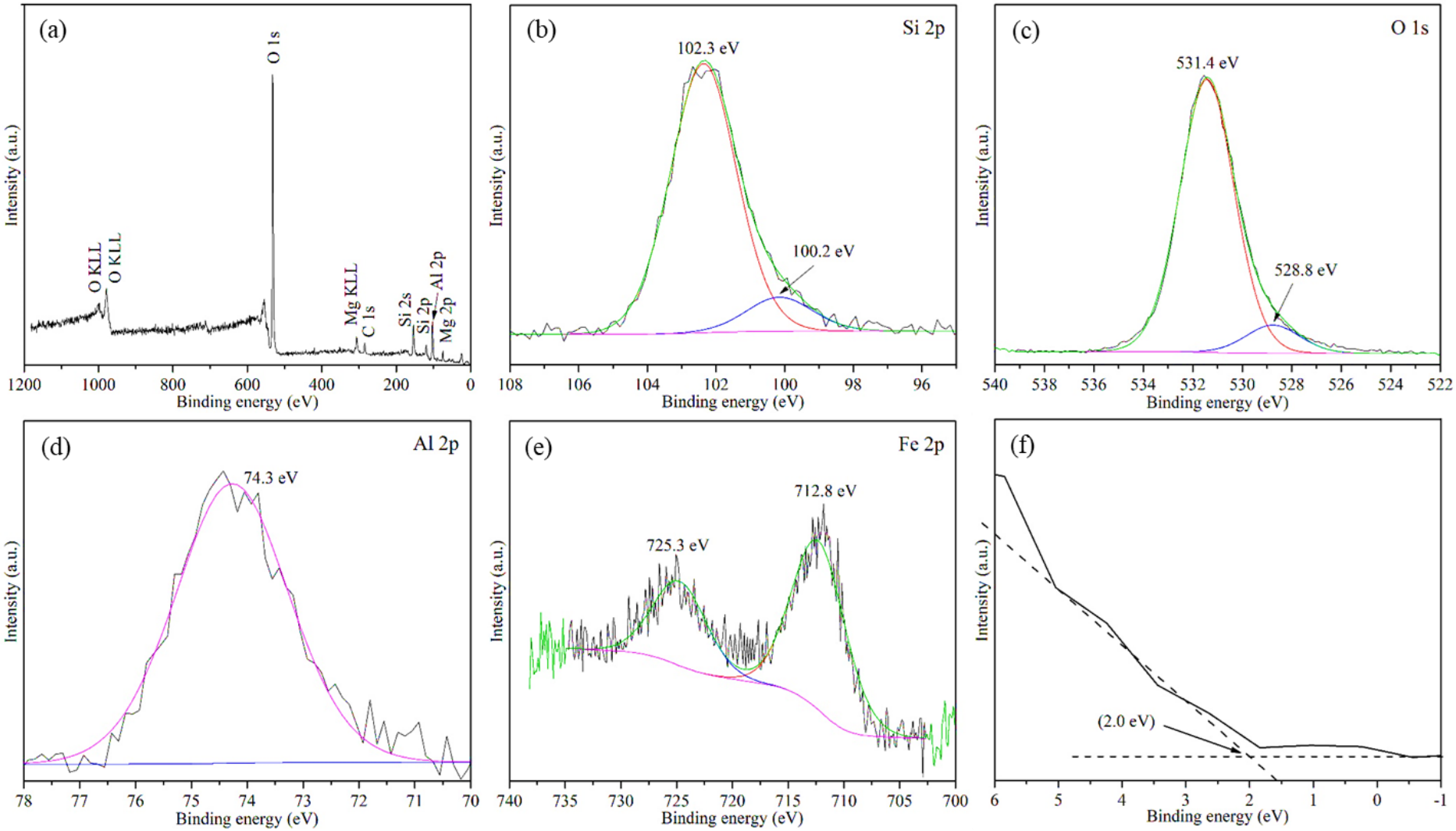

Fig. 3.5. XPS (a) survey and narrow scans of (b) Si 2p, (c) O 1s, (d) Al 2p (e) Fe 2p for 0.274Fe-Mt, and (f) valence band (VB) energy region.

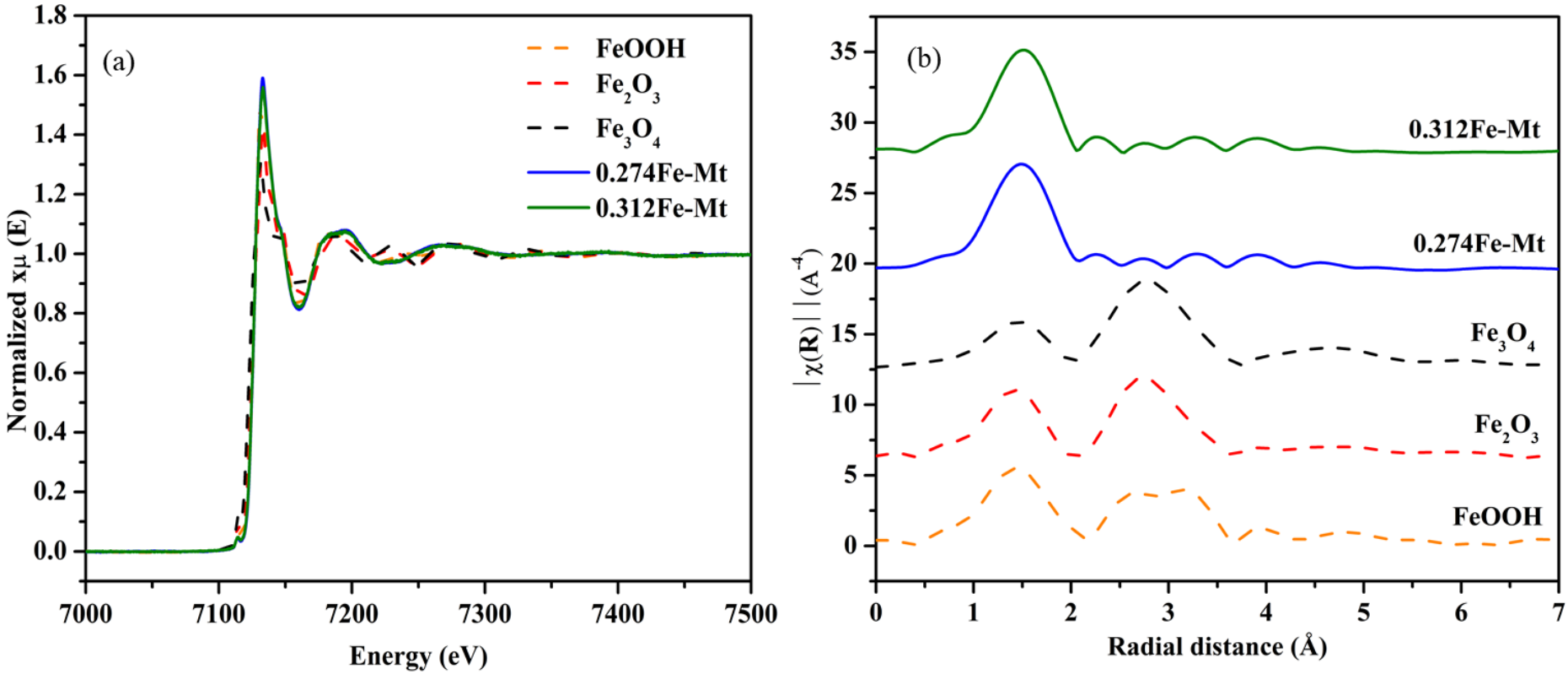

Fig. 3.6. (a) XANES and (b) FT-EXAFS spectra of Fe K-edge of 0.274Fe-Mt, 0.312Fe-Mt, FeOOH, Fe_2O_3, and Fe_3O_4.

Fig. 3.7 shows the surface morphology of Fe-Mt samples as evaluated by SEM. The parallel Mt layers aggregated closely in Fe-Mt, similar to pure Mt, and fine plate-like particles were found (**Fig. 3.8a**). Due to acid leaching, the margins of the Mt strata on the surface grew smoother and softer. As the amount of Fe^{III} added to the surface increased, the parallel Mt layers twisted, and some broke down into smaller pieces. As a result, the layers are less parallel, and the face-to-edge cross rises (**Fig. 3.8a-f**). This could be because Fe^{III} facilitates acid erosion of the surface Mt layers, but SEM cannot see the effect of acid on the bulk Mt. Furthermore, after Fe^{III} was added, the fine plate-like particles vanished. The well-swelled tiny particles can be easily collected by the micelles and decanted during the washing process because the Fe^{III} in the solution can form micelles.

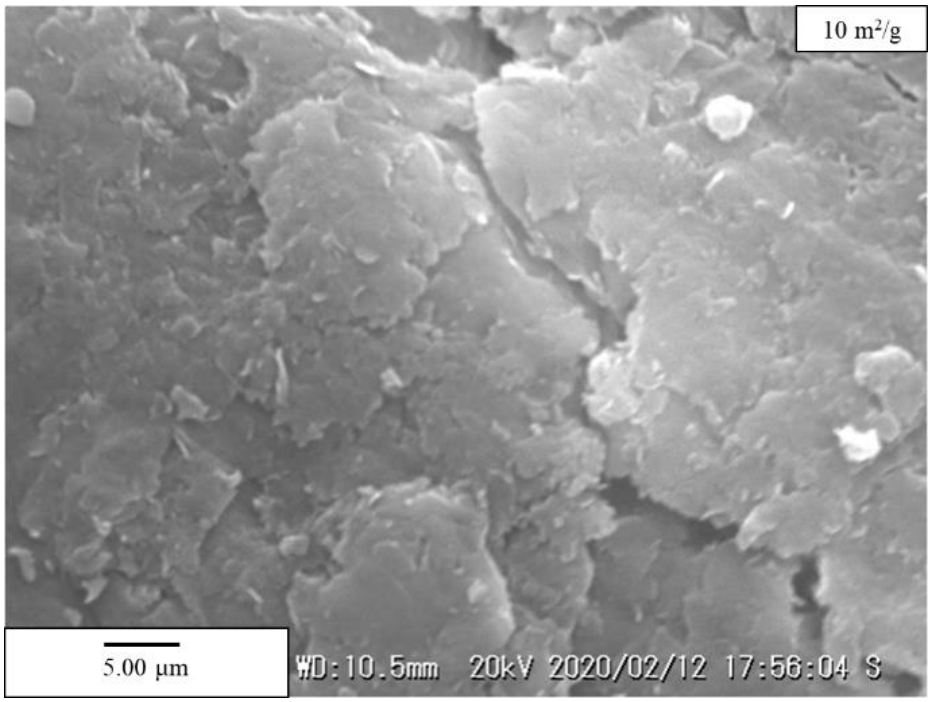

Fig. 3.7. SEM images of the original Mt.

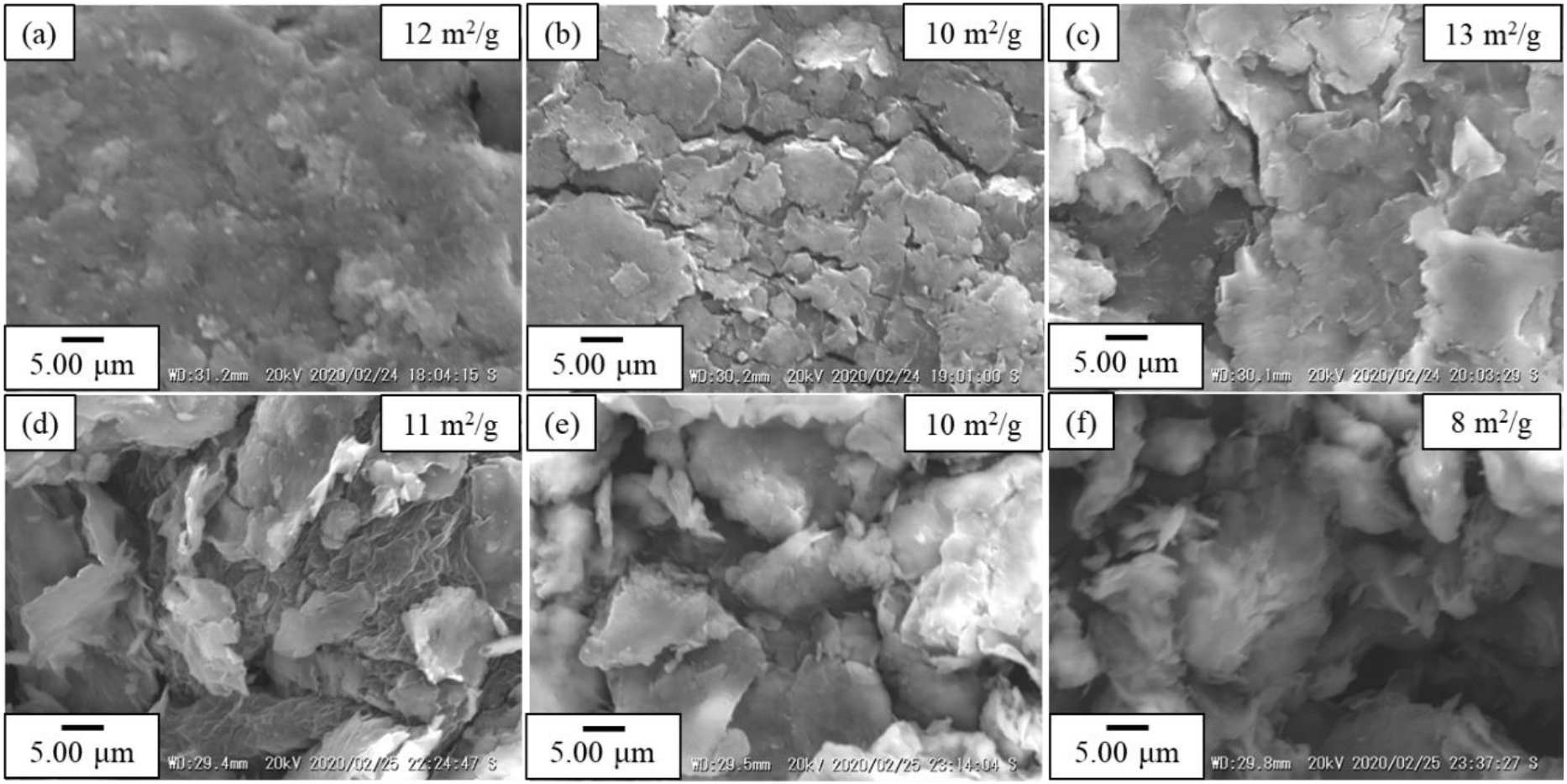

Fig. 3.8. SEM images of (a) Fe-Mt, (b) 0.091Fe-Mt, (c) 0.175Fe-Mt, (d) 0.274Fe-Mt, (e) 0.299Fe-Mt and (f) 0.312Fe-Mt.

Nitrogen gas (N_2) adsorption/desorption isotherms were used to further evaluate Fe-Mt (**Fig. 3.9**). Except for a decline in 0.312Fe-Mt (**Fig. 3.9, Table 3.2**), the specific surface areas (S_{BET}) of Fe-Mt remained stable, and the average pore size determined by the BJH technique gradually dropped (**Table 3.2**). As a result, the broken Mt layers on the surface only cut the pores into smaller sizes, but the negligible changes in the construction of the bulk Mt result in a small S_{BET} variation, confirming the hypothesis that Fe^{III} assistance to the acid erosion effect should only occur on the surface of Mt.

Table 3.2. S_{BET} and averaged pore size of Fe-Mt, 0.091Fe-Mt, 0.175Fe-Mt, 0.274Fe-Mt, 0.299Fe-Mt and 0.312Fe-Mt.

Sample	S_{BET} [1] (m^2/g)	Averaged pore size [2] (nm)
Fe-Mt	12.4	0.066
0.091Fe-Mt	10.1	0.063
0.175Fe-Mt	12.6	0.043
0.274Fe-Mt	11.2	0.043
0.299Fe-Mt	10.4	0.035
0.312Fe-Mt	7.8	0.034

[1] Calculated based on Brunauer–Emmett–Teller (BET) method.

[2] Calculated based on Barrett–Joyner–Hanlenda (BJH) method.

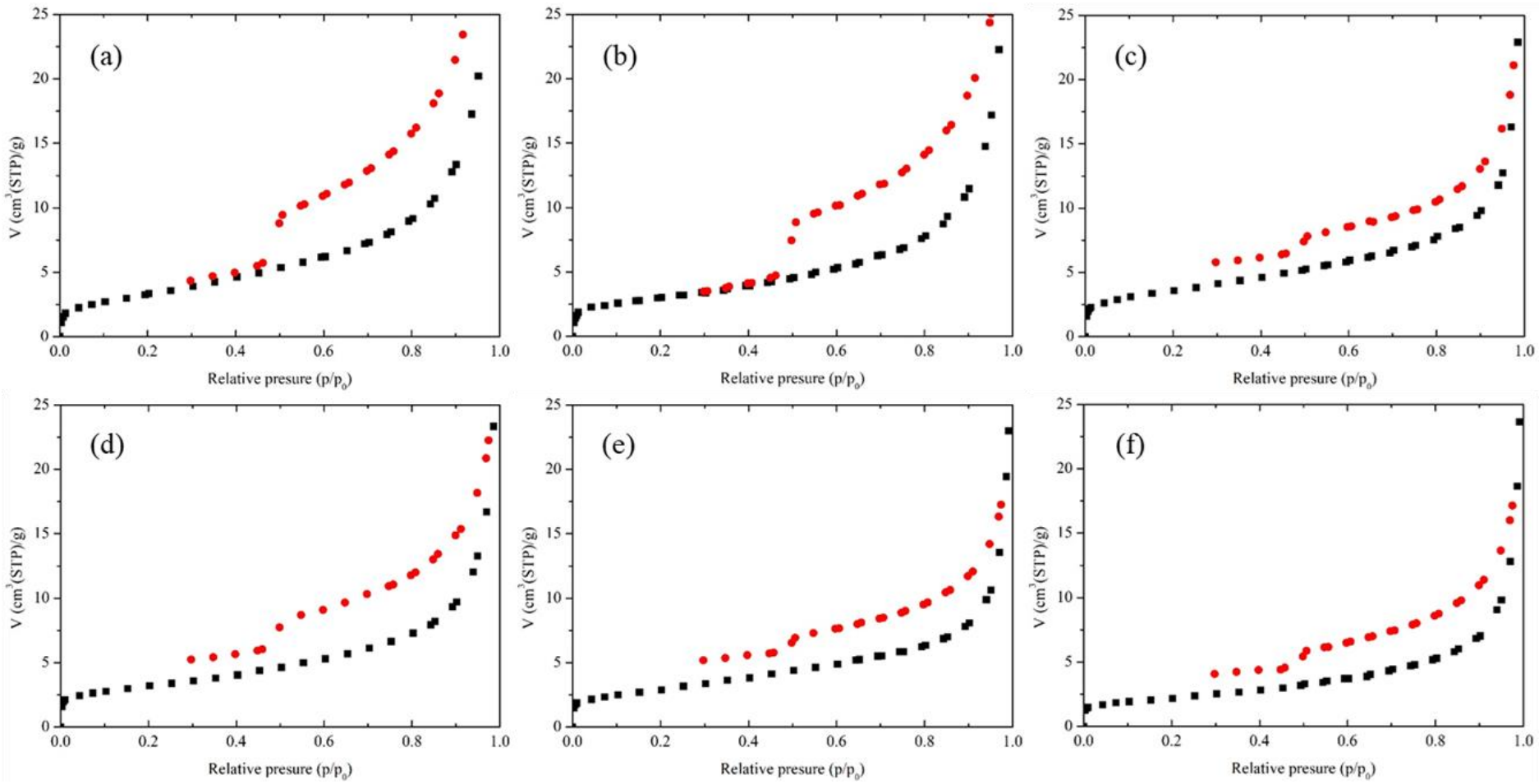

Fig. 3.9. N_2 adsorption/desorption isotherms of (a) Fe-Mt, (b) 0.091Fe-Mt, (c) 0.175Fe-Mt, (d) 0.274Fe-Mt, (e) 0.299Fe-Mt and (f) 0.312Fe-Mt.

3.3.2 The optical and photocatalytic properties

The diffuse reflectance UV-Vis (UV-DRS) spectra of Fe-Mt were obtained to evaluate the optical properties of the Fe-Mt and Fe-Mt samples, as shown in **Fig. 3.10a**. When compared to Fe-Mt (at 400 nm), the absorption edge of Fe-Mt samples had a considerable redshift toward the visible area and improved light absorption in both the UV and visible ranges. The photocatalytic activity for Cr^{VI} conversion was increased when the absorption band was extended. Furthermore, the Tauc approach was used to compute the optical band gap energy (*Eg*) of Fe-Mt samples, which can be expressed by the Kubelka–Munk function (eq. 3.1) [47]:

$$\alpha h\nu = k(h\nu - Eg)^{n/2} \quad (3.1)$$

where α is the absorption coefficient, *h* is the Planck constant, *k* is the proportionality constant, ν is the frequency of the photon, and *Eg* is the band gap energy. For the direct e^- transition, the n factor is 1; for the indirect e^- transition, it is 4. For Fe-Mt, 0.091Fe-Mt, 0.175Fe-Mt, 0.274Fe-Mt, 0.299Fe-Mt, and 0.312Fe-Mt (**Fig. 3.10 b**), the obtained *Eg* were 3.50 eV, 3.10 eV, 2.70 eV, 2.65 eV, 2.60 eV, and 2.60 eV, respectively. The stoichiometry Fe^{III} modification of Fe-Mt, 0.091Fe-Mt, 0.175Fe-Mt, and 0.274Fe-Mt was favorably linked with the improvement of light absorption by Fe-Mt as demonstrated by UV-DRS data (**Table 3.2**). In 0.274Fe-Mt, 0.299Fe-Mt, and 0.312Fe-Mt, the hypothesis that narrowing the *Eg* stopped further improvement of Fe^{III} modification was studied. The presence of Fe^{III} in the modified samples causes a new Fermi

level between the energy bands of Mt, resulting in a drop in *Eg* of Fe-Mt samples. Because the production of electrons has a maximum threshold, increasing Fe^{III} doping will eventually have minimal impact on improving the optical characteristics of Fe-Mt. Based on the VB and *Eg* measurements, the conduction band energy (CB) of Fe-Mt could be predicted to be 0.89 eV. Transient photocurrent response measurements and electrochemical impedance spectroscopy (EIS) were also used to explore the migration and production of electrons in the Fe-Mt and Fe-Mt, which were linked to photocatalytic performance for Cr^{VI} reduction. As shown in **Fig. 3.11a**, the photocurrent density of 0.274Fe-Mt was somewhat greater than that of Fe-Mt, implying that Fe modified Mt may improve light adsorption and electron generation under light illumination by lowering *Eg*. The increased photocurrent density of 0.274Fe-Mt compared to Fe-Mt is compatible with photocatalytic activity, implying that the photocurrent differential is considerable and can be utilized to claim improved electrochemical performance. Furthermore, as shown in **Fig. 3.11b**, the electrochemical impedance spectroscopy (EIS) spectra of both Fe-Mt and Fe-Mt were measured. The charge transfer capacity of the material is connected to the EIS Nyquist. The lower resistance for charge transfer relates to the smaller radius in 0.274Fe-Mt.

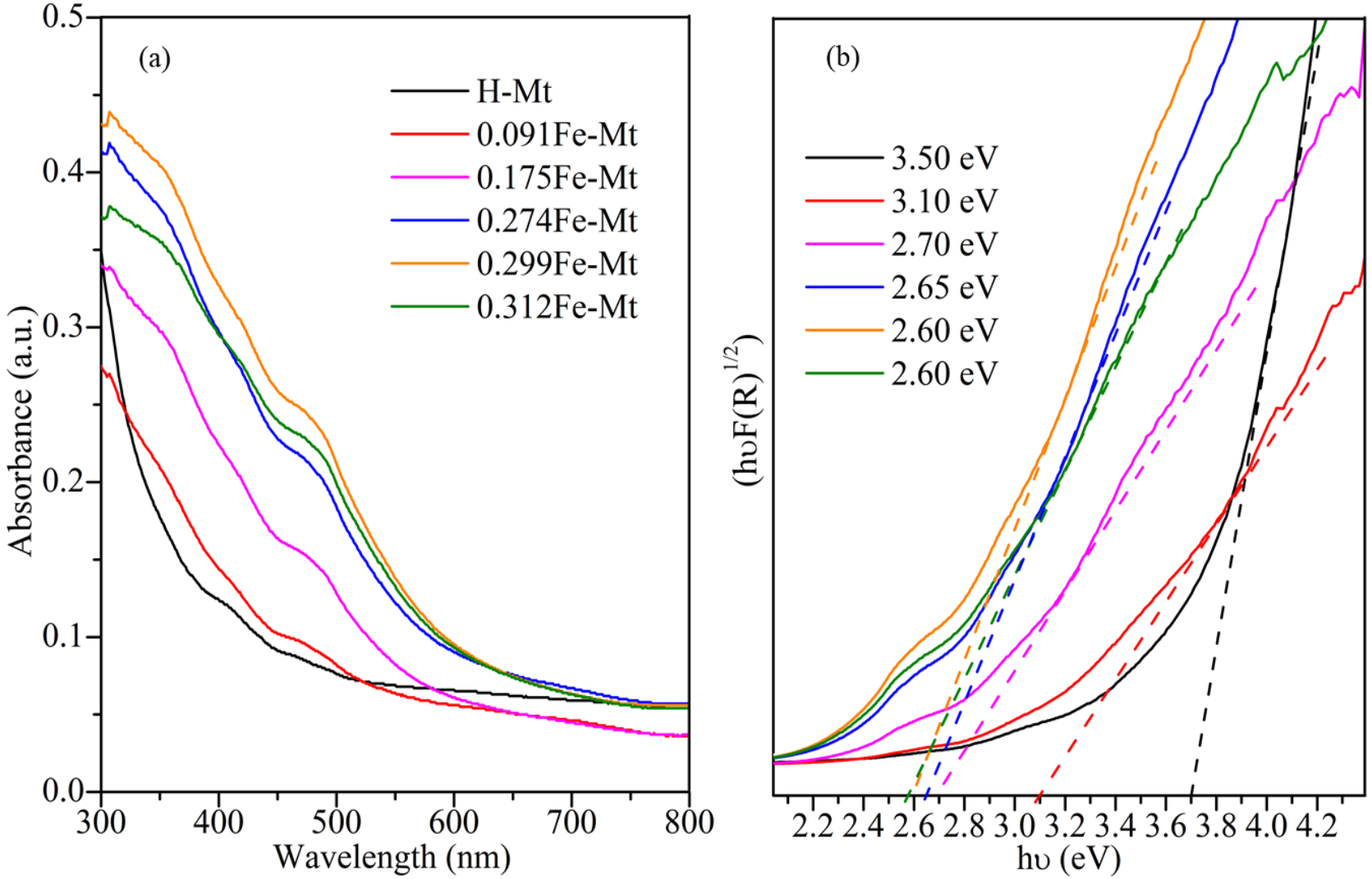

Fig. 3.10. (a) UV-DRS spectra and (b) Tauc plots of Fe-Mt, 0.091Fe-Mt, 0.175Fe-Mt, 0.274Fe-Mt, 0.299Fe-Mt and 0.312Fe-Mt.

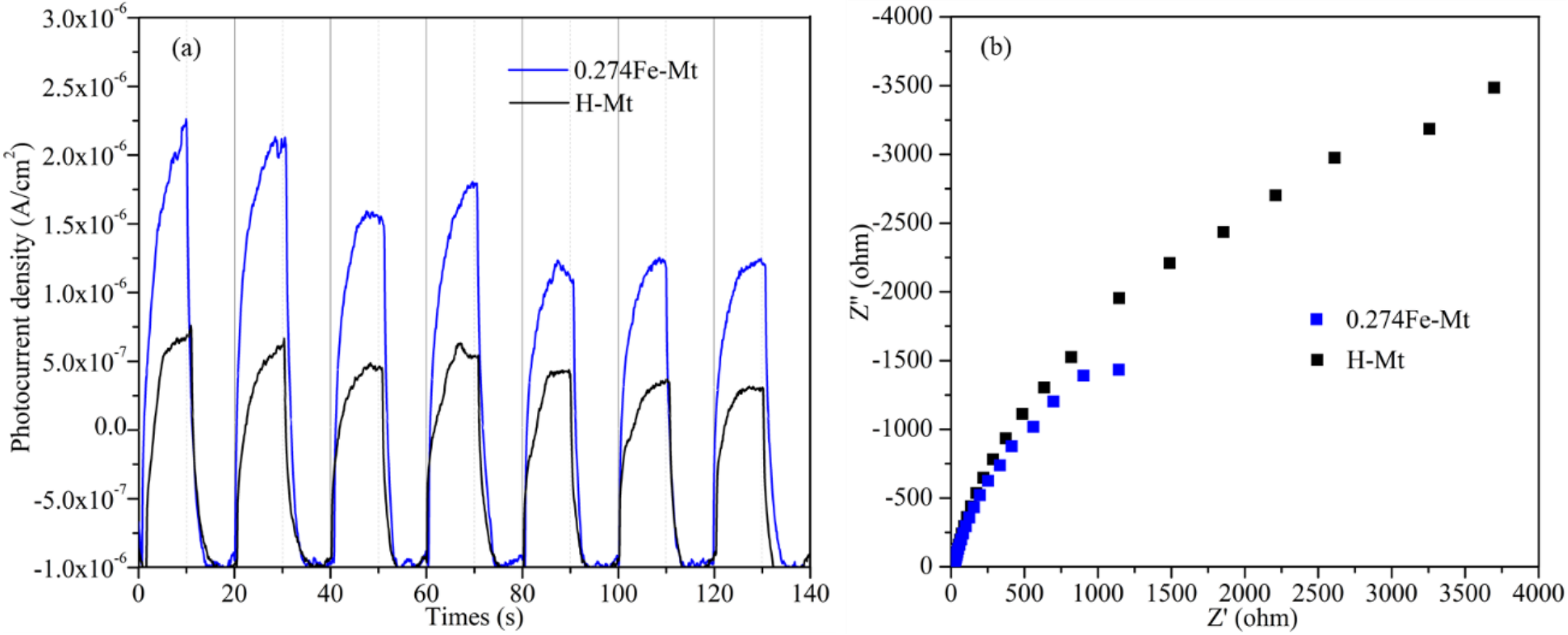

Fig. 3.11. (a) Photocurrent response and (b) EIS spectra for Fe-Mt and 0.274Fe-Mt.

3.3.3 Photocatalytic activity

Hematite (γ-Fe_2O_3), goethite (FeOOH), and magnetite (Fe_3O_4) were used for photocatalytic reduction of Cr^{VI} before the photocatalytic performance test for the synthesized Fe-Mt, as shown in **Fig. 3.12**. All Fe-Mt alloys, including Fe-Mt, performed better.

Fig. 3.13a shows the Cr^{VI} removal efficiency at pH 2 for the Fe-Mt and Fe-Mt samples. Cr^{VI} adsorption was found to be between 2% and 6% in dark circumstances. The possibility of a Fenton reaction in a Cr^{VI} solution system with a 0.274Fe-Mt dispersion was studied. It was discovered that the Cr^{VI} reduction via the 0.274Fe-Mt in dark (**Fig. 3.14**) could not happen via Fenton reaction (reaction under dark conditions), suggesting that the Cr^{VI} decrease should be due to photocatalytic reaction. **In Fig. 3.14**, the photocatalytic reduction of Cr^{VI} on 0.274Fe-Mt was compared using UV and visible light (300-1000 nm), solely visible light (400-750 nm), and only UV light (less than 400 nm). Because the light energy is sufficient for excitation of electrons from VB to CB with the *Eg* at 2.60 eV, it is clear that the Cr^{VI} reduction was achieved when the reaction was performed under UV or visible light. In the case of visible light, however, activity decreased due to lesser light energy. Due to the adsorption of Mt, the adsorption reached equilibrium in 5 minutes under both UV and visible light (300-1000 nm) irradiation. Under irradiation, Fe-Mt without Fe^{III} showed a 20% drop in Cr^{VI} in 60 minutes. A little amount of $Fe^{II/III}$ in the Mt structure was washed out to the interlayer, according to XRD data (**Fig. 3.2**). Although Fe-Mt had a poorer photocatalytic reduction performance than other Fe-Mt samples,

the presence of interlayer $Fe^{II/III}$ aided the photocatalytic performance of Fe-Mt when compared to the original Mt. Cr^{VI} remediation was aided by more Fe^{III} doping. Within 60 minutes of irradiation, the Cr^{VI} decrease was 22% and 35%, respectively, by 0.091Fe-Mt and 0.175Fe-Mt. Cr^{VI} removal reached the highest measured value of 47% in 0.274Fe-Mt, where the concentration of Fe^{III} was 0.274 mmol/g. The photocatalytic Cr^{VI} reduction of the 0.299Fe-Mt and 0.312Fe-Mt samples also dropped somewhat. The abundant Fe^{III} on the surface of Mt confined the statistically excited electrons, causing this event. Based on the *Eg* acquired by DRS, the redundant Fe^{III} had a negligible boosting influence on the excitation of electron-hole pairs (**Fig. 3.10**). More crucially, the excess Fe^{III} from the Cr^{VI} reduction will trap a portion of the statistically excited electron. Furthermore, the high Fe^{III} content of Fe-Mt reduces the interaction between Cr^{VI} and the surface of Fe-Mt, as evidenced by Cr^{VI} adsorption under dark conditions (**Fig. 3.13a**). Within 60 minutes of irradiation, the elimination of Cr^{VI} on 0.299Fe-Mt and 0.312Fe-Mt was 44% and 43%, respectively. The photocatalytic efficiency was greatly improved with the use of ethanol as a hole scavenger, with a 66% reduction of Cr^{VI} in 10 minutes and a 100% reduction of Cr^{VI} in 20 minutes on 0.274Fe-Mt. (**Fig. 3.16.**). Because Cr^{VI} can only be reduced rather than oxidized, the redox reaction of Cr^{VI} was postulated to take place at the electron acceptor energy level. eq. 3.2 shows the kinetics of the photocatalytic reaction adapted to the pseudo-first-order model:

$$-\ln\left(C/C_0\right) = kt \tag{3.2}$$

The residual and initially added concentrations of Cr^{VI} are represented by C and C_0 (mmol/g), and the rate constant is represented by k (min^{-1}). The values of k for each sample are 2.97×10^{-3}, 5.30×10^{-3}, 6.31×10^{-3}, 10.52×10^{-3}, 9.22×10^{-3}, and 9.08×10^{-3} min^{-1}, according to the kinetic graphs shown in **Fig. 3.13b**. With ethanol as the hole scavenger, 6.12×10^{-2} min^{-1} for 0.274Fe-Mt was obtained. The value of k is positively associated to the stoichiometric doping quantity of Fe^{III} in Fe-Mt samples with Fe^{III} addition lower than the CEC of Mt. When there was excess Fe^{III}, however, k dropped in 0.299Fe-Mt and 0.312Fe-Mt because excess Fe^{III} may hinder light transmission to the surface of Mt and diminish the quantity of active surface for Cr^{VI} reduction due to Fe^{III} trapping electrons.

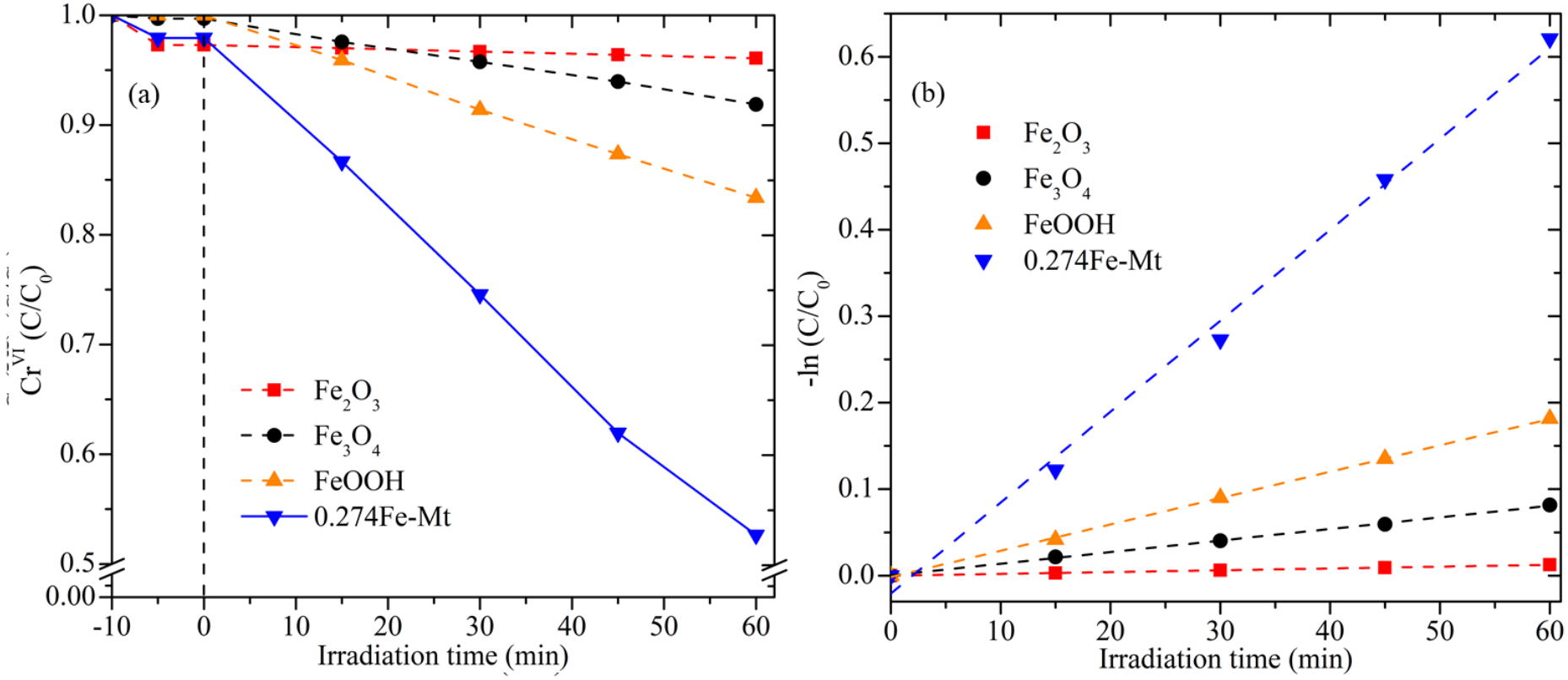

Fig. 3.12. (a) Adsorption and photocatalytic reduction and (b) pseudo-first-order kinetic modeling of Cr^{VI} over 0.274Fe-Mt, hematite (γ-Fe_2O_3), goethite (FeOOH), and magnetite (Fe_3O_4) under irradiation at pH 2.

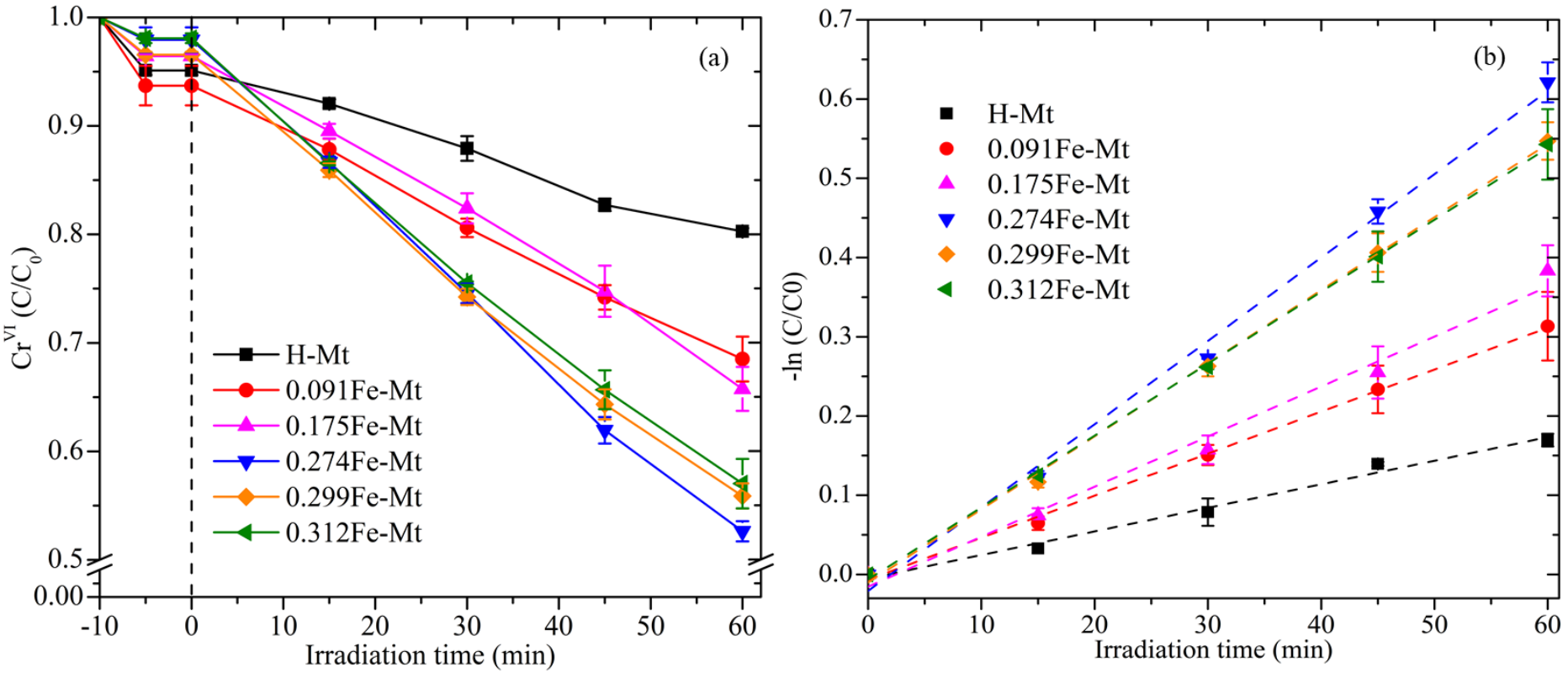

Fig. 3.13. (a) Photocatalytic reduction of Cr^{VI} under irradiation over Fe-Mt, 0.091Fe-Mt, 0.175Fe-Mt, 0.274Fe-Mt, 0.299Fe-Mt, and 0.312Fe-Mt at pH 2 and (b) corresponding pseudo-first-order kinetic plot.

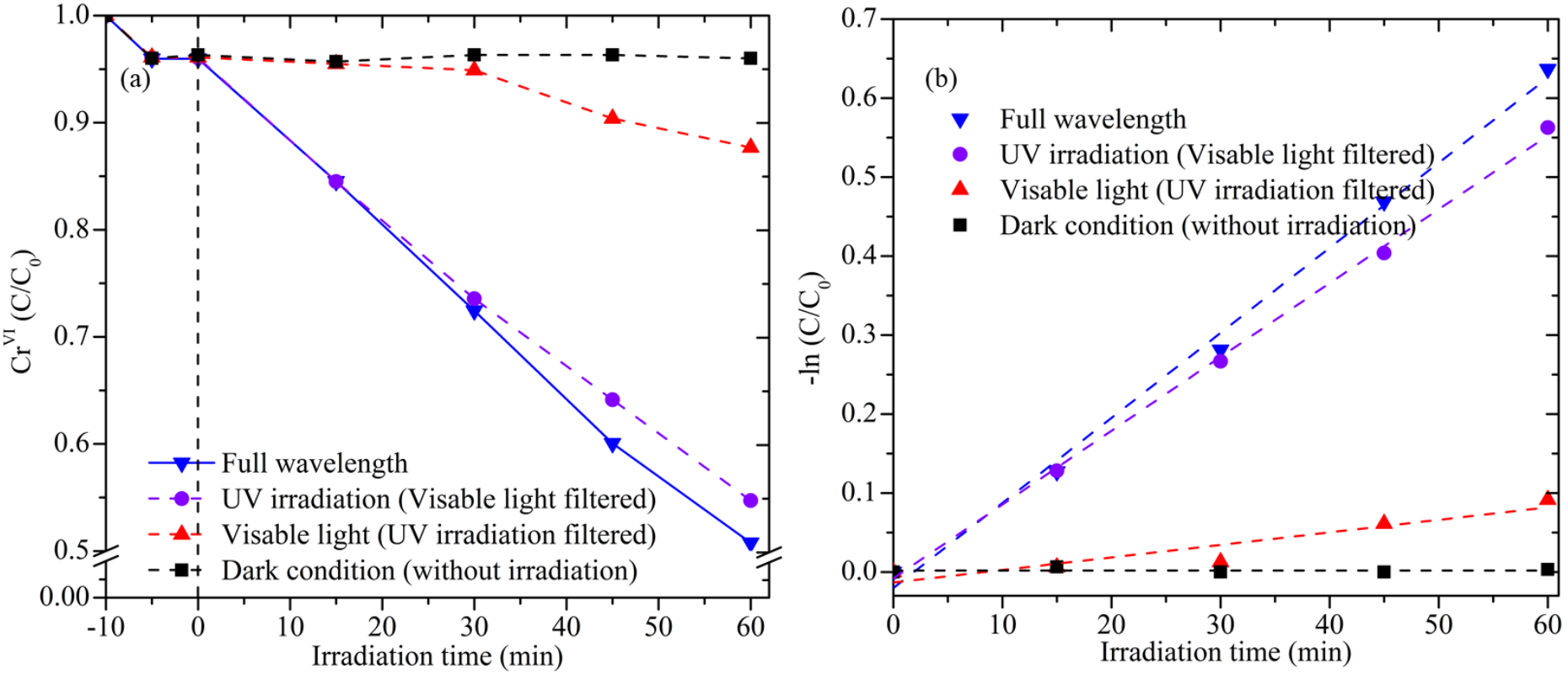

Fig. 3.14. (a) Adsorption and photocatalytic reduction, and (b) pseudo-first-order kinetic modeling of Cr^{VI} over 0.274Fe-Mt in the presence of UV and visible light (300-1000 nm), only visible light (400-750 nm), only UV light (less than 400 nm), and dark conditions at pH 2.

3.3.4 Effect of pH

The pH of wastewaters frequently varies a lot. As a result, this element must be considered, particularly in industrial applications （**Fig. 3.15**). The photocatalytic remediation of the mono-cation system of Cr^{VI} was explored with ethanol as the hole scavenger (an initial Cr^{VI} concentration of 10 ppm and a Fe-Mt dosage of 50 mg) because ethanol could greatly boost the photocatalytic efficiency of Fe-Mt (**Fig. 3.16**). The pH effect's achieved result is presented in **Fig. 3.15**. In more acidic media, there was more deterioration. The faster reaction rate of Cr^{VI} reduction under acidic settings than under neutral or basic conditions has been extensively established [74], owing to $Cr_2O_7^{2-}$ stronger oxidizing property under acidic conditions than CrO_4^{2-} under basic conditions. Furthermore, XRD analysis of the Fe-Mt residue produced following Cr^{VI} reduction at high pH revealed decreased interlayer space (**Fig. 3.17**). During the photocatalytic reaction, Fe^{III} can be released into the bulk solution, and both Fe^{III} and the converted Cr^{III} ions precipitated when the pH increased. Coprecipitation between Fe^{III} and Cr^{III} may have also happened, resulting in increased precipitation on the catalyst's surface and easier release of interlayer Fe^{III}, decreasing the Mt interlayer space.

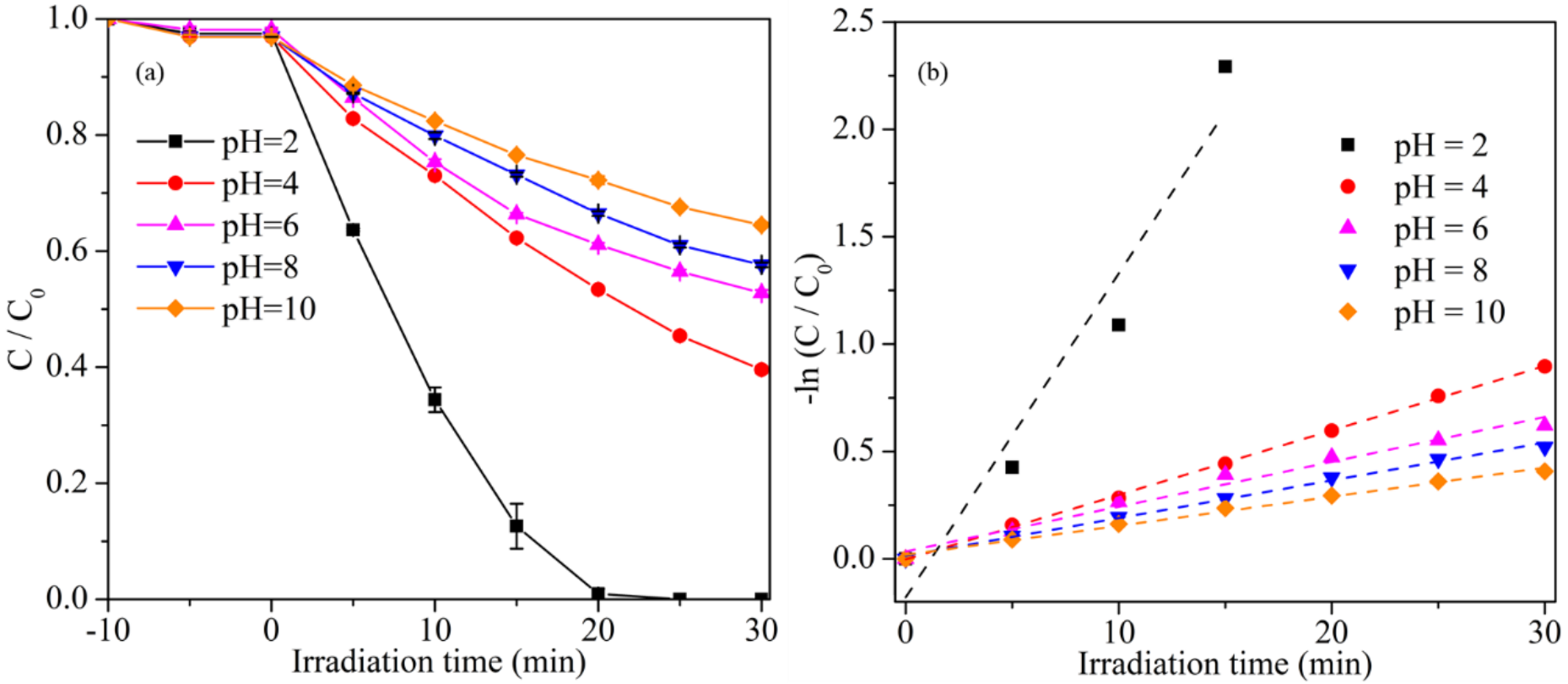

Fig. 3.15. Effect of pH on the (a) photocatalytic redox of Cr^{VI} by 0.274Fe-Mt with ethanol as scavenger under light irradiation and (b) the pseudo-first-order kinetic plot.

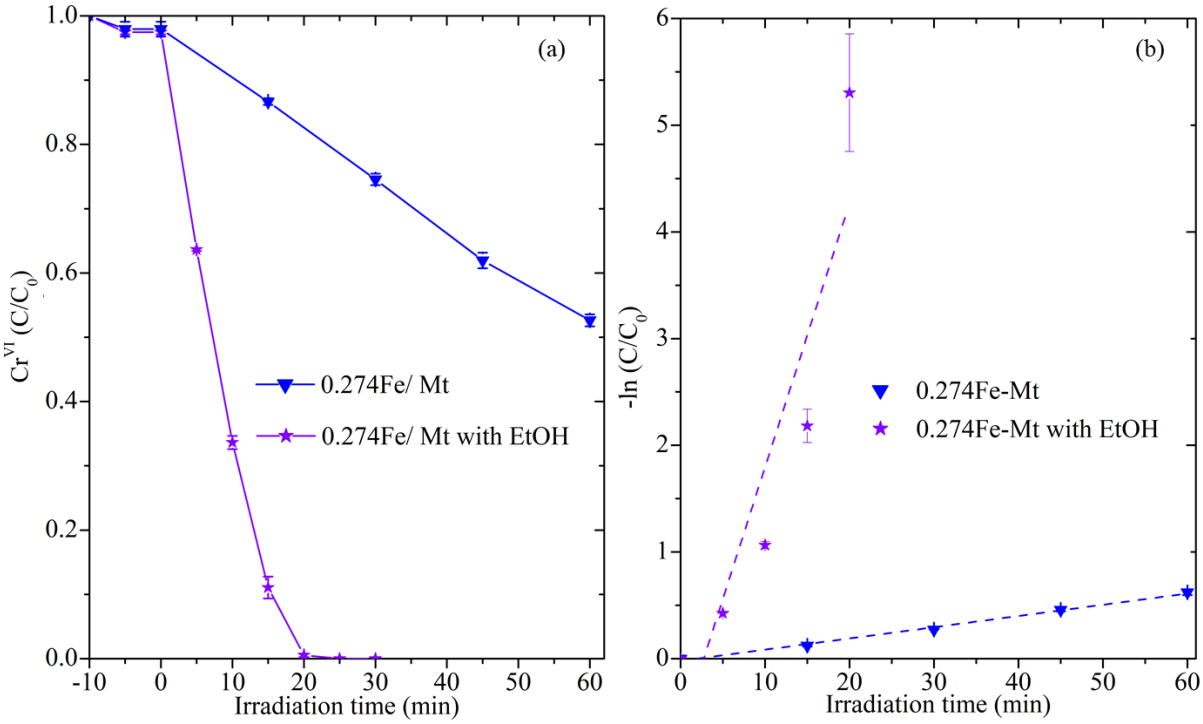

Fig. 3.16. (a) Adsorption and photocatalytic reduction and (b) pseudo-first-order kinetic modeling of Cr^{VI} over 0.274Fe-Mt with/ without ethanol as the hole scavenger under irradiation at pH 2.

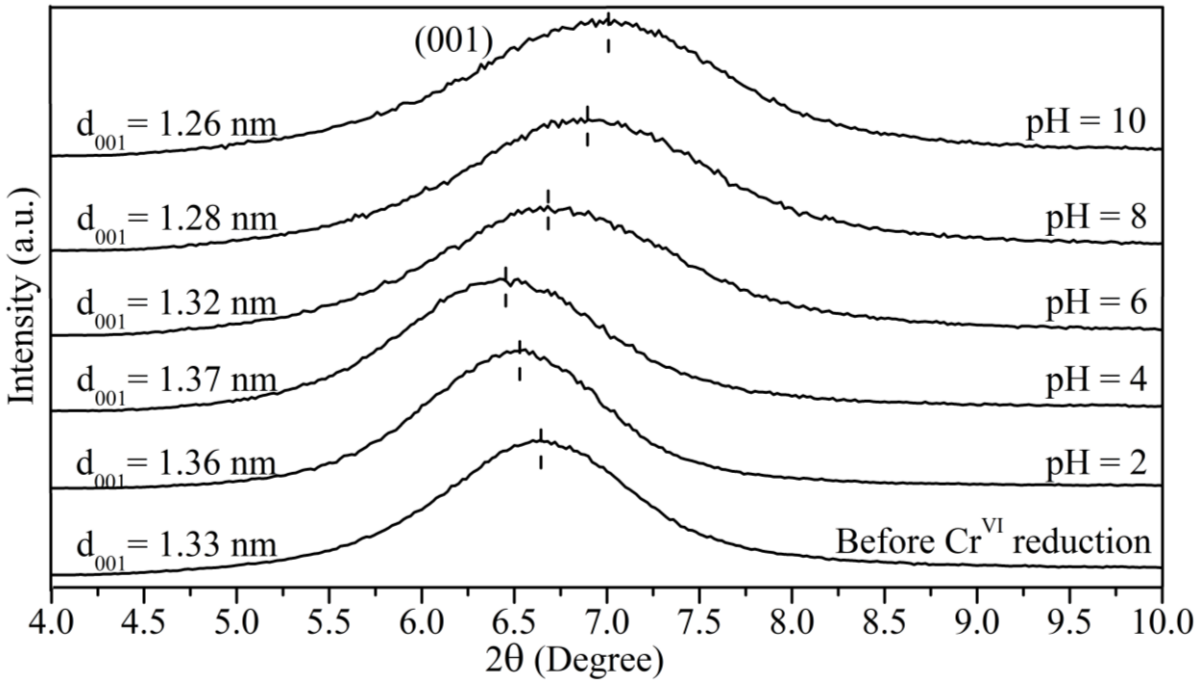

Fig. 3.17. The pH effect on XRD patterns for the solid residues after Cr^{VI} photocatalytic reduction by 0.274Fe-Mt.

3.3.5 Reusability test

One of the most important factors in determining a photocatalyst's capacity is its reusability. Even after five recycling cycles of 0.274Fe-Mt, which has the best photocatalytic performance for Cr^{VI} reduction, a high reduction efficiency was maintained. According to the results in **Fig. 3.18**, the first cycle achieved about 100.0% lowering efficiency for Cr^{VI} reduction. In the second cycle, the photocatalytic capacity dropped dramatically, resulting in an 89.7% degradation, following which the photocatalytic reduction capacity remained stable at 87%. Since the hydrated ionic size for Fe^{III} is 0.45 nm [59], and for Cr(Ⅲ) is 0.47 nm [60], XRD before and after photocatalytic remediation of Cr^{VI} presented in the pH effects section (**Fig. 3.17**) revealed a little increasing of the interlayer space for 0.274Fe-Mt. The incomplete development of the hydrated shell in the Mt interlayer accounts for the smaller interlayer distance than the hydrated ionic size. Furthermore, for the 0.274Fe-Mt before and after photocatalytic remediation of Cr^{VI}, FTIR (**Fig. 3.19**) and SEM (**Fig. 3.20**) examination were used. It has no change in FTIR spectra or SEM morphology, indicating that the Fe-Mt for Cr^{VI} reduction is quite stable.

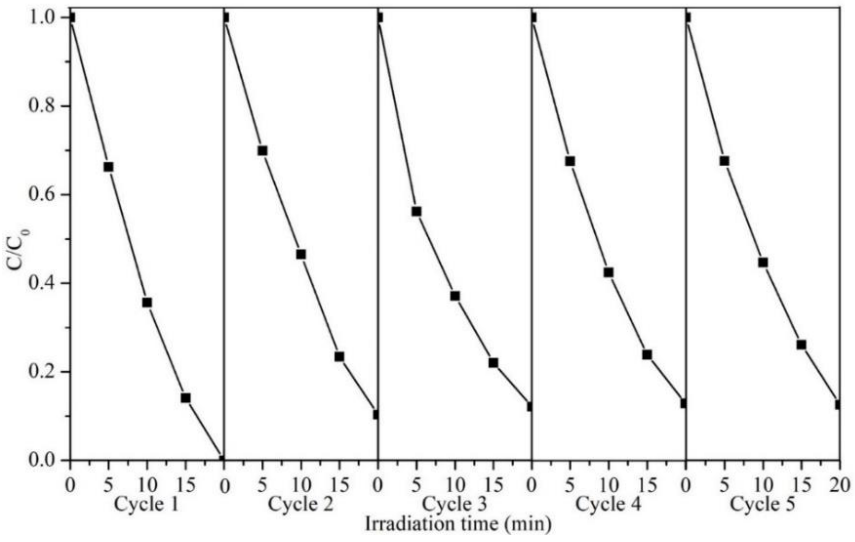

Fig. 3.18. Reusability test of photocatalytic Cr^{VI} reduction by 0.274Fe-Mt. Initial [Cr^{VI}] was 10 mg/L.

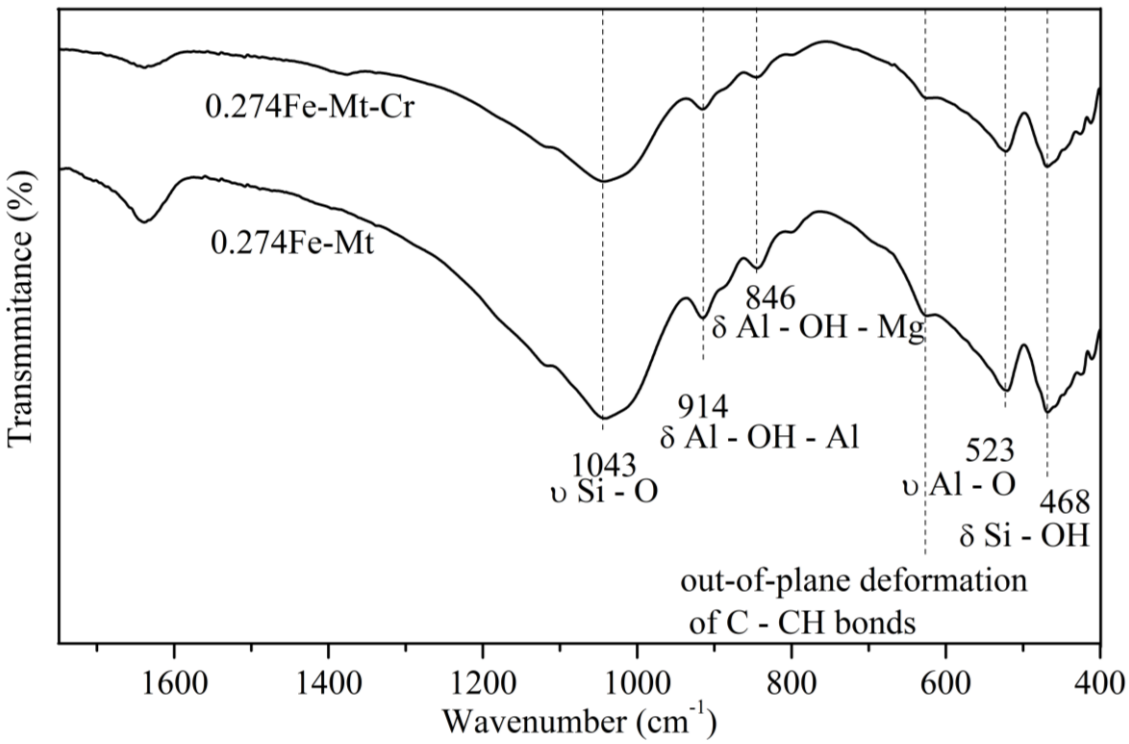

Fig. 3.19. FTIR spectra for 0.274Fe-Mt before and after photocatalytic remediation of Cr^{VI} with ethanol as the hole scavenger.

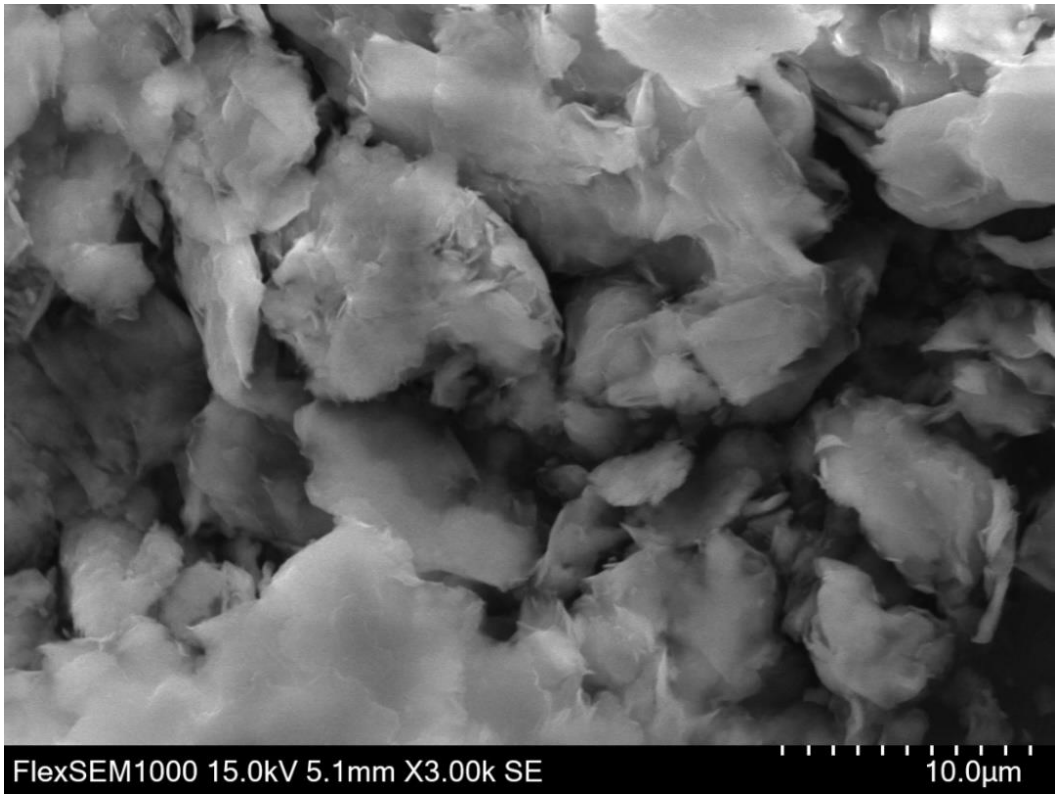

Fig. 3.20. SEM images of the 0.274Fe-Mt after the photocatalytic remediation of Cr^{VI} with ethanol as the hole scavenger.

3.3.6 Mechanism of Cr^{VI} reduction over Fe-Mt

Under illumination, the photocatalytic reaction began with the formation of hole-electron pairs [75], [76]. The origin Mt has a huge *Eg* of 5.16 eV and cannot operate in the presence of light [47]. Fe-Mt, on the other hand, has a lower *Eg* because Fe^{III}-Fermi level was produced [47]. Cr^{VI} photocatalytic reduction over Fe-Mt was shown in **Fig. 3.21**. The Fermi level was expected to be around -0.65 eV based on *Eg* and VB of 0.274Fe-Mt. The literature [47] mentions a decrease in *Eg* owing to Fe contaminants, as well as other related findings. Electrons were created and moved to the Fe^{III} formed Mid-gap state of Fe-Mt under light irradiation, concurrently leaving holes in the VB. Hexavalent Cr^{VI} can be converted to trivalent Cr^{VI} by accumulating electrons at the Fermi level. The photocatalytic reduction of Cr^{VI} on 0.274Fe-Mt was greatly improved when ethanol was used as a hole scavenger and electron donor. In the solution, the ejected electron in the conduction band converts Cr^{VI} to Cr^{III}. Due to ethanol quenching, reduced Cr^{III} is unable to enter the hole in the valance band, preventing Cr^{III} reoxidation in the valance band and promoting the photocatalytic reaction's kinetics. The reaction of holes with ethanol as a hole scavenger prevented the reoxidation of Cr^{III} [77], [78]. These findings demonstrated that the Fe^{III} function in Mt can boost photocatalytic activity by establishing a middle gap level, resulting in a reduction in Mt *Eg*. The following equations were used to describe all of the processes that occurred during the photocatalytic reaction with / without ethanol:

$$Fe/\,Mt \xrightarrow{h\nu} Fe/\,Mt\,(h^+/\,e^-) \tag{3.3}$$

$$6e^- + 3{Cr_2O_7}^{2-} + 42\,H^+ \rightarrow 6Cr^{III} + 21H_2O \tag{3.4}$$

$$Cr^{III} + 3h^+ \rightarrow Cr^{VI} \text{ (Without ethanol)} \tag{3.5}$$

$$CH_3OH + h^+ + Cr^{III} \rightarrow CH_3O^{\bullet -} + H^+ + Cr^{III} \text{ (With ethanol)} \tag{3.6}$$

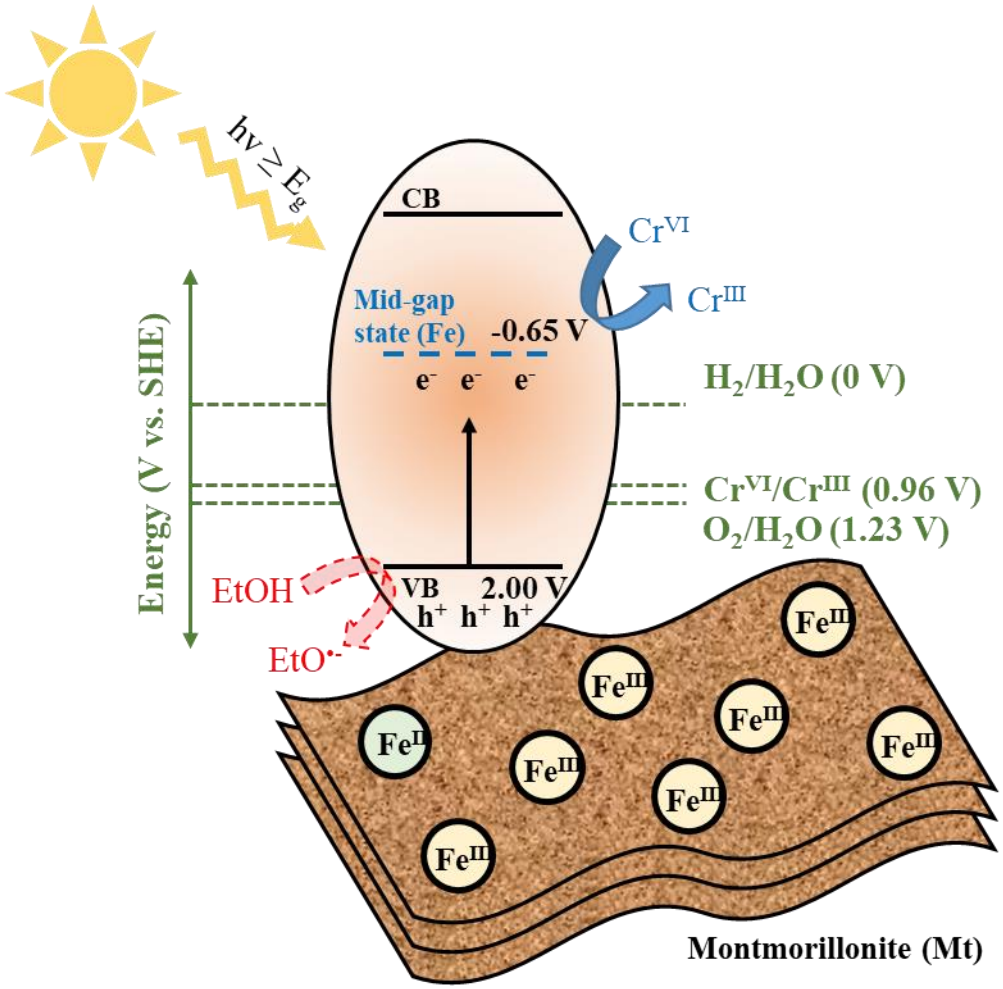

Fig. 3.21. Photocatalytic mechanism for Cr^{VI} reduction by 0.274Fe-Mt.

3.4 Conclusions

Fe^{III}-doped Mt was made by adsorbing Fe^{III} under acidic conditions. The intercalation of Fe(II/III) moved the 001 diffraction peak of the changed samples, including Fe-Mt and Fe-Mt. ICP-OES and AAS were used to validate ion release and adsorption during the preparation process. FTIR, XPS, and XANES were used to confirm these findings. The Fe k-edge XAS spectra of Fe-Mt samples oscillate differently than normal Fe_2O_3, Fe_3O_4 and FeOOH, indicating that Fe is intercalated in the Fe-Mt structure. Furthermore, the acid changes eroded the Mt surface, which was degraded again when Fe^{III} was added since Fe^{III} may replace Al at the octahedral location in Mt's structure. The performance of Fe^{III}-doped Mt samples for

photocatalytic Cr^{VI} redox remediation was clearly improved, owing to improved light adsorption, decreased *Eg*, and increased electron density and transfer. The creation of Fe^{III} Fermi levels between VB and CB in the Mt structure may be responsible for the improved optical characteristics in Fe-Mt. However, the redundant Fe^{III} suppressed photocatalytic Cr^{VI} reduction, most likely by reducing Cr^{VI} contact with the active surface and light shielding. This discovery opens up new possibilities for using modified clay as a photocatalyst in wastewater treatment and beyond.

References

[1] S. L. Prabavathi, P. S. Kumar, K. Saravanakumar, V. Muthuraj, and S. Karuthapandian, "A novel sulphur decorated 1-D MoO_3 nanorods: facile synthesis and high performance for photocatalytic reduction of hexavalent chromium," *Journal of Photochemistry and Photobiology A: Chemistry*, vol. 356, pp. 642–651, 2018.

[2] M. S. Jyothi, V. Nayak, M. Padaki, and R. G. Balakrishna, "Sunlight active PSf/TiO_2 hybrid membrane for elimination of chromium," *Journal of Photochemistry and Photobiology A: Chemistry*, vol. 339, pp. 89–94, 2017.

[3] O. M. Bankole, T. D. Olorunsola, and A. S. Ogunlaja, "Photocatalytic decontamination of toxic hexavalent chromium in water over graphitic carbon nitride supported sulfur nanoparticles," *Journal of Photochemistry and Photobiology A: Chemistry*, vol. 405, p. 112934, 2021.

[4] C. Chuaicham, S. Karthikeyan, R.R. Pawar, Y. Xiong, I. Dabo, B. Ohtani, Y. Kim, J. Tae Song, T. Ishihara, and K. Sasaki, "Energy-resolved distribution of electron traps for O/S-doped carbon nitrides by reversed double-beam photoacoustic spectroscopy and the photocatalytic reduction of Cr (VI)," *Chemical Communications*, vol. 56, no. 26, pp.

3793–3796, 2020.

[5] V. Kapil and J. Keogh, “Chromium toxicity: case studies in environmental medicine,” *Agency for toxic substances and disease registry, US Dept of Health and Human Services*, 1990.

[6] M. Costa, “Potential hazards of hexavalent chromate in our drinking water,” *Toxicol Appl Pharmacol*, vol. 188, no. 1, pp. 1–5, 2003.

[7] F. Edition, “Guidelines for drinking-water quality,” *WHO Chron*, vol. 38, no. 4, pp. 104–108, 2011.

[8] N. A. Oladoja, E. T. Anthony, I. A. Ololade, T. D. Saliu, and G. A. Bello, “Self-propagation combustion method for the synthesis of solar active Nano Ferrite for Cr (VI) reduction in aqua system,” *Journal of Photochemistry and Photobiology A: Chemistry*, vol. 353, pp. 229–239, 2018.

[9] D. W. Blowes, C. J. Ptacek, and J. L. Jambor, “In-situ remediation of Cr (VI)-contaminated groundwater using permeable reactive walls: laboratory studies,” *Environmental Science & Technology*, vol. 31, no. 12, pp. 3348–3357, 1997.

[10] Y. Li and H. Xue, “Determination of Cr (III) and Cr (VI) species in natural waters by catalytic cathodic stripping voltammetry,” *Analytica Chimica Acta*, vol. 448, no. 1–2, pp. 121–134, 2001.

[11] D. C. Schroeder and G. F. Lee, “Potential transformations of chromium in natural waters,” *Water, Air, and Soil Pollution*, vol. 4, no. 3, pp. 355–365, 1975.

[12] T. Papadam, N. P. Xekoukoulotakis, I. Poulios, and D. Mantzavinos, “Photocatalytic transformation of acid orange 20 and Cr (VI) in aqueous TiO_2 suspensions,” *Journal of Photochemistry and Photobiology A: Chemistry*, vol. 186, no. 2–3, pp. 308–315, 2007.

[13] S. G. Schrank, H. J. José, and R. Moreira, “Simultaneous photocatalytic Cr (VI) reduction and dye oxidation in a TiO_2 slurry reactor,” *Journal of photochemistry and*

photobiology A: Chemistry, vol. 147, no. 1, pp. 71–76, 2002.

[14] W. Xie, M. Zhang, D. Liu, W. Lei, L. Sun, and X. Wang, "Photocatalytic TiO2/porous BNNSs composites for simultaneous LR2B and Cr (VI) removal in wool dyeing bath," *Journal of Photochemistry and Photobiology A: Chemistry*, vol. 333, pp. 165–173, 2017.

[15] E. Rodrigues, O. Almeida, H. Brasil, D. Moraes, and M. A. L. dos Reis, "Adsorption of chromium (VI) on hydrotalcite-hydroxyapatite material doped with carbon nanotubes: equilibrium, kinetic and thermodynamic study," *Applied Clay Science*, vol. 172, pp. 57–64, 2019.

[16] J. B. Vincent, "The biochemistry of chromium," *J Nutr*, vol. 130, no. 4, pp. 715–718, 2000.

[17] K. GracePavithra, V. Jaikumar, P. S. Kumar, and P. SundarRajan, "A review on cleaner strategies for chromium industrial wastewater: present research and future perspective," *Journal of Cleaner Production*, vol. 228, pp. 580–593, 2019.

[18] K. Maeda, K. Teramura, D. Lu, T. Takata, N. Saito, Y. Inoue, and K. Domen, "Photocatalyst releasing hydrogen from water," *Nature*, vol. 440, no. 7082, p. 295, 2006.

[19] J. Low, B. Cheng, and J. Yu, "Surface modification and enhanced photocatalytic CO_2 reduction performance of TiO2: a review," *Applied Surface Science*, vol. 392, pp. 658–686, 2017.

[20] D. D. Dionysiou, G. L. Puma, J. Ye, J. Schneider, and D. Bahnemann, *Photocatalysis: applications*. Royal Society of Chemistry, 2016.

[21] B. Szczepanik, "Photocatalytic degradation of organic contaminants over clay-TiO_2 nanocomposites: A review," *Applied Clay Science*, vol. 141, pp. 227–239, 2017.

[22] D. Papoulis, K. Somalakidi, N. Todorova, C. Trapalis, D. Panagiotaras, D. Sygkridou, E. Stathatos, E. Gianni, A. Mavrikos, and S. Komarneni, "Sepiolite/TiO_2 and metal ion modified sepiolite/TiO_2 nanocomposites: synthesis, characterization and photocatalytic

activity in abatement of NOx gases," *Applied Clay Science*, vol. 179, p. 105156, 2019.

[23] P. Mohapatra, S. K. Samantaray, and K. Parida, "Photocatalytic reduction of hexavalent chromium in aqueous solution over sulphate modified titania," *Journal of Photochemistry and Photobiology A: Chemistry*, vol. 170, no. 2, pp. 189–194, 2005.

[24] W. Xie, E. Pakdel, Y. Liang, D. Liu, L. Sun, and X. Wang, "Natural melanin/TiO_2 hybrids for simultaneous removal of dyes and heavy metal ions under visible light," *Journal of Photochemistry and Photobiology A: Chemistry*, vol. 389, p. 112292, 2020.

[25] T. Velempini, E. Prabakaran, and K. Pillay, "Photocatalytic reductive applications of C-doped ZrO_2/PANI composite towards Cr (VI)," *Journal of Photochemistry and Photobiology A: Chemistry*, p. 113737, 2021.

[26] Z. Ai, Y. Cheng, L. Zhang, and J. Qiu, "Efficient removal of Cr (VI) from aqueous solution with Fe@ Fe_2O_3 core− shell nanowires," *Environ Sci Technol*, vol. 42, no. 18, pp. 6955–6960, 2008.

[27] P. Wang and I. M. C. Lo, "Synthesis of mesoporous magnetic γ-Fe_2O_3 and its application to Cr (VI) removal from contaminated water," *Water Res*, vol. 43, no. 15, pp. 3727–3734, 2009.

[28] C. Xu, P. Zhao, M. Cai, Z. Dan, S. Zeng, J. Du, P. Yang, and J. Xiong, "Enhanced photocatalytic reduction of Cr (VI) by Cu_2O/Bi_5O_7I microrods composites under visible light," *Journal of Photochemistry and Photobiology A: Chemistry*, vol. 395, p. 112495, 2020.

[29] Q. Yuan, L. Chen, M. Xiong, J. He, S. Luo, C. Au, and S.Yin., "$Cu_2O/BiVO_4$ heterostructures: synthesis and application in simultaneous photocatalytic oxidation of organic dyes and reduction of Cr (VI) under visible light," *Chemical Engineering Journal*, vol. 255, pp. 394–402, 2014.

[30] Y. Bai, L. Ye, T. Chen, P. Wang, L. Wang, X. Shi, and P. Wong, "Synthesis of hierarchical

bismuth-rich $Bi_4O_5Br_xI_{2-x}$ solid solutions for enhanced photocatalytic activities of CO_2 conversion and Cr (VI) reduction under visible light," *Applied Catalysis B: Environmental*, vol. 203, pp. 633–640, 2017.

[31] J. Liu, M. Dong, S. Zuo, and Y. Yu, "Solvothermal preparation of TiO_2/montmorillonite and photocatalytic activity," *Applied Clay Science*, vol. 43, no. 2, pp. 156–159, 2009.

[32] I. Fatimah, S. Wang, and D. Wulandari, "ZnO/montmorillonite for photocatalytic and photochemical degradation of methylene blue," *Applied Clay Science*, vol. 53, no. 4, pp. 553–560, 2011.

[33] J. Chen, G. Li, Z. He, and T. An, "Adsorption and degradation of model volatile organic compounds by a combined titania–montmorillonite–silica photocatalyst," *J Hazard Mater*, vol. 190, no. 1–3, pp. 416–423, 2011.

[34] A. Wu, D. Wang, C. Wei, X. Zhang, Z. Liu, P. Feng, X. Ou, Y. Qiang, H. Garcia, and J. Niu, "A comparative photocatalytic study of TiO_2 loaded on three natural clays with different morphologies," *Applied Clay Science*, vol. 183, p. 105352, 2019.

[35] H. Yoneyama, S. Haga, and S. Yamanaka, "Photocatalytic activities of microcrystalline titania incorporated in sheet silicates of clay," *The Journal of Physical Chemistry*, vol. 93, no. 12, pp. 4833–4837, 1989.

[36] A. E. Bianchi, M. Fernández, M. Pantanetti, R. Viña, I. Torriani, R. Sánchez, and G. Punte, "ODTMA+ and HDTMA+ organo-montmorillonites characterization: New insight by WAXS, SAXS and surface charge," *Applied Clay Science*, vol. 83–84, pp. 280–285, Oct. 2013, doi: 10.1016/j.clay.2013.08.032.

[37] V. K. Soni, T. Roy, S. Dhara, G. Choudhary, P. R. Sharma, and R. K. Sharma, "On the investigation of acid and surfactant modification of natural clay for photocatalytic water remediation," *Journal of Materials Science*, vol. 53, no. 14, pp. 10095–10110, Jul. 2018, doi: 10.1007/s10853-018-2308-2.

[38] N. Praneeth and S. Paria, “Clay-semiconductor nanocomposites for photocatalytic applications,” *Clay minerals: properties, occurrence and uses*, 2017.

[39] J. Liu and G. Zhang, “Recent advances in synthesis and applications of clay-based photocatalysts: a review,” *Physical Chemistry Chemical Physics*, vol. 16, no. 18, pp. 8178–8192, 2014.

[40] C. Li, Z. Sun, W. Huang, and S. Zheng, “Facile synthesis of g-C_3N_4/montmorillonite composite with enhanced visible light photodegradation of rhodamine B and tetracycline,” *J Taiwan Inst Chem Eng*, vol. 66, pp. 363–371, Sep. 2016, doi: 10.1016/j.jtice.2016.06.014.

[41] Z. Sun, C. Li, X. Du, S. Zheng, and G. Wang, “Facile synthesis of two clay minerals supported graphitic carbon nitride composites as highly efficient visible-light-driven photocatalysts,” *J Colloid Interface Sci*, vol. 511, pp. 268–276, 2018.

[42] R. S. Jack, G. A. Ayoko, M. O. Adebajo, and R. L. Frost, “A review of iron species for visible-light photocatalytic water purification,” *Environmental Science and Pollution Research*, vol. 22, no. 10, pp. 7439–7449, 2015, doi: 10.1007/s11356-015-4346-5.

[43] K. M. Parida and L. Mohapatra, “Carbonate intercalated Zn/Fe layered double hydroxide: A novel photocatalyst for the enhanced photo degradation of azo dyes,” *Chemical Engineering Journal*, vol. 179, pp. 131–139, 2012, doi: 10.1016/j.cej.2011.10.070.

[44] S. J. Kim, Y. Lee, D. K. Lee, J. W. Lee, and J. K. Kang, “Efficient Co-Fe layered double hydroxide photocatalysts for water oxidation under visible light,” *Journal of Materials Chemistry A*, vol. 2, no. 12, pp. 4136–4139, 2014, doi: 10.1039/c3ta14933a.

[45] W. P. Gates, J. S. Anderson, M. D. Raven, and G. J. Churchman, “Mineralogy of a bentonite from Miles, Queensland, Australia and characterisation of its acid activation products,” *Applied Clay Science*, vol. 20, no. 4–5, pp. 189–197, Jan. 2002, doi:

10.1016/S0169-1317(01)00072-2.

[46] R. S. Jack, G. A. Ayoko, M. O. Adebajo, and R. L. Frost, "A review of iron species for visible-light photocatalytic water purification," *Environmental Science and Pollution Research*, vol. 22, no. 10, pp. 7439–7449, May 2015, doi: 10.1007/s11356-015-4346-5.

[47] C. Chuaicham, Y. Xiong, K. Sekar,W. Chen, L. Zhang, B. Ohtani, I. Babo, and K. Sasaki, "A promising Zn-Ti layered double hydroxide/Fe-bearing montmorillonite composite as an efficient photocatalyst for Cr(VI) reduction: Insight into the role of Fe impurity in montmorillonite," *Applied Surface Science*, vol. 546, no. December 2020, p. 148835, 2021, doi: 10.1016/j.apsusc.2020.148835.

[48] R. Asahi, T. Morikawa, T. Ohwaki, K. Aoki, and Y. Taga, "Visible-light photocatalysis in nitrogen-doped titanium oxides," *Science (1979)*, vol. 293, no. 5528, pp. 269–271, 2001, doi: 10.1126/science.1061051.

[49] T. Ohno, Z. Miyamoto, K. Nishijima, H. Kanemitsu, and F. Xueyuan, "Sensitization of photocatalytic activity of S- or N-doped TiO_2 particles by adsorbing Fe3+ cations," *Applied Catalysis A: General*, vol. 302, no. 1, pp. 62–68, 2006, doi: 10.1016/j.apcata.2005.12.010.

[50] S. U. M. Khan, M. Al-Shahry, and W. B. Ingler, "Efficient photochemical water splitting by a chemically modified n-TiO2," *Science (1979)*, vol. 297, no. 5590, pp. 2243–2245, 2002, doi: 10.1126/science.1075035.

[51] T. H. Xie, X. Sun, and J. Lin, "Enhanced photocatalytic degradation of RhB driven by visible light-induced MMCT of Ti(IV)-O-Fe(II) formed in Fe-doped $SrTiO_3$," *Journal of Physical Chemistry C*, vol. 112, no. 26, pp. 9753–9759, 2008, doi: 10.1021/jp711797a.

[52] V.V. Krupskaya, S.V. Zakusin, E.A. Tyupina, O.V. Dorzhieva, A.P. Zhukhlistov, P.E. Belousov, and M.N. Timofeeva, "Experimental study of montmorillonite structure and transformation of its properties under treatment with inorganic acid solutions," *Minerals*,

vol. 7, no. 4, pp. 1–15, 2017, doi: 10.3390/min7040049.

[53] F. Bergaya and G. Lagaly, *Handbook of clay science*. Newnes, 2013.

[54] C. Wang, R. Wang, Y. Peng, J. Chen, and J. Li, "Iron tungsten mixed composite as a robust oxygen evolution electrocatalyst," *Chemical Communications*, vol. 55, no. 73, pp. 10944–10947, 2019.

[55] F. Bergaya and M. Vayer, "CEC of clays: Measurement by adsorption of a copper ethylenediamine complex," *Applied Clay Science*, vol. 12, no. 3, pp. 275–280, Jul. 1997, doi: 10.1016/S0169-1317(97)00012-4.

[56] A. E. Bianchi, M. Fernández, M. Pantanetti, R. Viña, I. Torriani, R. Sánchez, and G. Punte, "ODTMA$^+$ and HDTMA$^+$ organo-montmorillonites characterization: New insight by WAXS, SAXS and surface charge," *Applied Clay Science*, vol. 83–84, pp. 280–285, Oct. 2013, doi: 10.1016/J.CLAY.2013.08.032.

[57] L. Zhang, S. Kancharla, and K. Sasaki, "Synthesis and characterization of imidazole-bearing polymer-modified montmorillonite for adsorption of perchlorate," *Applied Clay Science*, vol. 199, p. 105859, 2020.

[58] J. Liu, H. Liu, Y. Li, and H. Wang, "Probing the coordination properties of glutathione with transition metal ions (Cr^{2+}, Mn^{2+}, Fe^{2+}, Co^{2+}, Ni^{2+}, Cu^{2+}, Zn^{2+}, Cd^{2+}, Hg^{2+}) by density functional theory," *Journal of Biological Physics*, vol. 40, no. 4, pp. 313–323, 2014, doi: 10.1007/s10867-014-9350-3.

[59] A. Uysal, D. Tuncer, E. Kir, and T. S. Koseoglu, "Recovery of nutrients from digested sludge as struvite with a combination process of acid hydrolysis and Donnan dialysis," *Water Science and Technology*, vol. 76, no. 10, pp. 2733–2741, Nov. 2017, doi: 10.2166/wst.2017.450.

[60] A. M. Ziyath, P. Mahbub, A. Goonetilleke, M. O. Adebajo, S. Kokot, and A. Oloyede, "Influence of Physical and Chemical Parameters on the Treatment of Heavy Metals in

Polluted Stormwater Using Zeolite—A Review," *Journal of Water Resource and Protection*, vol. 03, no. 10, pp. 758–767, 2011, doi: 10.4236/jwarp.2011.310086.

[61] Z. Jia and Y. Wang, "Covalently crosslinked graphene oxide membranes by esterification reactions for ions separation," *Journal of Materials Chemistry A*, vol. 3, no. 8, pp. 4405–4412, 2015, doi: 10.1039/c4ta06193d.

[62] W. Cheng, C. Liu, T. Tong, R. Epsztein, M. Sun, R. Verduzco, J. Ma, and M. Elimelech, "Selective removal of divalent cations by polyelectrolyte multilayer nanofiltration membrane: Role of polyelectrolyte charge, ion size, and ionic strength," *Journal of Membrane Science*, vol. 559, no. April, pp. 98–106, 2018, doi: 10.1016/j.memsci.2018.04.052.

[63] V. E. Barlette, L. C. G. Freitas, P. H. Guadagnini, and C. A. Bertran, "Hydration properties of Al3+ ion using empirical ion-water potential by Monte Carlo simulation," *J Braz Chem Soc*, vol. 19, no. 1, pp. 101–110, 2008, doi: 10.1590/S0103-50532008000100015.

[64] S. Paul, K. S. Choi, D. J. Lee, P. Sudhagar, and Y. S. Kang, "Factors affecting the performance of supercapacitors assembled with polypyrrole/multi-walled carbon nanotube composite electrodes," *Electrochimica Acta*, vol. 78, pp. 649–655, 2012, doi: 10.1016/j.electacta.2012.06.088.

[65] B. Tansel, "Significance of thermodynamic and physical characteristics on permeation of ions during membrane separation: Hydrated radius, hydration free energy and viscous effects," *Separation and Purification Technology*, vol. 86, pp. 119–126, 2012, doi: 10.1016/j.seppur.2011.10.033.

[66] E. Ghasemi and M. Sillanpää, "Ultrasound-assisted solid-phase extraction of parabens from environmental and biological samples using magnetic hydroxyapatite nanoparticles as an efficient and regenerable nanosorbent," *Microchimica Acta*, vol. 186,

no. 9, pp. 1–7, 2019.

[67] H. Ouhaddouch, A. Cheikh, M. O. B. Idrissi, M. Draoui, and M. Bouatia, “FT-IR spectroscopy applied for identification of a mineral drug substance in drug products: Application to bentonite,” *Journal of Spectroscopy*, vol. 2019, 2019.

[68] J. T. Kloprogge, L. Hickey, and R. L. Frost, “The effect of increasing layer charge on the infrared absorption spectra of synthetic beidellites,” *J Mater Sci Lett*, vol. 19, no. 13, pp. 1131–1134, 2000.

[69] F.G. Ferré, A Mairov, D. Iadicicco, M. Vanazzi, S. Bassini, M. Utili, M. Tarantino, M. Bragaglia, F.R. Lamastra, F. Nanni, L. Ceseracciu, Y. Serruys, P. Trocellier, L. Beck, K. Sridharan, M.G. Beghi, and F.Di Fonzo, “Corrosion and radiation resistant nanoceramic coatings for lead fast reactors,” *Corrosion Science*, vol. 124, pp. 80–92, 2017.

[70] W. Jichao, “On the cultivation of science college students’ innovative and entrepreneurial ability,” *Journal of China University of Petroleum (Edition of Social Sciences)*, vol. 5, pp. 106–109, 2016.

[71] A. Virnovskaia, S. Jørgensen, J. Hafizovic, Ø. Prytz, E. Kleimenov, M. Hävecker, H. Bluhm, A. Knop-Gericke, R. Schlögl, and U. Olsbye, “In situ XPS investigation of Pt (Sn)/Mg (Al) O catalysts during ethane dehydrogenation experiments,” *Surf Sci*, vol. 601, no. 1, pp. 30–43, 2007.

[72] F. Dong, Z. Zhao, T. Xiong, Z. Ni, W. Zhang, Y. Sun, and W. Ho, “In situ construction of g-C_3N_4/g-C_3N_4 metal-free heterojunction for enhanced visible-light photocatalysis,” *ACS Applied Materials and Interfaces*, vol. 5, no. 21, pp. 11392–11401, 2013, doi: 10.1021/am403653a.

[73] L. Zhu, H. Li, P. Xia, Z. Liu, and D. Xiong, “Hierarchical ZnO decorated with CeO_2 nanoparticles as the direct Z-scheme heterojunction for enhanced photocatalytic activity,” *ACS Appl Mater Interfaces*, vol. 10, no. 46, pp. 39679–39687, 2018.

[74] B. Vellaichamy, P. Periakaruppan, and B. Nagulan, "Reduction of Cr^{6+} from wastewater using a novel in situ-synthesized PANI/MnO2/TiO2 nanocomposite: renewable, selective, stable, and synergistic catalysis," *ACS Sustainable Chemistry & Engineering*, vol. 5, no. 10, pp. 9313–9324, 2017.

[75] X. Zhou, Q. Wang, G. Jiang, P. Liu, and Z. Yuan, "A novel conditioning process for enhancing dewaterability of waste activated sludge by combination of zero-valent iron and persulfate," *Bioresour Technol*, vol. 185, pp. 416–420, 2015.

[76] A. Gnanaprakasam, V. M. Sivakumar, P. L. Sivayogavalli, and M. Thirumarimurugan, "Characterization of TiO_2 and ZnO nanoparticles and their applications in photocatalytic degradation of azodyes," *Ecotoxicol Environ Saf*, vol. 121, pp. 121–125, 2015.

[77] W. Zhao, J. Zhang, X. Zhu, M. Zhang, J. Tang, M. Tan, and Y. Wang, "Enhanced nitrogen photofixation on Fe-doped TiO_2 with highly exposed (1 0 1) facets in the presence of ethanol as scavenger," *Applied Catalysis B: Environmental*, vol. 144, pp. 468–477, 2014.

[78] T. Tan, D. Beydoun, and R. Amal, "Effects of organic hole scavengers on the photocatalytic reduction of selenium anions," *Journal of Photochemistry and Photobiology A: Chemistry*, vol. 159, no. 3, pp. 273–280, 2003.

Chapter 4

Detection of the different roles of Fe^{III} in the interface between TiO_2 and Mt and in the structure of TiO_2 in the Fe^{III}-doped Mt/TiO_2 composites as photocatalysts

4.1 Introduction

Montmorillonite (Mt) can be found in abundance in the pedosphere [1], [2], and in some water systems [3]. It is a typical dioctahedral smectite with a 2:1 structure in which trivalent cations dominate the octahedral sheet [4]. Isomorphous substitution of Mg^{II}, Fe^{III}, Fe^{II}, and other cations for Al^{III} in the octahedrons and Al^{III} for Si^{VI} in the tetrahedrons results in a permanent negative charge on Mt layers, which is balanced by Na^{I}, Ca^{II}, Mg^{II}, K^{I}, and other cations [4]. Furthermore, Mt's swelling property [5], [6] makes it a viable choice for use as an absorbent [7]–[11]. Metal oxides (TiO_2, ZnO, Cu_2O, etc.) [12]–[18], layered double hydroxides (LDHs) based photocatalysts [19], metal-free organic photocatalysts (C_xN_y, BC_3, etc.) [20]–[22], or other photocatalysts [23]–[27] have all been combined with Mt to boost photocatalytic activity. One of the photocatalysts that is usually composed with Mt is titanium dioxide (TiO_2) [12], [13], [16], [17]. It is a typical photocatalyst that has been extensively investigated and used due to its strong photocatalytic activity, excellent physicochemical stability, biological inertness, reusable nature, and environmental friendliness [28]–[32]. Furthermore, Ti is abundantly dispersed throughout the crust, and TiO_2 is the compound's ruling formation [33]. However, as a photocatalyst, TiO_2 has been plagued by electron and hole recombination [34]–[36], a limited specific surface area, inadequate absorption capacity, particle aggregation, and other issues. To overcome these limitations, strategies such as element doping [37]–[41], composites synthesis [12], [13], [16], [17], [42], [43], morphology modification [44], [45], surface sanitization [46],

[47], and metal nanoparticle deposition [48], [49] were used. Compositing TiO_2 with Mt can improve TiO_2 dispersion on Mt layers while also increasing TiO_2 irradiation adsorption and photocatalytic activity. Furthermore, impurities absorbed on Mt make it easier to reach TiO_2 and boost photocatalytic effectiveness. Mt, on the other hand, is widely acknowledged as a supporting material with no photocatalytic activity [12], [13], [16], [17].

Mt might be endowed with photocatalytic activity thanks to iron. Based on molecular simulation, the d orbital of doped Fe formed a mid-gap energy level, which improved the photocatalytic performance of ZnTi-LDH/ Fe-bearing montmorillonite composite [19]. The Fe-octahedron structure in LDH has been postulated to be responsible for photocatalytic activity [50], with the exception of the molecular simulation. It was also hypothesized that the Metal-O-Fe oxo-bridge could reduce electron and hole recombination [51], [52]. Although the presence of Fe in clay was unknown, sepiolite, a phyllosilicate with a discontinuous tetrahedral sheet, was found to be capable of forming a heterojunction with graphene carbon nitride (g-C_3N_4) as a semiconductor [53]. However, the speciation of Fe in these investigations was unknown, and no direct characterization of Fe species involvement was disclosed. Because iron is one of the most abundant elements on the planet, it should be easy to get access to Mt in nature. TiO_2 can occur naturally, and Fe-doping in TiO_2 can red-shift irradiation adsorption to lower frequency with lower energy, narrowing the *Eg* of TiO_2 [54], [55]. It's fascinating to try to figure out how these three elements are connected.

To further understand the function of clay and iron in such composites, two types of Mt-TiO_2 composites with Fe^{III} doping were produced and subjected to phenol degradation. Contamination and environmental deterioration on a global scale are themes of significant concern today. Organic residues in wastewater have long been recognized as having the potential to harm living ecosystems as well as aquatic life and human health [56]–[58]. The aromatic nature of phenol makes it harder to breakdown [59]. Organic pollutants with comparable structures or that contain the benzene ring may be implicated in a photocatalytic reaction. Furthermore, phenol was suited for the produced composites because phenol adsorption on Mt could be maintained at a low concentration and for a short period of time.

The process for generating Fe-Mt/TiO_2, where Fe^{III} was first doped in TiO_2-$Ti(OH)_4$ sol-gel and then TiO_2 was grown on Mt layers, and Mt/Fe-TiO_2, where Fe^{III} was first doped in TiO_2-$Ti(OH)_4$ sol-gel and then TiO_2 was grown on Mt, has been published in this study. The activity of these two ferric-doped Mt/TiO_2 composites was tested, and the findings were examined to determine the mechanism of the photocatalytic reaction.

4.2 Materials and methods

4.2.1 Materials

Na-Mt (Kunipia-F) has a cation exchange capacity (CEC) of 1.114 mmol/g, according to

Kunimine Industries Co. Ltd. (Tokyo, Japan). Kumipia-F has the chemical formula $(Na_{0.97}Ca_{0.08})^{+1.13}$ $(Si_{7.68}Al_{0.32})$ $(Al_{2.94}Fe^{III}_{0.25}Fe^{II}_{0.03}Mg_{0.78})$ O_{20} $(OH)_4^{-1.13}\cdot nH_2O$, according to elemental analysis (method of ME-ICP61, ALS Global Ltd., North Vancouver, Canada). Iron(III) nitrate ninehydrate ($Fe(NO_3)_3\cdot 9H_2O$, 99.0%), iron(III) chloride chloride ($FeCl_3$, 95.0%), sodium hydroxide (NaOH, 97.0+%), hydrochloric acid (HCl, 1.17), and nitric acid (HNO_3, 1.38) were given for this work by Wako Pure Chemical Industries, Ltd. (Osaka, Japan). Titanium (IV) chloride was supplied by Kishida Chemical Co. Ltd. (Osaka, Japan) ($TiCl_4$, 99.0%). Millipore water with a pH of 6.31 was given by Synergy UV (Merck, Darmstadt, Germany).

4.2.2 Synthesis of Fe-Mt and Fe^{III} doped Mt/TiO_2 composites

To make Fe^{III}-doped Mt (Fe-Mt), make 200 mL of $Fe(NO_3)_3\cdot 9H_2O$ solution with 1 time CEC of Mt and adjust pH to 2 (±0.1) with 0.1 mol/L HNO_3 or NaOH. Mt was then disseminated in Fe^{III} ($Fe(NO_3)_3$) solution (S/L=10 g/L) and agitated for 1 hour at room temperature. Centrifugation was used to separate the solid residue, which was then washed three times to remove excess Fe^{III}, collected, lyophilized, powdered, and sieved (149 μm). The same technique was used to make acidified Mt (Fe-Mt), but without the inclusion of Fe^{III}. The Fe^{III} concentration was 0.274 mmol/g in he obtained Fe-Mt.

To make the $Ti(OH)_4/TiO_2$ sol-gel, first dissolve $TiCl_4$ and HCl in DI water. 0.83 M $TiCl_4$ and

1.0 M HCl were in the final solution. After that, the solution was swirled for 1 hour and then aged for 6 hours. The same process was used to make Fe-$Ti(OH)_4/TiO_2$ sol-gel. Before stirring and aging, only Fe^{III} ($FeCl_3$) was stoichiometrically comparable to 0.19 mmol/g Mt/TiO_2. After hydrolysis, a translucent $Ti(OH)_4/TiO_2$ sol-gel was created. Fe- $Ti(OH)_4/TiO_2$ sol-gel after hydrolysis (yellowish translucent).

Because the pH of $Ti(OH)_4/TiO_2$ sol was initially approximately 0, the acidity was adjusted to pH=2 before heterocoagulation using NaOH solution. Following adequate stirring for 30 minutes to obtain a homogenous dispersion, $Ti(OH)_4/TiO_2$ sol-gel was added to 1% Fe-Mt dispersion and Fe-$Ti(OH)_4/TiO_2$ sol-gel was added to 1% H-Mt dispersion. The theoretical TiO_2 content was 30 wt.%. Heterocoagulated Fe-Mt/$Ti(OH)_4/TiO_2$ and Mt/Fe-$Ti(OH)_4/TiO_2$ were extracted centrifuged at 8,300 rpm for 30 minutes after 20 hours of sedimentation at 70, 80, and 90 °C. The solid phase was lyophilized, crushed, and sieved (149 m) after being washed with ultra-pure water. The remaining Fe^{III} in the supernatant was detected using inductively coupled plasma-optical emission spectroscopy (ICP-OES, Perkin Elmer 8500, Waltham, MA, USA).

4.2.3 Solid characterization

The composites were studied using an X-ray fluorescence (XRF) microscope on a Shimadzu-EDX800 (Kyoto, Japan). Powder X-ray diffraction (XRD) patterns of materials were recorded

using an Ultima IV X-ray diffractometer (Rigaku, Akishima, Japan) with Cu Kα radiation generated at 40 kV and 40 mA, a divergence slit of 1.0 mm, an anti-scatter slit of 10 mm, and a receiving slit of 0.15 mm over a 2 of 2.0-10° at a step size of 0. 02°. FlexSEM 1000II and AZteclive light FX scanning electron microscopes (SEM-EDX) were used (Hitachi, Tokyo, Japan). We used the Aztec application from AZteclive light FX to process the EDX results, which included baseline correction. Transmission electron microscopy (TEM) was performed on a JEOL JEM-2100HCKM (Akishima, Japan). Diffuse reflectance spectroscopy (DRS) was performed in the range of 200-800 nm using a UV-2450 spectrophotometer (Shimadzu, Tokyo, Japan) with a diffuse-reflectance attachment, utilizing $BaSO_4$ as a reference. Solid state photoluminescence spectroscopy (PL) was performed using a JASCO F-6600 spectrofluorometer (Jasco, Tokyo, Japan). On an ESCA 5800 system (Ulvac-PHI, Kanagawa, Japan), X-ray photoelectron spectroscopy (XPS) was done with a monochromatic Al Kα X-ray source at 200 W. Narrow scans of N 1s and C 1s orbitals with passing energies of 23.5 and 58.7 eV were achieved using a survey scan with a passing energy of 187.85 eV from 0 to 1000 eV. Peak separation was conducted using Casa XPS software after eliminating a Shirley baseline (Version 2.3.16 PR 1.6). Peak binding energies were calibrated using EB [C 1s] = 284.6 eV. Electrochemical features of composites were investigated using 1280c AMETEK (Berkshire, United Kingdom) advanced measuring equipment, including photocurrent responsiveness and electrochemical impedance spectroscopy (EIS). Then, 200 mg of Fe-Mt/TiO_2 and Mt/Fe-TiO_2

composites were placed in a PAS cell with an electret condenser microphone on the top side and a quartz window on the bottom side, and the cell was run for at least 30 minutes under N_2 flow saturated with methanol vapor. A light beam from a Xe lamp with a grating monochromator modulated at 80 Hz was irradiated from 650 to 350 nm via the cell window to detect the PAS signal using a digital lock-in amplifier. The energy-resolved distribution of electron traps was calculated using the amount of light absorbance change for the collected electrons (ERDT).

4.2.4 Photocatalytic activity test

For the photocatalytic breakdown of phenol, a 300 W xenon lamp was employed as the light source. Twenty mg of photocatalyst were suspended in 100 mL of 10 mg/L phenol aqueous solution in a photoreactor with a cooling water jacket outside. With starters, for churning at 500 rpm in the dark, an adsorption-desorption equilibrium was obtained in less than 5 minutes. 1 mL of solution was extracted and filtered from the reaction system at regular intervals throughout irradiation. High performance liquid chromatography (HPLC) (Jasco: CO-2065 Plus, Jasco, Kyoto, Japan) measurement at a wavelength of 270 nm and mass balance calculations were used to quantify phenol and its intermediate intermediates. Before the photocatalytic materials were injected, 1 mol of ethanol, isopropanol, and para-benzoquinone were added to the scavenger test, as stated previously.

4.3 Results and discussion

4.3.1 Characterizations

ICP-OES was used to determine the stoichiometry of the Fe^{III} doping quantity. Because all of the injected Fe^{III} was confined in the solid phase, the concentration of Fe^{III} in the supernatant was lower than the detected value of ICP-OES in both types of composites, showing that the amount of Fe^{III} doping in the composites was equal.

The TiO_2 concentration in the Mt/Fe-TiO_2 is always larger than in the Fe-Mt/TiO_2 at all three synthesizing temperatures, with the greatest being at 70°C, according to the Ti/Al ratio determined by XRF analysis (**Table 4.1**). The TiO_2 content of the Mt/Fe-TiO_2 composites has a slightly negative temperature relativity, which is the polar opposite of the clay/TiO_2 composites [60] and the Fe-Mt/TiO_2 composites in this investigation. The content of the TiO_2 amount is hampered by the Fe^{III} location.

Table. 4.1. Elemental composition of Fe-Mt/TiO_2 and Mt/Fe-TiO_2 with different synthesis temperatures (70, 80, and 90 ℃) in wt%.

Temp. (℃)	Sample	Ti (%)	Fe (%)	Na (%)	Ca (%)	Mg (%)	Al (%)	Si (%)	TiO_2 wt. % (as Ti)
70	Fe-Mt/TiO_2	44.56	6.77	N.D.	N.D.	2.00	12.81	33.85	25.69
	Mt/Fe-TiO_2	49.24	5.19	N.D.	0.05	1.91	11.82	31.80	27.30
80	Fe-Mt/TiO_2	44.90	7.01	N.D.	N.D.	1.97	12.72	33.40	25.88
	Mt/Fe-TiO_2	46.15	6.45	N.D.	0.06	2.03	12.19	33.12	26.30
90	Fe-Mt/TiO_2	45.12	6.85	N.D.	N.D.	2.08	12.91	33.04	25.94
	Mt/Fe-TiO_2	47.20	6.80	N.D.	0.05	1.85	12.06	32.03	26.81

The XRD patterns in 4-60º in 2 of TiO_2, Fe-Mt/TiO_2, and Mt/Fe-TiO_2 heterocoagulated at 70 °C are shown in **Fig. 4.1a**, and in 20-35º in Fe-Mt/TiO_2 and Mt/Fe-TiO_2 synthesized at 70, 80, and 90 °C are shown in **Fig. 4.1b**. The representative 001, 002, 100, 003, and 101 reflection peaks for the Mt phase in Fe-Mt/TiO_2 and Mt/Fe-TiO_2 were found at 6.0-6.5, 13.8, 17.2, 19.8, and 35.2º (PDF 13-0259), respectively. The interlayer space was 0.42 nm for Fe-Mt/TiO_2 and 0.44 nm for Mt/Fe-TiO_2, which could be due to a smaller nanoparticle size of TiO_2 growth on the surface of each Mt layer in Fe-Mt/TiO_2 than in Mt/Fe-TiO_2, which could be related to a smaller nanoparticle size of TiO_2 growth on the surface of each Mt layer in Fe-M The pure TiO_2 phase showed 101, 004, and 200 anatase peaks at 25.4, 37.9, and 47.7° (PDF 99-0008), a weak broad 121 brookite peak at 30.4° (PDF 99-0020), and no rutile peak. However, in the XRD patterns of Fe-Mt/TiO_2 and Mt/Fe-TiO_2, the 110 peak of rutile (PDF 99-0090) was one of two prominent peaks; the other was the 101 peak of anatase. The 110 peak of rutile always shows similar relative intensity with anatase, especially for Fe-Mt/TiO_2.

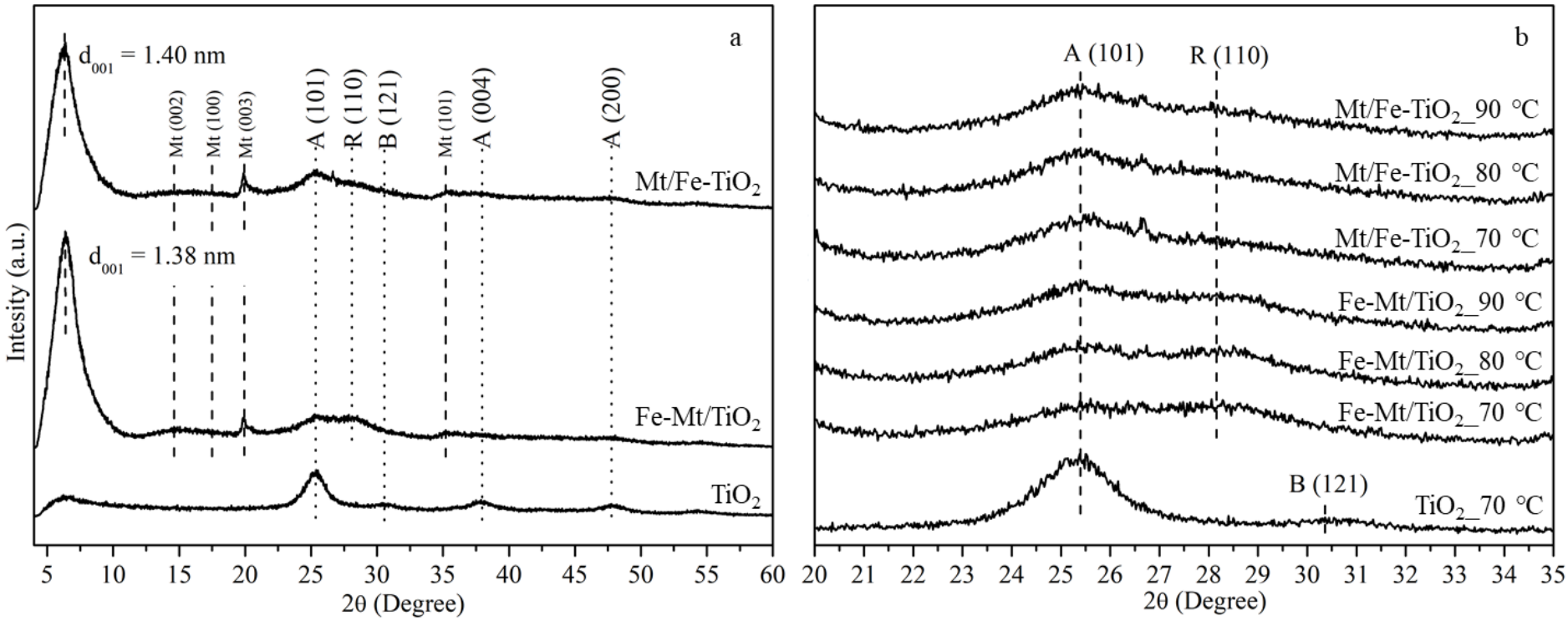

Fig. 4.1. XRD patterns (a) in 4-60º in 2θ of TiO_2, Fe-Mt/TiO_2 and Mt/Fe-TiO_2 synthesized at 70 °C, and (b) in 20-35º in 2θ of TiO_2 synthesized at 70 °C, Fe-Mt/TiO_2 and Mt/Fe-TiO_2 synthesized at 70, 80, and 90 °C. Montmorillonite: PDF 13-0259, anatase: PDF 99-0008, rutile: PDF 99-0090, and brookite: PDF 99-0020.

Peak fitting was used at 20.0-35.0º, as shown in **Fig. 4.2** and described in **Table 4.2**, to further understand how temperature and Fe^{III} location influence the TiO_2 phases. The peak at 25.4° was allocated as the anatase 101 peak, and the peak at 28.2-28.4° was assigned as the rutile 110 peak. Because the lower temperature is linked to a poorer anatase yield and crystallinity, only Fe-Mt/TiO_2 synthesized at 70 °C revealed an amorphous peak [60], [61]. In all composites, the FWHM of anatase and rutile were identical (**Table 4.2**). The TiO_2 peaks were broad, indicating that crystalline and amorphous anatase, crystalline and amorphous rutile, and isolated TiO_2 amorphous coexisted. In Fe-Mt/TiO_2, the anatase to rutile ratio (A/R) was lower than in Mt/Fe-TiO_2. Although higher temperatures were associated with more anatase in Fe-Mt/TiO_2 and less in Mt/Fe-TiO_2, this trend is substantially in line with the overall TiO_2 amount reported by XRF in **Table 4.1**. Because the ICP results already revealed that only the position of Fe^{III} rather than the amount of Fe^{III} can govern the production of TiO_2 on Mt aluminosilicate layers, the position of Fe^{III} had a greater impact on the A/R than the synthesizing temperature. Fe^{III} was intercalated in the interlayer or adsorbed onto the surface of Mt in Fe-Mt/TiO_2. The positively charged Fe^{III} repelled Ti^{VI}-containing groups linked to Mt layers by interacting with their negative charge. This could be one of the reasons that the concentration and size of TiO_2 nanoparticles on Fe-Mt/TiO_2 were lower than on Mt/Fe-TiO_2, and that the repelling of Fe^{III} to Ti^{VI}-containing groups had a greater impact on anatase formation. The position of Fe^{III} in the composites has a greater impact on the content, particle size, and phase ratio of A/R than temperature.

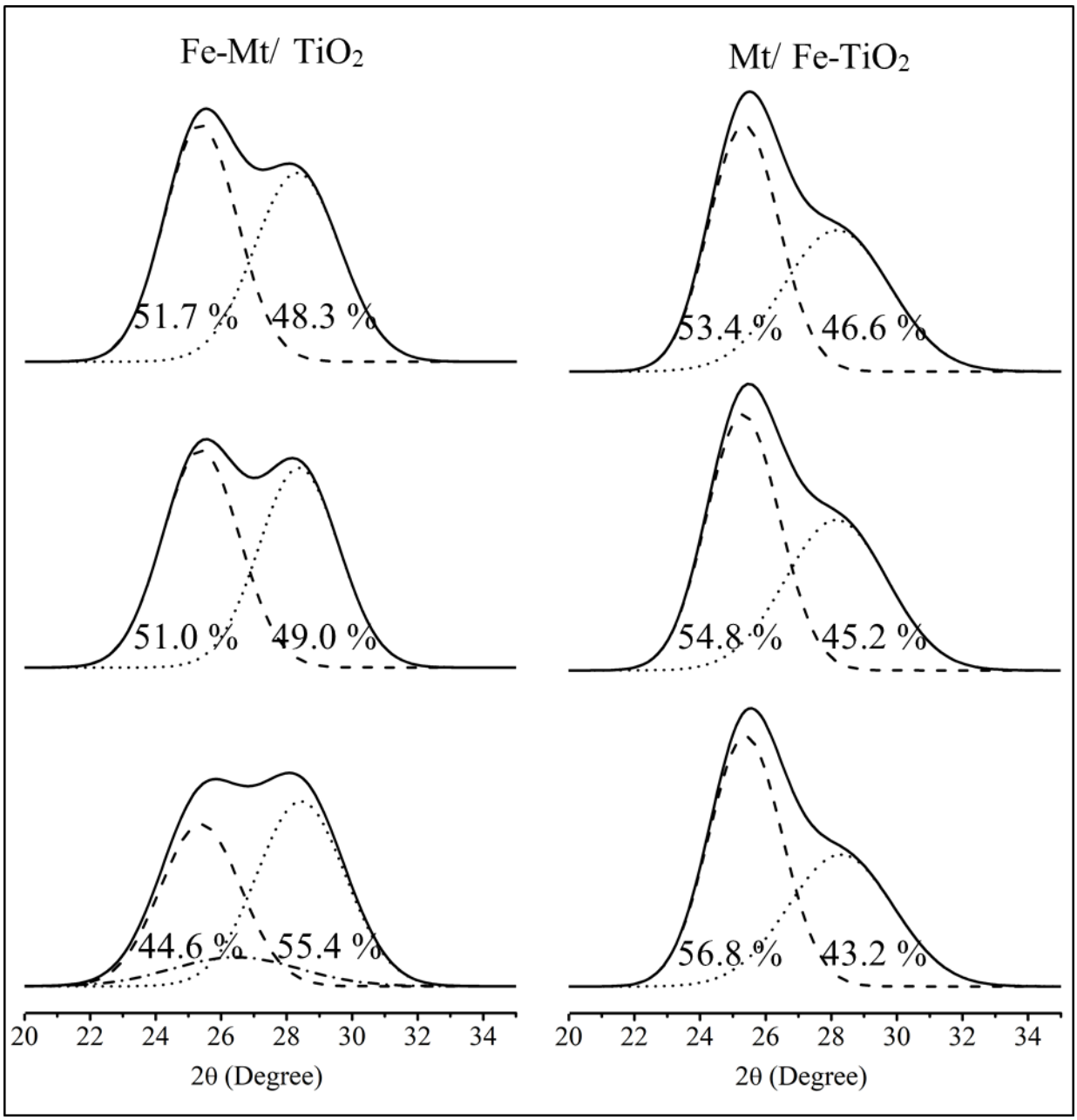

Fig. 4.2. Peak separation of the XRD peaks in 20.0-35.0º on 2θ for Fe-Mt/TiO_2, and Mt/Fe-TiO_2 with different heterocoagulating temperatures (70, 80, and 90 ℃). The peak in the dashed line is anatase, the peak in the dotted line is rutile, and the peak in dash and dot is amorphous TiO_2.

Table 4.2. Parameters after peak fitting and peak separation Fe-Mt/TiO_2 and Mt/Fe-TiO_2.

T (°C)	Parameters	Fe-Mt/TiO_2			Mt/Fe-TiO_2		
		Anatase	Rutile	Amorphous	Anatase	Rutile	Amorphous
90	Peak position (º)	25.4	28.3	N.D.	25.3	28.2	N.D.
	Intensity	177.1	141.5	N.D.	184.3	105.8	N.D.
	FWHM	2.6	3.1	N.D.	2.5	3.8	N.D.
	Peak area (%)	51.7	48.3	N.D.	53.4	46.6	N.D.
80	Peak position (º)	25.4	28.4	N.D.	25.3	28.2	N.D.
	Intensity	162.3	149.3	N.D.	191.4	112.5	N.D.
	FWHM	2.6	3.7	N.D.	2.6	3.7	N.D.
	Peak area (%)	51.0	49.0	N.D.	54.8	45.2	N.D.
70	Peak position (º)	25.4	28.4	26.4	25.4	28.3	N.D.
	Intensity	120.9	138.1	21.7	187.2	98.6	N.D.
	FWHM	2.9	3.2	4.5	2.6	3.8	N.D.
	Peak area (%)	39.6	49.3	11.1	56.8	43.2	N.D.

The morphology of the TiO_2, Fe-Mt/TiO_2, and Mt/FeTiO_2 was shown in μm scale on the SEM in **Fig. 4.3**. The particle size of pure TiO_2 was even larger than the layer stacked particles of Mt in the composites. The TEM images of Fe-Mt/TiO_2 in **Fig. 4.4a** and **b** also showed a random distribution of TiO_2 nanoparticles on the Mt layers, with TiO_2 particle sizes estimated to be 2-10 nm. In **Fig. 4.4c** and **d**, the indexed d spacing value from the crystal TiO_2 particles was acquired by showing the inverted FFT picture of TEM (**Fig. 4.5**). Because all the d values of TiO_2 lattice were slightly lower than the bulk values for anatase and rutile in JCPDS-ICDD, the observation direction should be inclined to the perpendicular of the Mt layer. The crossing of the anatase and rutile phases could indicate the formation of a heterojunction within TiO_2.

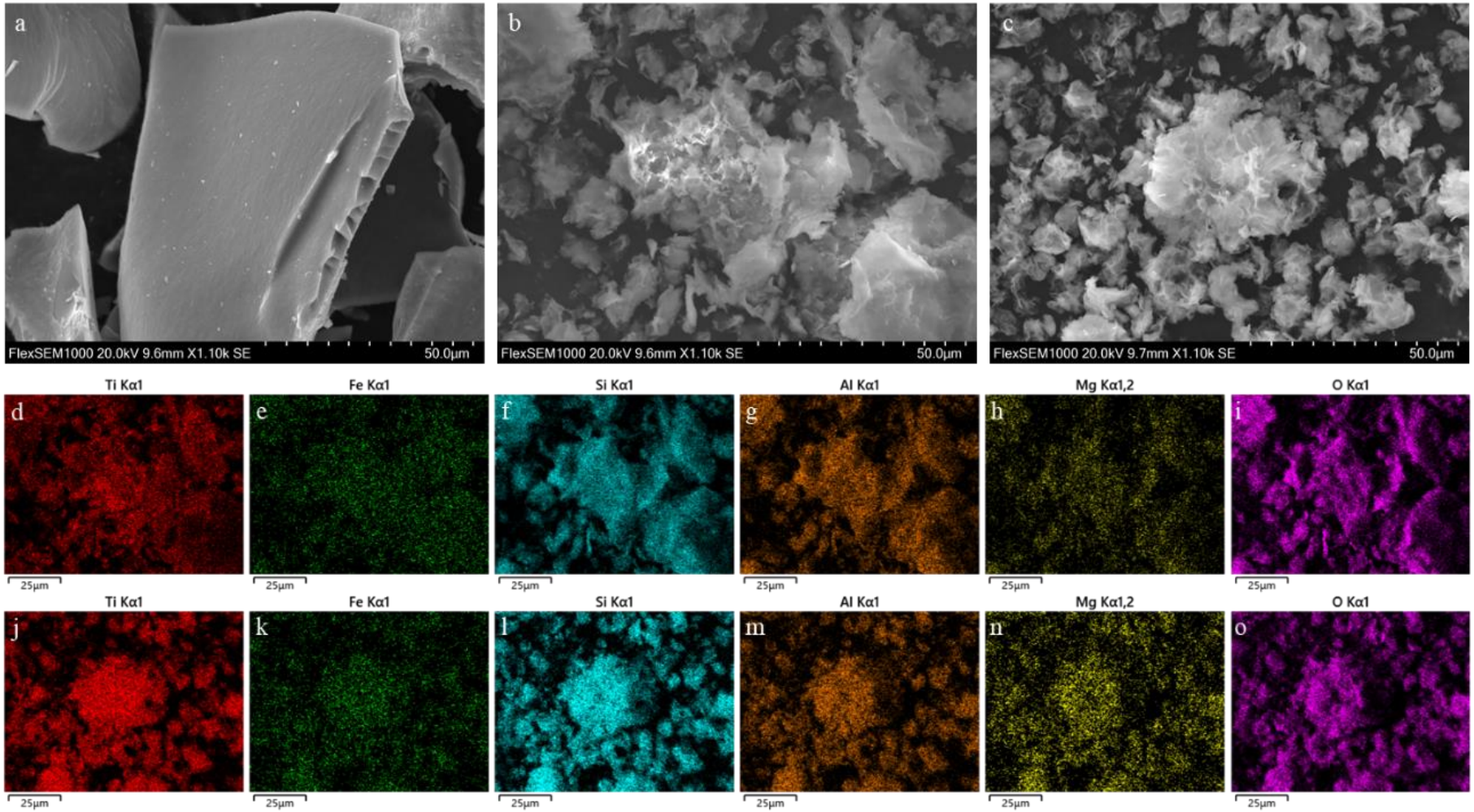

Fig. 4.3. SEM images of: (a) TiO_2, (b) Fe/Mt/TiO_2, and (c) Mt/ Fe-TiO_2, and SEM-EDX Kα maps of: Ti, Fe, Si, Al, Mg, and O for Fe/Mt/TiO_2 (d-i) and Mt/ Fe-TiO_2 (j-o). All the images are in the same scale.

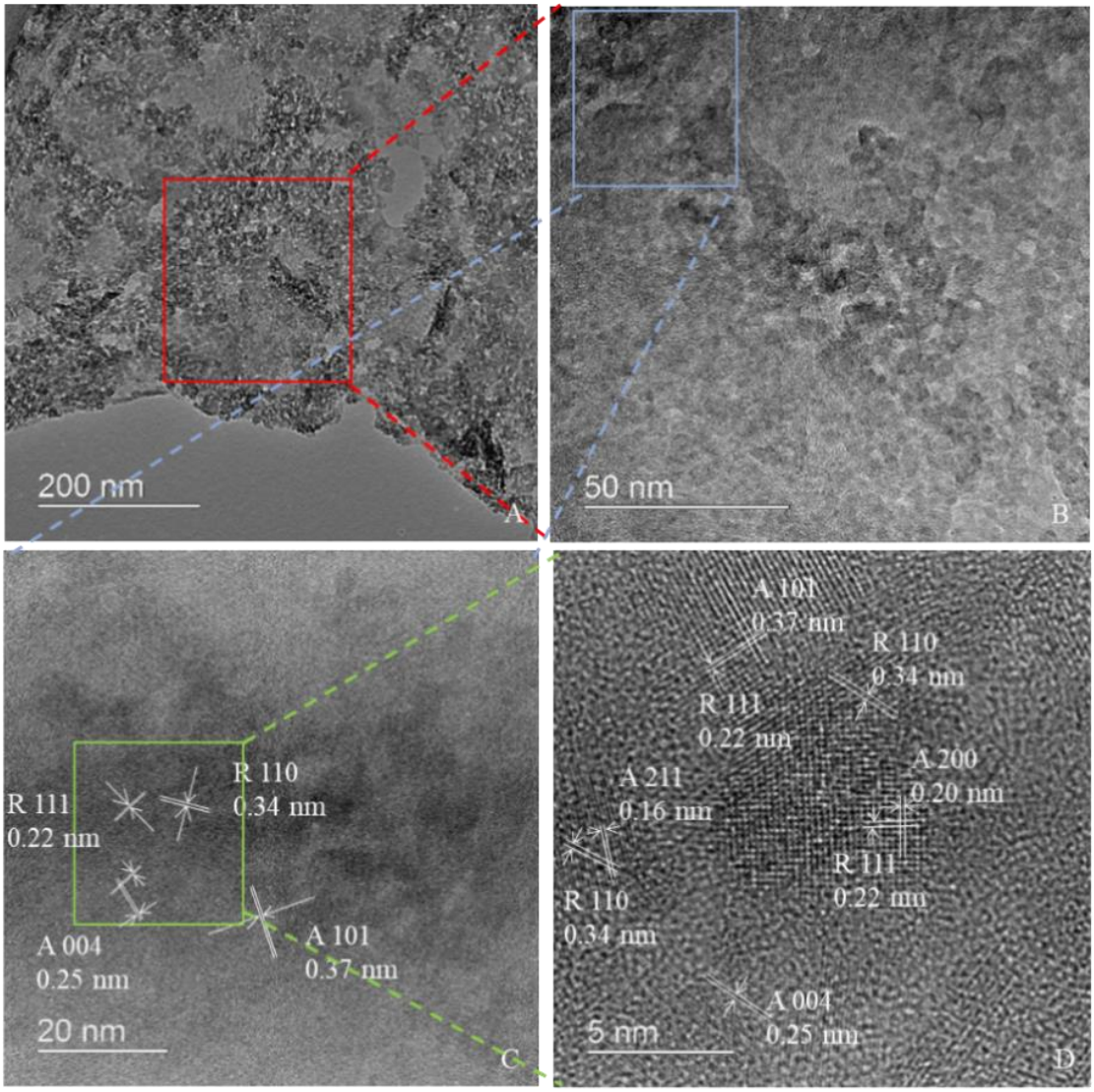

Fig. 4.4. TEM images of Fe-Mt/TiO_2 heterocoagulated at 70 ℃.

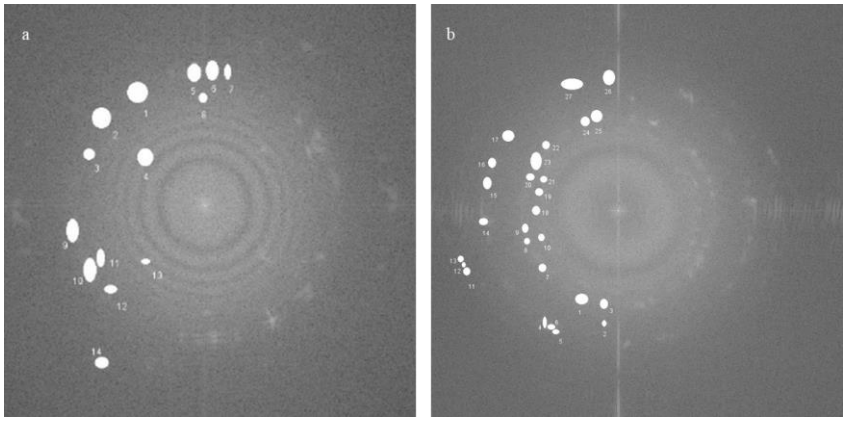

Fig. 4.5. Inverted FFT of TEM (a) Fig. 6c and (b) Fig. 6d of Fe-Mt/TiO_2 at 70℃.

4.3.2 Photocatalytic properties

Using the UV-DRS spectra (**Fig. 4.6**), it was discovered that both Fe-Mt/TiO_2 and Mt/Fe-TiO_2 displayed a red-shifting enlargement of the adsorption band when compared to pure TiO_2. This indicated that the composites had a greater optical capacity than pure TiO_2. It is required to boost the photocatalytic activity of the composites in order to achieve their full potential. Tauc can estimate the optical band gap energy (*Eg*) of TiO_2, Fe-Mt/TiO_2 and Mt/Fe-TiO_2 by using the Kubelka–Munk function, as illustrated in eq 4.1 [62], [63]:

$$\alpha hv = k(hv - Eg)^{n/2} \quad (4.1)$$

where *Eg* is the band gap-energy, *h* is the Planck constant, ν is the light frequency, *k* is the proportionality constant, and α is the absorption coefficient. In the event of a direct semiconductor transition, the value of n is 1; in the case of an indirect semiconductor transition, the number is 4. Both composites have a smaller *Eg* than TiO_2, with Fe-Mt/TiO_2 having a somewhat narrower *Eg* of 3.18 eV compared to Mt/Fe-TiO_2 of 3.20 eV. Compositing with Mt improves light absorption capacity of TiO_2, and the Fe^{III} in Mt has a marginally better optical property than Fe^{III} doped TiO_2.

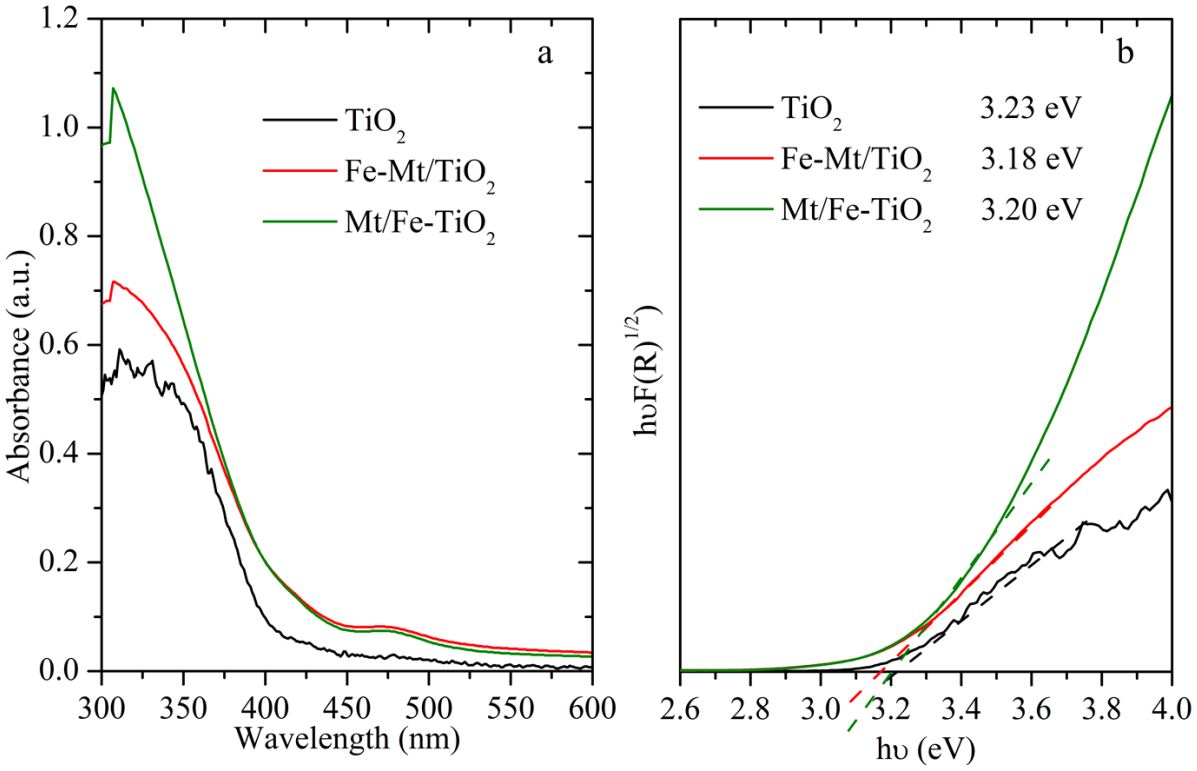

Fig. 4.6. (a) UV-DRS spectra and (b) Tauc plots of TiO_2, Fe-Mt/TiO_2, and Mt/Fe-TiO_2 heterocoagulated at 70 ℃.

PL was used to measure the recombination kinetics of electron-hole pairs (**Fig. 4.7**). The two composites showed lower luminous intensities than TiO_2, implying that Mt, as the supporting material for the core TiO_2 semiconductor, had a major impact on TiO_2 recombination depression. Furthermore, in Fe-Mt/TiO_2, electron-hole pair recombination was better regulated than in Mt/Fe-TiO_2. As a result, heterojunction between Fe^{III} activated Mt and TiO_2 was expected in Fe-Mt/TiO_2, because Fe^{III} can augment or endow clay photocatalytic activity. On the contrary, because Mt was not changed by Fe^{III}, no heterojunction between Mt and TiO_2 should arise in Mt/Fe-TiO_2. To narrow the *Eg* of TiO_2, all of the Fe^{III} in Mt/Fe-TiO_2 was doped

with TiO_2, and the Mt merely serves as a supporting material for the TiO_2 particles dispersing on. ERDT later in this publication proved the presence of heterojunction between the Mt and TiO_2 phases.

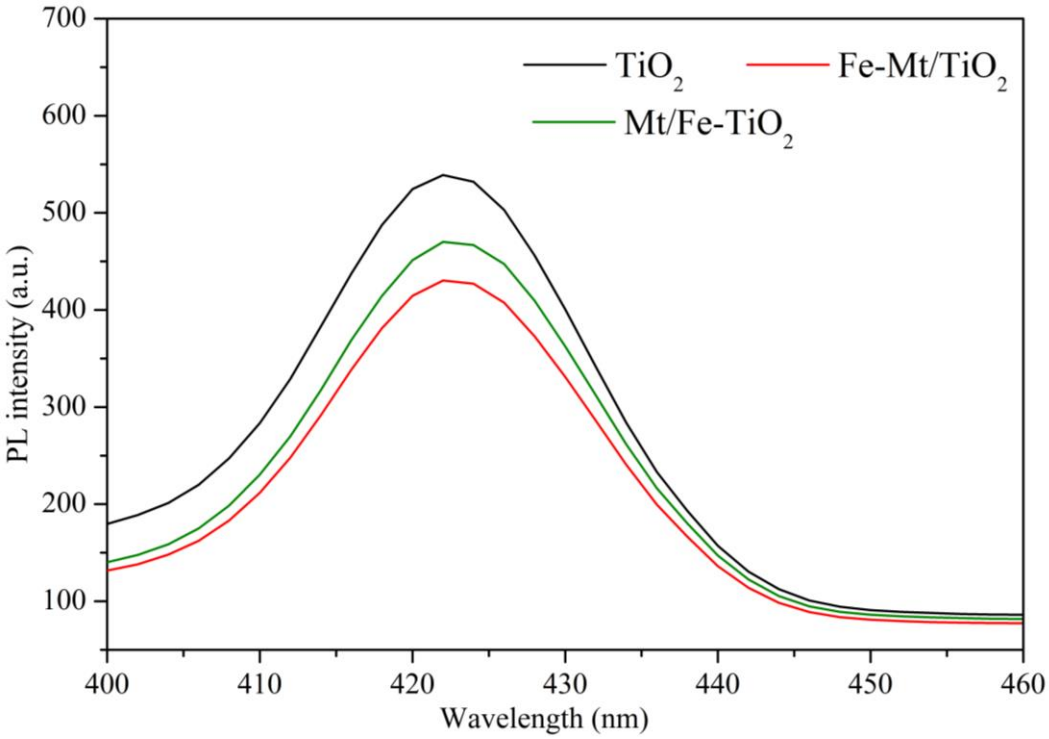

Fig. 4.7. Photoluminescence of TiO_2, Fe-Mt/TiO_2, and Mt/Fe-TiO_2 synthesized at 70 °C.

The chemical composition and electronic level of Fe-Mt/TiO_2 (**Fig. 4.8**) and Mt/Fe-TiO_2 (**Fig. 4.9**) were determined using XPS. The prominent peaks in the survey scan for both composites were identified as the O 1s, C 1s, Si 2p, Al 2p, and Ti 2p orbitals (**Fig. 4.8a** and **Fig 4.9a**). Peak assignments for Ti 2p, Fe 2p, Si 2p, C 1s, and O 1s orbitals were highlighted in the deconvoluted spectra for Fe-Mt/TiO_2 and Mt/Fe-TiO_2 (**Fig. 4.8b-f** and **Fig. 4.9b-f**) [64]–[69]. Fe^{III} $2p_{1/2}$ and

$2p_{3/2}$ were attributed to peaks in the Fe 2p area at 725.5 eV and 713.4 eV for Fe-Mt/TiO_2 (**Fig. 4.8c**) and 723.9 eV and 713.2 eV for Mt/Fe-TiO_2 (**Fig. 4.9c**) [65]. The VB of Fe-Mt/TiO_2 and Mt/Fe-TiO_2 were determined by intersecting the tangent line of the VB XPS with the x-axis [70], [71] in **Fig. 4.8f** and **Fig. 4.9f**. As a result, the CB for Fe-Mt/TiO_2 and Mt/Fe-TiO_2 may be determined to be -1.74 and -1.71 eV, respectively.

Transient photocurrent response measurements and EIS were used to look into the charge generation and migration properties. As shown in **Fig. 4.10a**, the photocurrent density dropped in the order Fe-Mt/TiO_2 > Mt/Fe-TiO_2 > TiO_2, suggesting that composites produce more charge than pure TiO_2 and that Fe-Mt/TiO_2 has a higher charge generation capability than Mt/Fe-TiO_2. The smaller radius of the EIS Nyquist diagram for composites than TiO_2, and the slightly smaller radius of Fe-Mt/TiO_2 than Mt/Fe-TiO_2 in **Fig. 4.10b**, suggests that charge transferring resistance is weaker on composites than TiO_2, and on Fe-Mt/TiO_2 than Mt/Fe-TiO_2.

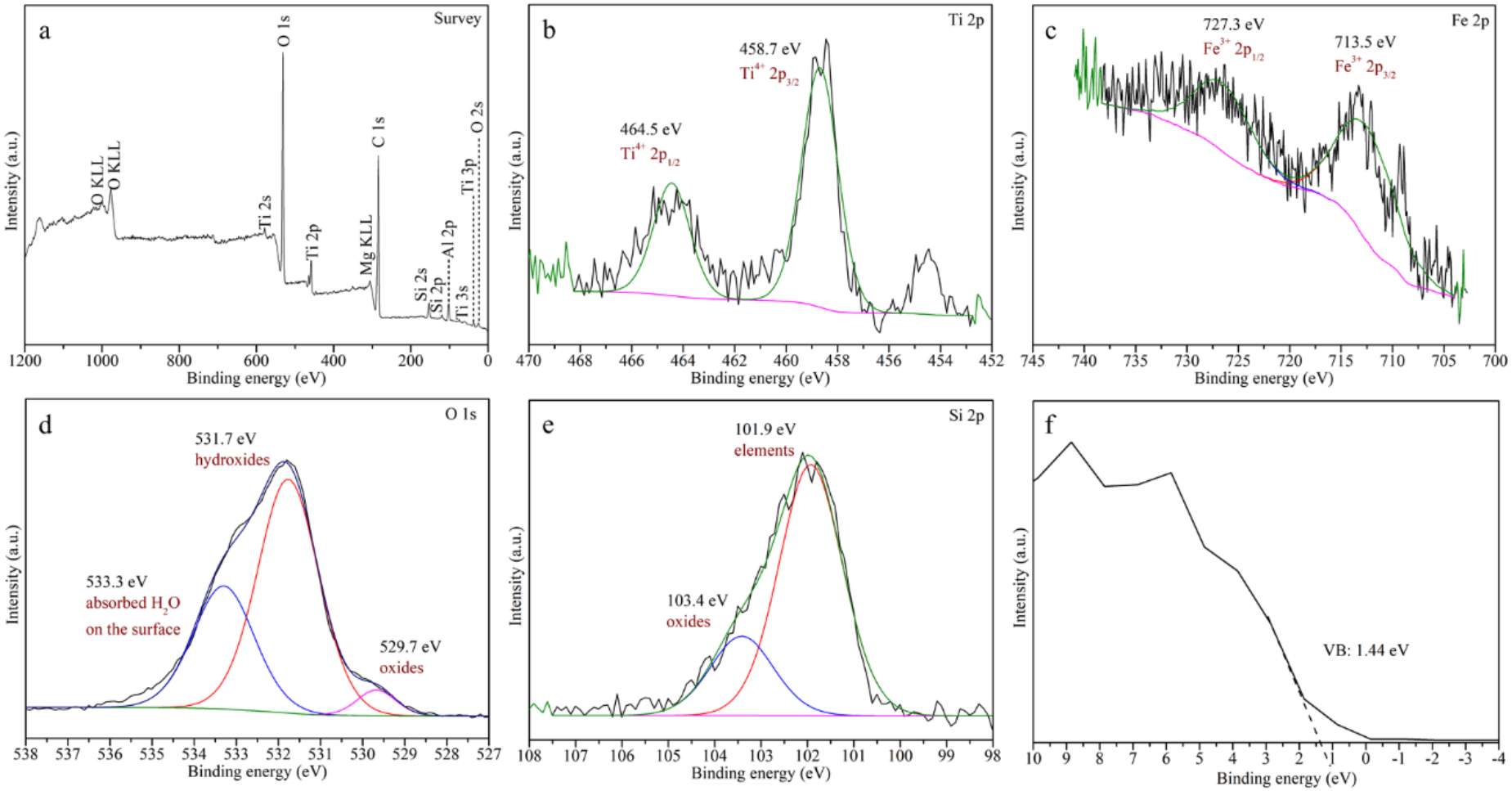

Fig. 4.8. XPS (a) survey, narrow scans of (b) Ti 2p, (c) Fe 2p, (d) O 1s, and (e) Si 2p orbitals and (f) VB XPS for Fe-Mt/TiO_2.

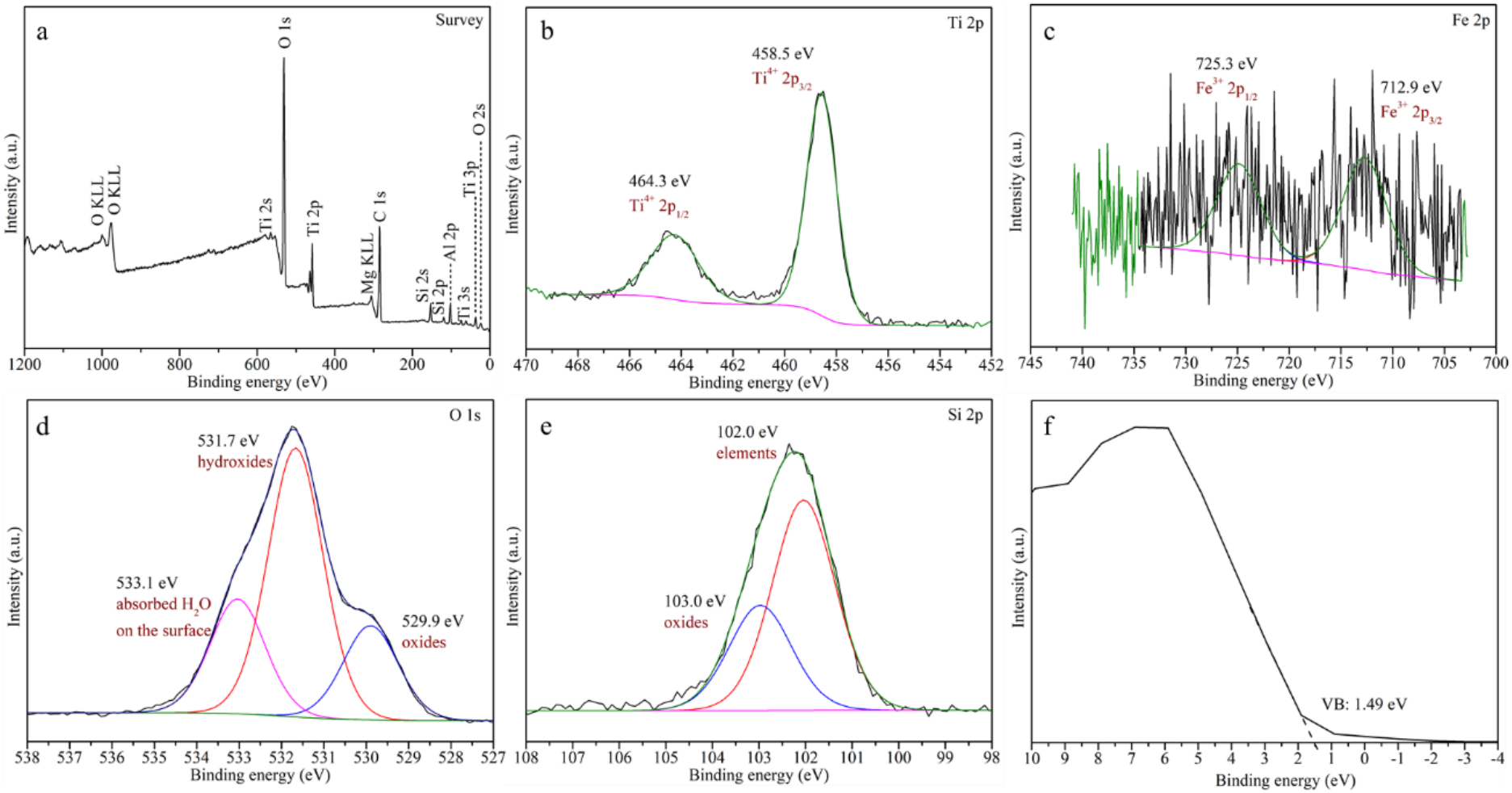

Fig. 4.9. XPS (a) survey, narrow scans of (b) Ti 2p, (c) Fe 2p, (d) O 1s, and (e) Si 2p orbitals and (f) VB XPS for Mt/Fe-TiO_2.

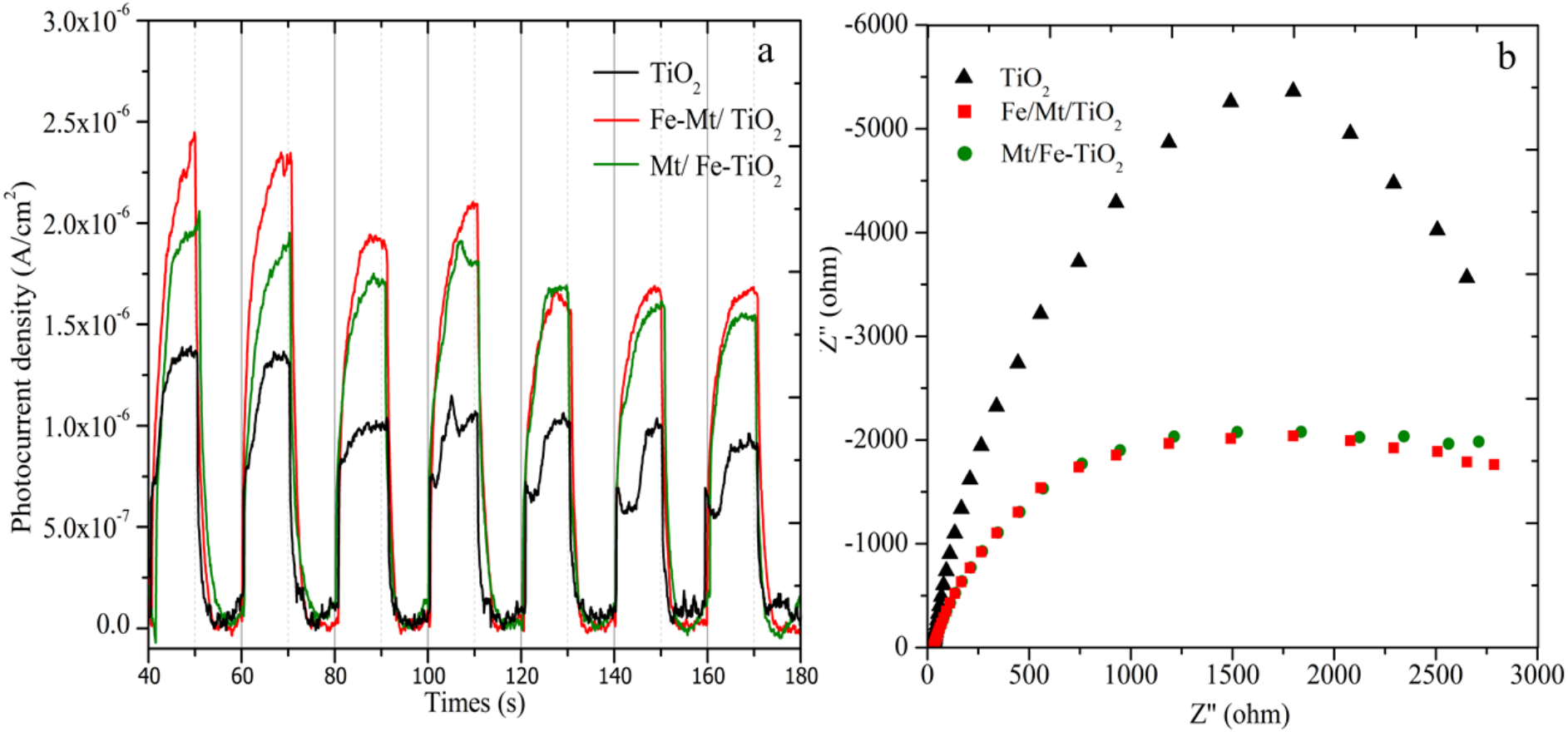

Fig. 4.10. (a) Photocurrent response and (b) EIS spectra for TiO_2, Fe-Mt/TiO_2, and Mt/Fe-TiO_2 synthesized at 70 °C.

The RDB-PAS test yielded the ERDT/CBB patterns (**Fig. 4.11**). It can show how the semiconductor's surface electrical property interferes with its photocatalytic activity, either directly or indirectly. Peak separation was used since the peaks in ERDT/CBB are broad and have a large overlapping region, as illustrated in **Fig. 4.12**, and the relevant parameters were reported in **Table 4.3**. Because only n-type semiconductors can be detected, and the Fe^{III} in Fe-Mt formed new Fermi levels receiving electrons, there was no ERDT signature in Fe-Mt. The ERDT of TiO_2 yielded three peaks: 2.96 eV for rutile (Crys.) (rutile (crystal)), 3.22 eV for rutile (amor.) (rutile (amorphous)), and 3.44 eV for rutile (amor.) coupled to anatase (Crys.). The contradicting results of no crystal anatase phase detection in ERDT and strong anatase peaks in XRD (**Fig. 4.2**) could indicate that crystal anatase resides primarily in the bulk rather than on the surface of TiO_2 particles and is preferentially attached by amorphous rutile.

In Fe-Mt/TiO_2 and Mt/Fe-TiO_2, the rutile (amorphous) coated on anatase (Crys.) can also be observed, and the peaks at 3.62 eV and 3.76 eV are assigned as two separate iso-TiO_2 peaks (amor.). Despite the absence of a crystal phase on the surface of the two composites, the relative total electron-trap densities of Fe-Mt/TiO_2 and Mt/Fe-TiO_2 are substantially greater than TiO_2, implying that the composites have a higher photocatalytic capacity than TiO_2. The ERDT patterns for Fe-Mt/TiO_2 and Mt/Fe-TiO_2 were nearly identical, except for the same relative total electron-trap densities value. Because the surface electron property of the TiO_2 in both composites is about the same, the TiO_2 in both composites should have roughly equal responsibility for the composite's photocatalytic activity. The Fe-Mt/TiO_2 has a smaller *Eg* (**Fig. 4.6**), lower electron-hole pair recombination (**Fig. 4.7**), stronger charge creation (**Fig. 4.10a**), and easier charge movement (**Fig. 4.10b**). As previously stated, the better photocatalytic property of Fe-Mt/TiO_2 over Mt/Fe-TiO_2 can be attributed to the heterojunction between Fe-Mt and TiO_2 in Fe-Mt/TiO_2, whereas Fe^{III} doping on Mt endows Mt with photocatalytic activity as a semiconductor rather than serving as a supporting material. For Fe-Mt/TiO_2 and Mt/Fe-

TiO_2, ERDT did not detect crystal anatase or crystal rutile. With the mixing and crossing of the crystal anatase, amorphous anatase, crystal rutile, and amorphous rutile, a very heterogeneous phase distribution in TiO_2 was expected, and the surface of the TiO_2 particles should be separated from the bulk for all TiO_2, Fe-Mt/TiO_2, and Mt/Fe-TiO_2.

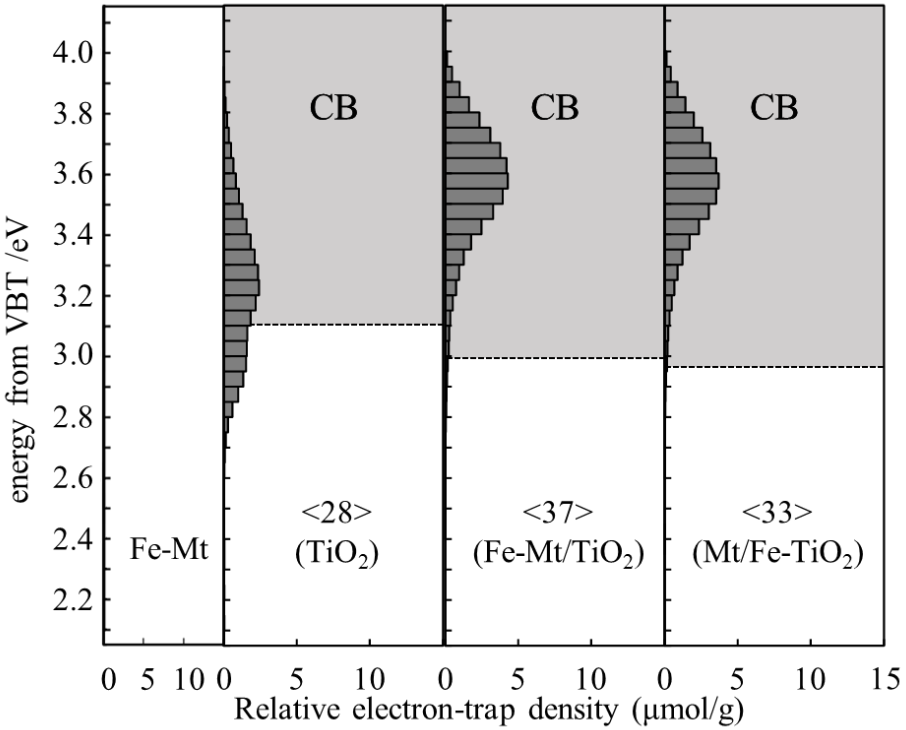

Fig. 4.11. ERDT/CBB patterns of Fe-Mt prepared at 25 °C and TiO_2, Fe-Mt/TiO_2, and Mt/Fe-TiO_2 synthesized at 70 °C as a function of energy (eV) from VBT combined with CBB plotted as a function of energy (eV). The relative total electron-trap density is indicated by the numbers in brackets.

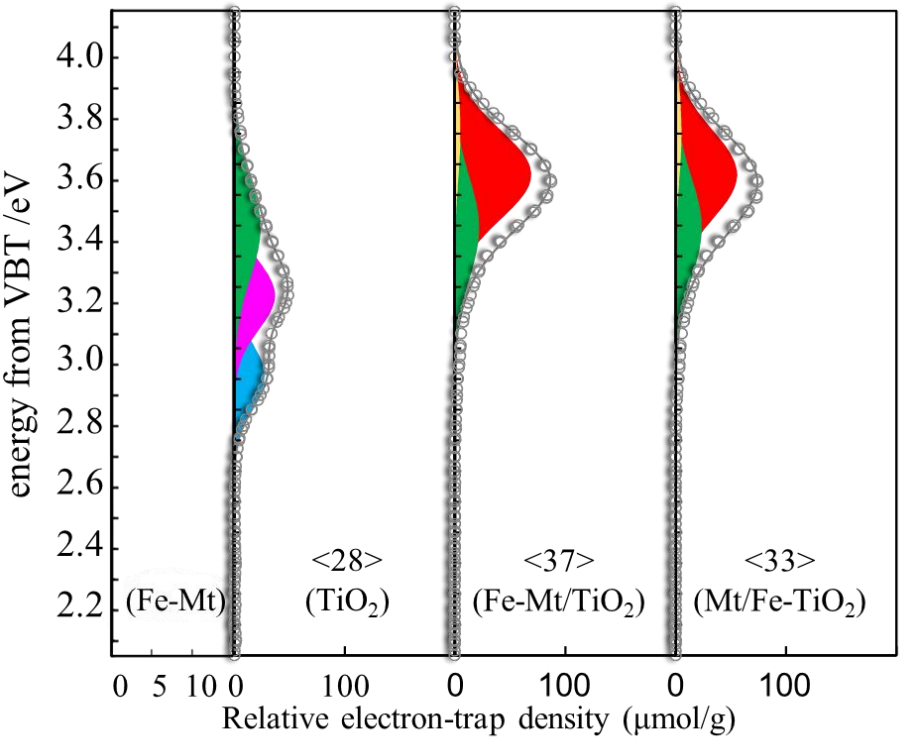

Fig. 4.12. ERDT peak fitting. The peaks are: rutile (Crys.) in blue, rutile (amor.) in pink, rutile (amor.) attached to anatase (Crys.) in green, and iso-TiO_2 (amor.) in red and yellow.

Table 4.3. Parameters of ERDT/CBB peak fitting for TiO_2, Fe-Mt/TiO_2, and Mt/Fe-TiO_2 synthesized at 70 ℃.

Sample	Peak Assignment	Peak position (eV)	Relative intensity (%)
TiO_2	rutile (Crys.[1])	2.96	31.1
	rutile (amor. [2])	3.22	42.0
	rutile (amor.) covered on anatase (Crys.)	3.44	27.0
Fe-Mt/TiO_2	rutile (amor.) covered on anatase (Crys.)	3.44	23.0
	iso.[3]-TiO_2 (amor.)	3.62	71.6
	iso.-TiO_2 (amor.)	3.76	5.4
Mt/Fe-TiO_2	rutile (amor.) covered on anatase (Crys.)	3.44	28.0
	iso.-TiO_2 (amor.)	3.62	65.7
	iso.-TiO_2 (amor.)	3.76	6.3

[1] Abbreviation for crystal.

[2] Abbreviation for amorphous.

[3] Abbreviation for isolated.

4.3.3 Photocatalytic activity

The photocatalytic activity of TiO_2, Fe-Mt/TiO_2 and Mt/Fe-TiO_2 were determined by measuring phenol degradation as a function of time and standardized by the weight% of TiO_2 (**Fig. 4.13a**). The applied photocatalysts physically absorbed about 3.2 -7.2% of the phenol. The composites had a better photocatalytic degradation efficiency of phenol than TiO_2, which is in line with the DRS, PL, photocurrent, and EIS. Fe-Mt/TiO_2 had a slightly higher phenol degradation than Mt/Fe-TiO_2, although the differences at different synthesis temperatures for both Fe-Mt/TiO_2 and Mt/Fe-TiO_2 were less than 1%. The Fe^{III} situated on Mt provided Mt photocatalytic activity, which then enabled the heterojunction between Fe-Mt and TiO_2 in Fe-Mt/TiO_2. Consequently, Fe-Mt/TiO_2 has stronger photocatalytic activity than Mt/Fe-TiO_2. Mt in Mt/Fe-TiO_2, on the other hand, serves merely as a supporting material with no photocatalytic activity. The changes in A/R suggested by the XRD data (**Fig. 4.2**) had little effect on the photocatalytic activity of the composites, which revealed that the surface photocatalytic character of the TiO_2 particles is almost the same. Not to note that the temperature parameter interfered with the phase distribution of TiO_2 particles on the Fe-Mt/TiO_2 and Mt/Fe-TiO_2 phases less than the location of Fe^{III} on the Fe-Mt/TiO_2 and Mt/Fe-TiO_2 phases. Pseudo-first-order kinetics (eq. 4.2) were used to simulate the photocatalytic reduction kinetics of phenol:

$$-\ln\left(C/C_0\right) = kt \tag{4.2}$$

where C and C_0 (mmol/g) are the residual and starting phenol concentrations, and parameter k (min^{-1}) is the pseudo-first order model's rate constant. The rate constants normalized by weight percentage of TiO_2 were 1.8×10^{-3} for TiO_2, 6.6×10^{-3}, 6.5×10^{-3}, and 6.0×10^{-3} for Fe-Mt/TiO_2 synthesized at 70 ℃, 80 ℃, and 90 ℃, and 6.0×10^{-3}, 6.1×10^{-3}, and 6.0×10^{-3} for Mt/Fe-TiO_2 synthesized at 70 ℃, 80 ℃, and 90 ℃. The observed characterizations, such as DRS, PL, photocurrent, and EIS, corroborate the photocatalytic activity findings (**Fig. 13b**).

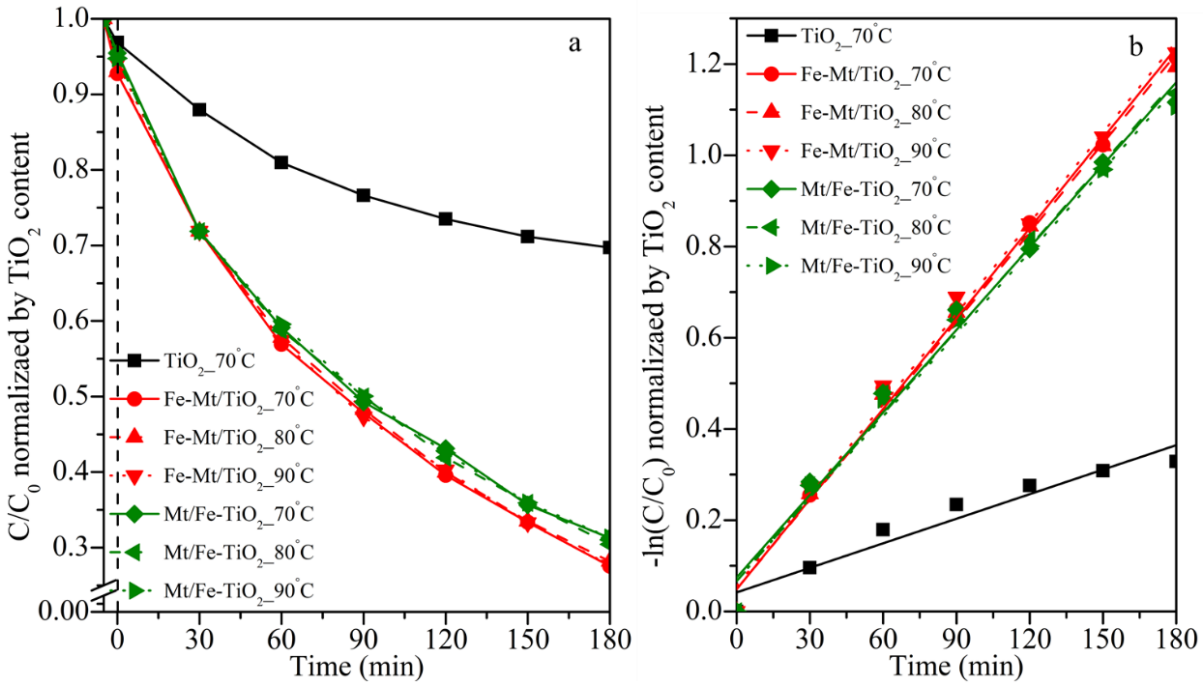

Fig. 4.13 (a) Photocatalytic degradation of phenol and (b) corresponding kinetics for TiO_2 synthesized at 70 °C, Fe-Mt/TiO_2 and Mt/Fe-TiO_2 synthesized at 70, 80, and 90 °C.

HPLC and prior studies [72], [73] validated the intermediate compounds produced during phenol degradation (**Fig. 4.14**). Initially, just the phenol peak (retention time τ = 8.92 min) could be seen. The phenol peak faded, and a new pyrocatechol peak (τ = 6.00 min) emerged within the first 15 minutes. Within 15 minutes, a tiny cis,cis-muconic acid peak (τ = 4.10 min) grew up as the pyrocatechol peak faded which was accompanied with the presence of a low-intensity benzoquinone peak (τ = 4.78 min). According to prior studies, one phenol molecule was reduced to pyrocatechol with one electron, and then one pyrocatechol was reduced to benzoquinone with two electrons and transferred to cis,cis- muconic acid which will be further degraded into succinic acid (τ = 2.43 min) and formic acid (τ = 2.27 min) (**Fig. 4.15**).

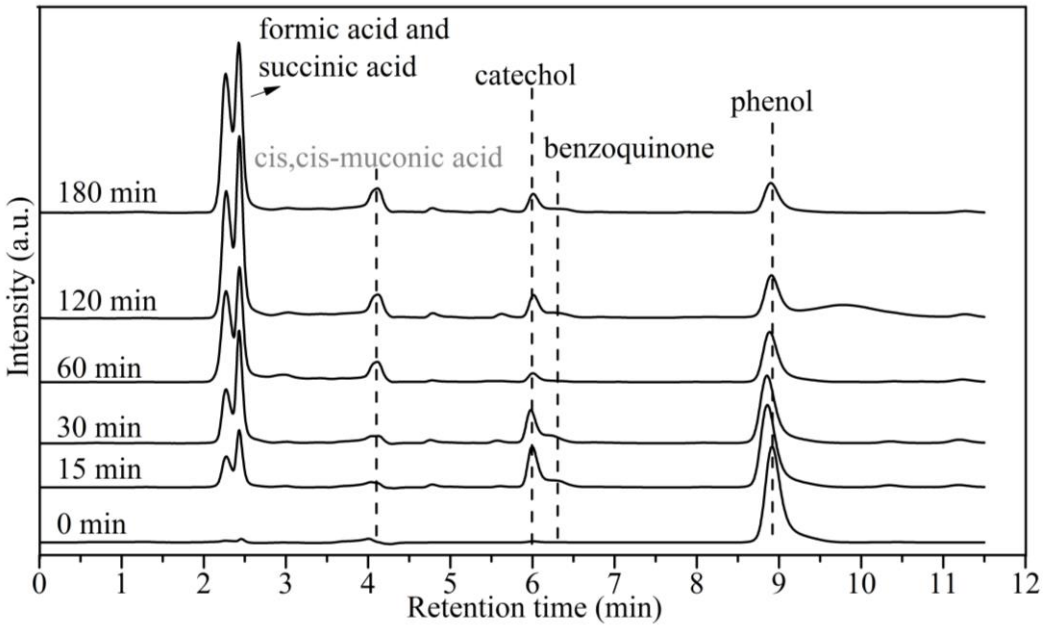

Fig. 4.14 Chromatograms of the byproducts for phenol degradation on Fe-Mt/TiO_2. The grayed-out "cis,cis-muconic acid" was based on references [72], [73].

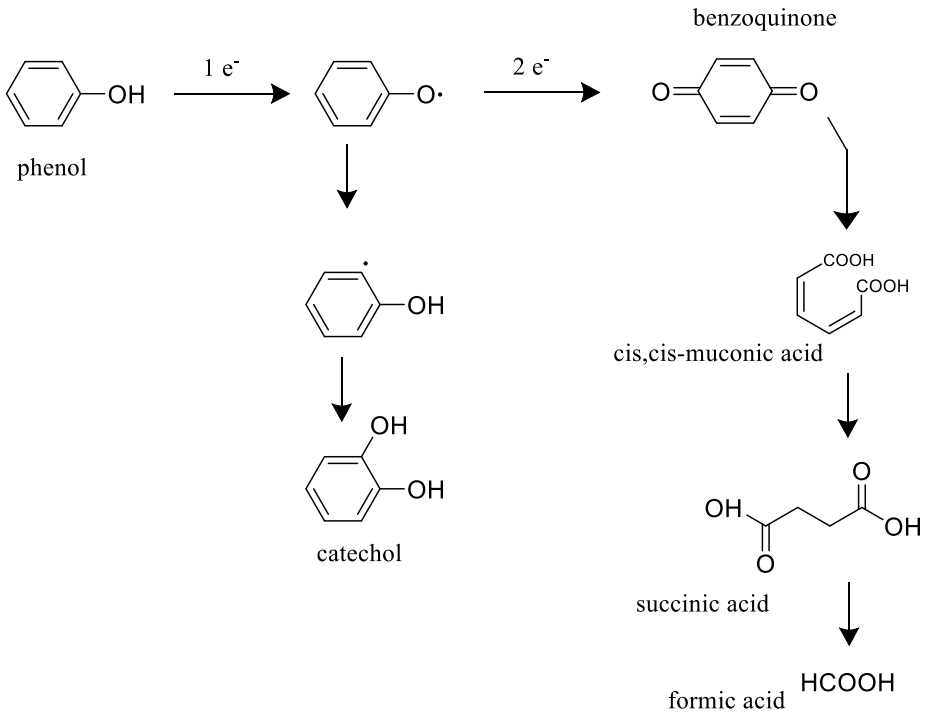

Fig. 4.15 The degradation and mineralization of phenol on Fe-Mt/TiO_2 synthesized at 70 °C.

4.3.4 Mechanism of phenol degradation over TiO_2, Fe-Mt/TiO_2, and Mt/Fe-TiO_2

In the photocatalytic destruction of phenol, several radicals such as $^{\bullet}OH$, $O_2^{\bullet-}$, and h^+ will be produced and cycled. The scavenger test can be used to quench matching radicals, preventing them from participating in the photocatalytic activity. As a result, it was possible to distinguish between the reactions of distinct radicals during photocatalytic processes. As illustrated in **Fig. 4.16**, phenol degradation on Fe-Mt/TiO_2 was achieved using ethanol as a hole scavenger, isopropanol as a $^{\bullet}OH$ scavenger, and para-benzoquinone as an $O_2^{\bullet-}$ radical scavenger. There was a clear suppression of the photocatalytic response by para-benzoquinone, but only a modest reduction in photocatalytic effectiveness by ethanol and isopropanol. As a result, $O_2^{\bullet-}$ is the radical mainly responsible for phenol degradation. The Fe-Mt/TiO_2 VB (**Fig. 4.8g**) derived from XPS VB is lower than the redox potential of $^{\bullet}OH$ generation and higher than the redox potential of $O_2^{\bullet-}$ production. As a result, the $^{\bullet}OH$ radical should not be created, and the $O_2^{\bullet-}$ radical should be the primary radical produced.

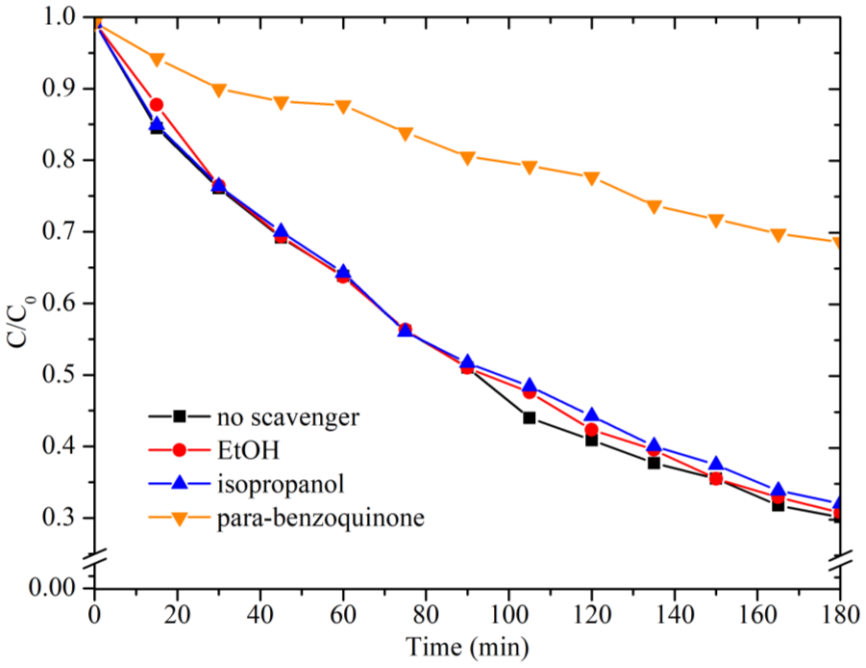

Fig. 4.16 Effect of radical scavengers on the photocatalytic degradation of phenol on Fe-Mt/TiO_2 synthesized at 70 °C.

The mechanisms for both Fe-Mt/TiO_2 and Mt/Fe-TiO_2 photocatalysis are depicted in **Fig. 4.17** based on prior characterizations and other research. VB XPS was used to determine the VB of TiO_2 in Fe-Mt/TiO_2 and Mt/Fe-TiO_2 (**Fig. 1.8g** and **Fig. 4.9g**), and the CB of the TiO_2 component was calculated using the VB and the *Eg* acquired from UV-DRS Tauc plots (**Fig. 4.6b**). The same contribution of the TiO_2 part in both Fe-Mt/TiO_2 and Mt/Fe-TiO_2 was inferred by the congenial surface photocatalytic property demonstrated by ERDT (**Fig. 4.12**). The photocatalytic characterization and performance of the two composites differed due to differences in Mt phase characteristics. Mt in Mt/ Fe-TiO_2 should only be used as a TiO_2 support material. The Fe-Mt in Fe-Mt/TiO_2, on the other hand, has photocatalytic activity and can cross with TiO_2. Because the VB of TiO_2 in both composites is lower than the redox potential of H_2O_2/$^{\bullet}OH$, h^+ in TiO_2's VB could not produce $^{\bullet}OH$. The increased electron donor level with a higher energy potential as the VB of Fe-Mt should be attributed to the small depression of $^{\bullet}OH$ found on the scavenger test of Fe-Mt/TiO_2. Fe^{III} in the Mt phase contributed more than in the TiO_2 phase.

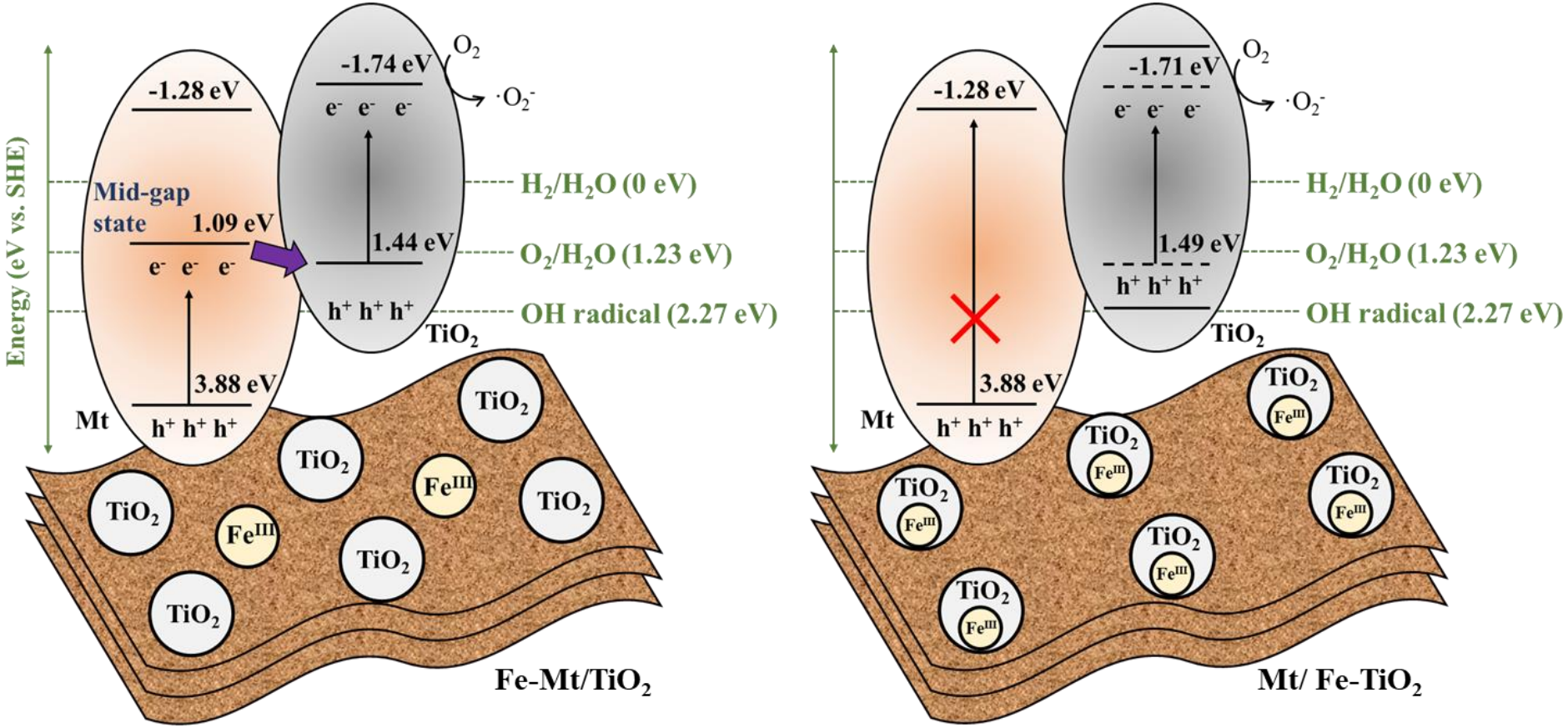

Fig. 4.17 Illustration of charge transfer on (a) Fe-Mt/TiO_2 and (b) Mt/Fe-TiO_2 during photocatalytic reaction synthesized at 70 °C.

4.4 Conclusions

Fe^{III} speciation was maintained as a trivalent cation during the synthesis of Fe-Mt/TiO_2 and Mt/Fe-TiO_2 composites by keeping the pH below 2, and the position of Fe^{III} was regulated by adding Fe^{III} sources at two separate points in the Fe-Mt/TiO_2 and Mt/Fe-TiO_2 synthesis procedures. Fe^{III} resides on Mt in the Fe-Mt/TiO_2 system, and Fe^{III} exists in TiO_2 in the Mt/Fe-TiO_2 system. When compared to the influence from the position of Fe^{III}, as demonstrated by XRF and peak fitting of XRD, the synthesis temperature had minor effect on TiO_2 content and anatase/rutile ratio. TEM also revealed a cross between anatase and rutile. DRS, PL, photocurrent, and EIS measurements revealed that Fe-Mt/TiO_2 has a narrower *Eg*, better recombination removal, a more significant reaction to irradiation, and lower charge transfer resistance than Mt/Fe-TiO_2. At 3 h of the photocatalytic reaction, Fe-Mt/TiO_2 achieved 71.8 - 72.5% photocatalytic phenol decomposition, while Mt/Fe-TiO_2 achieved 68.7 - 69.6% photocatalytic phenol decomposition. At various reaction intervals, the intermediate products were also deduced using the HPLC chorograms and basing on previous researches. The remarkable photocatalytic property of Fe-Mt/TiO_2 was consistent with its superior photocatalytic performance for the photocatalytic degradation of phenol, which was attributed to the critical role of Fe-Mt in Fe-Mt/TiO_2 as a semiconductor crossing with TiO_2 to form a heterojunction, while, in comparison, Mt in Mt/Fe-TiO_2 was still an insulator. The electron structure of Fe-Mt and TiO_2 in Fe-Mt/TiO_2, as well as TiO_2 in Mt/Fe-TiO_2, was seen using a combination of DRS, VB XPS, ERDT, and radical scavenger test. During the photocatalytic reaction, the $O_2^{\bullet-}$ radical was the dominating radical. The findings suggest that photocatalytic reactions on Mt and Fe^{III}-containing clay may occur. This will give a hint about the possible photocatalytic potential of Mt mineral.

Reference

[1] X. Gan, V. Teng, J. Xu, N. Zhang, W. Ren, L. Zhao, P. Christie, and Y. Luo., "Influences of kaolinite and montmorillonite on benzo [a] pyrene biodegradation by Paracoccus aminovorans HPD-2 and the underlying interface interaction mechanisms," *Pedosphere*, vol. 32, no. 2, pp. 246–255, 2022.

[2] P. Cai, Q. Huang, and X. Zhang, "Microcalorimetric studies of the effects of $MgCl_2$ concentrations and pH on the adsorption of DNA on montmorillonite, kaolinite and goethite," *Applied Clay Science*, vol. 32, no. 1–2, pp. 147–152, 2006.

[3] P. F. Low, "Nature and properties of water in montmorillonite-water systems," *Soil Science Society of America Journal*, vol. 43, no. 4, pp. 651–658, 1979.

[4] F. Bergaya and G. Lagaly, *Handbook of clay science*. Newnes, 2013.

[5] M. Segad, B. Jonsson, T. Åkesson, and B. Cabane, "Ca/Na montmorillonite: structure, forces and swelling properties," *Langmuir*, vol. 26, no. 8, pp. 5782–5790, 2010.

[6] K. Norrish, "The swelling of montmorillonite," *Discussions of the Faraday society*, vol. 18, pp. 120–134, 1954.

[7] K. G. Bhattacharyya and S. sen Gupta, "Kaolinite and montmorillonite as adsorbents for Fe (III), Co (II) and Ni (II) in aqueous medium," *Applied Clay Science*, vol. 41, no. 1–2, pp. 1–9, 2008.

[8] A. S. K. Kumar, R. Ramachandran, S. Kalidhasan, V. Rajesh, and N. Rajesh, "Potential application of dodecylamine modified sodium montmorillonite as an effective adsorbent for hexavalent chromium," *Chemical Engineering Journal*, vol. 211, pp. 396–405, 2012.

[9] J.-Q. Jiang, C. Cooper, and S. Ouki, "Comparison of modified montmorillonite adsorbents: part I: preparation, characterization and phenol adsorption," *Chemosphere*, vol. 47, no. 7, pp. 711–716, 2002.

[10] R. Zhu, Q. Chen, Q. Zhou, Y. Xi, J. Zhu, and H. He, "Adsorbents based on

montmorillonite for contaminant removal from water: A review," *Applied Clay Science*, vol. 123, pp. 239–258, 2016.

[11] L. Zhang, S. Kancharla, and K. Sasaki, "Synthesis and characterization of imidazole-bearing polymer-modified montmorillonite for adsorption of perchlorate," *Applied Clay Science*, vol. 199, p. 105859, 2020.

[12] M. Tahir and N. S. Amin, "Photocatalytic reduction of carbon dioxide with water vapors over montmorillonite modified TiO_2 nanocomposites," *Applied Catalysis B: Environmental*, vol. 142, pp. 512–522, 2013.

[13] R. Kun, K. Mogyorósi, and I. Dékány, "Synthesis and structural and photocatalytic properties of TiO2/montmorillonite nanocomposites," *Applied Clay Science*, vol. 32, no. 1–2, pp. 99–110, 2006.

[14] N. Gu, J. Gao, H. Li, Y. Wu, Y. Ma, and K. Wang, "Montmorillonite-supported with Cu_2O nanoparticles for damage and removal of Microcystis aeruginosa under visible light," *Applied Clay Science*, vol. 132, pp. 79–89, 2016.

[15] I. Fatimah, S. Wang, and D. Wulandari, "ZnO/montmorillonite for photocatalytic and photochemical degradation of methylene blue," *Applied Clay Science*, vol. 53, no. 4, pp. 553–560, 2011.

[16] L. Zhang, C. Chuaicham, V. Balakumar, B. Ohtani, and K. Sasaki, "Fabrication of Adsorbed Fe (III) and Structurally Doped Fe (III) in Montmorillonite/TiO_2 Composite for Photocatalytic Degradation of Phenol," *Minerals*, vol. 11, no. 12, p. 1381, 2021.

[17] J. Liu, M. Dong, S. Zuo, and Y. Yu, "Solvothermal preparation of TiO_2/montmorillonite and photocatalytic activity," *Applied Clay Science*, vol. 43, no. 2, pp. 156–159, 2009.

[18] K. Peng, L. Fu, H. Yang, and J. Ouyang, "Perovskite $LaFeO_3$/montmorillonite nanocomposites: synthesis, interface characteristics and enhanced photocatalytic activity," *Sci Rep*, vol. 6, no. 1, pp. 1–10, 2016.

[19] C. Chuaicham, Y. Xiong, K. Sekar,W. Chen, L. Zhang, B. Ohtani, I. Babo, and K. Sasaki, "A promising Zn-Ti layered double hydroxide/Fe-bearing montmorillonite composite as an efficient photocatalyst for Cr (VI) reduction: Insight into the role of Fe impurity in montmorillonite," *Applied Surface Science*, vol. 546, p. 148835, 2021.

[20] Y. Chen, Y. Yu, Z. Yan, T. Li, Q. Jing, and P. Liu, "Montmorillonite induced assembly of multi-element doped g-C_3N_4 nanosheets with enhanced activity for Rhodamine B photodegradation," *Applied Clay Science*, vol. 218, p. 106432, 2022.

[21] V. Balakumar, K. Sekar, C. Chuaicham, R. Manivannan, and K. Sasaki, "Synergistic ternary porous CN–PPy–MMt nanocomposite for efficient photocatalytic metronidazole mineralization: Performance, mechanism, and pathways," *Environmental Science: Nano*, vol. 8, no. 8, pp. 2261–2276, 2021.

[22] C. Li, Z. Sun, W. Huang, and S. Zheng, "Facile synthesis of g-C_3N_4/montmorillonite composite with enhanced visible light photodegradation of rhodamine B and tetracycline," *J Taiwan Inst Chem Eng*, vol. 66, pp. 363–371, Sep. 2016, doi: 10.1016/j.jtice.2016.06.014.

[23] L. Djouadi, H. Khalaf, H. Boukhatem, H. Boutoumi, A. Kezzime, J.A. Santaballa, and M. Canle, "Degradation of aqueous ketoprofen by heterogeneous photocatalysis using Bi_2S_3/TiO_2–Montmorillonite nanocomposites under simulated solar irradiation," *Applied Clay Science*, vol. 166, pp. 27–37, 2018.

[24] K. Peng, H. Wang, X. Li, J. Wang, L. Xu, H. Gao, M. Niu, M. Ma, and J. Yang, "One-step hydrothermal growth of MoS2 nanosheets/CdS nanoparticles heterostructures on montmorillonite for enhanced visible light photocatalytic activity," *Applied Clay Science*, vol. 175, pp. 86–93, 2019.

[25] P. P. Tun, J. Wang, T. T. Khaing, X. Wu, and G. Zhang, "Fabrication of functionalized plasmonic Ag loaded Bi_2O_3/montmorillonite nanocomposites for efficient

photocatalytic removal of antibiotics and organic dyes," *Journal of Alloys and Compounds*, vol. 818, p. 152836, 2020.

[26] C. Xu, H. Wu, and F. L. Gu, "Efficient adsorption and photocatalytic degradation of Rhodamine B under visible light irradiation over BiOBr/montmorillonite composites," *J Hazard Mater*, vol. 275, pp. 185–192, 2014.

[27] X. Li, F. Li, X. Lu, S. Zuo, C. Yao, and C. Ni, "Development of $Bi_2W_{1-x}Mo_xO_6$/Montmorillonite nanocomposite as efficient catalyst for photocatalytic desulfurization," *Journal of Alloys and Compounds*, vol. 709, pp. 285–292, 2017.

[28] Q. Guo, C. Zhou, Z. Ma, and X. Yang, "Fundamentals of TiO2 photocatalysis: concepts, mechanisms, and challenges," *Advanced Materials*, vol. 31, no. 50, p. 1901997, 2019.

[29] J. Schneider, M. Matsuoka, M. Takeuchi, J. Zhang, Y. Horiuchi, M. Anpo, and D.W. Bahnemann, "Understanding TiO_2 photocatalysis: mechanisms and materials," *Chem Rev*, vol. 114, no. 19, pp. 9919–9986, 2014.

[30] K. Hashimoto, H. Irie, and A. Fujishima, "TiO_2 photocatalysis: a historical overview and future prospects," *Jpn J Appl Phys*, vol. 44, no. 12R, p. 8269, 2005.

[31] K. Nakata and A. Fujishima, "TiO_2 photocatalysis: Design and applications," *Journal of photochemistry and photobiology C: Photochemistry Reviews*, vol. 13, no. 3, pp. 169–189, 2012.

[32] A. Fujishima, X. Zhang, and D. A. Tryk, "TiO_2 photocatalysis and related surface phenomena," *Surf Sci Rep*, vol. 63, no. 12, pp. 515–582, 2008.

[33] R. E. Krebs, *The history and use of our earth's chemical elements: a reference guide*. Greenwood Publishing Group, 2006.

[34] W. H. Leng, Z. Zhang, J. Q. Zhang, and C. N. Cao, "Investigation of the kinetics of a TiO_2 photoelectrocatalytic reaction involving charge transfer and recombination through surface states by electrochemical impedance spectroscopy," *The Journal of Physical*

Chemistry B, vol. 109, no. 31, pp. 15008–15023, 2005.

[35] A. J. Frank, N. Kopidakis, and J. van de Lagemaat, "Electrons in nanostructured TiO_2 solar cells: transport, recombination and photovoltaic properties," *Coordination Chemistry Reviews*, vol. 248, no. 13–14, pp. 1165–1179, 2004.

[36] R. Qian, H. Zong, J. Schneider, G. Zhou, T. Zhao, Y. Li, J. Yang, D.W. Bahnemann, and J. Pan, "Charge carrier trapping, recombination and transfer during TiO_2 photocatalysis: An overview," *Catalysis Today*, vol. 335, pp. 78–90, 2019.

[37] A. Zaleska, "Doped-TiO_2: a review," *Recent patents on engineering*, vol. 2, no. 3, pp. 157–164, 2008.

[38] M. V. Dozzi and E. Selli, "Doping TiO_2 with p-block elements: Effects on photocatalytic activity," *Journal of Photochemistry and Photobiology C: Photochemistry Reviews*, vol. 14, pp. 13–28, 2013.

[39] M. Xing, W. Fang, M. Nasir, Y. Ma, J. Zhang, and M. Anpo, "Self-doped Ti^{3+}-enhanced TiO_2 nanoparticles with a high-performance photocatalysis," *Journal of Catalysis*, vol. 297, pp. 236–243, 2013.

[40] D. Chen, Z. Jiang, J. Geng, Q. Wang, and D. Yang, "Carbon and nitrogen co-doped TiO_2 with enhanced visible-light photocatalytic activity," *Ind Eng Chem Res*, vol. 46, no. 9, pp. 2741–2746, 2007.

[41] X. Chen and C. Burda, "The electronic origin of the visible-light absorption properties of C-, N-and S-doped TiO_2 nanomaterials," *J Am Chem Soc*, vol. 130, no. 15, pp. 5018–5019, 2008.

[42] K. Woan, G. Pyrgiotakis, and W. Sigmund, "Photocatalytic Carbon-Nanotube–TiO_2 Composites," *Advanced Materials*, vol. 21, no. 21, pp. 2233–2239, Jun. 2009, doi: https://doi.org/10.1002/adma.200802738.

[43] B. Tang, H. Chen, H. Peng, Z. Wang, and W. Huang, "Graphene Modified TiO_2

Composite Photocatalysts: Mechanism, Progress and Perspective," *Nanomaterials*, vol. 8, no. 2, 2018, doi: 10.3390/nano8020105.

[44] W. K. Jo and T. S. Natarajan, "Influence of TiO_2 morphology on the photocatalytic efficiency of direct Z-scheme g-C_3N_4/TiO_2 photocatalysts for isoniazid degradation," *Chemical Engineering Journal*, vol. 281, pp. 549–565, Dec. 2015, doi: 10.1016/J.CEJ.2015.06.120.

[45] T. Ohno, K. Sarukawa, K. Tokieda, and M. Matsumura, "Morphology of a TiO_2 Photocatalyst (Degussa, P-25) Consisting of Anatase and Rutile Crystalline Phases," *Journal of Catalysis*, vol. 203, no. 1, pp. 82–86, Oct. 2001, doi: 10.1006/JCAT.2001.3316.

[46] S. Khan, I. A. Qazi, I. Hashmi, M. A. Awan, and N. U. S. S. Zaidi, "Synthesis of silver-doped titanium TiO_2 powder-coated surfaces and its ability to inactivate pseudomonas aeruginosa and bacillus subtilis," *Journal of Nanomaterials*, vol. 2013, Jan. 2013, doi: 10.1155/2013/531010.

[47] G. R. Khan and S. I. Malik, "Ag-enriched TiO_2 nanocoating apposite for self-sanitizing/ self-sterilizing/ self-disinfecting of glass surfaces," *Materials Chemistry and Physics*, vol. 282, p. 125803, Apr. 2022, doi: 10.1016/J.MATCHEMPHYS.2022.125803.

[48] S. C. Chan and M. A. Barteau, "Preparation of highly uniform Ag/TiO_2 and Au/TiO_2 supported nanoparticle catalysts by photodeposition," *Langmuir*, vol. 21, no. 12, pp. 5588–5595, Jun. 2005, doi: 10.1021/LA046887K/ASSET/IMAGES/LA046887K.SOCIAL.JPEG_V03.

[49] Z. Xiong, H. Wang, N. Xu, H. Li, B. Fang, Y. Zhao, J. Zhang, and C. Zheng, "Photocatalytic reduction of CO_2 on Pt^{2+}–Pt_0/TiO_2 nanoparticles under UV/Vis light irradiation: A combination of Pt^{2+} doping and Pt nanoparticles deposition," *International Journal of Hydrogen Energy*, vol. 40, no. 32, pp. 10049–10062, Aug. 2015, doi:

10.1016/J.IJHYDENE.2015.06.075.

[50] K. M. Parida and L. Mohapatra, “Carbonate intercalated Zn/Fe layered double hydroxide: A novel photocatalyst for the enhanced photo degradation of azo dyes,” *Chemical Engineering Journal*, vol. 179, pp. 131–139, 2012, doi: 10.1016/j.cej.2011.10.070.

[51] S. J. Kim, Y. Lee, D. K. Lee, J. W. Lee, and J. K. Kang, “Efficient Co-Fe layered double hydroxide photocatalysts for water oxidation under visible light,” *Journal of Materials Chemistry A*, vol. 2, no. 12, pp. 4136–4139, 2014, doi: 10.1039/c3ta14933a.

[52] T. H. Xie, X. Sun, and J. Lin, “Enhanced photocatalytic degradation of RhB driven by visible light-induced MMCT of Ti(IV)-O-Fe(II) formed in Fe-doped $SrTiO_3$,” *Journal of Physical Chemistry C*, vol. 112, no. 26, pp. 9753–9759, 2008, doi: 10.1021/jp711797a.

[53] C. Chuaicham, R. R. Pawar, S. Karthikeyan, B. Ohtani, and K. Sasaki, “Fabrication and characterization of ternary sepiolite/g-C_3N_4/Pd composites for improvement of photocatalytic degradation of ciprofloxacin under visible light irradiation,” *Journal of Colloid and Interface Science*, vol. 577, pp. 397–405, Oct. 2020, doi: 10.1016/J.JCIS.2020.05.064.

[54] D. H. Kim, H. S. Hong, S. J. Kim, J. S. Song, and K. S. Lee, “Photocatalytic behaviors and structural characterization of nanocrystalline Fe-doped TiO_2 synthesized by mechanical alloying,” *Journal of Alloys and Compounds*, vol. 375, no. 1–2, pp. 259–264, Jul. 2004, doi: 10.1016/J.JALLCOM.2003.11.044.

[55] G. Shao, “Red Shift in Manganese- and Iron-Doped TiO_2: A DFT+U Analysis,” *Journal of Physical Chemistry C*, vol. 113, no. 16, pp. 6800–6808, Apr. 2009, doi: 10.1021/JP810923R.

[56] Y. Wen, G. Schoups, and N. van de Giesen, “Organic pollution of rivers: Combined threats of urbanization, livestock farming and global climate change,” *Scientific Reports*

2017 7:1, vol. 7, no. 1, pp. 1–9, Feb. 2017, doi: 10.1038/srep43289.

[57] D. J. Lapworth, N. Baran, M. E. Stuart, and R. S. Ward, "Emerging organic contaminants in groundwater: A review of sources, fate and occurrence," *Environmental Pollution*, vol. 163, pp. 287–303, Apr. 2012, doi: 10.1016/J.ENVPOL.2011.12.034.

[58] O. Lefebvre and R. Moletta, "Treatment of organic pollution in industrial saline wastewater: A literature review," *Water Research*, vol. 40, no. 20, pp. 3671–3682, Dec. 2006, doi: 10.1016/J.WATRES.2006.08.027.

[59] R. M. Bruce, J. Santodonato, and M. W. Neal, "Summary review of the health effects associated with phenol," *Toxicology and Industrial Health*, vol. 3, no. 4, pp. 535–568, Jun. 1987, doi: 10.1177/074823378700300407.

[60] Y. Wang, L. Zhang, K. Deng, X. Chen, and Z. Zou, "Low temperature synthesis and photocatalytic activity of rutile TiO_2 nanorod superstructures," *The Journal of Physical Chemistry C*, vol. 111, no. 6, pp. 2709–2714, 2007.

[61] W. Zhou, F. Sun, K. Pan, G. Tian, B. Jiang, Z. Ren, C. Tian, and H. Fu, "Well-Ordered Large-Pore Mesoporous Anatase TiO_2 with Remarkably High Thermal Stability and Improved Crystallinity: Preparation, Characterization, and Photocatalytic Performance," *Advanced Functional Materials*, vol. 21, no. 10, pp. 1922–1930, May 2011, doi: 10.1002/ADFM.201002535.

[62] J. Tauc, "Optical properties and electronic structure of amorphous Ge and Si," *Materials Research Bulletin*, vol. 3, no. 1, pp. 37–46, Jan. 1968, doi: 10.1016/0025-5408(68)90023-8.

[63] S. Said Abdullahi, S. Güner, I. Murtala Musa, and B. ISMAIL Adamu, "Sımple Method for The Determınatıon of Band Gap of a Nanopowdered Sample Usıng Kubelka Munk Theory ESSENTIAL ROLE OF SURFACTANT ON TITANIUM DIOXIDE-ROSELLE DYE SENSITIZED SOLAR CELL View project," 2016, Accessed: Mar. 24,

2022. [Online]. Available: https://www.researchgate.net/publication/305810656

[64] B. Bharti, S. Kumar, H.-N. Lee, and R. Kumar, "Formation of oxygen vacancies and Ti^{3+} state in TiO_2 thin film and enhanced optical properties by air plasma treatment," *Sci Rep*, vol. 6, no. 1, pp. 1–12, 2016.

[65] H. Lv, H. Zhao, T. Cao, L. Qian, Y. Wang, and G. Zhao, "Efficient degradation of high concentration azo-dye wastewater by heterogeneous Fenton process with iron-based metal-organic framework," *Journal of Molecular Catalysis A: Chemical*, vol. 400, pp. 81–89, 2015.

[66] W. Jichao, "On the cultivation of science college students' innovative and entrepreneurial ability," *Journal of China University of Petroleum (Edition of Social Sciences)*, vol. 5, pp. 106–109, 2016.

[67] L. Wu, Y. Li, S. Li, Z. Li, G. Tang, W. Qi, L. Xue, X. Ge, and L. Ding, "Method for estimating ionicities of oxides using O1s photoelectron spectra," *AIP Advances*, vol. 5, no. 9, p. 97210, 2015.

[68] F.G. Ferré, A Mairov, D. Iadicicco, M. Vanazzi, S. Bassini, M. Utili, M. Tarantino, M. Bragaglia, F.R. Lamastra, F. Nanni, L. Ceseracciu, Y. Serruys, P. Trocellier, L. Beck, K. Sridharan, M.G. Beghi, and F.Di Fonzo, "Corrosion and radiation resistant nanoceramic coatings for lead fast reactors," *Corrosion Science*, vol. 124, pp. 80–92, 2017.

[69] T. P. Nguyen and S. Lefrant, "XPS study of SiO thin films and SiO-metal interfaces," *Journal of Physics: Condensed Matter*, vol. 1, no. 31, p. 5197, 1989.

[70] F. Dong, Z. Zhao, T. Xiong, Z. Ni, W. Zhang, Y. Sun, and W. Ho, "In situ construction of g-C_3N_4/g-C_3N_4 metal-free heterojunction for enhanced visible-light photocatalysis," *ACS Appl Mater Interfaces*, vol. 5, no. 21, pp. 11392–11401, 2013.

[71] X. Su, J. Yang, X. Yu, Y. Zhu, and Y. Zhang, "In situ grown hierarchical 50%BiOCl/BiOI hollow flowerlike microspheres on reduced graphene oxide nanosheets for enhanced

visible-light photocatalytic degradation of rhodamine B," *Applied Surface Science*, vol. 433, pp. 502–512, 2018, doi: 10.1016/j.apsusc.2017.09.258.

[72] D. Wu, Y. Xiong, M. He, S. Yang, J. Cai, Z. Wu, S. Sun, X. Chen, and W.D. Wu, "Determination of phenol degradation in chloride ion rich water by ferrate using a chromatographic method in combination with on-line mass spectrometry analysis," *Analytical Methods*, vol. 11, no. 36, pp. 4651–4658, Sep. 2019, doi: 10.1039/C9AY01527B.

[73] F.C.S. Paschoalino, M.P. Paschoalino, E. Jord, and W.F. Jardim, "Evaluation of TiO_2, ZnO, CuO and Ga_2O_3 on the Photocatalytic Degradation of Phenol Using an Annular-Flow Photocatalytic Reactor," *Open Journal of Physical Chemistry*, vol. 2, no. 3, pp. 135–140, Aug. 2012, doi: 10.4236/OJPC.2012.23018.

Chapter 5

Functions of physically adsorbed Fe^{III} and structurally doped Fe^{III} in montmorillonite/ TiO_2 composite for photocatalytic oxidation of phenol

5.1 Introduction

Mt and Fe^{III} are abundant in nature, and Ti is the ninth most abundant element (0.63% by mass) and the seventh most prevalent metal in the Earth's crust. Ti is found in practically every living creature, as well as bodies of water, rocks, and soils. Titanium dioxide (TiO_2) is the most prevalent substance, a prominent photocatalyst that has been studied and used in scientific research and industry for a long time. TiO_2 is a low-cost photocatalytic material that is highly photocatalytically active, non-toxic, and chemically stable under most conditions. However, TiO_2's photocatalytic activity is hampered by its comparatively wide energy bandgap (*Eg*) and recombination of electrons (e^-) and holes (h^+). Furthermore, TiO_2 nanoparticles tend to agglomerate, making separation from water challenging. Numerous tactics, such as morphology modification [1], [2], surface sensitization [3], [4], metal nanoparticle deposition [5], [6], element doping [7], [8], and production of composite materials with other materials [9], [10], have been used to address these obstacles.

Montmorillonite (Mt) is a common supporting material used in TiO_2 composites to prevent TiO_2 particle aggregation because the TiO_2 particle sizes were lowered and the TiO_2 particle distribution was improved in the Mt layers. Furthermore, TiO_2's photocatalytic efficacy can be improved by drastically reducing fine particle sizes [11]–[13]. Mt is a 2:1 clay mineral with a layered structure and exchangeable interlayer cations [14]–[16], and it is abundant in nature [16], [17]. As a result, Mt exhibits outstanding adsorption properties, particularly for positively charged compounds with large relative surface areas. Aside from that, Mt is reasonably stable across a wide pH range. Mt is a good supporting material for producing composites because of all of these features [18]–[20]. However, due to its high bandgap, it lacks photocatalytic characteristics [21]. In that stratum, iron is the fourth most abundant element. Furthermore, in the visible region of the spectrum, iron species are one of the least poisonous and least expensive photocatalytic chemicals. The trace levels of iron found in natural minerals, on the

other hand, have been overlooked. Much research have suggested that iron doping in materials can enhance or improve photocatalytic properties. In photocatalytic processes, a non-negligible boosting effect has been produced in layered double hydroxide (LDH) (or other clay) containing $Fe^{II/III}$ [22]–[24]. In the case of iron doping, a middle-gap electron trap state was produced using density functional theory (DFT) calculations, which improved the photocatalytic efficacy of the ZnTi-LDH/clay samples [25]. These research, however, did not address whether the Fe^{III} was in the form of a cation, metal oxide, metal hydroxide, or other compounds. Furthermore, the position of Fe^{III} in the composite was unknown.

Since the Fe^{III} ion in TiO_2 can introduce a Fermi level as an electron donor or acceptor, narrowing the *Eg* of TiO_2 and red shifting the irradiation adsorption of TiO_2, numerous investigations have been conducted [26]–[28]. It has also been postulated that when a metal transitions to TiO_2, oxygen vacancies form, which act as charge trapping sites, increasing the production of active radicals [29], [30].

Two varieties of Mt-TiO_2 composites with Fe^{III} doping materials were manufactured and applied to the phenol degradation to better understand the role of clay and iron in such sorts of composites. Pollution and devastation of the environment on a worldwide scale is a major problem nowadays [31]–[33]. Toxic to humans, microbes, animals, plants, and ecosystems, refractory organics with aromatic structures are one of the most dangerous pollutants [34], [35]. Organic contaminants must be remedied as soon as possible. One aromatic ring and one hydroxyl group make up phenol. Phenolic chemicals are found all over the place and are harmful at low quantities [36]. More crucially, the adsorption or repulsion of Mt can be avoided if phenol is kept neutrally charged at pH 10 [37]. As a result, detecting photocatalytic degradation of materials in phenol can provide information about their photocatalytic ability in other organics.

The distribution of Fe^{III} on Mt/TiO_2 composites was regulated in this study by altering the timing of Fe^{III} addition to the composites. As a result, the involvement of Fe^{III} in the composites can be deduced based on its location. The entire synthesis process was carried out at pH 2 to prevent the formation of any iron oxides and/or iron hydroxides. The process for making Fe/Mt/TiO_2, in which Fe^{III} was adsorbed in the surface of the composites, and *x*Fe-Mt/(1-*x*) Fe-TiO_2, in which Fe^{III} was doped in the structure of the TiO_2 in the composites, has been detailed. These two Fe^{III}-doped Mt/TiO_2 composites were used to photocatalyzed phenol degradation. The composites were used to suggest a photocatalytic process for phenol degradation.

5.2 Materials and methods

5.2.1 Materials

Kunimine Industries Co. Ltd. purchased Na-Mt (Kunipia-F) having a cation exchange capacity (CEC) of 1.114 mmol/g (Bergaya and Vayer, 1997). (Tokyo, Japan). The chemical formula of Kunipia-F was calculated to be $(Na_{0.97}Ca_{0.08})^{+1.13}$ $(Si_{7.68}Al_{0.32})$ $(Al_{2.94}FeIII_{0.25}FeII_{0.03}Mg_{0.78})$ O_{20} $(OH)_4^{-1.13} \cdot nH_2O$, according to elemental analysis (method ME-ICP61, ALS Global Ltd., North Vancouver, Canada). Wako Pure Chemical Industries, Ltd. (Osaka, Japan) provided iron(III) nitrate ninehydrate ($Fe(NO_3)_3 9H_2O$, 99.0%), iron(III) chloride ($FeCl_3$, 95.0%), sodium hydroxide (NaOH, 97.0+%), hydrochloric acid (HCl, 1.17), and nitric acid (HNO_3, 1.38) for

the study. Kishida Chemical Co., Ltd. (Osaka, Japan) and Synergy UV (Merck, Darmstadt, Germany) provided Titanium(IV) chloride ($TiCl_4$, 99.0%) and Millipore water with pH 6.31, respectively.

5.2.2 Preparation of iron-modified Mt and clay/TiO_2 composites

Mt was added to an HNO_3 solution with a pH of 2 and vigorously agitated at room temperature for 1 hour (S/L = 10 g/L) to make protonated Mt (H-Mt). The H-Mt were then centrifuged, rinsed, collected, lyophilized, powdered, and sieved (149 m) separately. Ti $(OH)_4/TiO_2$ nanoparticles were produced in aqueous medium using the sol–gel process, and subsequently $TiCl_4$ and HCl were added to Milli-Q water. The resulting solution included 0.83 M $TiCl_4$ and 1.0 M HCl, and it was agitated for 1 hour before being allowed to rest for 6 hours. A nearly transparent, stable $Ti(OH)_4/TiO_2$ sol–gel was obtained through hydrolysis.

Because $Ti(OH)_4/TiO_2$ sol had an initial pH of around 0, the acidity was changed to pH = 2 by the addition of a NaOH solution before heterocoagulation. The Sol–gel was then added to a 1% H-Mt suspension (g clay/100 mL water). Meanwhile, Fe^{III} eqv. to 0.274 mmol/g Mt was applied only to *x*Fe-Mt/(1-*x*)Fe-TiO_2 samples. For 30 minutes, both types of samples were vigorously mixed. TiO_2 would have a theoretical concentration of 30% (m/m). The composites precipitated after 20 hours of sedimentation at 70°C, 80°C, and 90°C. Fe^{III} was added immediately after sedimentation to Fe/Mt/TiO_2 samples. All of the suspensions were agitated

for another 1 hour before being centrifuged for 30 minutes at 8300 rpm. The solid substance was washed with Milli-Q water before being freeze-dried for 24 hours, crushed, and sieved (149 μm). The inductively coupled plasma-optical emission spectroscopy was used to identify residual Fe^{III} in the supernatant (ICP-OES, Perkin Elmer 8500, Waltham, MA, USA). Because the synthesis temperature had negligible effect on the photocatalytic activity of the Fe/Mt/TiO_2 composites, the samples synthesized at 70 °C were the major focus for comparison (**Fig. 5.1**).

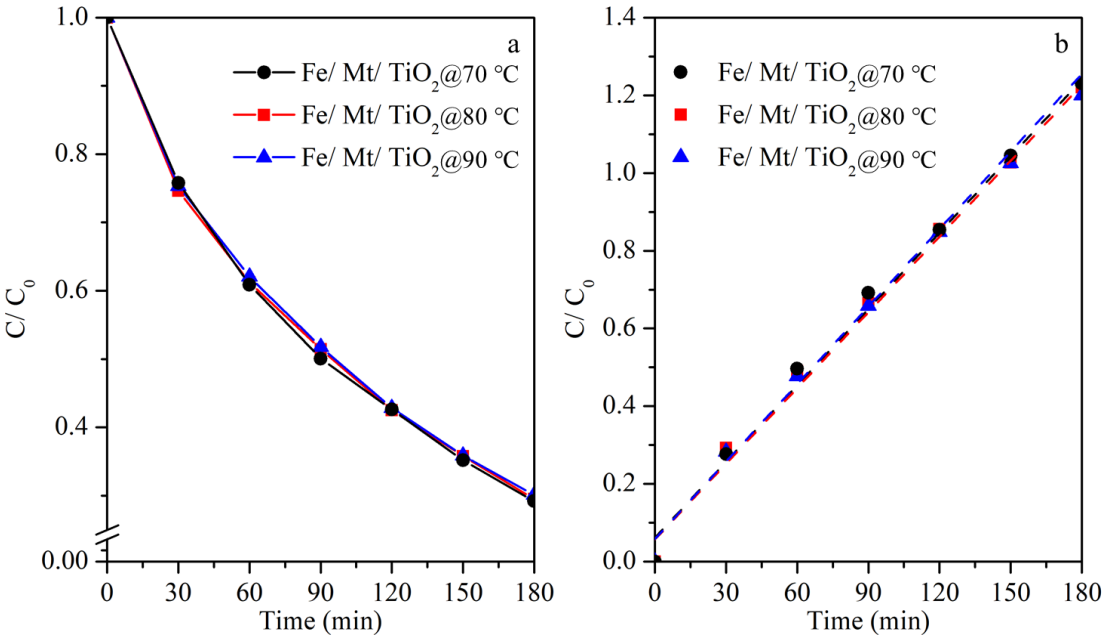

Fig. 5.1. Photocatalytic degradation and kinetics of phenol by Fe/Mt/TiO_2 synthesized at 70, 80 and 90 °C.

5.2.3 Solid characterization

X-ray fluorescence was used to examine the composites that resulted (XRF, Shimadzu-EDX800, Kyoto, Japan). Cu Kα radiation produced at 40 kV and 40 mA, a divergence slit of 1.0 mm, an anti-scatter slit of 10 mm, and a receiving slit of 0.15 mm over a 2 of 2.0–10°, with a step size of 0.02° and a scanning speed of 2°/min, were used to record powder X-ray diffraction (XRD) patterns of materials with an Ultima IV X-ray diffractometer (Rigaku, Akishima, Japan). X-ray photoelectron spectroscopy (XPS) was performed using a monochromatic Al Kα X-ray source at 200 W on an ESCA 5800 system (Ulvac-PHI, Kanagawa, Japan). A survey scan was performed with a passing energy of 187.85 eV from 0 to 1000 eV, as well as narrow scans of N 1 s and C 1 s orbitals with passing values of 23.5 and 58.7 eV. Following the elimination of a Shirley baseline, peak separation was conducted using Casa XPS software (Version 2.3.16 PR 1.6). E_B [C 1s] = 284.6 eV was used to calibrate peak binding energies (EB). FlexSEM 1000II and AZteclive light FX scanning electron microscopes (SEM-EDX) were used (Hitachi, Tokyo, Japan). We used the Aztec application from AZteclive light FX to process the EDX results, which included baseline correction. A JEM-2100HCKM, JEOL transmission electron microscope (TEM) and EDX were used (Akishima, Japan). On a UV-2450 spectrophotometer (Shimadza, Tokyo, Japan) with a diffuse reflectance attachment and $BaSO_4$ as a reference, diffuse reflectance spectroscopy (DRS) was performed with a range of 200–800 nm. A JASCO F-6600 spectrofluorometer (Jasco, Tokyo, Japan) was used to

perform solid-state photoluminescence spectroscopy (PL). The 1280c AMETEK advanced measuring technology (Berkshire, United Kingdom) was used to investigate electrochemical features of composites, such as photocurrent response and electrochemical impedance spectroscopy (EIS). Later, 200 mg of Fe/Mt/TiO_2 and *x*Fe-Mt/(1-*x*)Fe-TiO_2 composites were placed in a periodic acid–Schiff (PAS) cell with an electret condenser microphone and a quartz window on top for a minimum of 30 minutes under N_2 flow saturated with methanol vapor. A light beam in the range of 650 nm–350 nm was emitted through the cell window from a Xe lamp with a grating monochromator modulated at 80 Hz using a light chopper to detect the PAS signal using a digital lock-in amplifier. Calculating the amount of light absorbance change for the collected electrons yielded the energy-resolved distribution of electron traps (ERDT).

5.2.4 Photocatalytic activity test

Under the irradiation of a 300 W xenon lamp, the photocatalytic activity of produced compounds was evaluated for phenol degradation. In a photoreactor with a cooling water jacket outside, 20 mg of photocatalyst were suspended in 100 mL of 10 mg/L phenol aqueous solution prior to irradiation. To reach an adsorption–desorption equilibrium, the suspensions were agitated for 5 minutes at 500 rpm in the dark. Approximately 1 mL of solution was collected from the reaction cell at regular intervals during the irradiation procedure, and the photocatalyst

was removed using a 0.45-m cellulose acetate membrane filter. After that, high-performance liquid chromatography (HPLC) [38] was used to evaluate the solutions. By measuring the absorption of these compounds at a wavelength of 270 nm, the quantities of phenol and its breakdown products were calculated. Scavenger tests and reusability tests were conducted according to the techniques outlined above. Before the photocatalytic materials were introduced, 50 mmol of ethanol, isopropanol, and para-benzoquinone were added.

5.3 Results and discussion

5.3.1 Characterizations

ICP-OES was used to detect the residual Fe^{III} after filtration of the produced Fe/Mt/TiO_2 and *x*Fe-Mt/(1-*x*)Fe-TiO_2. Because the Fe^{III} concentration was below the ICP's detection limit, practically all of the added Fe^{III} was doped in the composites. As a result, the amount of Fe^{III} doped in each composite was the same, and this should not be a determining factor in the photocatalytic properties of the samples.

The wt. % of TiO_2 phase in the entire composite was calculated using XRF (**Table 5.1**). When comparing Fe/Mt/TiO_2 to *x*Fe-Mt/(1-*x*)Fe-TiO_2, Fe/Mt/TiO_2 kept slightly more TiO_2 than *x*Fe-Mt/(1-*x*)Fe-TiO_2, but the difference was not significant. When the product was synthesized at 80 °C, the maximum TiO_2 content was obtained. In prior research [39–41], the best temperature

for the maximum TiO_2 production was found to be 70 °C when compared to clay/TiO_2 composites synthesis without Fe^{III}. For the maximum TiO_2 yield, the inclusion of Fe^{III} in composites necessitated a higher synthetic temperature.

Table 5.1. Elemental composition of Fe/Mt/TiO_2 and *x*Fe-Mt/(1-*x*)Fe-TiO_2 with different synthesis temperatures (70 °C, 80 °C, and 90 °C) in wt%.

T (°C)	Sample	Na (%)	Mg (%)	Al (%)	Si (%)	Ca (%)	Ti (%)	Fe (%)	TiO_2 (%)
90	Fe/Mt/TiO_2	N.D.	1.84	11.78	31.08	0.05	50.07	5.19	27.63
	*x*Fe-Mt/(1-*x*)Fe-TiO_2	N.D.	1.97	12.28	32.28	0.05	47.49	5.92	26.74
80	Fe/Mt/TiO_2	N.D.	1.86	11.65	30.74	0.04	49.62	6.10	27.65
	*x*Fe-Mt/(1-*x*)Fe-TiO_2	N.D.	1.86	11.80	30.54	0.07	48.80	6.94	27.50
70	Fe/Mt/TiO_2	N.D.	1.88	12.29	32.29	0.03	48.23	5.28	26.91
	*x*Fe-Mt/(1-*x*)Fe-TiO_2	N.D.	1.88	12.04	32.14	0.08	47.19	6.66	26.77

The original Mt, Fe^{III} cation-doped Mt (Fe-Mt) synthesized at ambient temperature, TiO_2, Fe/Mt/TiO_2, and *x*Fe-Mt/(1-*x*)Fe-TiO_2 synthesized at 70 °C XRD patterns were investigated, and the XRD pattern of these samples was displayed in **Fig. 5.2**. Mt's 001 peaks comprised the interlayer distance and one layer thickness (0.96 nm) [42]. When compared to the original Mt (0.25 nm), the interlayer distances in Fe-Mt, Fe/Mt/TiO_2, and *x*Fe-Mt/(1-*x*)Fe-TiO_2 were practically the same (0.42/0.43 nm), implying that only Fe^{III} ion exchange with the interlayer cations in Mt occurred during composite synthesis. Furthermore, TiO_2 should only be

distributed on Mt surface. Fe^{III} has hydrated ionic diameters of 0.45 nm [42]. The Van der Waals force may disperse the lower interlayer distances of the Mt in the composites, rather than the ionic sizes, among the aluminosilicate layers extruding from the hydrated shell of Fe^{III}, which are poorly formed [42].

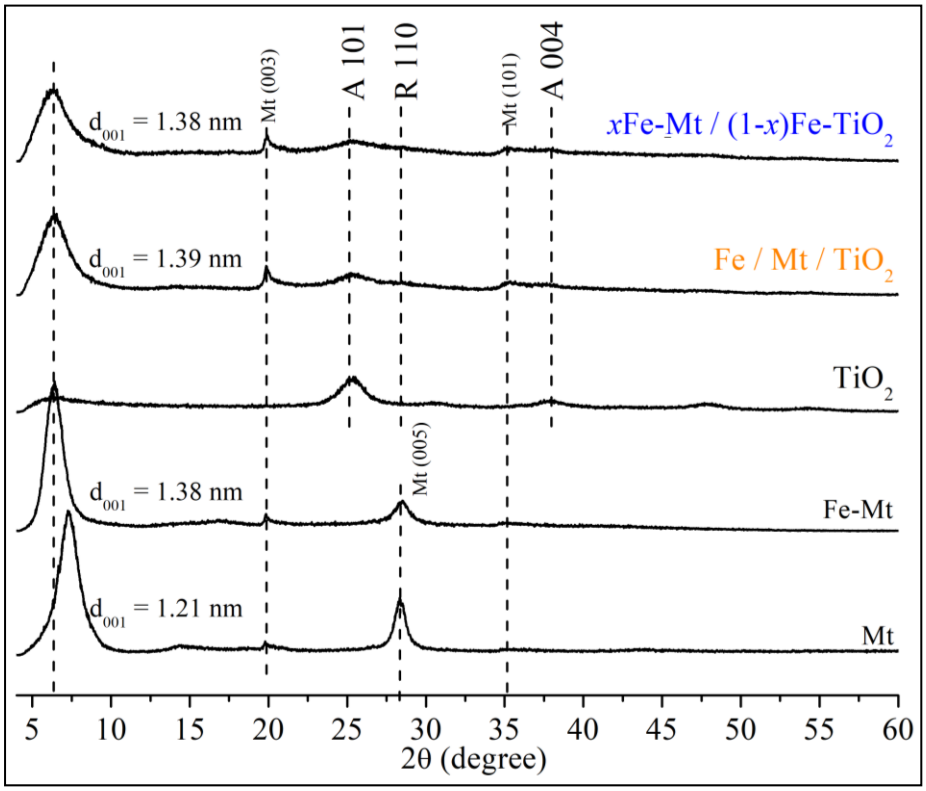

Fig. 5.2. XRD patterns of original Mt, Fe-Mt synthesized at RT, TiO_2, Fe/Mt/TiO_2, and *x*Fe-Mt/(1-*x*)Fe-TiO_2 synthesized at 70 °C.

For the pristine TiO_2, only a single anatase phase was seen. The 101 and 004 anatase phase peaks at 25.4 and 37.9° (JCPDS No. 21–1272) were observed for both Fe/Mt/TiO_2 and *x*Fe-Mt/(1-*x*)Fe-TiO_2. At 28.3°, the 110 peak of rutile was also produced. Mt reflection peaks 001, 003, and 101 in the composites were found at 6.0–6.5, 19.8, and 35.2 degrees, respectively [43].

Different synthetic temperatures clarified the development of TiO_2 in the composites, and their XRD patterns are shown in **Fig. 5.3**.

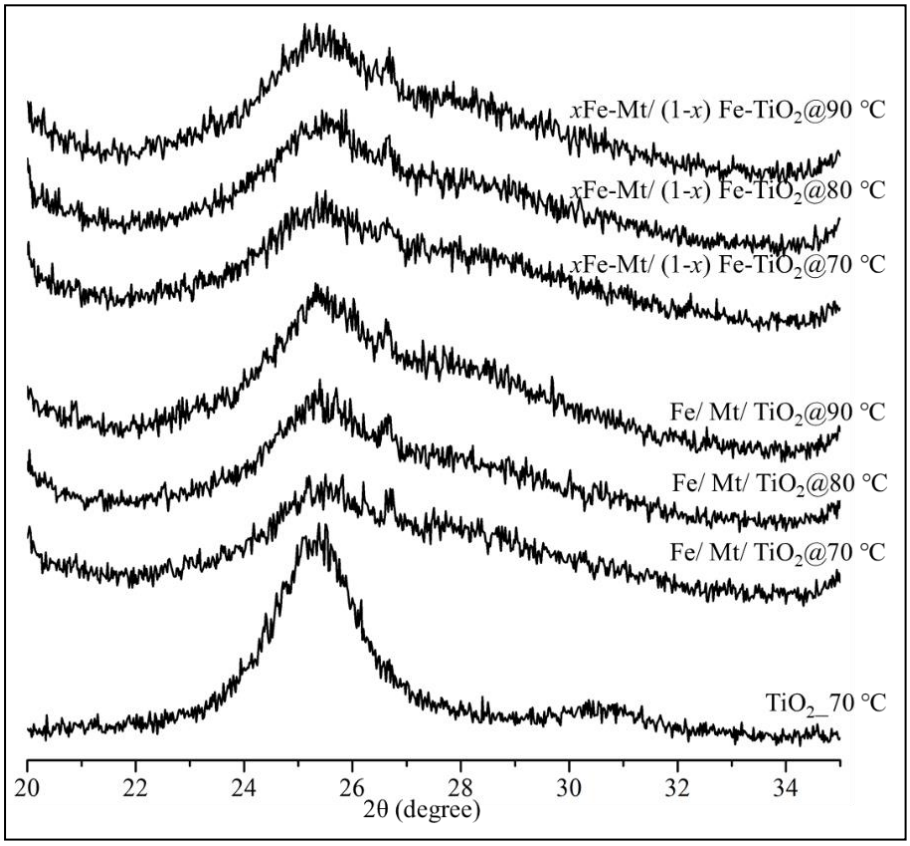

Fig. 5.3. XRD patterns of TiO_2, Fe/Mt/TiO_2 and *x*Fe-Mt/(1-*x*)Fe-TiO_2 synthesized at 70 ℃, 80 ℃ and 90 ℃.

In **Fig. 5.4**, peak separation was used to examine the XRD patterns in greater depth. The 110 diffraction of rutile at 28.2–28.4° and the normal 101 diffraction of anatase at 25.4° were well suited. **Table 5.2** contains the parameters following peak fitting. The broad peaks of all the samples, as well as the large full width at half maximum (FWHM) values for anatase and rutile, showed a low crystallinity of the TiO_2 phase on the Mt layers. At three synthesized temperatures, the TiO_2 concentration of *x*Fe-Mt/(1-*x*)Fe-TiO_2 was higher than Fe/Mt/TiO_2, and the Fe^{III} in TiO_2 can improve the crystallization of the anatase phase. From 80 to 90 °C,

increasing the temperature improves anatase crystallization in Fe/Mt/TiO_2, but decreases it in *x*Fe-Mt/(1-*x*)Fe-TiO_2. Only the location of Fe^{III} can govern the formation of TiO_2 phases on the aluminosilicate layers of Mt, as shown by ICP-OES analysis. To compare with earlier investigations, Fe/Mt/TiO_2 and *x*Fe-Mt/(1-*x*)Fe-TiO_2 synthesized at 70 °C were used for the following characterizations.

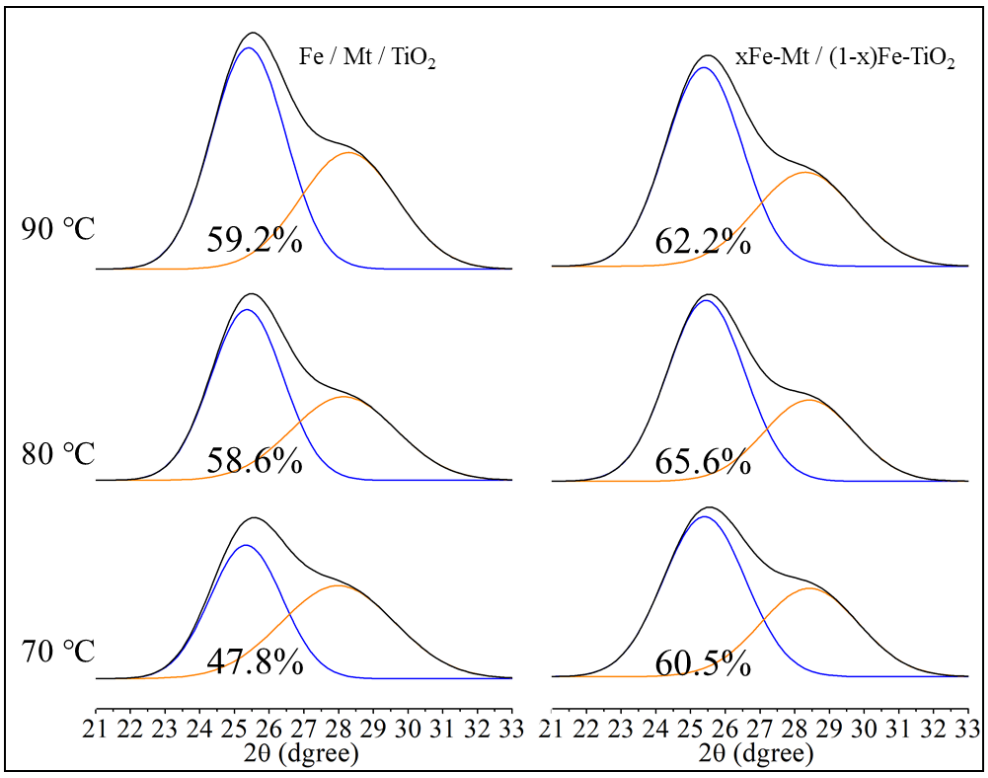

Fig. 5.4. Peak fitting of the XRD patterns (20–35° in 2θ) of Fe/Mt/TiO_2 and *x*Fe-Mt/(1-*x*)Fe-TiO_2 with different synthesis temperatures (70, 80, and 90 °C). Peaks in blue were from anatase and peaks in yellow were from rutile.

Table .5.2. Parameters of XRD peak fitting of Fe/Mt/TiO_2 and *x*Fe-Mt/(1-*x*)Fe-TiO_2.

T (°C)	Parameters	Fe/Mt/TiO_2		*x*Fe-Mt/(1-*x*)Fe-TiO_2	
		Anatase	Rutile	Anatase	Rutile
90	Centroid (º)	25.4	28.3	25.4	28.3
	Intensity	227.3	119.7	204.1	96.5
	FWHM	2.5	3.3	2.6	3.4
	Area IntgP (%)	59.2	40.8	62.2	37.8
80	Centroid (º)	25.4	28.1	25.4	28.4
	Intensity	175.3	85.8	185.7	83.4
	FWHM	2.5	3.5	2.6	3.1
	Area IntgP (%)	58.6	41.4	65.6	34.4
70	Centroid (º)	25.3	28.0	25.4	28.4
	Intensity	137.1	95.5	164.4	90.7
	FWHM	2.5	3.8	2.8	3.3
	Area IntgP (%)	47.8	52.2	60.5	39.5

SEM observation was used to analyze the morphology of TiO_2, Fe/Mt/TiO_2, and *x*Fe-Mt/(1-*x*)Fe-TiO_2 composites in μm scale (**Fig. 5.5**). In the Fe/Mt/TiO_2 and *x*Fe-Mt/(1-*x*)Fe-TiO_2 composites, the TiO_2 particle sizes in the Mt layer were greatly reduced; furthermore, the Mt stacking layers in Fe/Mt/TiO_2 and *x*Fe-Mt/(1-*x*)Fe-TiO_2 were even smaller than in pure TiO_2. The TiO_2 nanoparticles densely coated the surface of the Mt particles in both the Fe/Mt/TiO_2 (**Fig. 5.5d–i**) and *x*Fe-Mt/(1-*x*)Fe-TiO_2 (**Fig. 5.5j–o**). TEM-EDX was used to examine the TiO_2 coating of the Mt layers in Fe/Mt/TiO_2 at the nanoscale scale, as shown in **Fig. 5.6**. In the Ti-empty/-lacking zones, the Al distribution was more intense, indicating that TiO_2 particles in the Mt layers were overlapping. The occlusion of TiO_2 is to blame for the low-intensity distribution of Al in the Ti-concentrated region. The rather homogenous distribution of Fe^{III} on all of the Mt phase, TiO_2 phase, and the interface between the Mt and TiO_2 phases was suggested by the even distribution of Fe.

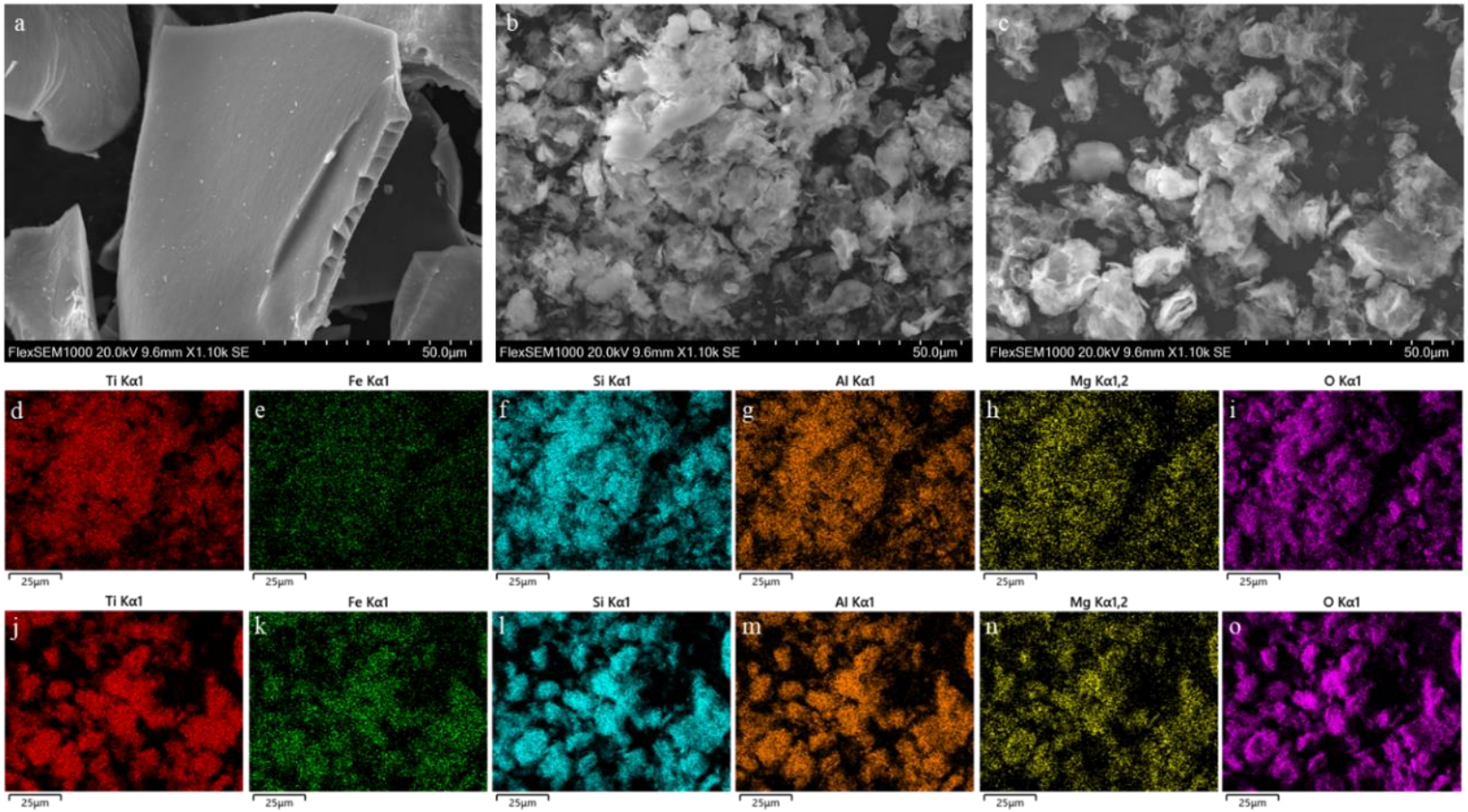

Fig. 5.5. SEM images of: (**a**) TiO_2; (**b**) Fe/Mt/TiO_2; and (**c**) *x*Fe-Mt/(1-*x*)Fe-TiO_2. SEM-EDX Kα maps of: (**d**) titanium; (**e**) iron; (**f**) silica; (**g**) aluminum; (**h**) magnesium; and (**i**) oxygen for Fe/Mt/TiO_2. SEM-EDX Kα maps of: (**j**) titanium; (**k**) iron; (**l**) silica; (**m**) aluminum; (**n**) magnesium; and (**o**) oxygen for *x*Fe-Mt/(1-*x*)Fe-TiO_2. Scale bars were adjusted to be the same and indicate 50.00 µm.

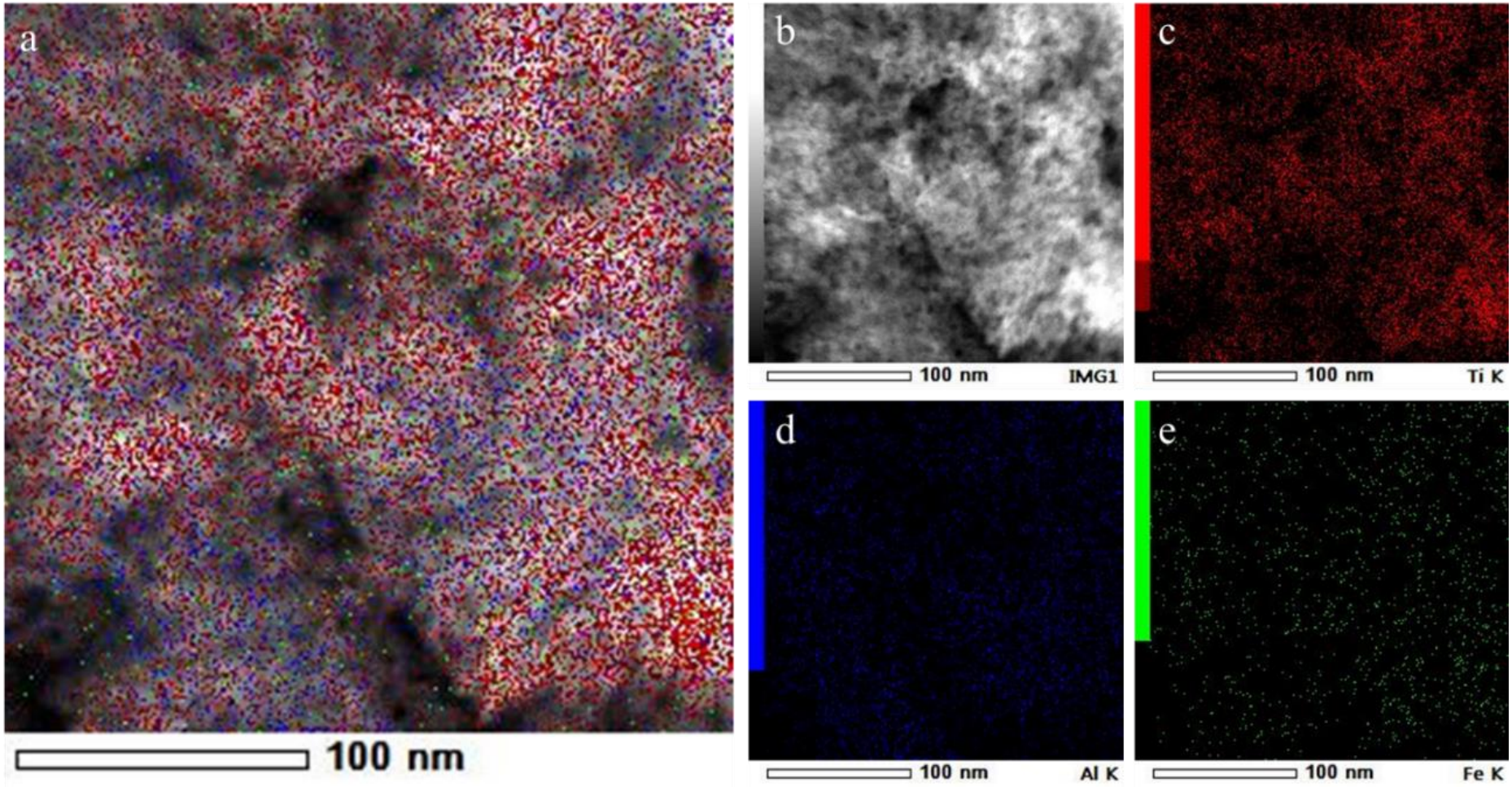

Fig. 5.6. Images of: (**a**) TEM-EDX, (**b**) TEM images, and Kα maps of: (**c**) titanium; (**d**) aluminum; and (**e**) iron for Fe/Mt/TiO_2.

XPS was used to study the electronic level and chemical composition of Fe/Mt/TiO_2 and *x*Fe-Mt/(1-*x*)Fe-TiO_2, as shown in **Figures 5.7** and **5.8**. The main peaks assigned to the Ti 2p orbitals were raised from TiO_2, while the dominant peaks attributed to the O 1s, Si 2p, and Al 2p orbitals were raised from Mt in the wide-scan spectra for Fe/Mt/TiO_2 and *x*Fe-Mt/(1-*x*)Fe-TiO_2 (**Fig. 5.7a** and **5.8a**). **In Fig. 5.7b** and **5.8b**, the deconvolution peaks from the Ti 2p orbitals represented two peaks for Fe/Mt/TiO_2 and *x*Fe-Mt/(1-*x*)Fe-TiO_2. The Ti^{IV} $2p_{1/2}$ and $2p_{3/2}$ orbitals were attributed to the peaks at 464.3–464.4 and 458.7 eV [44]. The Fe 2p deconvoluted spectra (**Fig. 5.7c** and **5.8c**) for both composites revealed two peaks at 723.9–725.5 and 713.2–713.4 eV, which are ascribed to Fe^{III} $2p_{1/2}$ and $2p_{3/2}$, respectively [45]. Peaks at 533.0–534.3, 531.7–531.9, and 530.1–531.0 eV in the O 1s region of Fe/Mt/TiO_2 and *x*Fe-Mt/(1-*x*)Fe-TiO_2 (**Fig. 5.7d** and **5.8d**) originate from absorbed H_2O on the surface, hydroxide bonds, and oxide bonds, respectively [47–49]. **Fig. 5.7e** and **5.8e** indicate that the peak raised at 102.5 in both composites is assigned to tetrahedral Si—O [49]. By drawing the straight tangent line to the VB spectra of the Fe/Mt/TiO_2 and *x*Fe-Mt/(1-*x*)Fe-TiO_2 samples in **Fig. 5.7f** and **5.8f** [50], [51], the valence band (VB) on top of the Fe/Mt/TiO_2 and *x*Fe-Mt/(1-*x*)Fe-TiO_2 samples was determined, and the values are 1.72 and 1.95 eV.

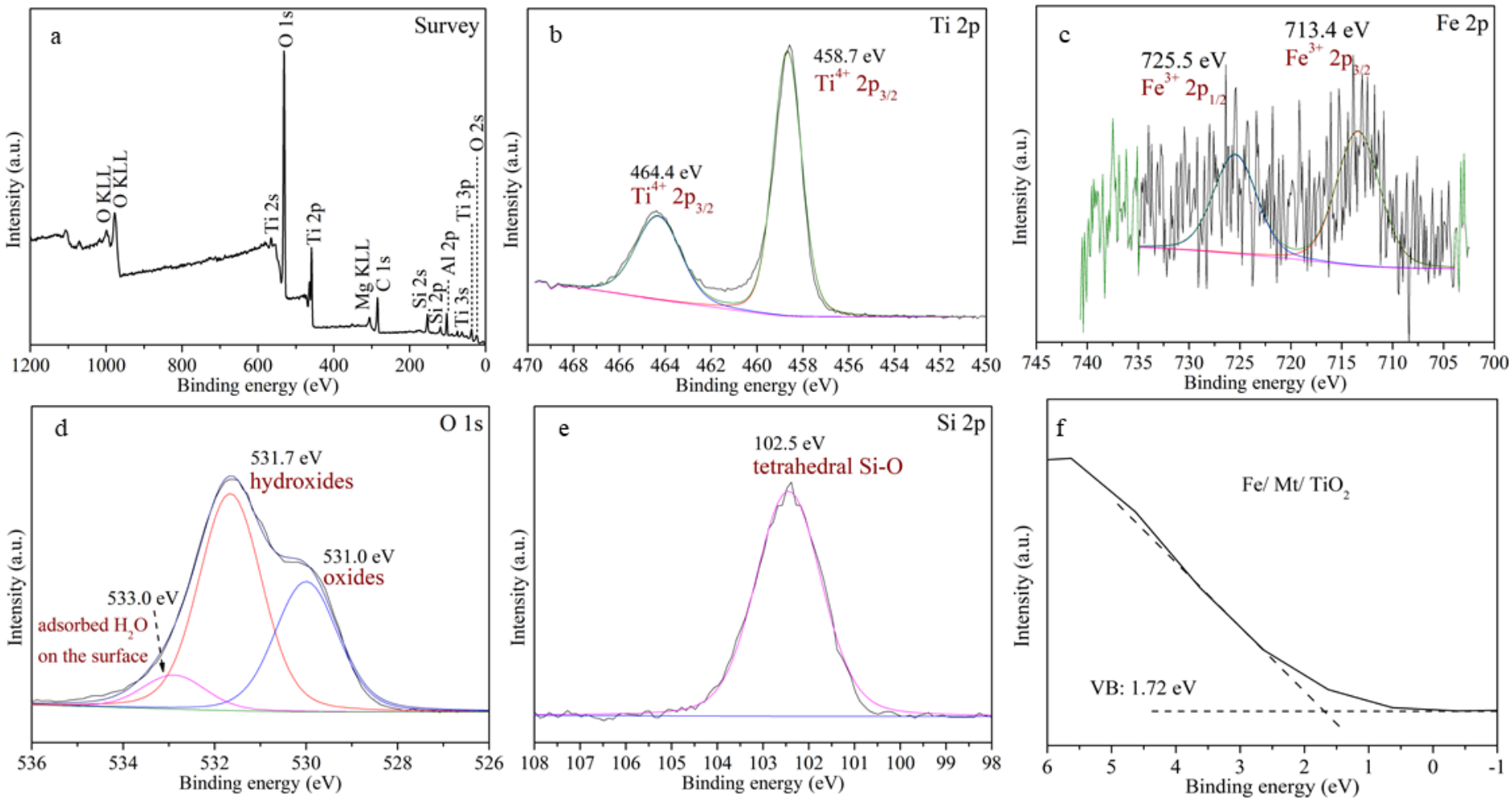

Fig. 5.7. XPS (a) survey, narrow scans of (b) Ti 2p, (c) Fe 2p, (d) O 1s, and (e) Si 2p orbitals and (f) VB XPS for Fe/Mt/TiO_2.

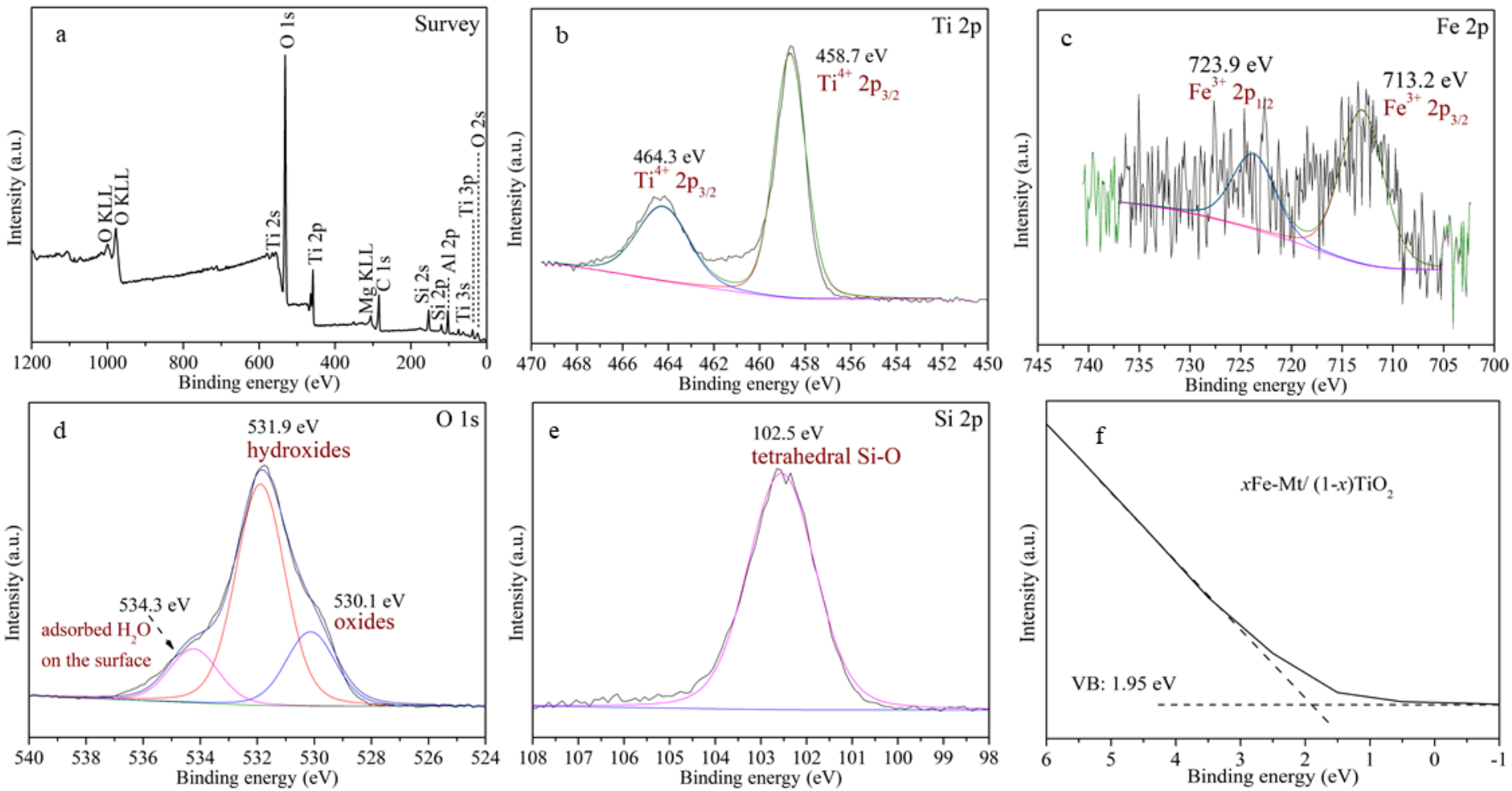

Fig. 5.8. XPS (a) survey, narrow scans of (b) Ti 2p, (c) Fe 2p, (d) O 1s, and (e) Si 2p orbitals and (f) VB XPS for *x*Fe-Mt/(1-*x*)Fe-TiO$_2$.

5.3.2 Investigation of optical and charge separation properties

The UV-DRS spectra of TiO_2, Fe/Mt/TiO_2, and *x*Fe-Mt/(1-*x*)Fe-TiO_2 (**Fig. 5.9a**) revealed that both composites displayed increased absorbance in the visible light range compared to TiO_2. The *x*Fe-Mt/(1-*x*)Fe-TiO_2 showed a modest red shift in the absorption edge when compared to Fe/Mt/TiO_2, and such an expansion in the absorption band considerably altered the optical characteristics of samples. The optical bandgap energy (*Eg*) of Fe-Mt can be calculated using the Tauc graphing Kubelka–Munk function versus energy, as shown in **Fig. 5.9b** [54–56]:

$$\alpha hv = k(hv - Eg)^{n/2} \quad (5.1)$$

where the absorption coefficient, Planck constant, light frequency, proportionality constant, and bandgap energy are denoted by α, *h*, υ, *k*, and *Eg*, respectively. The n = 1 for direct transitions and n = 4 for indirect transitions [55]. The predicted *Eg* of samples for TiO_2, Fe/Mt/TiO_2, and *x*Fe-Mt/(1-*x*)Fe-TiO_2 were ~3.24, 3.24, and 3.19 eV, respectively (**Fig. 5.9b**). The reduced *Eg* of *x*Fe-Mt/(1-*x*)Fe-TiO_2 was attributed to the Fe^{III} doping in TiO_2 [58, 59].

PL was used to determine the recombination rate of e^--h^+ pairs (**Fig. 5.10**). The increased PL intensity of TiO_2 compared to the other two composites revealed that the composite's improved charge separation efficiency was primarily attributable to Mt effects. In compared to Fe/Mt/TiO_2, *x*Fe-Mt/(1-*x*)Fe-TiO_2 had a lower luminous intensity, which could be because the doped Fe^{III} in the TiO_2 structure generated the middle-gap state to prevent the e^--h^+ pairs from recombination in the TiO_2. The transfer and generation of electrons in TiO_2, Fe/Mt/TiO_2, and *x*Fe-Mt/(1-*x*)Fe-TiO_2 were also examined using transient photocurrent response measurements and EIS to associate with photocatalytic phenol degradation activity. The photocurrent density was rated Fe/Mt/TiO_2 > *x*Fe-Mt/(1-*x*)Fe-TiO_2 > TiO_2 as shown in **Fig. 5.11a**. In addition, as shown in **Fig. 5.11b**, the EIS spectra of TiO_2, Fe/Mt/TiO_2, and *x*Fe-Mt/(1-*x*)Fe-TiO_2 were measured. The Fe/Mt/TiO_2 had a reduced radius of the EIS Nyquist diagram, implying a lower charge transfer resistance to improve photocatalytic activity.

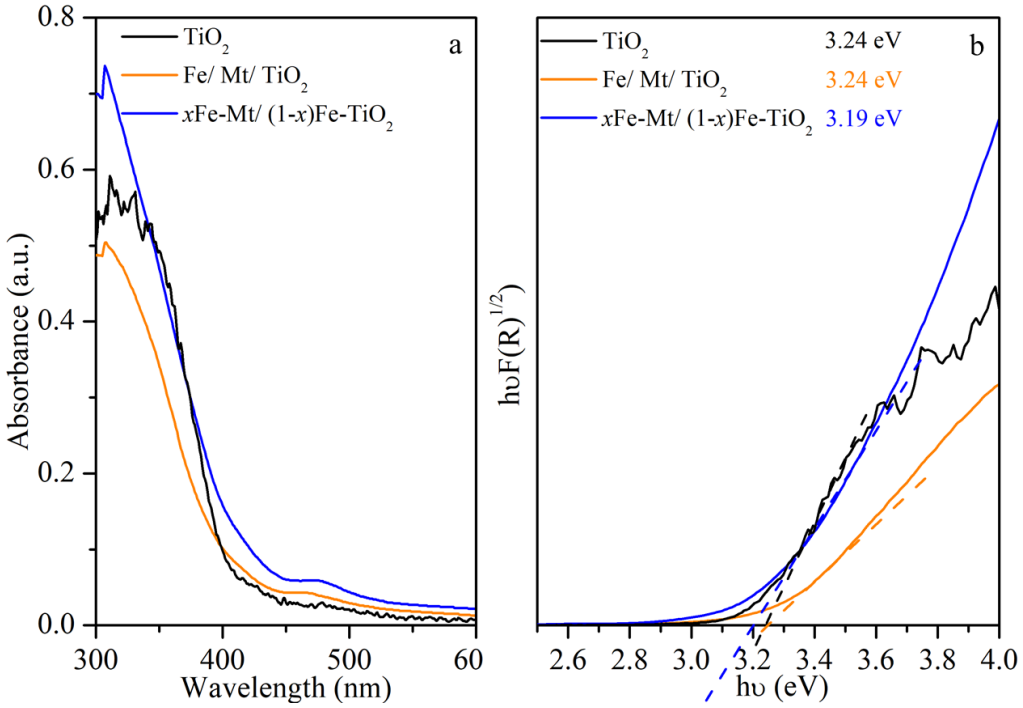

Fig. 5.9. (**a**) DRS-UV spectra; (**b**) corresponding Tauc plots of Fe/Mt/TiO_2 and *x*Fe-Mt/(1-*x*)Fe-TiO_2 synthesized at 70 °C

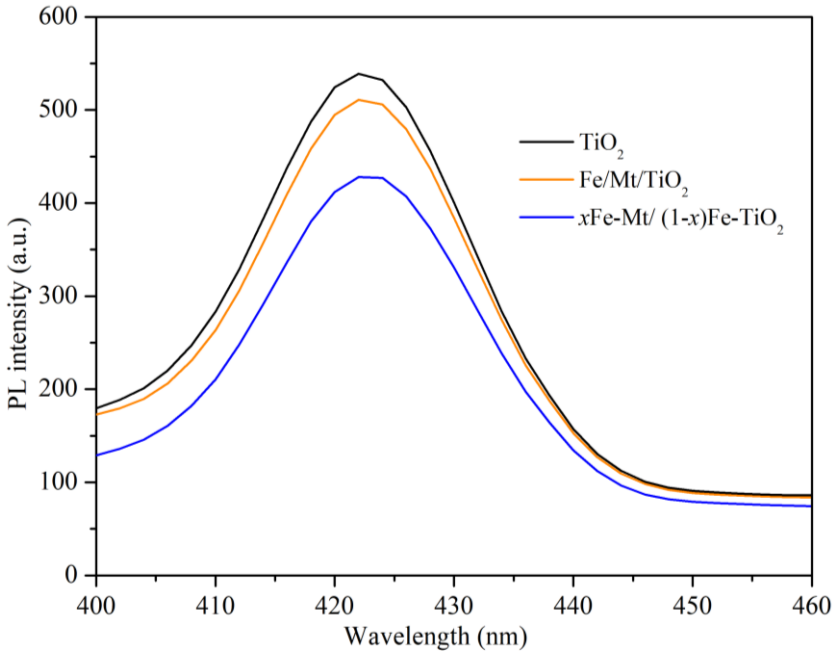

Fig. 5.10. Photoluminescence of Fe/Mt/TiO_2 and *x*Fe-Mt/(1-*x*)Fe-TiO_2 at 70 °C.

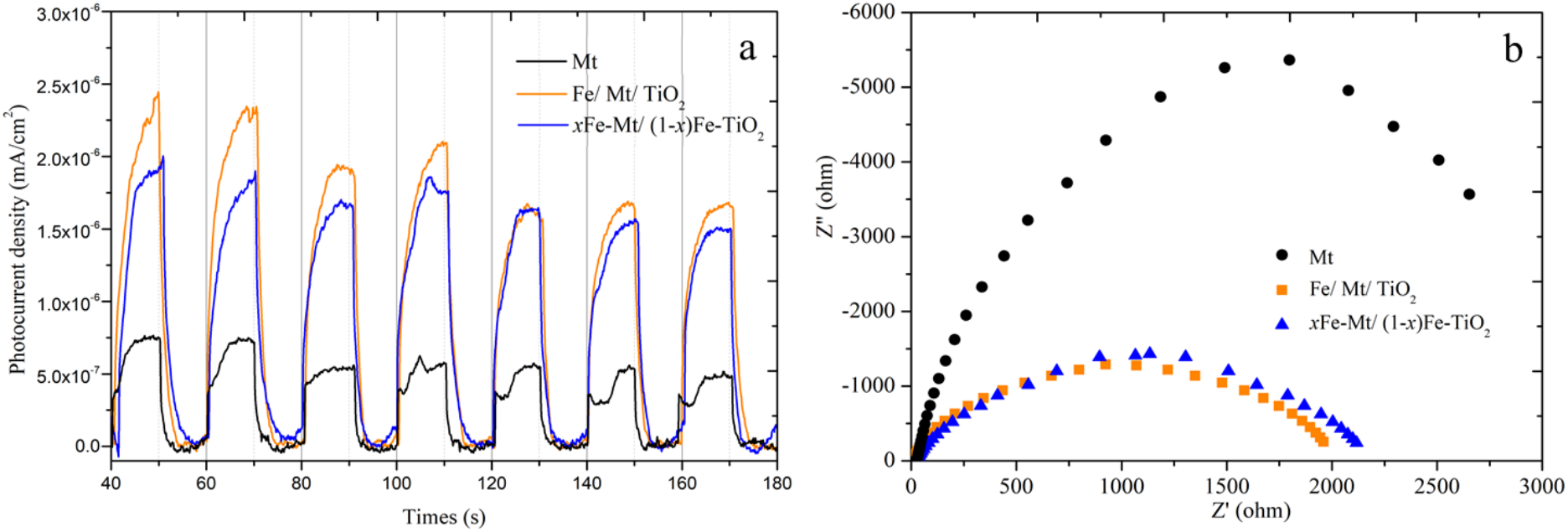

Fig. 5.11. (**a**) Photocurrent density versus time measurements of Mt, Fe/Mt/TiO_2, and *x*Fe-Mt/(1-*x*)Fe-TiO_2 synthesized at 70 °C under 0 V versus Ag/AgCl bias; (**b**) Nyquist plots of the EIS spectra of Mt, Fe/Mt/TiO_2, and *x*Fe-Mt/(1-*x*)Fe-TiO_2 synthesized at 70 °C.

5.3.3 Photocatalytic activity

Fig. 5.12a shows the photocatalytic removal of phenol using TiO_2, Fe/Mt/TiO_2, and *x*Fe-Mt/(1-*x*)Fe-TiO_2 as a function of reaction time. All of the samples showed a little amount of phenol adsorption in the dark. Adsorption, on the other hand, reached equilibrium within the first 5 minutes and happened mostly on the surface of the samples by physical adsorption. In comparison, the Fe/Mt/TiO_2 photocatalytic performance on phenol degradation for 3 hours was 94.6%. The photocatalytic activity of the composite can be improved by adsorption Fe^{III} on the surface or the Mt interlayer. The photocatalytic reduction kinetics of phenol (eq. 5.2) agree well with pseudo-first-order kinetics (**Fig. 5.12b**) [58]:

$$-\ln\left(C/C_0\right) = kt \tag{5.2}$$

where C and C_0 (mmol/g) are the residual and initial phenol concentrations, respectively, and parameter k (min^{-1}) is the pseudo-first-order model's rate constant. **Table 5.3** lists the parameters for the pseudo-first-order. For all three samples, the correlation coefficient (R^2) for the pseudo-first-order is greater than 0.980, and the chi-square is -4 orders of magnitude. As a result, the pseudo-first-order model can be used to forecast kinetics. For TiO_2, Fe/Mt/TiO_2, and *x*Fe-Mt/(1-*x*)Fe-TiO_2, the rate constants are 0.015, 0.022, and 0.037 min^{-1}, respectively. Fe/Mt/TiO_2 and *x*Fe-Mt/(1-*x*)Fe-TiO_2 were shown to be extremely efficient. Most importantly, the *x*Fe-Mt/(1-*x*)Fe-TiO_2 exhibited a greater capacity than the Fe/Mt/TiO_2, which is in line with the photocurrent but contradicts the DRS and PL results.

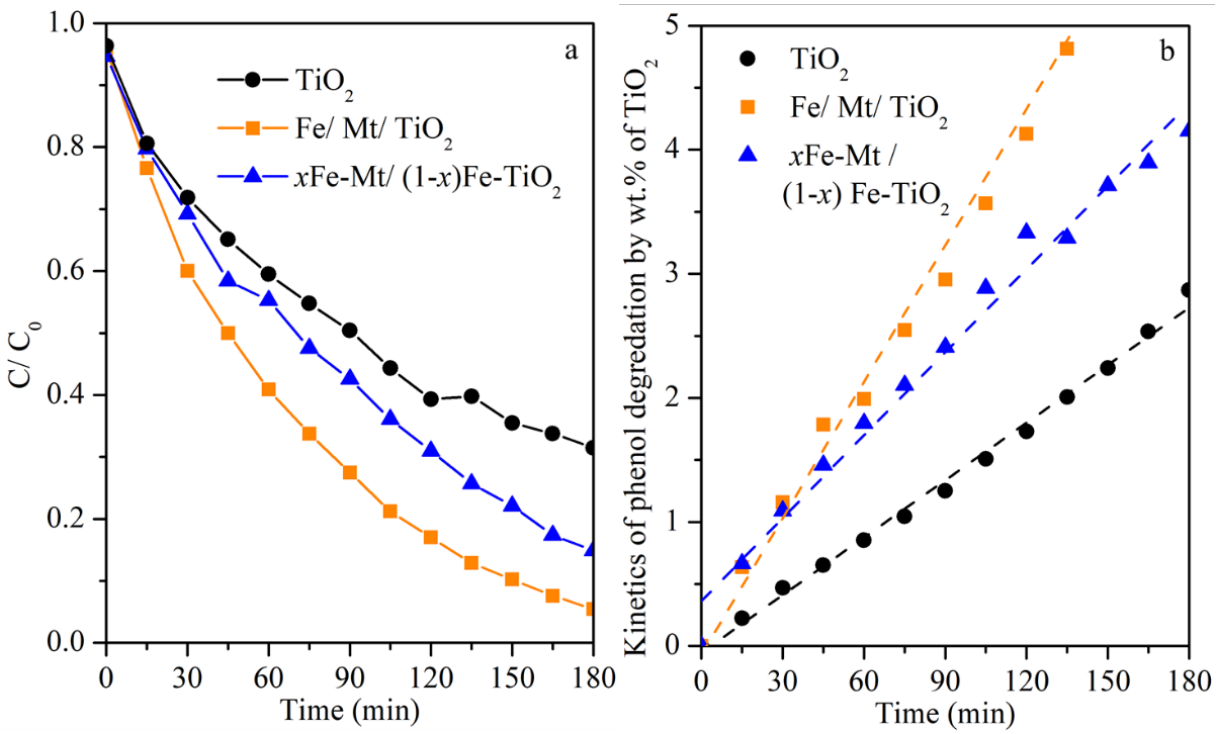

Fig. 5.12. (**a**) Photocatalytic degradation and (**b**) kinetics of phenol by TiO_2, Fe/Mt/TiO_2 and *x*Fe-Mt/(1-*x*)Fe-TiO_2 composites synthesized at 70 °C.

Table 5.3. Parameters of pseudo-first-order kinetics for the photocatalytic degradation of phenol on TiO_2, Fe/Mt/TiO_2 and *x*Fe-Mt/(1-*x*)Fe-TiO_2.

Samples	k_1 (min^{-1})	R^2	χ^2
TiO_2	0.015	0.991	$9.923 \cdot 10^{-4}$
Fe/Mt/TiO_2	0.022	0.981	$8.894 \cdot 10^{-4}$
*x*Fe-Mt/(1-*x*)Fe-TiO_2	0.037	0.994	$3.395 \cdot 10^{-4}$

The chemical stability of the Fe/Mt/TiO_2, which had the superior photocatalytic performance during the photocatalytic oxidation of phenol, was investigated using the reusability test (**Fig. 5.13**). For three cycles, high photocatalytic degradation of phenol in Fe/Mt/TiO_2 was maintained at over 93.1%. The mass loss of the samples during washing should account for the small decline in photocatalytic performance after the first cycle.

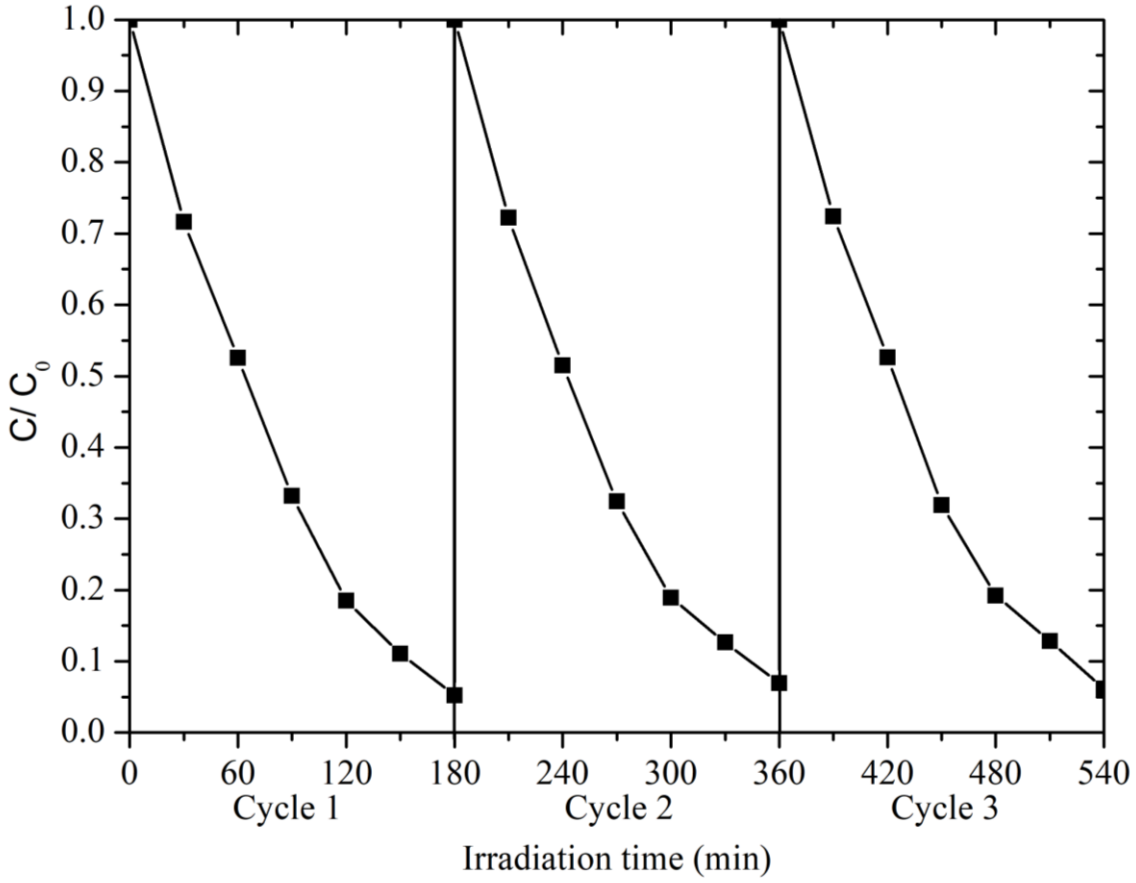

Fig. 5.13. Reusability test of Fe/Mt/TiO_2 synthesized at 70 °C for phenol degradation.

5.3.4 ERDT patterns of TiO_2, Fe/Mt/TiO_2, and *x*Fe-Mt/(1-*x*)Fe-TiO_2

The surface electrical characteristics of Fe-Mt, TiO_2, Fe/Mt/TiO_2, and *x*Fe-Mt/(1-*x*)Fe-TiO_2 were investigated using reversed double-beam photoacoustic spectroscopy (RDB-PAS). The surface photocatalytic characteristics of the measured samples might be inferred from the

acquired ERDT [59]. The ERDT patterns for Fe-Mt, TiO_2, Fe/Mt/TiO_2, and *x*Fe-Mt/(1-*x*)Fe-TiO_2 are shown in **Fig. 5.14**, with the values listed in **Table 5.4**. Because Fe^{III} formed a Fermi level as an electron donor, which is a p-type feature of semiconductor, Fe-Mt had no electron trap (ETs) on ERDT. For the TiO_2, Fe/Mt/TiO_2, and *x*Fe-Mt/(1-*x*)Fe-TiO_2, the energy-reversed distribution of electron traps appeared at energy ranges of 2.20–4.00 eV. This indicated that the composites' surfaces were covered in TiO_2 phases. Peak separation was used to fit the electron trapping patterns of TiO_2. Crystal rutile, amorphous rutile, and amorphous rutile coated with crystal anatase were assigned to three peaks at 2.96, 3.22, and 3.44 eV, respectively. The amorphous phase's dominance was compatible with the TiO_2's low crystallinity, as shown by XRD data (**Fig. 5.4** and **Table 5.2**). The Fe/Mt/TiO_2 and *x*Fe-Mt/(1-*x*)Fe-TiO_2 ERDT patterns were also isolated. The amorphous rutile covered in crystal anatase, which also appeared in the TiO_2 pattern, has a peak at 3.44 eV. For photocatalytic reactions, crystal TiO_2 should be the major fraction, and the amorphous phase may develop photocatalytic activity due to the presence of crystal phase in TiO_2 [62–64]. Amorphous TiO_2 covered the crystal anatase in both composites. Photocatalytic activity should be limited to amorphous TiO_2 in direct contact with the crystal phase. The intensity of this type of rutile peak in Fe/Mt/TiO_2 (85.4%) was twice as high as in *x*Fe-Mt/(1-*x*)Fe-TiO_2 (43.5%). As a result of this finding, the *x*Fe-Mt/(1-*x*)Fe-TiO_2 had lower photocatalytic activity for phenol degradation than the Fe/Mt/TiO_2. Both the 3.62 and 3.76 eV electron accumulation peaks were attributed to isolated amorphous TiO_2 that will not come into contact with the TiO_2 crystal phase. The photocatalytic activity of this TiO_2 on the composite was expected to be insignificant. Furthermore, the total intensity of the isolated TiO_2 phase on the *x*Fe-Mt/(1-*x*)Fe-TiO_2 was substantially higher than on the Fe/Mt/TiO_2, suggesting that it may overlap with the photocatalytically active amorphous rutile, reducing charge generation and transfer.

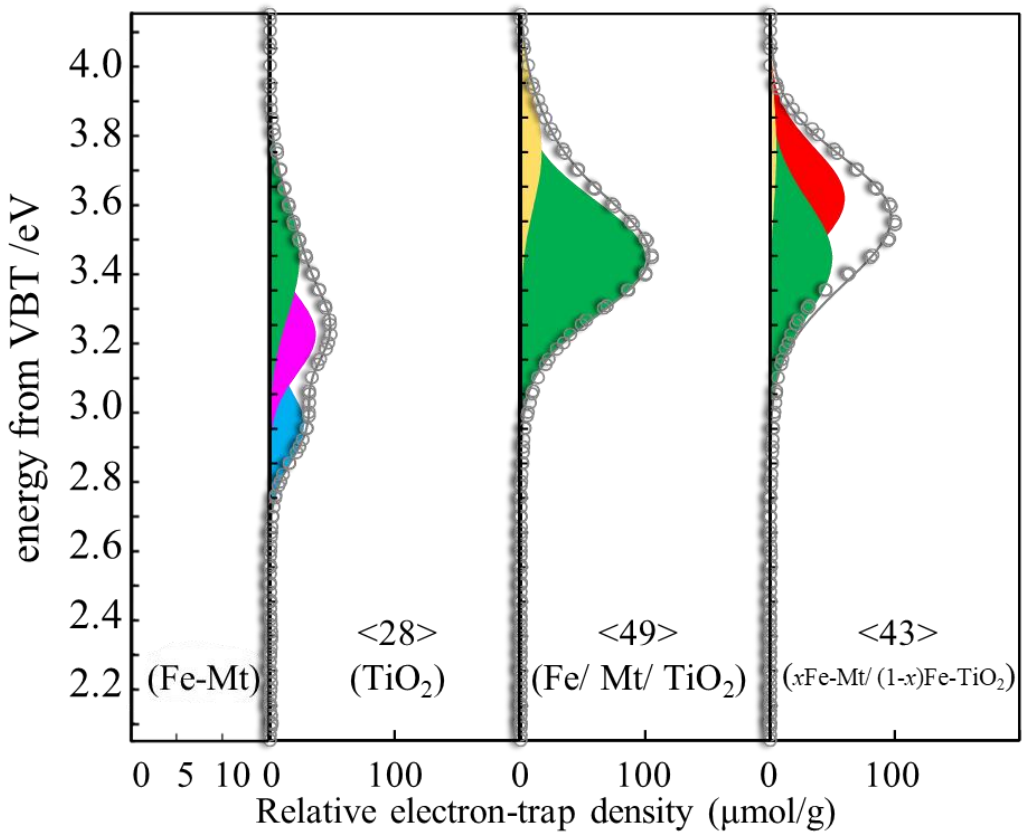

Fig. 5.14. Peak separation of representative energy-resolved distribution of electron traps (ERDTs) patterns of Fe-Mt synthesized at RT, TiO_2, Fe/Mt/TiO_2, and *x*Fe-Mt/(1-*x*)Fe-TiO_2 produced at 70 °C. The ERDTs patterns were displayed as a function of energy (eV) from the valence band top (VBT) paired with CBB. The relative total electron trap density is indicated by the numbers in brackets. Crystal rutile, amorphous rutile, amorphous rutile coated on crystal anatase, and isolated amorphous TiO_2 were assigned to the peaks at 2.96, 3.22, 3.44, and 3.62–3.76 eV and shown in blue, pink, green, yellow, and red. The Fe-Mt as a n-type semiconductor didn't show any peak.

Table 5.4. Parameters of ERDT peak fitting of Fe/Mt/TiO_2 and *x*Fe-Mt/(1-*x*)Fe-TiO_2. c-R, a-R, a-R on c-A, and iso-TiO_2 are the abbreviation of crystal rutile, amorphous rutile, amorphous rutile covered on crystal anatase, and isolated amorphous TiO_2, respectively.

Sample	Peak Assignment	Peak Position (eV)	Relative Intensity (%)
TiO_2	c-R	2.96	31.1
	a-R	3.22	42.0
	a-R on c-A	3.44	27.0
	iso-TiO_2	3.62	N.D.
	iso-TiO_2	3.76	N.D.
Fe/Mt/TiO_2	c-R	2.96	N.D.
	a-R	3.22	N.D.
	a-R on c-A	3.44	43.5
	iso-TiO_2	3.62	52.2
	iso-TiO_2	3.76	4.3
*x*Fe-Mt/(1-*x*)Fe-TiO_2	c-R	2.96	N.D.
	a-R	3.22	N.D.
	a-R on c-A	3.44	85.4
	iso-TiO_2	3.62	N.D.
	iso-TiO_2	3.76	14.6

5.3.5 Radical scavenger tests

The photocatalytic reaction is triggered by the radicals created during the light irradiation process. Radical scavengers were applied throughout the photocatalytic degradation of phenol in Fe/Mt/TiO_2, which is the best photocatalyst, to discover which radical can be formed largely

during the photocatalytic activity (**Fig. 5.15**). The h^+ scavenger is ethanol, while the $\cdot OH^-$ scavenger is isopropanol. With a rate constant of 0.014 for both, the addition of ethanol and isopropanol had a minor effect on the photocatalytic activity of the Fe/Mt/TiO_2. It means that the main radical sources for the photocatalytic reaction should not be h^+ and $\cdot OH^-$. With the addition of para-benzoquinone, an $\cdot O_2^-$ radical scavenger, the photocatalytic degradation of phenol was significantly reduced, with a rate constant of 0.010. As a result, the dominating radical in the photocatalytic breakdown of phenol is oxygen. This is understandable because the VB predicted from XPS data was higher than the $\cdot OH^-$ production's reduction potential. As a result, the Fe/Mt/TiO_2 system should not directly create the $\cdot OH^-$ radical.

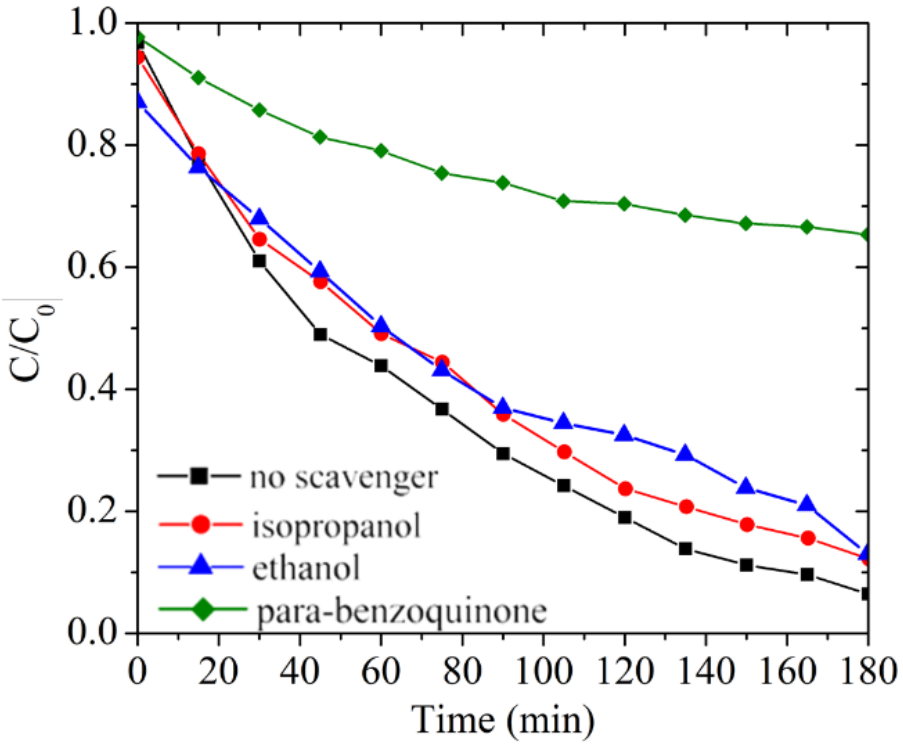

Fig. 5.15. Effects of radical scavengers (ethanol, isopropanol, and para-benzoquinone) on photocatalytic phenol degradation in Fe/Mt/TiO_2 composites manufactured at 70°C. The $\cdot OH^-$ scavenger is isopropanol, the h^+ scavenger is ethanol, and the $\cdot O_2^-$ scavenger is para-benzoquinone.

5.3.6 Photocatalytic mechanisms

The mechanisms of Fe/Mt/TiO_2 and *x*Fe-Mt/(1-*x*)Fe-TiO_2 might be hypothesized based on the previous findings (**Fig. 5.16**). The crystal anatase will not be immediately exposed on the surface in either composite, but will be in touch with the amorphous rutile, which serves as the major photocatalyst. In the Fe/Mt/TiO_2, the amount of amorphous rutile covered in crystal anatase was roughly twice that of the *x*Fe-Mt/(1-*x*)Fe-TiO_2. In *x*Fe-Mt/(1-*x*)Fe-TiO_2, on the other hand, the amount of isolated amorphous anatase and rutile overlapping with the photocatalytic active sites was substantially higher. These two elements combined to give the Fe/Mt/TiO_2 a higher photocatalytic activity than the *x*Fe-Mt/(1-*x*)Fe-TiO_2. According to DRS and *Eg* measurements, the TiO_2 phase in Fe/Mt/TiO_2 has an *Eg* of 3.24 eV, with VB energy levels of 1.75 eV and CB energy levels of 1.49 eV. Furthermore, the TiO_2 phase in the *x*Fe-Mt/(1-*x*)Fe-TiO_2 has an *Eg* of 3.19 eV, with VB energy levels of 1.95 eV and CB energy levels of -1.24 eV. The Fe/Mt/TiO_2 and *x*Fe-Mt/(1-*x*)Fe-TiO_2 VBTs are both lower than the reduction potential of $\cdot OH^-$ generation [25]. As a result, the photocatalytic breakdown of phenol should be unaffected by h^+ and $\cdot OH^-$. Furthermore, the Fe/Mt/TiO_2 radical scavenger test demonstrated that $\cdot O_2^-$ should be the dominant radical during the photocatalytic reaction. In both composites, the Fe^{III} on the interlayer and surface of the Mt may generate a new Fermi level [25] and form heterojunctions with the bulk TiO_2 to reduce charge recombination and promote electron transport.

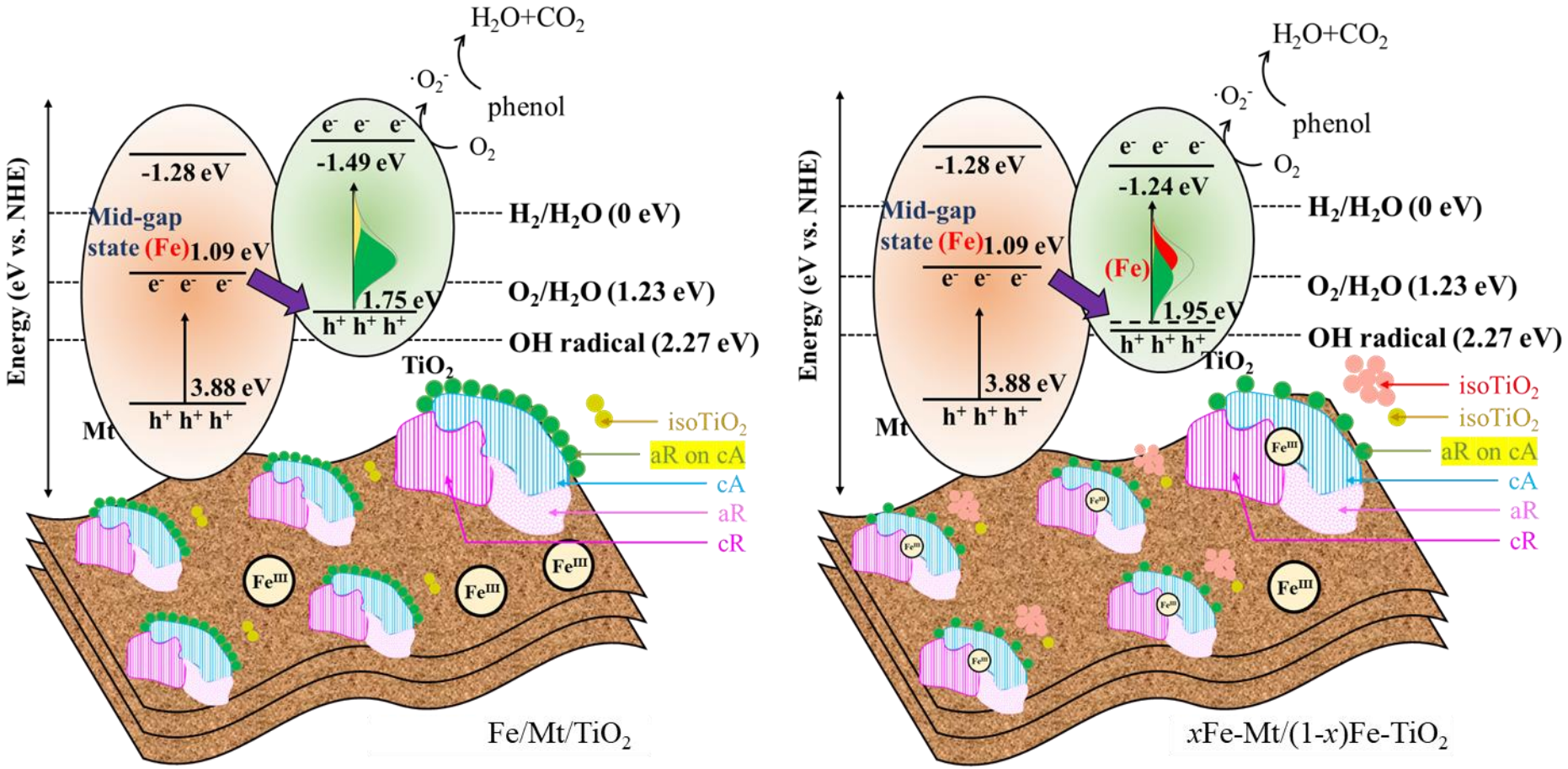

Fig. 5.16. The band edge positions of Fe/Mt/TiO_2 and *x*Fe-Mt/(1-*x*)Fe-TiO_2 with respect to standard hydrogen electrode (SHE), where the E(vs SHE) =− (E(vs vacuum)–4.44) V.

5.4 Conclusions

The Fe/Mt/TiO_2 composite was made by doping Fe^{III} cations into the Mt/TiO_2 composite after it was formed, whereas the *x*Fe-Mt/(1-*x*)Fe-TiO_2 composite was made by doping Fe^{III} cations during the Mt/TiO_2 composite creation. The Fe^{III} cations in the Fe/Mt/TiO_2 were predicted to be on the surface of the composite and in the Mt interlayers, whereas the Fe^{III} cations in the *x*Fe-Mt/(1-*x*)Fe-TiO_2 were predicted to be in the TiO_2 and Mt structures. The varied positions of the doped Fe^{III} in the composite interfere with the TiO_2 content in the composite being formed. The Fe/Mt/TiO_2 wt% TiO_2 was usually higher (26.91–27.63%) than the *x*Fe-Mt/(1-*x*)Fe-TiO_2 wt% TiO_2 (26.77–27.5%), but the anatase to rutile ratio was always lower (0.92–1.45 for Fe/Mt/TiO_2 and 1.53–1.91 for *x*Fe-Mt/(1-*x*)Fe-TiO_2). Due to the creation of the heterojunction between TiO_2 and Mt, as well as the insertion of Fe^{III} into the composites, both composites' optical and electrochemical characteristics, and photocatalytic phenol degradation activity, were superior than pure TiO_2. The *x*Fe-Mt/(1-*x*)Fe-TiO_2 composite had greater light absorption abilities (*Eg*: 3.19 eV) than the Fe/Mt/TiO_2 composite (*Eg*: 3.24 eV), which was validated by DRS results because the doped Fe^{III} in the TiO_2 structure generates a new electronic state, lowering the *Eg*. The Fe/Mt/TiO_2 had a stronger ability to generate charge, as evidenced by a higher peak intensity in the photocurrent and a smaller radius in the EIS. The Fe/Mt/TiO_2 photocatalytic degradation of phenol was 94.6%, which was greater than the *x*Fe-Mt/(1-*x*)Fe-TiO_2 photocatalytic degradation of 85.1%. These are attributed to larger active fractions of amorphous rutile covered in crystal anatase on the composite's surface (two times higher than *x*Fe-Mt/(1-*x*)Fe-TiO_2, as validated by ERDT data. Furthermore, the $\cdot O_2^-$ radical was crucial in the photocatalytic destruction of phenol. As a result, Fe^{III}-modified Mt/TiO_2 composites could be used as an alternate material for photocatalytic treatment of water contaminants.

References

[1] G. Cerrato, L. Marchese, and C. Morterra, “Structural and morphological modifications of sintering microcrystalline TiO_2: an XRD, HRTEM and FTIR study,” *Applied Surface Science*, vol. 70, pp. 200–205, 1993.

[2] W. Zhaobin, X. Qin, G. Xiexian, E. L. Sham, P. Grange, and B. Delmon, “Titania-modified hydrodesulphurization catalysts: I. Effect of preparation techniques on morphology and properties of TiO_2—Al_2O_3 carrier,” *Appl Catal*, vol. 63, no. 1, pp. 305–317, 1990.

[3] J. Wen, X. Li, W. Liu, Y. Fang, J. Xie, and Y. Xu, “Photocatalysis fundamentals and surface modification of TiO_2 nanomaterials,” *Chinese Journal of Catalysis*, vol. 36, no. 12, pp. 2049–2070, 2015.

[4] J. Wang and Z. Lin, “Dye-sensitized TiO_2 nanotube solar cells with markedly enhanced performance via rational surface engineering,” *Chemistry of Materials*, vol. 22, no. 2, pp. 579–584, 2010.

[5] Z. Bian, T. Tachikawa, W. Kim, W. Choi, and T. Majima, “Superior electron transport and photocatalytic abilities of metal-nanoparticle-loaded TiO_2 superstructures,” *The Journal of Physical Chemistry C*, vol. 116, no. 48, pp. 25444–25453, 2012.

[6] P. D. Cozzoli, E. Fanizza, R. Comparelli, M. L. Curri, A. Agostiano, and D. Laub, “Role of metal nanoparticles in TiO_2/Ag nanocomposite-based microheterogeneous photocatalysis,” *The Journal of Physical Chemistry B*, vol. 108, no. 28, pp. 9623–9630, 2004.

[7] M. V. Dozzi and E. Selli, “Doping TiO_2 with p-block elements: Effects on photocatalytic activity,” *Journal of Photochemistry and Photobiology C: Photochemistry Reviews*, vol. 14, pp. 13–28, 2013.

[8] A. Zaleska, "Doped-TiO_2: a review," *Recent patents on engineering*, vol. 2, no. 3, pp. 157–164, 2008.

[9] S. Fukahori, H. Ichiura, T. Kitaoka, and H. Tanaka, "Capturing of bisphenol A photodecomposition intermediates by composite TiO_2–zeolite sheets," *Applied Catalysis B: Environmental*, vol. 46, no. 3, pp. 453–462, 2003.

[10] N. Todorova, T. Giannakopoulou, S. Karapati, D. Petridis, T. Vaimakis, and C. Trapalis, "Composite TiO_2/clays materials for photocatalytic NOx oxidation," *Appl Surf Sci*, vol. 319, pp. 113–120, 2014.

[11] A. Mohammad, M. E. Khan, M. H. Cho, and T. Yoon, "Fabrication of binary SnO_2/TiO_2 nanocomposites under a sonication-assisted approach: Tuning of band-gap and water depollution applications under visible light irradiation," *Ceramics International*, vol. 47, no. 11, pp. 15073–15081, 2021.

[12] A. Mohammad, M. E. Khan, M. H. Cho, and T. Yoon, "Adsorption promoted visible-light-induced photocatalytic degradation of antibiotic tetracycline by tin oxide/cerium oxide nanocomposite," *Applied Surface Science*, p. 150337, 2021.

[13] M. E. Khan, M. M. Khan, B.-K. Min, and M. H. Cho, "Microbial fuel cell assisted band gap narrowed TiO_2 for visible light-induced photocatalytic activities and power generation," *Sci Rep*, vol. 8, no. 1, pp. 1–12, 2018.

[14] G. Damian, F. Damian, Z. Szakács, G. Iepure, and D. Aştefanei, "Mineralogical and Physico-Chemical Characterization of the Oraşu-Nou (Romania) Bentonite Resources," *Minerals* , vol. 11, no. 9. 2021. doi: 10.3390/min11090938.

[15] F. Laufek, I. Hanusová, J. Svoboda, R. Vašíček, J. Najser, M. Koubova, M. Čurda, F. Pticen, L. Vaculíková, H. Sun, and D. Mašín, "Mineralogical, Geochemical and Geotechnical Study of BCV 2017 Bentonite—The Initial State and the State following

Thermal Treatment at 200 °C," *Minerals* , vol. 11, no. 8. 2021. doi: 10.3390/min11080871.

[16] J. D. DeWitt, P. G. Chirico, M. A. Alessi, and K. M. Boston, "Remote Sensing Inventory and Geospatial Analysis of Brick Kilns and Clay Quarrying in Kabul, Afghanistan," *Minerals* , vol. 11, no. 3. 2021. doi: 10.3390/min11030296.

[17] C. Li, Z. Li, T. Wu, Y. Luo, J. Zhao, X. Li, W. Yang, and X. Chen, "Metallogenic Characteristics and Formation Mechanism of Naomugeng Clay-Type Lithium Deposit in Central Inner Mongolia, China," *Minerals* , vol. 11, no. 3. 2021. doi: 10.3390/min11030238.

[18] C. Belver, J. Bedia, and J. J. Rodriguez, "Titania–clay heterostructures with solar photocatalytic applications," *Applied Catalysis B: Environmental*, vol. 176, pp. 278–287, 2015.

[19] D. Papoulis, S. Komarneni, D. Panagiotaras, E. Stathatos, D. Toli, K.C. Christoforidis, M. Fernández-García, H. Li, S. Yin, T. Sato, and H. Katsuki, "Halloysite–TiO_2 nanocomposites: synthesis, characterization and photocatalytic activity," *Applied Catalysis B: Environmental*, vol. 132, pp. 416–422, 2013.

[20] J. Liu and G. Zhang, "Recent advances in synthesis and applications of clay-based photocatalysts: a review," *Physical Chemistry Chemical Physics*, vol. 16, no. 18, pp. 8178–8192, 2014.

[21] H. Man-Chao, F. Zhi-Jie, and Z. Ping, "Atomic and electronic structures of montmorillonite in soft rock," *Chinese Physics B*, vol. 18, no. 7, p. 2933, 2009.

[22] R. S. Jack, G. A. Ayoko, M. O. Adebajo, and R. L. Frost, "A review of iron species for visible-light photocatalytic water purification," *Environmental Science and Pollution Research*, vol. 22, no. 10, pp. 7439–7449, 2015, doi: 10.1007/s11356-015-4346-5.

[23] K. M. Parida and L. Mohapatra, “Carbonate intercalated Zn/Fe layered double hydroxide: A novel photocatalyst for the enhanced photo degradation of azo dyes,” *Chemical Engineering Journal*, vol. 179, pp. 131–139, 2012, doi: 10.1016/j.cej.2011.10.070.

[24] S. J. Kim, Y. Lee, D. K. Lee, J. W. Lee, and J. K. Kang, “Efficient Co-Fe layered double hydroxide photocatalysts for water oxidation under visible light,” *Journal of Materials Chemistry A*, vol. 2, no. 12, pp. 4136–4139, 2014, doi: 10.1039/c3ta14933a.

[25] C. Chuaicham, Y. Xiong, K. Sekar,W. Chen, L. Zhang, B. Ohtani, I. Babo, and K. Sasaki, “A promising Zn-Ti layered double hydroxide/Fe-bearing montmorillonite composite as an efficient photocatalyst for Cr(VI) reduction: Insight into the role of Fe impurity in montmorillonite,” *Applied Surface Science*, vol. 546, no. December 2020, p. 148835, 2021, doi: 10.1016/j.apsusc.2020.148835.

[26] X. Zheng, Y. Li, W. You, G. Lei, Y. Cao, Y. Zhang, and L. Jiang, “Construction of Fe-doped TiO_{2-x} ultrathin nanosheets with rich oxygen vacancies for highly efficient oxidation of H_2S,” *Chemical Engineering Journal*, vol. 430, p. 132917, 2022.

[27] N. Kanjana, W. Maiaugree, P. Poolcharuansin, and P. Laokul, “Synthesis and characterization of Fe-doped TiO_2 hollow spheres for dye-sensitized solar cell applications,” *Materials Science and Engineering: B*, vol. 271, p. 115311, 2021.

[28] A. Mancuso, O. Sacco, V. Vaiano, D. Sannino, S. Pragliola, V. Venditto, and N. Morante, “Visible light active Fe-Pr co-doped TiO_2 for water pollutants degradation,” *Catalysis Today*, 2021.

[29] F. Kara, M. Kurban, and B. Coşkun, “Evaluation of electronic transport and optical response of two-dimensional Fe-doped TiO_2 thin films for photodetector applications,” *Optik (Stuttg)*, vol. 210, p. 164605, 2020.

[30] W. Pezeshkian and S. J. Marrink, “Simulating realistic membrane shapes,” *Current Opinion in Cell Biology*, vol. 71, pp. 103–111, 2021.

[31] D. J. Lapworth, N. Baran, M. E. Stuart, and R. S. Ward, “Emerging organic contaminants in groundwater: a review of sources, fate and occurrence,” *Environmental pollution*, vol. 163, pp. 287–303, 2012.

[32] G. L. Daly and F. Wania, “Organic contaminants in mountains,” *Environ Sci Technol*, vol. 39, no. 2, pp. 385–398, 2005.

[33] I. Alkorta and C. Garbisu, “Phytoremediation of organic contaminants in soils,” *Bioresour Technol*, vol. 79, no. 3, pp. 273–276, 2001.

[34] J. Kim, P. Du, W. Liu, C. Luo, H. Zhao, and C.-H. Huang, “Cobalt/Peracetic acid: advanced oxidation of aromatic organic compounds by acetylperoxyl radicals,” *Environ Sci Technol*, vol. 54, no. 8, pp. 5268–5278, 2020.

[35] B. C. Hodges, E. L. Cates, and J.-H. Kim, “Challenges and prospects of advanced oxidation water treatment processes using catalytic nanomaterials,” *Nature Nanotechnology*, vol. 13, no. 8, pp. 642–650, 2018, doi: 10.1038/s41565-018-0216-x.

[36] S. Mohammadi, A. Kargari, H. Sanaeepur, K. Abbassian, A. Najafi, and E. Mofarrah, “Phenol removal from industrial wastewaters: a short review,” *Desalination and Water Treatment*, vol. 53, no. 8, pp. 2215–2234, 2015.

[37] J. Jover, R. Bosque, and J. Sales, “Neural network based QSPR study for predicting pKa of phenols in different solvents,” *Qsar & Combinatorial Science*, vol. 26, no. 3, pp. 385–397, 2007.

[38] A. Srikhaow, S. M. Smith, K. Uraisin, K. Suttiponparnit, C. Kongmark, and C. Chuaicham, “Catalytic remediation of phenol contaminated wastewater using Cu–Zn hydroxide nitrate,” *RSC Adv*, vol. 6, no. 43, pp. 36766–36774, 2016.

[39] Y. Zhang, H. Gan, and G. Zhang, "A novel mixed-phase TiO_2/kaolinite composites and their photocatalytic activity for degradation of organic contaminants," *Chemical Engineering Journal*, vol. 172, no. 2–3, pp. 936–943, 2011.

[40] Y. Zhang, Y. Guo, G. Zhang, and Y. Gao, "Stable TiO_2/rectorite: preparation, characterization and photocatalytic activity," *Appl Clay Sci*, vol. 51, no. 3, pp. 335–340, 2011.

[41] Y. Wang, L. Zhang, K. Deng, X. Chen, and Z. Zou, "Low temperature synthesis and photocatalytic activity of rutile TiO_2 nanorod superstructures," *The Journal of Physical Chemistry C*, vol. 111, no. 6, pp. 2709–2714, 2007.

[42] B. Tansel, "Significance of thermodynamic and physical characteristics on permeation of ions during membrane separation: Hydrated radius, hydration free energy and viscous effects," *Separation and Purification Technology*, vol. 86, pp. 119–126, 2012, doi: 10.1016/j.seppur.2011.10.033.

[43] H. Liu, D. Chaudhary, S. Yusa, and M. O. Tadé, "Glycerol/starch/Na^+-montmorillonite nanocomposites: A XRD, FTIR, DSC and 1H NMR study," *Carbohydrate Polymers*, vol. 83, no. 4, pp. 1591–1597, 2011.

[44] B. Bharti, S. Kumar, H.-N. Lee, and R. Kumar, "Formation of oxygen vacancies and Ti^{3+} state in TiO_2 thin film and enhanced optical properties by air plasma treatment," *Sci Rep*, vol. 6, no. 1, pp. 1–12, 2016.

[45] H. Lv, H. Zhao, T. Cao, L. Qian, Y. Wang, and G. Zhao, "Efficient degradation of high concentration azo-dye wastewater by heterogeneous Fenton process with iron-based metal-organic framework," *Journal of Molecular Catalysis A: Chemical*, vol. 400, pp. 81–89, 2015.

[46] W. Jichao, “On the cultivation of science college students’ innovative and entrepreneurial ability,” *Journal of China University of Petroleum (Edition of Social Sciences)*, vol. 5, pp. 106–109, 2016.

[47] L. Wu, Y. Li, S. Li, Z.. Li, G.. Tang, W. Qi, L. Xue, X. Ge, and L. Ding, “Method for estimating ionicities of oxides using O1s photoelectron spectra,” *AIP Advances*, vol. 5, no. 9, p. 97210, 2015.

[48] C. Chuaicham, S. Karthikeyan, R.R. Pawar, Y. Xiong, I. Dabo, B. Ohtani, Y. Kim, J. Tae Song, T. Ishihara, and K. Sasaki, “Energy-resolved distribution of electron traps for O/S-doped carbon nitrides by reversed double-beam photoacoustic spectroscopy and the photocatalytic reduction of Cr (VI),” *Chemical Communications*, vol. 56, no. 26, pp. 3793–3796, 2020.

[49] T. P. Nguyen and S. Lefrant, “XPS study of SiO thin films and SiO-metal interfaces,” *Journal of Physics: Condensed Matter*, vol. 1, no. 31, p. 5197, 1989.

[50] F. Dong, Z. Zhao, T. Xiong, Z. Ni, W. Zhang, Y. Sun, and W. Ho, “In situ construction of g-C_3N_4/g-C_3N_4 metal-free heterojunction for enhanced visible-light photocatalysis,” *ACS Applied Materials and Interfaces*, vol. 5, no. 21, pp. 11392–11401, 2013, doi: 10.1021/am403653a.

[51] X. Su, J. Yang, X. Yu, Y. Zhu, and Y. Zhang, “In situ grown hierarchical 50%BiOCl/BiOI hollow flowerlike microspheres on reduced graphene oxide nanosheets for enhanced visible-light photocatalytic degradation of rhodamine B,” *Applied Surface Science*, vol. 433, pp. 502–512, 2018, doi: 10.1016/j.apsusc.2017.09.258.

[52] Y. Yamada, T. Nakamura, M. Endo, A. Wakamiya, and Y. Kanemitsu, “Near-band-edge optical responses of solution-processed organic–inorganic hybrid perovskite $CH_3NH_3PbI_3$ on mesoporous TiO_2 electrodes,” *Applied Physics Express*, vol. 7, no. 3, p. 32302, 2014.

[53] K. Sekar *et al.*, "Surfactant-and template-free hydrothermal assembly of Cu_2O visible light photocatalysts for trimethoprim degradation," *Applied Catalysis B: Environmental*, vol. 284, p. 119741, 2021.

[54] K. Sekar, C. Chuaicham, B. Vellaichamy, W. Li, W. Zhuang, X. Lu, B. Ohtani, K. Sasaki, "Cubic Cu_2O nanoparticles decorated on TiO_2 nanofiber heterostructure as an excellent synergistic photocatalyst for H_2 production and sulfamethoxazole degradation," *Applied Catalysis B: Environmental*, vol. 294, p. 120221, 2021.

[55] C. Chuaicham, S. Karthikeyan, J. T. Song, T. Ishihara, B. Ohtani, and K. Sasaki, "Importance of $ZnTiO_3$ phase in ZnTi-mixed metal oxide photocatalysts derived from layered double hydroxide," *ACS Appl Mater Interfaces*, vol. 12, no. 8, pp. 9169–9180, 2020.

[56] S. Sood, A. Umar, S. K. Mehta, and S. K. Kansal, "Highly effective Fe-doped TiO_2 nanoparticles photocatalysts for visible-light driven photocatalytic degradation of toxic organic compounds," *J Colloid Interface Sci*, vol. 450, pp. 213–223, 2015.

[57] T. Ali, P. Tripathi, A. Azam, W. Raza, A.S. Ahmed, A. Ahmed, and M. Muneer, "Photocatalytic performance of Fe-doped TiO_2 nanoparticles under visible-light irradiation," *Materials Research Express*, vol. 4, no. 1, p. 15022, 2017.

[58] M. J. Benotti, B. D. Stanford, E. C. Wert, and S. A. Snyder, "Evaluation of a photocatalytic reactor membrane pilot system for the removal of pharmaceuticals and endocrine disrupting compounds from water," *Water Res*, vol. 43, no. 6, pp. 1513–1522, 2009.

[59] A. Nitta, M. Takashima, N. Murakami, M. Takase, and B. Ohtani, "Reversed double-beam photoacoustic spectroscopy of metal-oxide powders for estimation of their energy-resolved distribution of electron traps and electronic-band structure," *Electrochimica Acta*, vol. 264, pp. 83–90, Feb. 2018, doi: 10.1016/j.electacta.2017.12.160.

[60] D. Su, S. Dou, and G. Wang, “Anatase TiO_2: better anode material than amorphous and rutile phases of TiO_2 for Na-ion batteries,” *Chemistry of Materials*, vol. 27, no. 17, pp. 6022–6029, 2015.

[61] M. M. Viana, N. D. S. Mohallem, D. R. Miquita, K. Balzuweit, and E. Silva-Pinto, “Preparation of amorphous and crystalline Ag/TiO_2 nanocomposite thin films,” *Applied Surface Science*, vol. 265, pp. 130–136, 2013.

[62] M. Lottiaux, C. Boulesteix, G. Nihoul, F. Varnier, F. Flory, R. Galindo, and E. Pelletier, “Morphology and structure of TiO_2 thin layers vs. thickness and substrate temperature,” *Thin Solid Films*, vol. 170, no. 1, pp. 107–126, 1989.

Chapter 6

Conclusions

Simple Fe^{III} adsorption in acid produced Fe^{III}-doped Mt. Intercalation of $Fe^{II/III}$ moved the 001 diffraction peak of changed materials, including H/Mt and Fe/Mt. Ion release and adsorption were confirmed by ICP-OES and AAS. FTIR, XPS, and XANES validated these findings. It confirms the intercalated Fe form in the Fe/ Mt structure. The acid changes also eroded the Mt surface, which was damaged when Fe^{III} was introduced since Fe^{III} can replace Al in the Mt structure. The performance of Fe^{III}-doped Mt samples for photocatalytic Cr^{VI} redox remediation was clearly improved due to improved light adsorption, decreased Eg, and improved electron density and transfer. Fermi levels between VB and CB in the Mt structure may be responsible for the improved optical characteristics in Fe/ Mt. However, the redundant Fe^{III} inhibited Cr^{VI} contact with the active surface and light shielding. As a photocatalyst, modified clay can now be used for wastewater treatment and beyond.

Fe^{III} speciation was maintained as a trivalent cation during the synthesis of Fe-Mt/TiO_2 and Mt/Fe-TiO_2 composites by keeping the pH below 2, and the position of Fe^{III} was regulated by adding Fe^{III} sources at two distinct points in the Fe/Mt/TiO_2 and Mt/Fe-TiO_2 synthesis procedures. Fe^{III} resides on Mt in the Fe-Mt/TiO_2 system, whereas Fe^{III} exists in TiO_2 in the Mt/Fe-TiO_2 system. When compared to the influence from the position of Fe^{III}, as demonstrated by XRF and peak fitting of XRD, the synthesis temperature had minor effect on TiO_2 content and anatase/rutile ratio. TEM also revealed a cross between anatase and rutile. DRS, PL, photocurrent, and EIS measurements revealed that Fe-Mt/TiO_2 has a narrower *Eg*, better recombination removal, a more significant reaction to irradiation, and lower charge transfer resistance than Mt/Fe-TiO_2. At 3 hours, Fe-Mt/TiO_2 achieved 71.8 percent - 72.5 percent photocatalytic destruction of phenol, while Mt/Fe-TiO_2 achieved 68.7% - 69.6% photocatalytic decomposition of phenol. At various reaction intervals, the intermediate products were also deduced using the chorograms. The remarkable photocatalytic property of Fe-Mt/TiO_2 was

consistent with its superior photocatalytic performance for the photocatalytic degradation of phenol, which was attributed to the critical role of Fe/Mt in Fe-Mt/TiO_2 as a semiconductor crossing with TiO_2 to form a heterojunction, despite the fact that Mt in Mt/Fe-TiO_2 was still an insulator. The electron structure of Fe/Mt and TiO_2 in Fe-Mt/TiO_2, as well as TiO_2 in Mt/Fe-TiO_2, was seen using a combination of DRS, VB XPS, ERDT, and radical scavenger test. During the photocatalytic reaction, the $^{\bullet}O_2^-$ radical was the dominating radical. The findings suggest that photocatalytic reactions on Mt and Fe^{III}-containing clay may occur.

The Fe/Mt/TiO_2 composite was made by doping Fe^{III} cations into the Mt/TiO_2 composite after it was formed, whereas the *x*Fe-Mt/(1-*x*)Fe-TiO_2 composite was made by doping Fe^{III} cations during the Mt/TiO_2 composite creation. The Fe^{III} cations in the Fe/Mt/TiO_2 composite should be found on the surface and in the interlayers of the Mt, whereas the Fe^{III} cations in the *x*Fe-Mt/(1-*x*)Fe-TiO_2 composite should be found in the TiO_2 and Mt structures. The varied positions of the doped Fe^{III} in the composite interfere with the TiO_2 content in the composite being formed. The Fe/Mt/TiO_2 had a higher TiO_2 wt% (26.91–27.63%) than the *x*Fe-Mt/(1-*x*)Fe-TiO_2 (26.77–27.50%), although the anatase to rutile ratio was usually lower (0.92–1.45 for Fe/Mt/TiO_2 and 1.53–1.91 for *x*Fe-Mt/(1-*x*)Fe-TiO_2). Due to the creation of the heterojunction between TiO_2 and Mt, as well as the insertion of Fe^{III} into the composites, both composites' optical and electrochemical characteristics, as well as photocatalytic phenol degradation activity, were superior than pure TiO_2. Because the doped Fe^{III} in the structure of the TiO_2 provides a new electronic state to reduce the *Eg*, the *x*Fe-Mt/(1-*x*)Fe-TiO_2 composite demonstrated greater light absorption abilities (Eg: 3.19 eV) than the Fe/Mt/TiO_2 composite (Eg: 3.24 eV), as proven by DRS results. The Fe/Mt/TiO_2 combination, on the other hand, had a greater charge production ability, as evidenced by a higher peak intensity in the photocurrent and a smaller radius in the EIS. The Fe/Mt/TiO_2 photocatalytic degradation of phenol was 94.6%, which was greater than the *x*Fe-Mt/(1-*x*)Fe-TiO_2 photocatalytic degradation of 85.1%.

These are attributed to larger active fractions of amorphous rutile covered in crystal anatase on the composite's surface (two times higher than *x*Fe-Mt/(1-*x*)Fe-TiO_2, as validated by ERDT data. Furthermore, the $^{\bullet}O_2^-$ radical was crucial in the photocatalytic destruction of phenol. As a result, Fe^{III}-modified Mt/TiO_2 composites could be used as an alternate material for photocatalytic treatment of water contaminants.

To sum up, Fe^{III}, Mt, and TiO_2 have the potential to be extensively used in practice and application because of no emission of second contamination. Moreover, nature abounds in all three substances. Thus, the highly conceivable combination could activate a photocatalytic reaction in nature especially in the shallow water system and in the atmosphere. Besides, TiO_2 already been commercially utilized, the addition of montmorillonite or other clay minerals may further improve the photocatalytic efficiency of the main photocatalyst, not only as a supporting material, but also trigger the red shift of the light adsorption for the TiO_2 composed with clay with the controlling effect of Fe^{III}.

Acknowledgement

First, want to thank Prof. Keiko Sasaki for her advice, support, constructive criticism, and encouragement. She spent countless hours on my Ph.D. research, presentation practice, and manuscript. Besides, her scientific research spirit of continuous knowledge and exploration encourages me to continue to understand the field of scientific research. I am glad to be her student.

The committee members for my evaluation, Assoc. Prof. Hajime Miki at the Department of Earth Resources Engineering, Kyushu University, and Prof. Kunihiko Nakashima at the Department of Materials Science and Engineering, Kyushu University, deserve sincere thanks for their advice, comments, encouragement, and inspiration for other research applications.

I also want to express my thanks to Prof. Bunsho Ohtani at Institute for Catalysis, Hokkaido University, for reversed double-beam photoacoustic spectroscopy experiment.

I am also grateful to Assoc. Prof. Zhen Li at the Department of Resources and Environment, Nanjing Agricultural University, China, who sent me to Prof. Keiko Sasaki, and constantly give me encouragement, support, and advice.

Prof. Tsuyoshi Hirajima and Assoc. Prof. Naoko Okibe provided advise, insightful comments, and assistance. Also, thank Ms. Makiko Samba.

Dr. Chitiphon Chuaicham has my sincere gratitude. He gave me vital assistance, training, and criticisms for me to accompalish my Ph.D. I also appreciate the members of the mineral processing, recycling, and environmental remediation laboratory, Dr. Binglin Guo, Dr. Karthikeyan Sekar, Dr. Balakumar Vellaichamy, Dr. Gde Pandhe Wisnu Suyantara, Dr. Kojo Twum Konadu, Dr. Quanzhi Tian, Dr. Mengmeng Wang, Kaiqian Shu, Diego Moizes

Mendoza Flores, Shugo Nagato, Ryoutaro Sakai, Yuki Semoto, Kaito Hayashi, Cindy, Takumi Inoue, Taiki Kondo, Hiroki Fukuda, Efendi Rihan, Berdakh Danitarov, Idol Phann, Yuika Kaeazoe, Ryoji Ogi, Ikumi Suyama, Yuto Noguchi, Shigo Yoshida, Dr. Keishi Oyama, Dr. Santisak Kitjanukit, Niko Dian Pahlevi, Shunsuke Imamura, Shingou Nakama, Yuta Kamura, Yoshikazu Hayashi, Yusuke Hotta, Yuta Era, Tanaka Yu, Kyohei Takamatsu, and others at mineral processing lab members for helping, discussions, suggestions, and friendship.

My mother Shumei Liu, fiancé Ren Zhu, and family are my primary sources of support. I love you. Your support and encouragement were crucial. I am also appreciating my dear friends, Kaixuan Wu, Yunxiao Hu, Kailing Huang, and Yajun Jiang. I am so lucky to have you supporting me. Thank you, Jiuzhou Tang, Yizhou Luo, and the group chat "*Fengzhengxian*", you gave me a healing accompany.

Last but not least, I'm grateful to the Advanced Graduate Program in Global Strategy for Green Asia for financing my degree. Hokkaido University's Institute for Catalysis supported the reversed double-beam photoacoustic spectroscopy experiment.